To the Graduate Council:

I am submitting herewith a dissertation written by Peng Liu entitled "Fundamental Studies of Hydrogen Attack in C-0.5Mo Steel and Weldments Applied in Petroleum and Petrochemical Industries." I have examined the final copy of this dissertation for form and content and recommend that it be accepted in partial fulfillment of the requirements for the degree of Doctor of Philosophy, with a major in Metallurgical Engineering.

Carl D. Lundin, Major Professor

We have read this dissertation
and recommend its acceptance:

Charlie R. Brooks

Raymond A. Buchanan

David C. Joy

Accepted for the Council:

Interim Vice Provost and
Dean of The Graduate School

Fundamental Studies of Hydrogen Attack in C-0.5Mo Steel and Weldments Applied in Petroleum and Petrochemical Industries

A Dissertation Presented for the

Doctor of Philosophy

Degree

The University of Tennessee, Knoxville

Peng Liu

August 2001

DEDICATION

This dissertation is dedicated to

My parents

Mr. Zhizhong Liu
刘志忠

Mrs. Shuyun C. Liu
曹树云

My wife and son

Dongqing L. Liu
李冬青

Yiming Liu
刘一鸣

for their love, faith, and strength

ACKNOWLEDGMENTS

The author sincerely acknowledges his major advisor, Dr. Carl D. Lundin, for his invaluable guidance, encouragement, and support throughout his graduate study and research. Sincere appreciation is also extended to the committee members, Dr. Charlie R. Brooks, Dr. Raymond A. Buchanan, and Dr. David C. Joy for their academic advice and encouragement.

The financial support provided through The Materials Properties Council / The American Petroleum Institute (MPC/API) is gratefully acknowledged. Expert advice from Dr. Martin Prager, Executive Director of Materials Properties Council, is especially acknowledged. The author appreciates the assistance from Chevron Research and Technology Company, Equilon Enterprises LLC (Shell & Texaco), BP Oil Company, Arco Products Company, Koch Petroleum Group, and Japan Steel Works, Ltd., who supplied the experimental materials.

Grateful appreciation is extended to Dr. John R. Dunlap, Mr. Gregory L. Jones, and Mr. Raymond Bellamy for their technical assistance for utilizing electron microscope facilities and sample assembly. The author sincerely expresses his thanks to Mr. Yan Cui, Mrs. Songqing Wen, and Mr. Mark Morrison for their generous help.

ABSTRACT

High temperature hydrogen attack (HTHA) is a form of surface decarburization, internal decarburization, and / or intergranular cracking in steels exposed to high temperature (> 400°F) and high hydrogen pressure. Hydrogen attack is an irreversible process which can cause permanent damage resulting in degradation of mechanical properties and failures such as leakage, bursting, fire, and/or explosion.

The continuous progression of hydrogen attack in C-0.5Mo steel and weldments below the C-0.5Mo Nelson Curve has caused a significant concern for the integrity and serviceability of C-0.5Mo steel utilized for pressure vessels and piping in the petroleum refinery and petrochemical industries. In accord with the demands of these industries, fundamental studies of hydrogen attack in C-0.5Mo steel and weldments were accomplished in terms of:

(1) Quantitative methodologies for hydrogen damage evaluation;

(2) Hydrogen damage assessment of service exposed weldments and autoclave exposed materials;

(3) Effects of carbon and alloying elements, heat treatments, hot and cold working, welding processes and postweld heat treatment (PWHT) on hydrogen attack susceptibility;

(4) Development of continuous cooling transformation (CCT) diagrams for C-0.5Mo base metals and the coarse grained heat-affected zone (CGHAZ);

(5) Carbide evaluation for the C-0.5Mo steel after service exposure and heat treatment;

(6) Methane evolution by the reaction of hydrogen and carbides;

(7) Hydrogen diffusion and methane pressure through the wall thickness of one-sided hydrogen exposure assembly;

(8) Hydrogen attack mechanism and hydrogen attack limit modeling.

In conjunction with this research, a state-of-the-art literature review was implemented to provide a comprehensive overview of the published research efforts on hydrogen attack studies. The evolution of "Nelson Curves" for carbon steel, C-0.5Mo, and Cr-Mo steels was historically reviewed in regard to design applications and limitations. Testing techniques for hydrogen attack assessment were summarized under the categories of hydrogen exposure testing, mechanical evaluation, and dilatometric swelling testing.

In this study, 24 heats extracted from service exposed C-0.5Mo steel components were received for hydrogen attack evaluation using quantitative metallographic analysis, "Cryo-cracking" fractographic technique, methane determination, carbon concentration measurements, and advanced ultrasonic testing technique. Hydrogen attack damage was found in 9 out of the 24 service exposed heats. The hydrogen damaged heats were operated below the C-0.5Mo Nelson Curve with the exception of MPC-15 (on the Nelson Curve).

Hydrogen damage parameters in terms of the fraction of damaged grain boundary length (FL%) and the fraction of damaged grain boundary area (FA%)

were defined for quantitative damage evaluation using optical light microcopy (OLM), scanning electron microscopy (SEM), and image analysis software (NIH Image). Hydrogen attack damage profiles were determined within the wall of service damaged heats and the one-side exposed assembly. It was found that hydrogen attack damage is extensive adjacent to the surface exposed to hydrogen and progressively decreases through the wall thickness. The progression of hydrogen attack in terms of methane bubble nucleation, bubble coalescence, and microcracking was revealed through the wall thickness using OLM and SEM. The SEM "Cryo-cracking" technique was demonstrated as a unique method for hydrogen damage evaluation and methane bubble size determination. A relationship of bubble size and the fraction of damaged grain boundaries (FL%, FA%) was established. Methodologies for hydrogen damage examination are recommended based on the morphology of hydrogen attack damage in terms of isolated bubbles and aligned bubbles (SEM) or microcracks (UT, OLM, SEM).

Methane concentration was determined by measuring hydrogen dissociated from methane using gas chromatography and Leco vacuum fusion methods. A relationship of hydrogen damage (FA%, FL%) and methane concentration was established for hydrogen damage assessment using methane determination approach.

One-side hydrogen exposure testing was developed by using a box-like assembly to simulate the hydrogen attack condition of pressure vessels and

piping. The box-like assembly was designed with a sloping wall. The one-side hydrogen exposure testing successfully simulated hydrogen attack behavior in pressure vessels and piping. A gradient of hydrogen damage was observed within the wall thickness using SEM and methane determination. In accordance with the examination of the maximum damaged depth for three sections with different wall thickness (44 mm, 29 mm, and 13 mm), it was found that the fraction of damaged depth is independent of the wall thickness if the exposure condition is the same and a steady state hydrogen gradient is established.

The effects of carbon, alloying elements, heat treatment, welding, postweld heat treatment, and hot and cold working on hydrogen attack susceptibility were investigated. It is demonstrated that low carbon and the addition of carbide-forming elements (Mn, V, Cr) in steel enhances the resistance to hydrogen attack.

The CGHAZ is most susceptible to hydrogen attack in weldments. More extensive hydrogen attack cracks are found in the CGHAZ with low heat input (35 KJ/in, SMAW) than in the CGHAZ with high heat input (100 KJ/in, SMAW). Hydrogen attack susceptibility in the CGHAZ was reduced by postweld heat treatment. Low carbon weld metal and the fine-grained HAZ regions (FGHAZ) were demonstrated to be minimally susceptible to hydrogen attack.

Hydrogen attack susceptibility was ranked for the materials in normalized & tempered (N&T), annealed only, annealed & tempered, and hot & cold worked conditions based on metallographic examination. It was found that the cold

worked and annealed materials are the most susceptible to hydrogen attack. With increase in plastic deformation of cold working, hydrogen attack susceptibility increases as well. The extent of hydrogen attack cracking tends to decrease with an increase in hot working deformation. Hydrogen attack damage is reduced with an increase in tempering temperature. Hydrogen attack susceptibility for the annealed & tempered, N&T, and hot worked materials is similar and they are better than the cold worked and annealed materials.

For microstructure characterization, CCT diagrams were developed for two heats of C-0.5Mo steel (0.21%C, 0.15%C) in heat treatment and welding conditions using Gleeble thermal simulation testing and high speed dilatometry techniques. Microstructures and carbides were studied for the tempered materials using optical light microscopy (OLM), scanning electron microscopy (SEM) and transmission electron microscopy (TEM) coupled with convergent beam diffraction technique and energy dispersive spectroscopy (EDS). The predominant carbides were identified as M_3C for the service exposed heats and N&T materials. During prolonged tempering heat treatment or PWHT (1150°F-15 hours), carbide evolution occurred from M_3C to $M_{23}C_6$ and Mo_2C type carbides. $M_{23}C_6$ and Mo_2C type carbides are more stable in comparison to M_3C and can enhance hydrogen attack resistance.

Methane evolution was investigated by using autoclave exposure testing and methane determination techniques. The results indicate that methane formation starts at the beginning of the hydrogen exposure at 850°F-500 psi H_2.

An in-situ methane bubble nucleation mechanism was proposed based on the volume change caused by hydrogen-carbide reaction.

Equilibrium methane pressure distribution through the wall of one-side exposure assembly was calculated based on hydrogen diffusion and thermodynamics model. Using a criterion of sintering force ($P_{CH4} > 2\sigma / \rho$) the maximum damage depths of one-side exposed samples were calculated and demonstrated to be consistent with the measurement results.

A hydrogen attack mechanism was developed for one-side hydrogen exposure. Reaction of hydrogen and carbon or carbides occurs through the wall thickness simultaneously resulting in the formation of methane bubbles at grain boundaries or carbide/matrix interfaces. Methane bubbles may nucleate in-situ where the reaction of carbides (Fe_3C) and hydrogen occurs. The rates of methane formation, bubble nucleation and growth depend on hydrogen pressure and temperature. Because of the hydrogen concentration gradient within the wall, methane bubble nucleation rate is more rapid near the surface exposed to the hydrogen than for a distance from the surface. With the reaction of hydrogen and carbides or carbon and accumulation of methane, methane pressure builds up in the bubbles. Consequently, a gradient of methane pressure is established within the wall. Methane bubbles grow when the methane pressure is greater than the sintering force ($2\sigma/\rho$). Therefore, a gradient of hydrogen attack damage and a maximum damaged depth were observed through the wall as demonstrated in the service exposed and one-side exposed assembly.

In accordance with the investigation of the database used for C-0.5Mo Nelson Curve development, it was found that the C-0.5Mo Nelson Curve in API Publication 941 was defined based on an insufficient and unreliable database. According to the database generated in this research, a modified hydrogen attack limit was defined for C-0.5Mo steel, below which hydrogen attack might not occur for approximately 28 years. The modified hydrogen attack limit is below the carbon steel Nelson Curve in API Publication 941. Because hydrogen attack is a time-dependent process, it is suggested that the time for safe operation should be stated on Nelson Curves.

A model of hydrogen attack limit for C-0.5Mo steel was developed by applying a critical value of -9.0 to the hydrogen attack parameter (P_w). The hydrogen attack limit calculated by using the model satisfies the modified hydrogen attack limit defined in this research. Based on this model, the exposure time for the C-0.5Mo Nelson Curve defined in API Publication 941 was determined as 10,500 hours (14 months). It further indicates that the C-0.5Mo Nelson Curve defined in API Publication 941 is not valid for long term operating conditions. This model emphasizes that hydrogen attack is a time dependent process. In addition to the operating temperature and hydrogen partial pressure, safe operational times should be stated on the Nelson Curves.

TABLE OF CONTENTS

1. INTRODUCTION 1

2. LITERATURE REVIEW 10

2.1 Nelson Curves 10

2.2 Methodology for Hydrogen Attack Evaluation 13

2.2.1 Autoclave Exposure Techniques 13

2.2.2 Tensile Testing 17

2.2.3 Charpy Impact Testing 26

2.2.4 Creep Rupture Testing 26

2.2.5 Wedge-Opening Loading Testing 28

2.2.6 Dilatometric Swelling Testing 31

2.3.7 Nondestructive Examination of Hydrogen Attack 33

2.3 Characteristics of Hydrogen Attack 38

2.3.1 Incubation 38

2.3.2 Hydrogen Attack Damage Morphology 39

2.3.3 Heat Treatment Effect 40

2.3.4 Alloying Element Effects 52

2.3.5 Hydrogen and Carbide Reaction 55

2.3.6 Hydrogen Attack Modeling 62

3. MATERIALS AND EXPERIMENTAL PROCEDURES 64

3.1 Materials 64

3.2 Experimental Procedures 71

3.2.1 Hydrogen Service Exposure 71

3.2.2 Hydrogen Autoclave Exposure 71

3.2.3 Metallographic Evaluation 80

3.2.4 Methane Determination 83

3.2.5 Carbon Determination 84

3.2.6 Hardness Testing..... 86
3.2.7 Gleeble Simulation and Dilatometry..... 86
3.2.8 Ultrasonic Testing 87

4. EXPERIMENTAL RESULTS AND DISCUSSION..... 89
4.1 Hydrogen Attack Damage in Service Exposed Components..... 89
4.1.1 Hydrogen Attack in Heat Exchanger (MPC-18, 19, & 20)..... 90
4.1.1.1 Ultrasonic Inspection..... 93
4.1.1.2 Metallographic Examination..... 97
4.1.1.3 Quantification of Hydrogen Damage..... 112
4.1.1.4 Methane Determination..... 144
4.1.1.5 Carbon Concentration and Hardness..... 150
4.1.1.6 Stress Assessment..... 154
4.1.2 MPC-9..... 156
4.1.2.1 Metallographic Evaluation..... 156
4.1.2.2 Hydrogen Damage Quantification..... 163
4.1.2.3 Carbon Concentration..... 165
4.1.3 MPC-11..... 167
4.1.3.1 Ultrasonic Inspection..... 167
4.1.3.2 Hydrogen Damage Quantification..... 168
4.1.4 MPC-21 and MPC-22..... 175
4.1.5 MPC-26 and MPC-27..... 180
4.1.6 Summary of Service Exposed Component Evaluation..... 186
4.2 Evaluation of Hydrogen Attack in Autoclave Exposed Samples..... 190
4.2.1 Hydrogen Attack Damage in One-Side Exposed Assembly..... 190
4.2.1.1 Metallographic Evaluation..... 191
4.2.1.2 Methane Determination..... 202
4.2.2 Effects of Carbon and Alloying Elements..... 207
4.2.3 Heat Treatments..... 210

4.2.4 Welding and PWHT..... 217
4.2.5 Hot and Cold Working..... 221
4.2.6 Summary of Autoclave Exposure Results..... 231
4.3 Phase Transformations and Carbide Evolution..... 233
4.3.1 Heat Treatment CCT Diagrams..... 234
4.3.2 Welding CCT Diagrams..... 237
4.3.3 Carbide Evolution..... 243

5. MECHANISM OF HYDROGEN ATTACK..... 269
5.1 Methane Bubble Nucleation and Methane Evolution..... 271
5.2 Hydrogen Diffusion and Concentration through the Wall of One-Side Exposure Assembly..... 277
5.3 Methane Pressure..... 279
5.4 Hydrogen Attack Mechanism..... 290
5.5 Modeling of Hydrogen Attack Limit (Nelson Curve)..... 296
5.6 Methodology for Hydrogen Attack Evaluation..... 304

6. CONCLUSIONS..... 310

7. FUTURE WORK..... 321

REFERENCES..... 322

VITA..... 340

LIST OF TABLES

Table		
3.1	Chemical composition of the received heats of C-0.5Mo steel for hydrogen attack evaluation (wt%).....	65
3.1	Chemical composition of the received heats of C-0.5Mo steel for hydrogen attack evaluation (wt%, continued).....	66
3.1	Chemical composition of the received heats of C-0.5Mo steel for hydrogen attack evaluation (wt%, continued).....	67
3.2	Available operational conditions for the received heats of C-0.5Mo steel.....	72
4.1	Chemical composition of a long seam weld metal in heat exchanger channel (MPC-18).....	92
4.2	Hydrogen content in the materials without hydrogen exposure.....	147
4.3	Chemical composition of carbon steel (SA-516-70) and C-Mn-0.5Mo (SA-508, SA-533), 1.25Cr-0.5Mo materials (wt%).....	208
4.4	Carbide identification results for annealed and annealed & tempered MPC-25 materials using X-ray diffraction technique.....	262

LIST OF FIGURES

Figure		
1.1	Nelson Curves for carbon steel and 1Cr-0.5Mo, 1.25Cr-0.5Mo, 2.25Cr-1Mo, 2.25Cr-1Mo-V, 3Cr-1Mo, 6Cr-0.5Mo steels in the fifth edition of the API Publication 941.....	3
1.2	Nelson Curves for carbon steel and 1Cr-0.5Mo, 1.25Cr-0.5Mo steels in the fifth edition of the API Publication 941.....	5
2.1	Hydrogen autoclave exposure without stress application.....	14
2.2	Hydrogen autoclave exposure with applied stress.....	16
2.3	Schematic diagram of hydrogen autoclave apparatus for one-side hydrogen exposure.....	18
2.4	Ductility and toughness degradation indices (Φ_R, Φ_E) as a function of hydrogen attack parameter (P_w) for C-0.5Mo steel.....	20
2.5	Ductility and toughness degradation indices (Φ_R, Φ_E) as a function of hydrogen attack parameter (P_w) for the HAZ of C-0.5Mo with and without PWHT.....	21
2.6	Ductility and toughness degradation indices (Φ_R, Φ_E) as a function of hydrogen attack parameter (P_v) for C-0.5Mo steel.....	22
2.7	Ductility and toughness degradation indices (Φ_R, Φ_E) as a function of hydrogen attack parameter (P_v) for the HAZ of C-0.5Mo with and without PWHT.....	23
2.8	Tensile strength degradation of SAE 1020 steel exposed to 525°C (977°F) and 3.5 MN/m^2 (508 psi) for 240 hours....	25
2.9	Creep curves of 2.25Cr-1Mo steel (N&T) with and without hydrogen exposure.....	27

Figure

2.10 Stress rupture in the CGHAZ of 2.25Cr-1Mo weld exposed to hydrogen pressure 3 ksi (850°F-33 ksi-10387 hrs)..... 29

2.11 Flow-diagram of wedge-opening-loading test procedure..... 30

2.12 Schematic diagram of dilatometric apparatus and specimen..... 32

2.13 Dilatometric swelling test result for A516 steel exposed to 4.4 MPa (0.6 ksi) hydrogen pressure at 455°C (850°F)..... 34

2.14 Acoustic emission time delay (time lag) as a function of exposure time (2.8 ksi H_2)..... 37

2.15 Typical methane bubbles in carbon steel after hydrogen exposure..... 41

2.16 Intergranular cracking morphology of hydrogen attack with internal decarburization..... 42

2.17 Effect of tempering temperature on the hydrogen content dissociated from methane gas..... 44

2.18 Effect of the PWHT temperature on the hydrogen content dissociated from methane gas..... 45

2.19 Hydrogen attack critical temperature as a function of the PWHT temperature for simulated HAZ and normalized base metal (C-0.5Mo)..... 48

2.20 Room temperature tensile and hardness results for hydrogen exposed 1.25Cr-0.5Mo steel (520°C/968°F-2.6 ksi H_2-1000 hrs.) in comparison with unexposed condition..... 51

2.21 Influence of hydrogen attack on the ductility of 2.25Cr-1Mo, 2.25Cr-1Mo-V, 3Cr-1Mo-V, and 9Cr-1Mo-V/Nb steels..... 54

2.22 Effect of alloying elements on hydrogen attack in 2.25Cr-1Mo steel..... 56

Figure

2.23	Standard free energy for carbide formation ($\Delta G°$, KJ/mole).....	58
2.24	Effect of Mo on the carbide evolution during tempering.....	60
3.1	Typical microstructures of the received heats of C-0.5Mo steel.....	69
3.2	Typical microstructures of the received heats of C-0.5Mo steel.....	70
3.3	Schematic of the autoclave used for high temperature and high hydrogen pressure exposure testing.....	73
3.4	Schematic of the box-like sample for one-sided hydrogen exposure testing.....	75
3.5	Dimensions of half part of the box-like sample with a sloping wall for one-sided hydrogen exposure testing.....	76
3.6	Photograph of the box-like sample for one-sided hydrogen exposure testing.....	78
3.7	Schematic shown the assembly of one-sided hydrogen exposure testing.....	79
3.8	Oerlikon-Yanaco Hydrogen Analyzer, samplers, and samples encapsulated in quartz tubes for methane determination.....	85
4.1	Operating conditions (temperatures and hydrogen partial pressures) for the service exposed heats superimposed on the Nelson Curve for C-0.5Mo steel.....	91
4.2	A schematic drawing of the sample with a long seam weld extracted from heat exchanger channel (MPC-18) for UT inspection.....	94

Figure

4.3	A typical UT C-scan image of the sample with a long seam weld extracted from heat exchanger channel (central portion, MPC-18).....	95
4.4	Enlarged view of the weld metal area with numerical values of the UT reflection depth (MPC-18).....	96
4.5	Enlarged view of the indication at Location 1 shown in Figure 4.3 (MPC-18).....	98
4.6	Enlarged view of the indication at Location 2 shown in Figure 4.3 (MPC-18).....	99
4.7	Cross section profiles of the reflection depth along A-A and B-B (MPC-18).....	100
4.8	3-D presentation of the C-scan image of the sample with a long seam weld in heat exchanger channel (central portion, MPC-18).....	101
4.9	Cross section of the base metal extracted from heat exchanger channel (central portion, MPC-18).....	103
4.10	Hydrogen attack cracks adjacent to the ID surface of heat changer channel (central portion, MPC-18).....	104
4.11	Hydrogen attack cracks at the location approximately 0.5" depth from the ID surface of heat changer channel (central portion, MPC-18).....	105
4.12	No hydrogen attack damage adjacent to the OD surface of the heat changer channel (central portion, MPC-18).....	106
4.13	Cross section of long seam weld extracted from the central portion of heat exchanger channel (MPC-18).....	107
4.14	Hydrogen attack cracks in the CGHAZ adjacent to the ID (central portion of heat exchanger channel, MPC-18).....	108

Figure

4.15	Hydrogen attack cracks in the FGHAZ adjacent to the ID (central portion of heat exchanger channel, MPC-18).....	110
4.16	No hydrogen attack crack in the long seam weld metal adjacent to the ID (central portion of heat exchanger channel, MPC-18).....	111
4.17	Cross section of the tube sheet for hydrogen attack damage evaluation.....	113
4.18	Hydrogen attack cracks adjacent to the surface of Side A (tube sheet, MPC-20).....	114
4.19	Hydrogen attack cracks at the location of 1 7/8" deep from the surface of Side A (tube sheet, MPC-20).....	115
4.20	Hydrogen attack cracks adjacent to the surface of Side B (tube sheet, MPC-20).....	116
4.21	Schematic to depict the locations where photomicrographs were taken for hydrogen attack damage quantification through wall thickness of heat exchanger channel (MPC-18).....	118
4.22	Comparison of original photomicrograph (a) and enhanced NIH image (b) of hydrogen attack cracks.....	119
4.23	Hydrogen attack damage profiles (FL%) within the wall (central portion and near flange, MPC-18).....	120
4.24	SEM "Cryo-cracking" sample preparation for hydrogen attack evaluation.....	122
4.25	SEM images of hydrogen attack damage with coalesced methane bubbles on the grain boundaries adjacent to the ID surface (central portion of the channel, MPC-18).....	123
4.26	SEM images of hydrogen attack damage with coalesced methane bubbles on the grain boundaries at the location of 6 mm deep from the ID surface (central portion of the channel, MPC-18).....	124

Figure

4.27	SEM images of hydrogen attack damage with methane bubbles along grain boundaries at the location of 19 mm deep from the ID surface (central portion of the channel, MPC-18).....	125
4.28	Hydrogen attack cracking and methane bubbles along grain boundaries on the polished and etched sample adjacent to the ID (central portion of the channel, MPC-18).....	127
4.29	Coalesced methane bubbles along grain boundaries on the polished and etched sample at the location of 6 mm deep from the ID (central portion of the channel, MPC-18).....	128
4.30	Isolated methane bubbles along grain boundaries on the polished and etched sample at the location of 19 mm deep from the ID (central portion of the channel, MPC-18).....	129
4.31	Hydrogen damage profile (FA%) through the wall of the heat exchanger channel (central portion, MPC-18).....	130
4.32	Comparison of FL% (OLM) and FA% (SEM) used to quantify hydrogen damage through the wall of the heat exchanger channel (central portion, MPC-18).....	130
4.33	Figure 4.33 Profile of bubble diameters through the wall of the heat exchanger channel (central portion, MPC-18).....	132
4.34	Coalesced methane bubbles on the grain boundaries adjacent to the ID surface (near flange, MPC-18).....	134
4.35	Methane bubbles along the grain boundaries at the location of 5 mm deep from the ID surface (near flange, MPC-18).....	135
4.36	Hydrogen damage profile (FA%) through wall thickness of heat exchanger channel (near flange, MPC-18).....	136
4.37	Profile of average bubble diameter through wall thickness of the heat exchanger channel (near flange, MPC-18).....	136

Figure

4.38	Hydrogen attack cracks at grain boundaries in polished and etched sample adjacent to the ID (near the flange, MPC-18).....	137
4.39	Methane bubbles initiated at grain boundaries at the location of 5 mm deep from the ID surface in the polished and etched sample (near flange, MPC-18).....	138
4.40	Comparison of hydrogen attack damage profiles (FA%) within the wall of heat exchanger channel in the central portion and near the flange (MPC-18).....	139
4.41	Correlation of methane bubble size and the fraction of damaged grain boundary area (FA%, MPC-18).....	139
4.42	Hydrogen damage profiles in terms of damaged F/F, F/B boundaries and total damaged boundaries (FL%) within the wall of tube sheet (MPC-20).....	141
4.43	Comparison of hydrogen damage profiles of FA% (SEM) .and FL% (OLM) within the wall of tube sheet (MPC-20).....	141
4.44	Typical hydrogen damaged F/F boundaries with methane bubbles and carbides (16 mm from Side A, tube sheet, MPC-20).....	142
4.45	Typical hydrogen damaged F/B boundaries with methane bubbles and carbides (45 mm from Side A, tube sheet, MPC-20).....	143
4.46	Sample extraction in different depths through the wall thickness of heat exchanger channel for methane determination (MPC-18).....	145
4.47	Methane concentration (hydrogen dissociated from methane) profiles within wall thickness of the exchanger channel (central portion, MPC-18).....	146
4.48	Methane concentration (hydrogen dissociated from methane) profiles within wall thickness of the exchanger channel (near flange, MPC-18).....	149

Figure

4.49	Comparison of methane concentration (hydrogen dissociated from methane) profiles within the wall thickness of heat exchanger channel in the central portion and near the flange (MPC-18).....	149
4.50	Relationship of the fraction of damaged grain boundaries (FA%, FL%) and the methane concentration determined by hydrogen measurements.....	151
4.51	Carbon concentration and DCI profiles within the wall thickness of the exchanger channel (central portion, MPC-18).....	151
4.52	Hardness and HDI for the base metal, CGHAZ, and weld metal of the long seam weld (central portion of the channel, MPC-18).....	153
4.53	Hydrogen attack crack and methane bubbles along F/B grain boundary (MPC-9).....	158
4.54	Methane bubbles formed at sub-grain boundaries in bainitic region (MPC-9).....	159
4.55	Methane bubbles along F/F grain boundaries (MPC-9).....	160
4.56	Typical SEM images of methane bubbles and carbides on F/B grain boundaries (MPC-9).....	161
4.57	Typical SEM images of methane bubbles on F/F grain boundaries (MPC-9).....	162
4.58	Hydrogen damage profiles (FA%, FL%) through wall thickness (MPC-9).....	164
4.59	Relationship of methane bubble diameter and fraction of hydrogen damage (FA%, FL%, MPC-9, MPC-18).....	164
4.60	Relationship of hydrogen attack damage (FA%, FL%) and methane content (or hydrogen content, MPC-9, MPC-18).....	166

Figure

4.61	Profiles of carbon concentration and decarburization index (DCI%) through wall thickness (MPC-9).....	166
4.62	3-D presentation of ultrasonic testing C-scan image of hydrogen damage (MPC-11).....	169
4.63	Numerical index of the reflection depth from OD surface in a zoom view area (MPC-11).....	169
4.64	Ultrasonic testing B-scan images of hydrogen damage in two cross sections (MPC-11).....	170
4.65	Hydrogen attack cracks in the heat exchanger shell material (MPC-11).....	171
4.66	Hydrogen attack cracks and internal decarburization in MPC-11.....	173
4.67	Hydrogen damage profile (FL%) through wall thickness (MPC-11).....	174
4.68	Relationship of hydrogen attack damage (FA%, FL%) and methane content.....	174
4.69	Methane concentration through the wall thickness of heat exchanger channel (MPC-21).....	177
4.70	Methane bubbles at the interface of carbides and ferrite matrix (MPC-21).....	178
4.71	SEM images of hydrogen attacked grain boundary in the tube sheet (MPC-22).....	179
4.72	Schematic of the boat sample for hydrogen damage evaluation (MPC-26 and 27).....	181
4.73	Cross section of the boat sample with 410 stainless steel cladding.....	181
4.74	Completely decarburized region adjacent to the interfaces between Ni interlayer and C-0.5Mo steel (MPC-27).....	183

Figure

4.75	Isolated methane bubbles at F/B boundary in MPC-27.....	184
4.76	Isolated methane bubble at F/F boundary in MPC-27.....	185
4.77	Aligned and isolated bubbles adjacent to the outside surface of one-side exposed assembly (44 mm thick, MPC3).....	192
4.78	Isolated bubbles at depth of 18 mm from the outside surface of one-side exposed assembly (44 mm thick, MPC-3).....	193
4.79	Isolated bubbles at depth of 28 mm from the outside surface of one-side exposed assembly (44 mm thick, MPC-3).....	194
4.80	Hydrogen damage profile through the wall of one-side exposed assembly (44 mm thick, MPC-3).....	195
4.81	Hydrogen damage as a function of fraction of wall thickness of one-side exposed assembly (44 mm thick, MPC-3).....	195
4.82	Profile of average bubble diameter through the wall of one-side exposed assembly (44 mm thick, MPC-3).....	197
4.83	Correlation between hydrogen attack damage (FA% and FL%) and average bubble diameter for service exposed and one-side exposed assembly.....	197
4.84	Hydrogen damage profile through the wall of one-side exposed assembly (29 mm thick, MPC-3).....	198
4.85	Hydrogen damage as a function of fraction of wall thickness of one-side exposed assembly (29 mm thick, MPC-3).....	199
4.86	Hydrogen damage profile through the wall of one-side exposed assembly (13 mm thick, MPC-3).....	199

Figure

4.87	Hydrogen damage as a function of fraction of wall thickness of one-side exposed assembly (13 mm thick, MPC-3).....	199
4.88	Hydrogen damage as a function of the fraction of wall thickness for three samples (13, 29, and 44 mm, MPC-3).....	201
4.89	Methane concentration profile through the wall of one-side exposed assembly (44 mm thick, MPC-3).....	203
4.90	Methane concentration as a function of fraction of wall thickness of one-side exposed assembly (44 mm thick, MPC-3).....	203
4.91	Methane concentration profile through the wall of one-side exposed assembly (29 mm thick, MPC-3).....	204
4.92	Methane concentration as a function of fraction of wall thickness of one-side exposed assembly (29 mm thick, MPC-3).....	204
4.93	Methane concentration profile through the wall of one-side exposed assembly (13 mm thick, MPC-3).....	205
4.94	Methane concentration as a function of fraction of wall thickness of one-side exposed assembly (13 mm thick, MPC-3).....	205
4.95	Methane concentration as a function of fraction of wall thickness of the three samples (44, 29, 13 mm thick, MPC-3).....	206
4.96	Relationship of the fraction of damaged grain boundaries (FA%, FL%) and the methane concentration in accordance with the service exposure and one-sided exposure database.....	206
4.97	Effect of Mo/C ratio on hydrogen attack susceptibility of C-0.5Mo.....	209
4.98	Hydrogen attack susceptibility of carbon steel, C-0.5Mo, C-Mn-0.5Mo and 1.25Cr-0.5Mo materials.....	211

Figure

4.99 Hydrogen attack cracking in N&T material (MPC-3, 1650°F-2 hrs. & 1150°F-2 hrs.) after hydrogen exposure at 900°F-900 psi-1248 hrs.+950°F-900 psi-288 hrs..... 213

4.100 Hydrogen attack cracking in annealed only material (MPC-3, 1652°F-3 hrs.) after hydrogen exposure at 900°F-900 psi-1248 hrs.+950°F-900 psi-288 hrs..... 214

4.101 Hydrogen attack cracking in annealed & tempered material (1283°F-15 hrs., MPC-3) after hydrogen exposure at 900°F-900 psi-1248 hrs.+950°F-900 psi-288 hrs..... 215

4.102 Hydrogen attack cracking in annealed & tempered material (1337°F-15 hrs., MPC-3) after hydrogen exposure at 900°F-900 psi-1248 hrs.+950°F-900 psi-288 hrs..... 216

4.103 Hydrogen attack cracks in the CGHAZ of SMAW weld (MPC-15) at heat inputs of 35 KJ/in and 100 KJ/in exposed to 900°F-900 psi H_2-1248 hrs. + 950°F-900 psi H_2-288 hrs.... 219

4.104 Effect of PWHT (1150°F-4hrs.) on hydrogen attack in the CGHAZ (MPC-3)..... 220

4.105 No hydrogen attack damage in the FGHAZ of SMAW with heat input of 100 KJ/in after hydrogen exposure (900°F-900 psi-1248 hrs. + 950°F-900 psi-288 hrs.)..... 222

4.106 Comparison of hydrogen attack susceptibility of autogenous GTAW fusion zone (26 KJ/in) and SMAW weld metal (100 KJ/in) after hydrogen exposure (900°F-900 psi-1248 hrs. + 950°F-900 psi-288 hrs.)..... 223

4.107 Hydrogen attack damage in cold rolled material (MPC-3, 5%, 900°F-900 psi H_2-1248 hrs. + 950°F-900 psi H_2-288 hrs.)..... 225

4.108 Hydrogen attack damage in cold rolled material (MPC-3, 10%, 900°F-900 psi H_2-1248 hrs. + 950°F-900 psi H_2-288 hrs.)..... 226

Figure

4.109 Hydrogen attack damage in cold rolled material (MPC-3, 20%, 900°F-900 psi H_2-1248 hrs. + 950°F-900 psi H_2-288 hrs.)..... 227

4.110 Hydrogen attack damage in hot rolled material (MPC-3, 5%, 900°F-900 psi H_2-1248 hrs. + 950°F-900 psi H_2-288 hrs.)..... 228

4.111 Hydrogen attack damage in hot rolled material (MPC-3, 10%, 900°F-900 psi H_2-1248 hrs. + 950°F-900 psi H_2-288 hrs.)..... 229

4.112 Hydrogen attack damage in hot rolled material (MPC-3, 20%, 900°F-900 psi H_2-1248 hrs. + 950°F-900 psi H_2-288 hrs.)..... 230

4.113 CCT diagram for C-0.5Mo steel with high carbon content (MPC-3, 0.21%C)..... 235

4.114 Martensite microstructure at cooling rate of 6000 C°/min (MPC-3, 463 HV)..... 236

4.115 Microstructure of ferrite and bainite at cooling rate of 20 C°/min (MPC-3, 187 HV)..... 238

4.116 CCT diagram for C-0.5Mo steel with low carbon content (MPC-13, 0.15%C)..... 239

4.117 Welding CCT diagram for the CGHAZ of C-0.5Mo steel with high carbon content (MPC-3, 0.21%C)..... 241

4.118 Welding CCT diagram for the CGHAZ of C-0.5Mo steel with low carbon content (MPC-13, 0.15%C)..... 242

4.119 Carbide morphology in bainitic region (MPC-3, 20 C°/min, SEM)..... 244

4.120 Carbide morphology in bainitic region (MPC-3, 20 C°/min, TEM)..... 245

4.121 Carbide morphology in pearlitic region (MPC-3, 1 C°/min, SEM)..... 246

Figure

4.122 Carbide morphology in pearlitic region (MPC-3, 1 C°/min, TEM)..... 247

4.123 Diffraction pattern of M_3C carbide in the bainitic region (MPC-3, 20 C°/min)..... 248

4.124 EDS spectrum of M_3C carbide (MPC-3, 20 C°/min)..... 248

4.125 Spheroidized carbides in tempered bainite region (MPC-3, 20 C°/min, 1150°F for 15 hrs., SEM)..... 250

4.126 Spheroidized carbides in pearlite region after tempering (MPC-3, 1 C°/min, 1150°F-15 hrs., SEM)..... 251

4.127 Diffraction pattern of $M_{23}C_6$ carbide in tempered bainitic region (MPC-3, 20 C°/min, 1150°F-15 hrs.)..... 252

4.128 EDS spectrum of $M_{23}C_6$ carbide in tempered bainite region (MPC-3, 20 C°/min, 1150°F-15 hrs.)..... 252

4.129 Pearlite microstructure in annealed material (MPC-25)..... 253

4.130 TEM carbide images in pearlitic region of the annealed material (MPC-25)..... 254

4.131 TEM carbide images at F/F grain boundaries and in ferrite grain matrix in the annealed material (MPC-25)..... 255

4.132 A representative EDS spectrum of M_3C carbide in the annealed material (MPC-25)..... 256

4.133 A representative EDS spectrum of Mo_2C carbide in the annealed material (MPC-25)..... 256

4.134 Spheroidized carbides in pearlite region in the annealed & tempered material (MPC-25, 1283°F-15 hrs., SEM)..... 258

4.135 Carbide morphology in pearlite region of annealed & tempered material (MPC-25, 1283°F-15 hrs., TEM)..... 259

Figure

4.136	Carbide morphology in ferrite grain matrix of annealed & tempered material (MPC-25, 1283°F-15 hrs., TEM).....	260
4.137	A representative EDS spectrum of $M_{23}C_6$ carbide in the annealed & tempered material (MPC-25, 1283°F-15 hrs.).....	261
4.138	Typical X-ray diffraction spectra of the carbides extracted from annealed & tempered material (MPC-25, 1283°F-15 hrs.).....	263
4.139	Carbide morphology in bainitic regions of service exposed material (MPC-18).....	264
4.140	A representative EDS spectrum of M_3C carbide in the annealed & tempered material (MPC-25, 1283°F-15 hrs.).....	265
4.141	Carbide morphology in ferrite grain matrix and along F/F grain boundary of service exposed material (MPC-18).....	266
4.142	A representative EDS spectrum of Mo_2C carbide in service exposed material (MPC-18).....	267
5.1	Methane concentration as a function of exposure time (MPC-3, N&T, 850°F-500 psi H_2).....	272
5.2	Isolated methane bubbles initiated at carbide/ferrite interfaces and grain boundaries (MPC-3, N&T, 850°F-500 psi H_2-159 hrs.).....	274
5.3	In-situ methane bubble nucleation by the reaction of carbides and hydrogen in service exposed C-0.5Mo material (MPC-15, 770°F-550 psi H_2-30 years).....	276
5.4	Calculated hydrogen concentration (a) and equivalent "hydrogen pressure" (b) profiles through the wall (44 mm) of one-sided exposure assembly (900°F-900 psi H_2-1248 hrs.+950°F-900 psi H_2-288 hrs.).....	280

Figure

5.5 Calculated hydrogen concentration (a) and equivalent "hydrogen pressure" (b) profiles through the wall (29 mm) of one-sided exposure assembly (900°F-900 psi H_2-1248 hrs.+950°F-900 psi H_2-288 hrs.)..... 281

5.6 Calculated hydrogen concentration (a) and equivalent "hydrogen pressure" (b) profiles through the wall (13 mm) of one-sided exposure assembly (900°F-900 psi H_2-1248 hrs.+950°F-900 psi H_2-288 hrs.)..... 282

5.7 Methane formation free energy as a function of temperature for the reaction of hydrogen and Fe_3C carbide..... 285

5.8 Calculated methane pressure profile through the wall (44 mm) of the one-side exposure assembly (900°F-900 psi H_2-1248 hrs.+950°F-900 psi H_2-288 hrs.)..... 285

5.9 Calculated methane pressure profile through the wall (29 mm) of the one-side exposure assembly (900°F-900 psi H_2-1248 hrs.+950°F-900 psi H_2-288 hrs.)..... 286

5.10 Calculated methane pressure profile through the wall (13 mm) of the one-side exposure assembly (900°F-900 psi H_2-1248 hrs.+950°F-900 psi H_2-288 hrs.)..... 286

5.11 Comparison of methane pressure derived from the experimental data and calculated results..... 288

5.12 Methane pressure as a function of hydrogen pressure at temperatures of 500°F and 700°F for the reaction of hydrogen and Fe_3C, Mo_2C, and $Cr_{23}C_6$..... 291

5.13 A flow chart showing hydrogen attack progression in steels..... 292

5.14 Hydrogen attack mechanism within the wall of the one-side exposed assembly..... 295

5.15 Comparison of modified hydrogen attack limit and modeling with the C-0.5Mo Nelson Curve in API Publication 941..... 298

Figure

5.16	Relationship of hydrogen attack damage (FA% & FL%) and the hydrogen attack parameter (P_w).....	301
5.17	Hydrogen attack limits as a function of time defined by modeling.....	303
5.18	Comparison of hydrogen attack limits as a function of time defined by modeling and documented in API Publication 941 for C-0.5Mo.....	305
5.19	Relationship of hydrogen attack damage (FA% and FL%) and hydrogen content dissociated from methane.....	306
5.20	Relationship of average bubble diameter and hydrogen attack damage level (FA% and FL%).....	307

CHAPTER 1

INTRODUCTION

C-0.5Mo and Cr-Mo steels are widely utilized for equipment employed in the petroleum refinery and petrochemical industries. High temperature hydrogen attack (HTHA) is one of the major problems encountered with these steels. Hydrogen attack damage is a form of surface decarburization, internal decarburization, methane bubble formation, and cracking in steels exposed to high temperature and high pressure hydrogen. Hydrogen attack is an irreversible phenomena and causes permanent damage resulting in degradation of mechanical strength and ductility. Consequently, it can lead to failures such as leakage, bursting, fire, and explosion.

Hydrogen attack was recognized in the early 1900's [1]. It was reported that internal decarburization and cracking were found in plain carbon steel vessels used for ammonia synthesis. Since that time, hydrogen attack has been observed in process equipment operated in the presence of high temperature and high pressure hydrogen. A systematic study of hydrogen attack was implemented by Inglis and Andrews [2]. Their extensive research effort contributed to the investigation of hydrogen attack behavior in mild steel, and Ni-Cr-Mo, Cr-V, 3Cr, Cr-Si, 6Cr steels. It was demonstrated in their work that hydrogen attack is related to temperature, hydrogen partial pressure, stress, chemical composition, and microstructure. In addition, extensive hydrogen

attack is often found in the weld heat-affected zone (HAZ). Postweld heat treatment (PWHT) has been suggested to as a way to mitigate hydrogen attack in the HAZ.

In 1948, Evans [3] reported failures of carbon steel components caused by hydrogen attack in a Du Pont ammonia process plant. Metallographic evaluation showed that 12 of the 29 evaluated components, including converters, heat exchangers, and piping, disclosed recognizable hydrogen attack damage after being operated for two years. It was concluded that carbon steels containing 0.10-0.35% carbon are susceptible to hydrogen attack at a hydrogen pressure of 350 psi and temperatures above 570°F.

In the 1940's, Nelson [4, 5] contributed his great efforts to aggregate data regarding the operating experience in petroleum and petrochemical industry and developed a set of curves, known as "Nelson Curves," for design and fabrication of pressure vessels and piping in high temperature hydrogen service. Hydrogen attack is of particular concern in hydrotreating, reforming, and hydrocracking units at a temperature of above approximately 400°F and hydrogen partial pressure of 100 psi. The Nelson Curves have been accepted by The American Petroleum Institute (API, API Publication 941) and five successive editions have been published as relevant guidelines for petroleum and petrochemical industry practice since 1970. Figure 1.1 presents the Nelson Curves for carbon steel, 1Cr-0.5Mo, 1.25Cr-0.5Mo, 2.25Cr-1Mo, 2.25Cr-1Mo-V, 3Cr-1Mo, and 6Cr-0.5Mo as shown in the fifth edition of API Publication 941 [6].

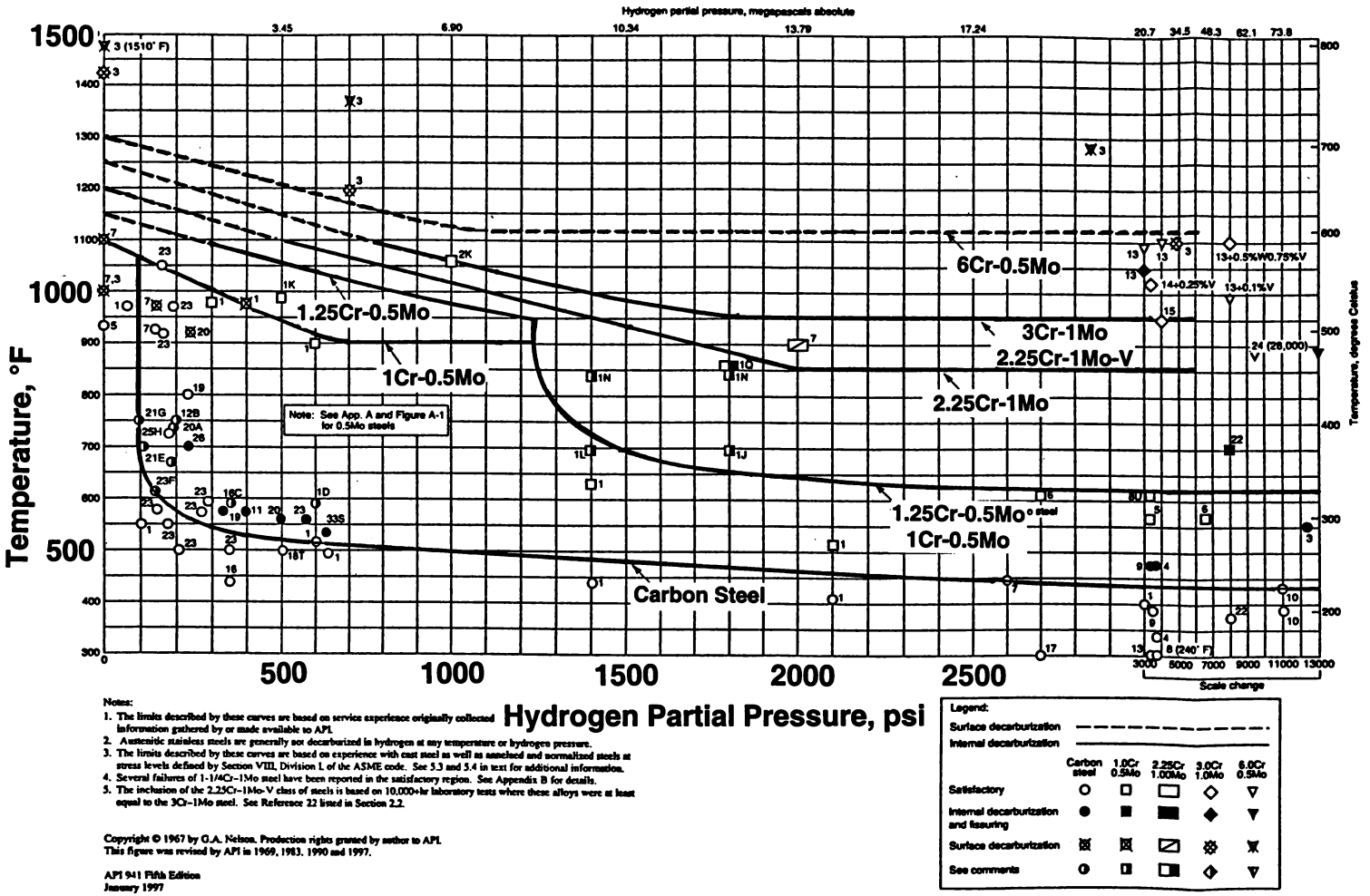


Figure 1.1 Nelson Curves for carbon steel and 1Cr-0.5Mo, 1.25Cr-0.5Mo, 2.25Cr-1Mo, 2.25Cr-1Mo-V, 3Cr-1Mo, 6Cr-0.5Mo steels in the fifth edition of the API Publication 941 [6].

The Nelson Curves provide operating limits for the combination of temperature and hydrogen partial pressure above which hydrogen attack occurs.

Hydrogen attack incidents below the Nelson Curve for C-0.5Mo steel began to emerge as a problem in the 1970's. In 1977, several failures caused by hydrogen attack were documented for C-0.5Mo components in petroleum refinery service. For example, a failure in a Chicago area refinery involved the rupture of an 18" diameter pipe. The resulting explosion and fire caused considerable damage to a catalytic reformer unit [7]. In the 1980's and 1990's, the number of hydrogen attack cases reportedly increased at a rapid rate. One of the failure cases of C-0.5Mo steel components occurred in an ammonia plant in 1984 [8]. The plant was commissioned in 1971. After 13 years of operation, a feed line to an ammonia converter "shattered". The instantaneous release of energy and resulting fire was catastrophic. The operating temperature and hydrogen pressure were 545°F and 2239 psi, respectively, the combinations of which are below the C-0.5Mo Nelson Curve as shown in Figure 1.2 [6]. Metallographic evaluation showed an advanced stage of hydrogen attack in the heat-affected zone of the piping and fittings.

Continuous unsatisfactory service experience with C-0.5Mo steel components has left the petroleum and petrochemical industry in a difficult position. For instance, in 1998, severe hydrogen attack damage was observed in a C-0.5Mo steel heat exchanger channel [9]. This heat exchanger channel was operated at a pressure of 1000 psi (950 psi H_2 and 50 psi CH_4) and

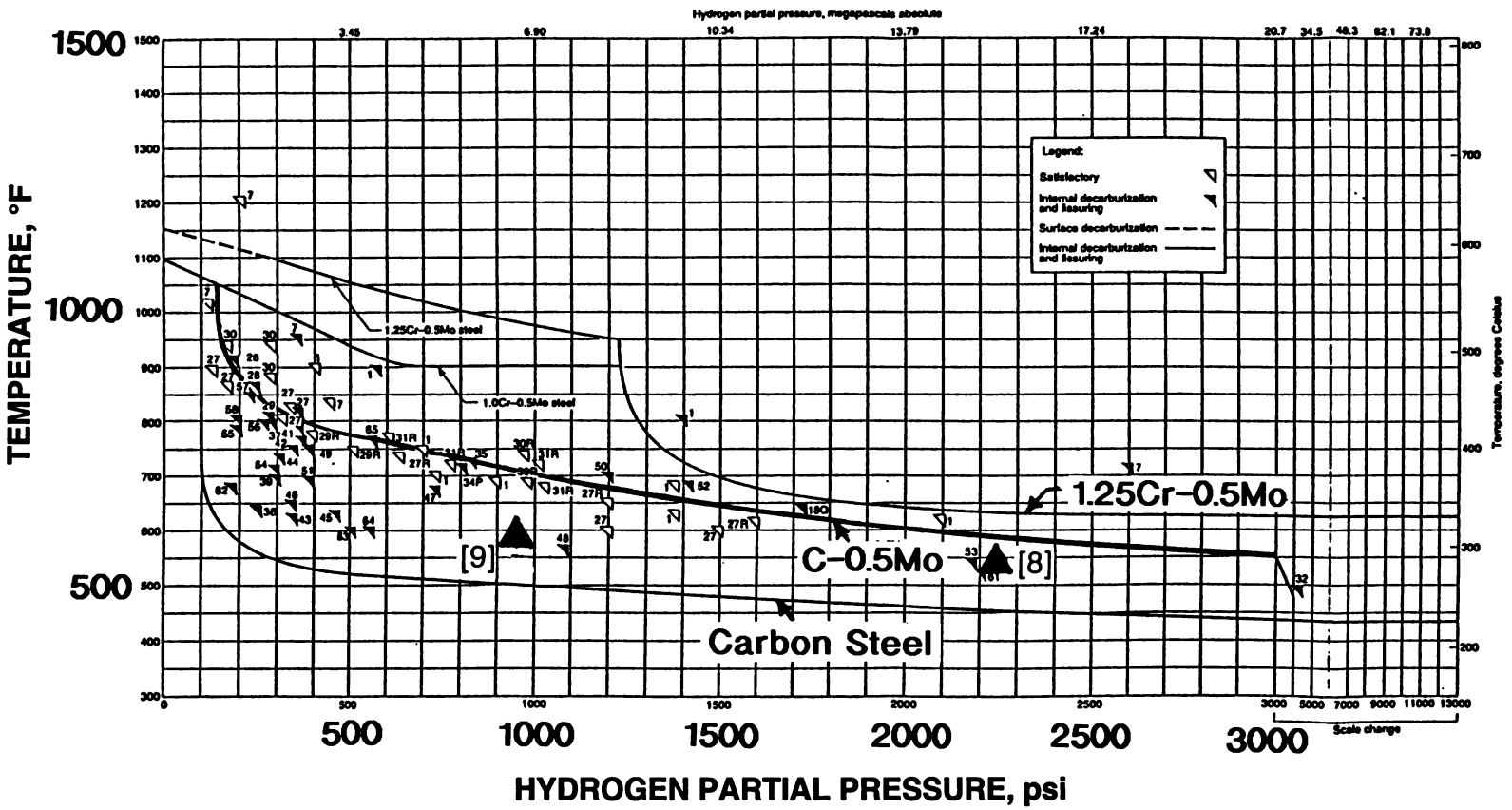


Figure 1.2 Nelson Curves for carbon steel and 1Cr-0.5Mo, 1.25Cr-0.5Mo steels in the fifth edition of the API Publication 941 [6].

temperature of 580°F for 28 years, the combination of which places the material below the Nelson Curve as indicated in Figure 1.2 [9].

Because of the incomplete understanding of the hydrogen attack occurrences below the C-0.5Mo Nelson Curve, further research on hydrogen attack behavior was required to assist in identifying the hydrogen attack mechanism, establishing a methodology to assess hydrogen attack damage and develop modeling to predict hydrogen attack. Therefore, fundamental research on hydrogen attack was crucial to enhancement of basic understanding, predict life and enhance operational longevity.

Japan Steel Works, Ltd. investigated the effect of metallurgical factors on hydrogen attack resistance in C-0.5Mo steel in recent years [10, 11]. Metallographic evaluations were conducted for 156 heats of C-0.5Mo steel that were exposed to high pressure hydrogen at elevated temperature. Hydrogen attack damage was found in 12 heats and was related to "abnormal" $M_{23}C_6$ globular carbides. The effect of tempering and PWHT temperatures on the hydrogen attack was also investigated.

Modeling-based approaches have been conducted to evaluate hydrogen attack behavior in steels depending on stress, temperature, hydrogen pressure and microstructure. The hydrogen attack process has been modeled on three scales: microscopic, mesoscopic, and macroscopic scale [12-14]. The microscopic scale model considers the growth of a single cavity due to grain boundary diffusion and creep driven by the methane pressure and the local

stress state around the cavity. This model describes the microvoid growth as a function of methane pressure, stress state, microvoid radius and spacing, as well as creep and diffusion parameters. The mescoscopic scale model extends the microscopic relationships to an aggregate of grains using the finite element method. The effect of methane pressures on the hydrogen attack evolution and stress distribution was also investigated. Two cavitation modes were introduced: a creep deformation mode and a non-creep deformation mode. In the creep deformation mode, grains can deform significantly and cavities primarily form on the grain boundaries perpendicular to the maximum principal stress. In the non-creep deformation mode, creep deformation is negligible and cavities occur uniformly on all grain boundaries facets. Furthermore, a continuum of damage can be incorporated into a finite element model to calculate hydrogen damage evolution, stress distribution, and service life for a pressure vessel exposed to high pressure hydrogen at elevated temperature. Based on the developed models, the hydrogen attack rate under various conditions may be determined and Nelson type curves can be computed for different steels [13-16].

The American Petroleum Institute (API) and the Materials Properties Council (MPC) have been inspired by the demands of the petroleum refinery and petrochemical industry and have undertaken a research program to study hydrogen attack behavior of C-0.5Mo steel. The API/MPC research program involves three areas of interest:

(1). Metallurgical evaluation of hydrogen attack damage in C-0.5Mo steel and weldments;

(2). Hydrogen attack mechanisms and modeling;

(3). Non-destructive evaluation (NDE).

The objectives of this research are to screen high temperature hydrogen service exposed components and establish a database, to develop a quantitative methodology for hydrogen attack damage evaluation, and to conduct high temperature hydrogen attack simulations for hydrogen pressure containing components. In addition, a hydrogen attack model is to be approached based on hydrogen attack mechanism postulated.

In conjunction with this research, a state-of-the-art literature review on high temperature hydrogen attack was accomplished and the aspects of Nelson Curve evolution and applications, testing techniques for hydrogen attack evaluation, characteristics of hydrogen attack in steels, and modeling of hydrogen attack were addressed.

In this dissertation, 24 heats extracted from service exposed C-0.5Mo steel components were received for hydrogen attack damage evaluation using quantitative metallographic techniques, carbon concentration measurements, and methane gas determination. "One-side" hydrogen exposure tests were designed to simulate exposure condition of hydrogen attack in pressure vessels. The effects of heat treatment, welding, postweld heat treatment, and cold and hot working on hydrogen attack susceptibility were investigated. For

microstructural characterization, continuous cooling diagrams were developed for two heats of C-0.5Mo steel for heat treatment and welding conditions. Carbide evolution upon tempering and postweld heat treatments was studied. The interaction of hydrogen with carbides was studied to develop a model for hydrogen attack prediction.

CHAPTER 2

LITERATURE REVIEW

2.1 Nelson Curves

Nelson Curves are a set of curves that were developed based on the examination of hydrogen attack resistance of steel components in commercial installations. Nelson Curves provide limits of operating temperature and hydrogen partial pressure for carbon steel and C-0.5Mo, 1Cr-0.5Mo, 1.25Cr-0.5Mo, 2.25Cr-1Mo, 2.25Cr-1Mo-V, 3Cr-1Mo, 6Cr-0.5Mo steels as shown in Figures 1.1 and 1.2 [6]. Above the respective Nelson Curve (solid lines), hydrogen attack in terms of internal decarburization and cracking can occur in combination with exposure temperature and hydrogen pressure. In addition, surface decarburization limits are also provided in the Nelson Curves (dashed lines).

The dashed lines represent the tendency for steels to decarburize on the surface while they are exposed to a hydrogen environment at high temperature. Surface decarburization does not produce fissures. The solid curves represent the tendency for steels to decarburize internally with resultant intergranular cracking caused by methane bubble formation, growth, and coalescence along grain boundaries. As shown in Figures 1.1 and 1.2, hydrogen attack susceptibility of steels declines in the order of carbon steel and C-0.5Mo, 1Cr-0.5Mo, 1.25Cr-0.5Mo, 2.25Cr-1Mo, 2.25Cr-1Mo-V, 3Cr-1Mo, 6Cr-0.5Mo steels.

Nelson Curves have been applied to the design and fabrication of pressure vessels and piping in petroleum refinery and petrochemical industry in which hydrogen or hydrogen containing fluid is processed, stored, or handled. The development of the Nelson Curves was based on operating experience and experimental data gathered since the 1940's [17-19]. Five editions of API Publication 941 since 1970 have been published [6, 20-23]. The Nelson Curves depict operating hydrogen pressure and temperature limits for carbon steel, C-0.5Mo, and Cr-Mo steels. The data for satisfactory performance were plotted only for samples or equipment exposed for at least one year. Unsatisfactory performance from plant or laboratory data was plotted regardless of the extent of exposure time. The data to support Nelson Curves were obtained from a variety of commercial processes and laboratory experiments, which were operated at high temperature and high hydrogen pressure. Some data were obtained from unpublished reports and private communications.

C-0.5Mo steel has shown unsatisfactory service in petroleum refineries and petrochemical industries at the conditions below the C-0.5Mo Nelson Curve. Since 1970, a series of hydrogen attack occurrences below the C-0.5Mo Nelson Curve have reduced the confidence in the position of the Nelson Curve. Therefore, the C-0.5Mo Nelson Curve in the second edition of API document (API Publication 941) was lowered to reflect a number of plant experiences that involved hydrogen attack of C-0.5Mo equipment [21]. The operating limit in the Nelson Curve of C-0.5Mo steel was reduced 100°F due to

failures below the original Nelson Curve in the first edition of API Publication 941. The hydrogen attack instances of C-0.5Mo steel equipment which occurred below the Nelson Curve have demonstrated that any C-0.5Mo equipment operating above the carbon steel Nelson Curve should be considered to be at a risk of hydrogen attack. However, the operating temperature and hydrogen pressure limit for hydrogen attack has not been precisely defined for C-0.5Mo.

Nelson Curves were developed based on the experience with the steels produced in accordance with earlier design codes. Thus, the Nelson Curves may not represent the behavior of currently developed materials and heat treatment conditions. Nelson Curves do not represent the behavior of weld metal, heat-affected zone (HAZ), and postweld heat treatment. Potential effects of other gaseous components are not identifiable or accountable from the Nelson Curves [24]. Effects of carbon, impurities, inclusions, and manufacturing processes were not accounted for the Nelson Curves. It also has been shown that C-0.5Mo steels with a carbon content greater than 0.2% experienced hydrogen attack in the HAZ below the Nelson Curve [25]. External stress effects were not considered in Nelson Curve establishment.

2.2 Methodology for Hydrogen Attack Evaluation

2.2.1 Autoclave Exposure Techniques

Hydrogen autoclave exposure testing is a technique in which samples are exposed to high temperature and high pressure hydrogen for hydrogen attack susceptibility assessment. In general, three types of hydrogen autoclave exposure techniques were applied: static hydrogen exposure without applied stress, static hydrogen exposure with applied stress, and one-side hydrogen exposure techniques [26-30].

Figure 2.1 schematically shows an autoclave apparatus utilized without an applied stress [26]. Samples are sealed inside a stainless steel tube with one end of flange connected to a hydrogen cylinder. Before exposing the samples to high pressure hydrogen, air in the autoclave is vented out using a mechanical pump. A small amount of hydrogen is then bled into the stainless steel autoclave and pumped out. The autoclave should be purged in this manner several times to ensure no air is inside the autoclave before being pressurized. The purging operation usually lasts for three to five hours. Because hydrogen tends to leak slowly from an autoclave during high temperature exposure, it is necessary to pressurize the autoclave to a value higher than the desired test pressure until the pressure reaches a nominal value. When a hydrogen exposure is completed the furnace power is turned off. The hydrogen atmosphere vents until the furnace cools down to ambient

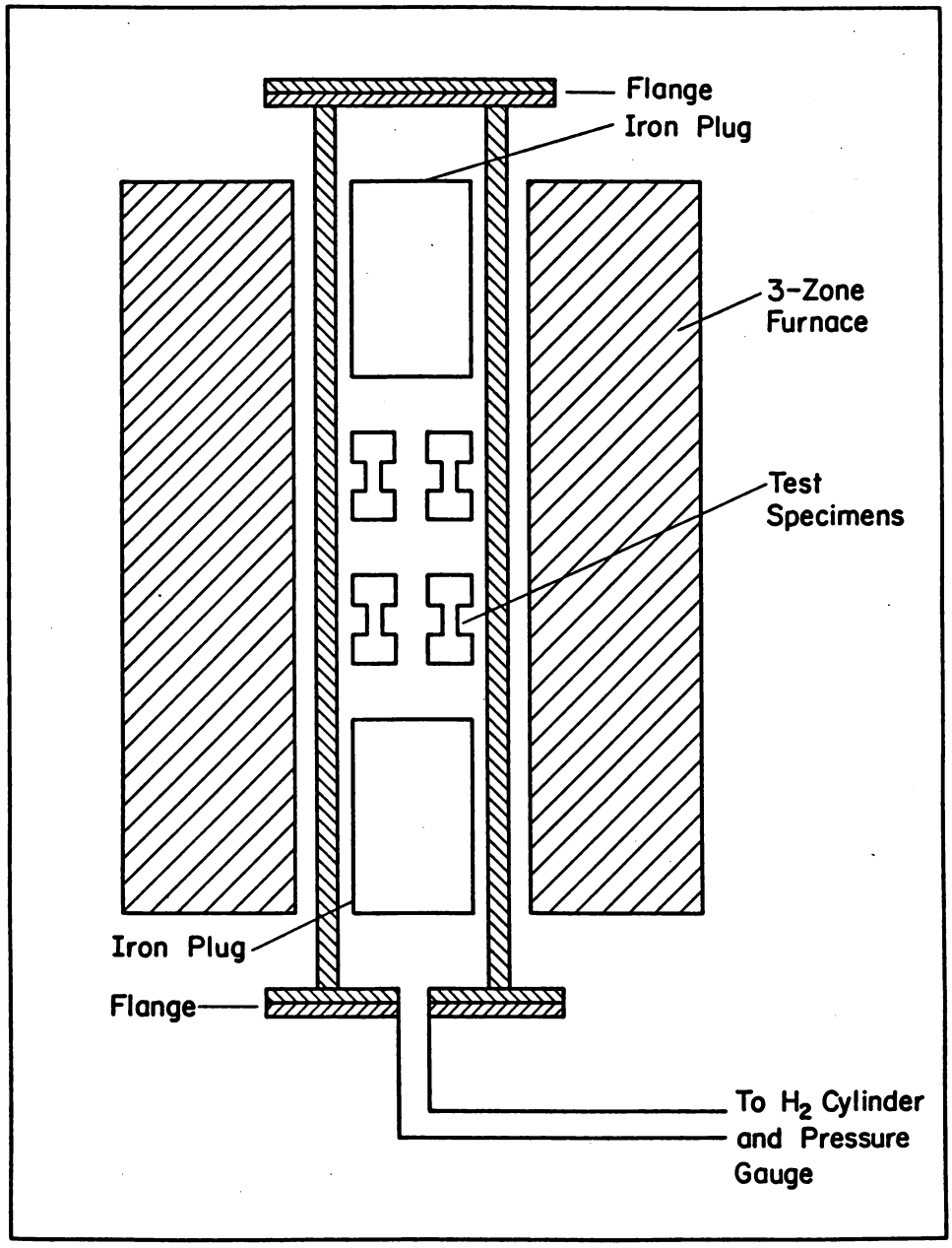


Figure 2.1 Hydrogen exposure autoclave without stress application [26].

temperature. This shutdown procedure is used to prevent the dissociation of methane inside the bubbles and to make sure that the furnace is cold before closure of any of the high-pressure valves. After autoclave exposure, the samples can be assessed metallographically and mechanically.

Figure 2.2 shows an autoclave exposure test apparatus with applied stress [26]. This hydrogen exposure procedure is similar to the procedure as discussed above with the exception of applied stress. The samples exposed to high hydrogen pressure under a simultaneously applied stress are tested with a creep apparatus enclosed in a high pressure hydrogen chamber. A linear voltage displacement transducer is placed at the bottom of the autoclave to monitor creep strain.

Many researchers have attempted to study hydrogen attack phenomenon using autoclave exposure techniques by statically exposing samples to high hydrogen pressures and high temperatures. However, the static techniques do not accurately simulate actual exposure conditions encountered in pressure vessels and piping in which high hydrogen pressures are internal. Therefore, to obtain a better understanding of the hydrogen attack phenomenon in pressure vessels, a one-side exposure technique was designed by Stueber [28] and subsequently used by Arnold [29] and Geiger [30, 31]. This technique allows a steady state hydrogen flux and a hydrogen gradient to be established within the component wall by exposing the internal surface of a hollow cylinder to high

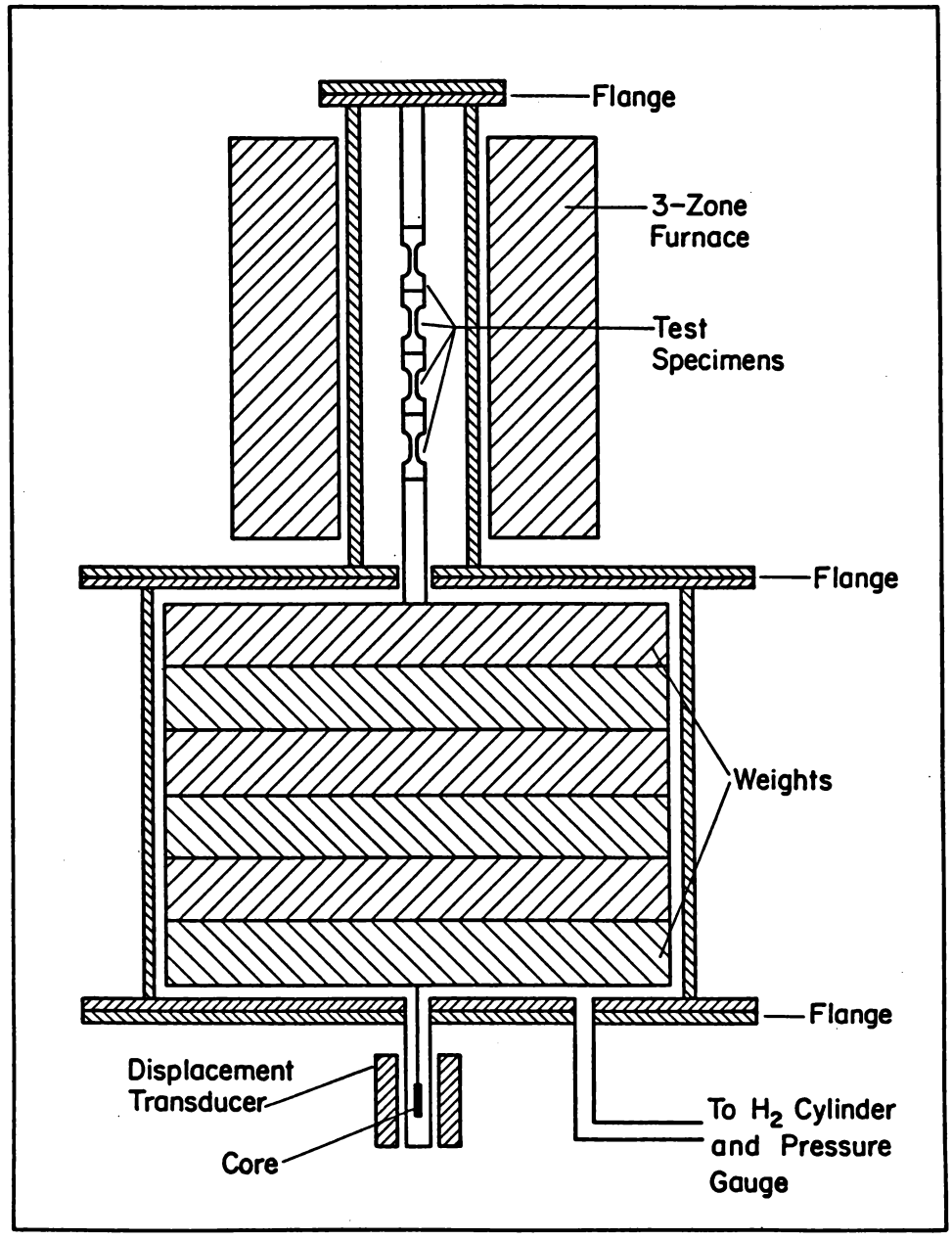


Figure 2.2 Hydrogen autoclave exposure with applied stress [26].

pressure hydrogen and by maintaining vacuum condition on the external surface.

The exposure apparatus for one-side exposure is equipped with two furnaces, a gas chromatograph for hydrogen and methane gas analysis, and soap bubble flow meters for gaseous flow rate measurements as shown in Figure 2.3 [31]. In this one-side exposure test, hydrogen attack can be monitored using a gas flow rate meter, which measures the permeation rate of hydrogen through the cylindrical specimen. As hydrogen attack cracking develops, the effective thickness of the cylindrical specimen decreases and the permeation rate increases. In addition, hydrogen attack reactions and decarburization at the internal surface of the cylindrical sample are monitored by analyzing methane and hydrogen in the effluent gas. The amount of methane in the effluent relates to the degree of surface decarburization, blisters, and cracks, which release methane to the interior of the cylindrical sample.

2.2.2 Tensile Testing

Hydrogen attack has been demonstrated to deteriorate mechanical properties of steels, in terms of tensile strength, ductility, impact toughness and creep rupture properties. The mechanical property tests such as tensile, Charpy impact, hardness, bending, creep rupture, and wedge-opening-loading tests are applied for the evaluation of hydrogen attack in steels [16, 32-37].

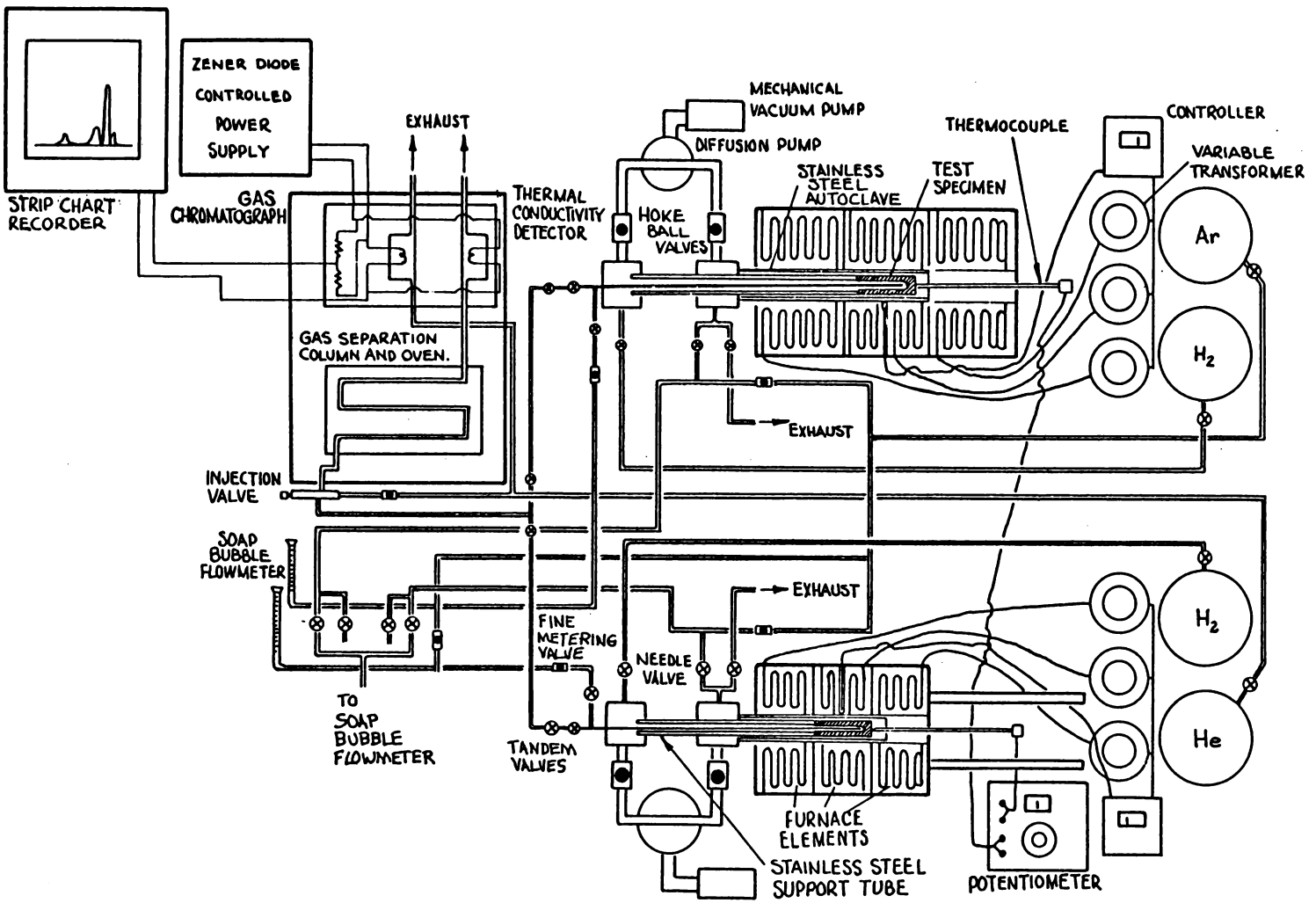


Figure 2.3 Schematic diagram of hydrogen autoclave apparatus for one-side hydrogen exposure [31].

After high temperature hydrogen exposure, tensile tests can be conducted at ambient temperature to assess hydrogen attack susceptibility. Two criteria of tensile testing were used for hydrogen attack evaluation, ductility degradation index and strength degradation index. The ductility index (Φ_R%) was defined by The Japan Pressure Vessel Research Council (JPVRC) as [32]:

$$\Phi_R\,(\%) = (R_0 - R) / R_0$$

where R_0 and R are the values of reduction in area tested before and after high temperature hydrogen exposure, respectively. Furthermore, the ductility degradation index was correlated to two hydrogen attack parameters (P_W, P_V) which are functions of exposure temperature (T, °K), hydrogen partial pressure (P_{H_2}, kg/cm^2), and exposure time (t, hour). For C-0.5Mo steel, the hydrogen attack parameters of P_W, and P_V are expressed as:

$$P_W = 3 \log P_{H_2} + \log t - 9918 / T$$

$$P_V = \log P_{H_2} + 3.09 \times 10^{-4}\, T\, (\text{Log } t + 14)$$

Figures 2.4 through 2.7 show the ductility degradation indexes as functions of hydrogen exposure parameters of P_w and P_v for C-0.5Mo base metal and HAZ. The critical hydrogen exposure parameters of $P_w^{cr.}$ and $P_V^{cr.}$ are:

$P_w^{cr.} = -4.80$	$P_V^{cr.} = 5.80$	for base metal
$P_w^{cr.} = -7.90$	$P_V^{cr.} = 4.90$	for HAZ without PWHT
$P_w^{cr.} = -5.25$	$P_V^{cr.} = 5.60$	for HAZ with PWHT

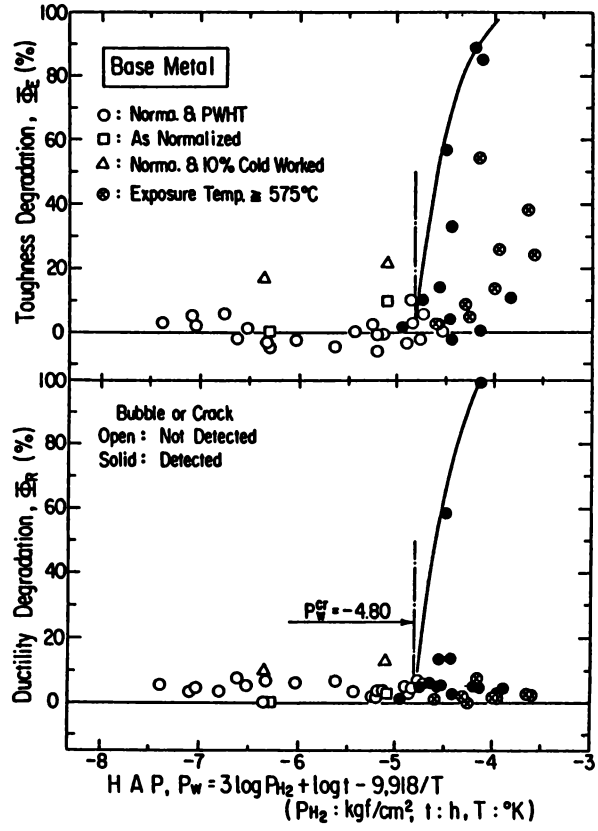


Figure 2.4 Ductility and toughness degradation indices (Φ_R, Φ_E) as a function of hydrogen attack parameter (P_w) for C-0.5Mo steel [32].

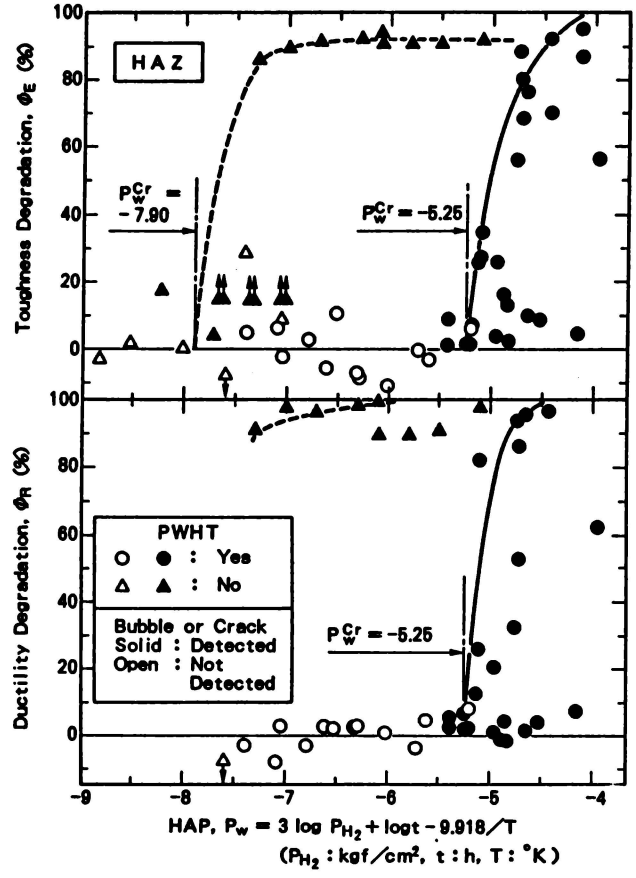


Figure 2.5 Ductility and toughness degradation indices (Φ_R, Φ_E) as a function of hydrogen attack parameter (P_w) for the HAZ of C-0.5Mo with and without PWHT [32].

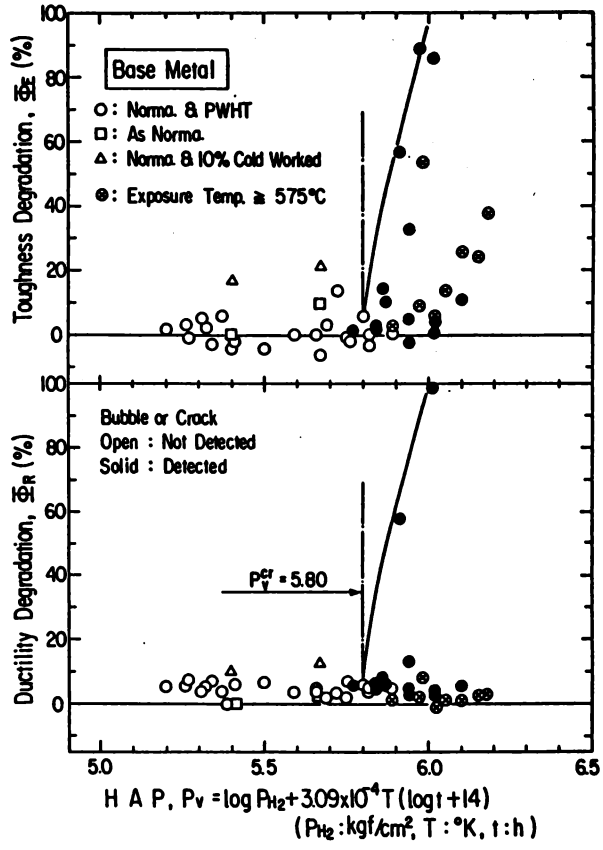


Figure 2.6 Ductility and toughness degradation indices (Φ_R, Φ_E) as a function of hydrogen attack parameter (P_V) for C-0.5Mo steel [32].

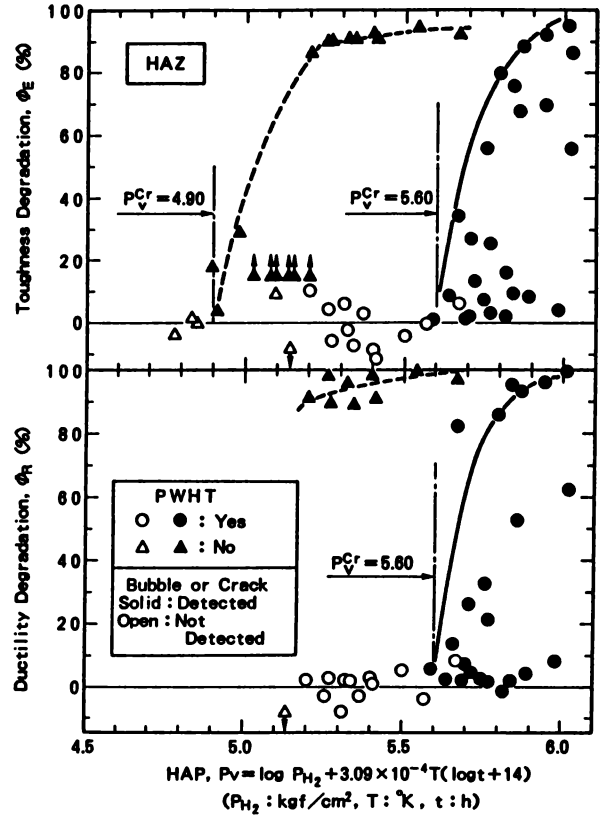


Figure 2.7 Ductility and toughness degradation indices (Φ_R, Φ_E) as a function of hydrogen attack parameter (P_V) for the HAZ of C-0.5Mo with and without PWHT [32].

The critical hydrogen exposure parameters ($P_w^{cr.}$, $P_V^{cr.}$) for the HAZ are less than those for the base metal. These results indicate that the HAZ is more susceptible to hydrogen attack than base metal. The PWHT enhanced the hydrogen attack resistance for the HAZ.

It should be stated that the ductility degradation index was caused by the combination of thermal effect and hydrogen attack. To eliminate the thermal influence, R_0 should be determined by using a sample exposed to Ar at the same temperature.

In addition to the ductility degradation index, a strength degradation index (SDI) from tensile tests was defined as [24, 33]:

$$SDI\ (\%) = (UTS_{Ar} - UTS_{H_2}) / (UTS_{Ar} - 50)$$

UTS_{Ar} and UTS_{H_2} (ksi) are tensile strengths after exposing to Ar and hydrogen at the same temperature. The strength degradation index was used for the assessment of hydrogen attack in 2.25Cr-1Mo steel. Since a hydrogen attack mechanism is related to decarburization, a completely damaged 2.25Cr-1Mo steel was assumed to be a carbon-free Cr-Mo steel with an estimated tensile strength of approximately 50 ksi. This defined a hydrogen damage parameter of 100%. Figure 2.8 shows tensile strength degradation after hydrogen autoclave exposure in contrast to the strength after heat treatment in vacuum condition for SAE 1020 steel [24]. The strength degradation index was computed as 36%.

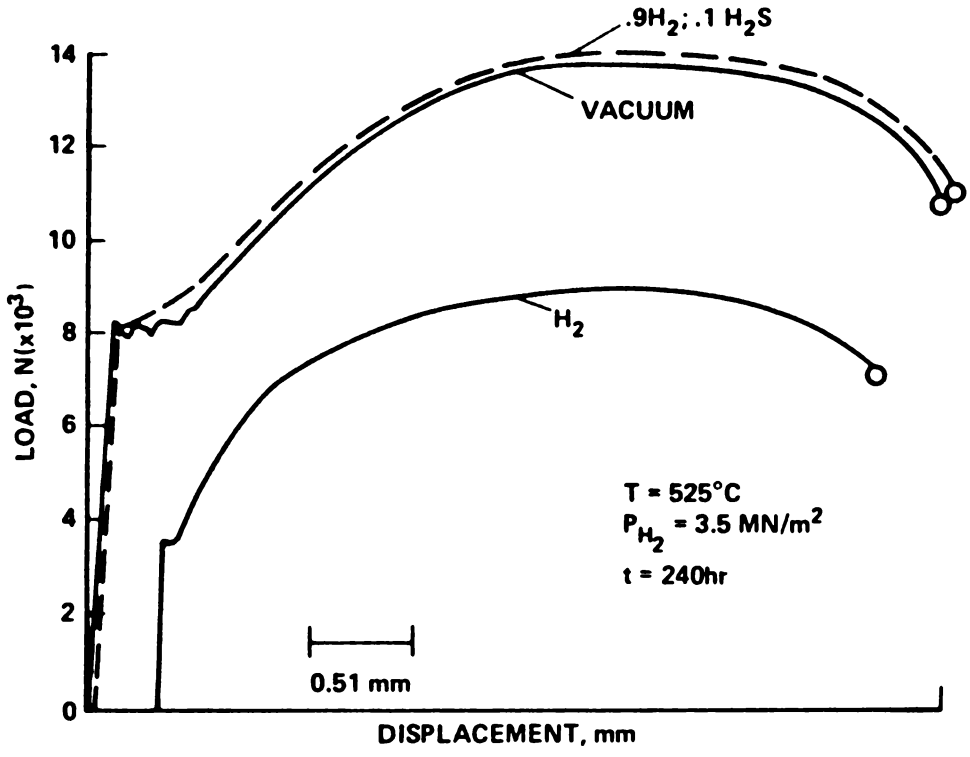


Figure 2.8 Tensile strength degradation of SAE 1020 steel exposed to 525°C (977°F) and 3.5 MN/m^2 (508 psi) for 240 hours [24].

2.2.3 Charpy Impact Testing

Toughness degradation due to hydrogen attack can be ranked by toughness degradation Index (Φ_E%) [32]:

$$\Phi_E\,(\%) = (E_0 - E) / E_0$$

where E_0 and E are absorbed energy in impact tests before and after high temperature hydrogen exposure, respectively. The influence of hydrogen exposure parameters (P_w, P_v) on the toughness degradation index is shown in Figures 2.4 through 2.7. The critical exposure parameters ($P_w^{cr.}$ and $P_v^{cr.}$) for C-0.5Mo base metal and the HAZ are consistent with those determined by using the ductility degradation index. Charpy impact up-shelf-energy was also used as an evaluation parameter for hydrogen attack damage evaluation [34].

2.2.4 Creep Rupture Testing

For hydrogen attack damage evaluation, there are two types of creep rupture testing: creep testing in hydrogen or creep testing in air after exposure to high temperature hydrogen [26, 27, 34-36]. Creep rate, rupture strength, rupture life, reduction in area, and/or elongation are utilized as the parameters for hydrogen attack assessment.

Figure 2.9 shows the comparison of the creep curves of 2.25Cr-1Mo steel tested at 600°C (1112°F) with and without hydrogen exposure [36]. The specimens were exposed to hydrogen pressure of 13.8 MPa (2 ksi) at 600°C (1112°F) for 20 days. The creep rates for the hydrogen exposed specimens are

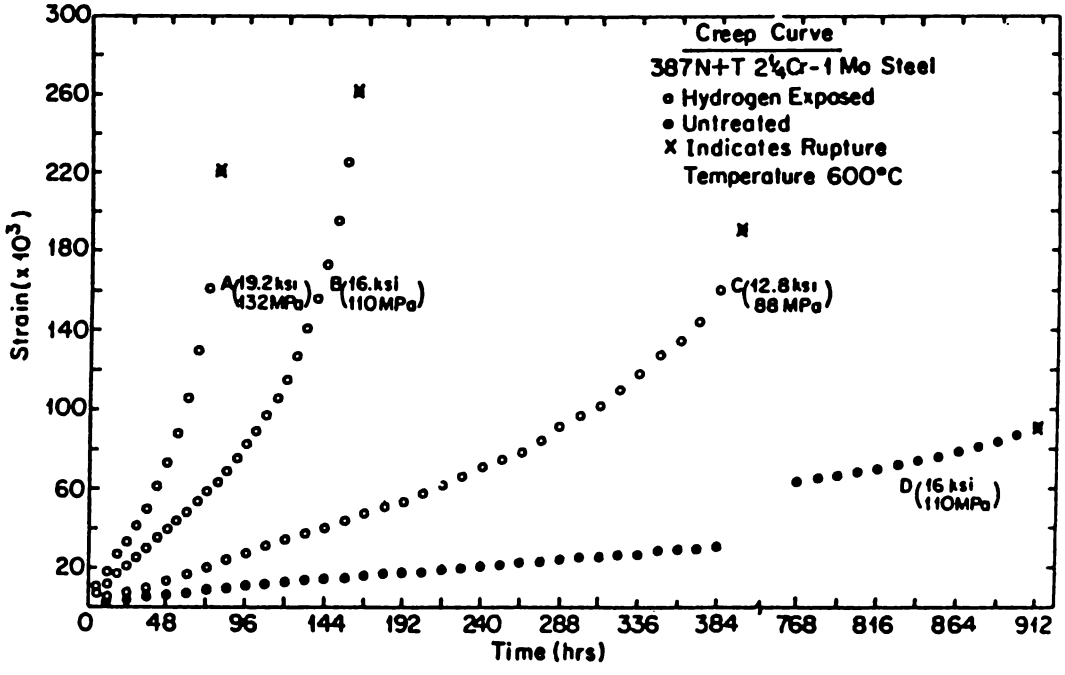


Figure 2.9 Creep curves of 2.25Cr-1Mo steel (N&T) with and without hydrogen exposure [36].

greater and the creep rupture lives are shorter than the unexposed specimens since the hydrogen-exposed specimens contained hydrogen attack damage. The specimens with prior hydrogen exposure failed at shorter times as the applied stress was increased.

Creep rupture tests in hydrogen were conducted for a database development in order to quantify the effects of important variables on the hydrogen attack susceptibility of 2.25Cr-1Mo and vanadium modified 2.25Cr-1Mo steel weldments. Hydrogen attack susceptibility appeared to be greatest in the CGHAZ as shown in Figure 2.10 [35].

2.2.5 Wedge-Opening-Loading Testing

Figure 2.11 shows the wedge-opening-loading (WOL) test procedure [37]. The WOL test can be conducted during specimen exposure to high temperature hydrogen or after exposure to high temperature hydrogen. A modified wedge-opening-loading (MWOL) test was used for study of stress-assisted hydrogen attack cracking in 2.25Cr-1Mo steels at elevated temperature [38-41]. Crack growth rates were measured in high temperature and hydrogen pressure in a stainless steel autoclave. Crack growth was measured using a direct current potential drop method. Crack growth rates were determined as a function of temperature and the hydrogen exposure pressures. It is concluded that accelerated crack growth rates were caused by raising the temperature. Incorporating the high pressure hydrogen, the crack growth rate increases

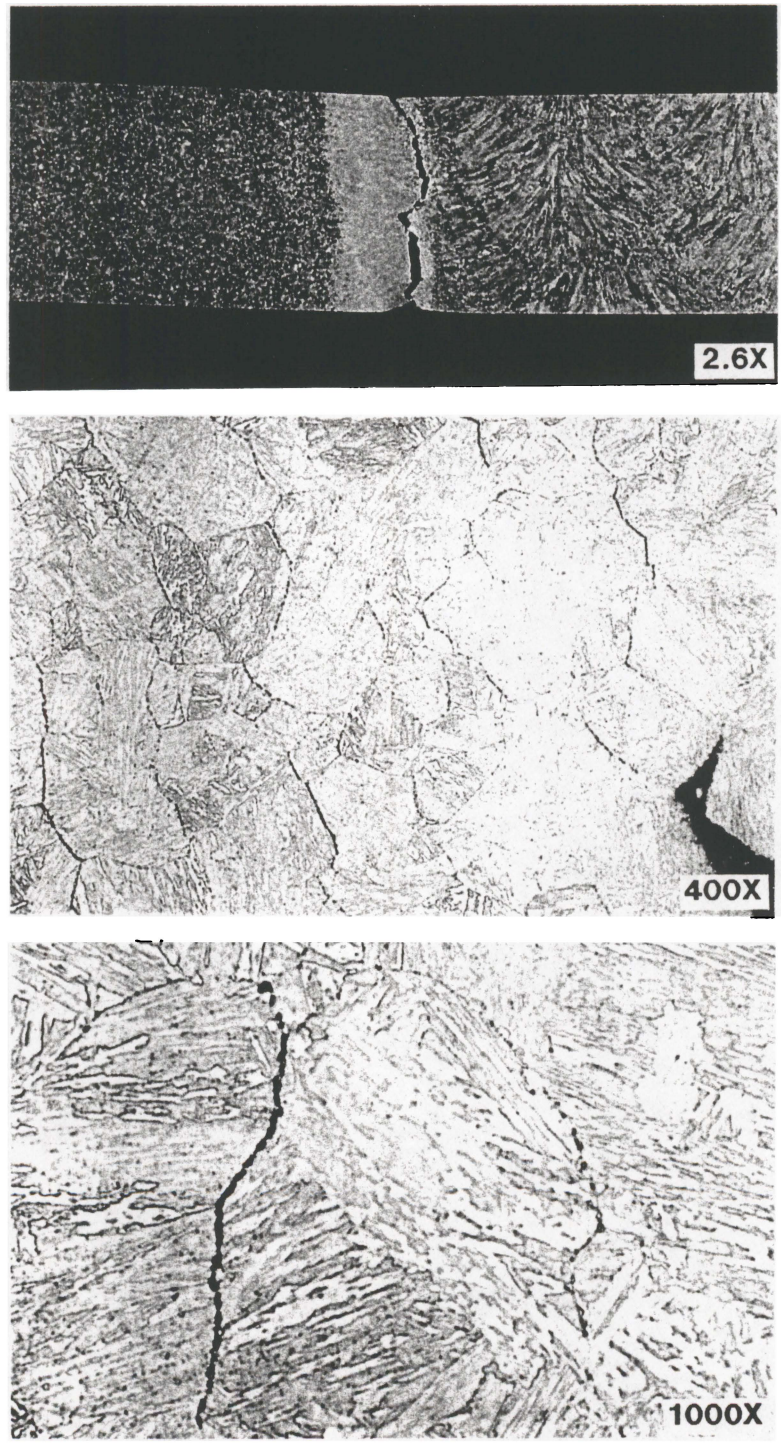


Figure 2.10 Stress rupture in the CGHAZ of 2.25Cr-1Mo weld exposed to hydrogen pressure 3 ksi (850°F-33 ksi-10387 hrs) [35].

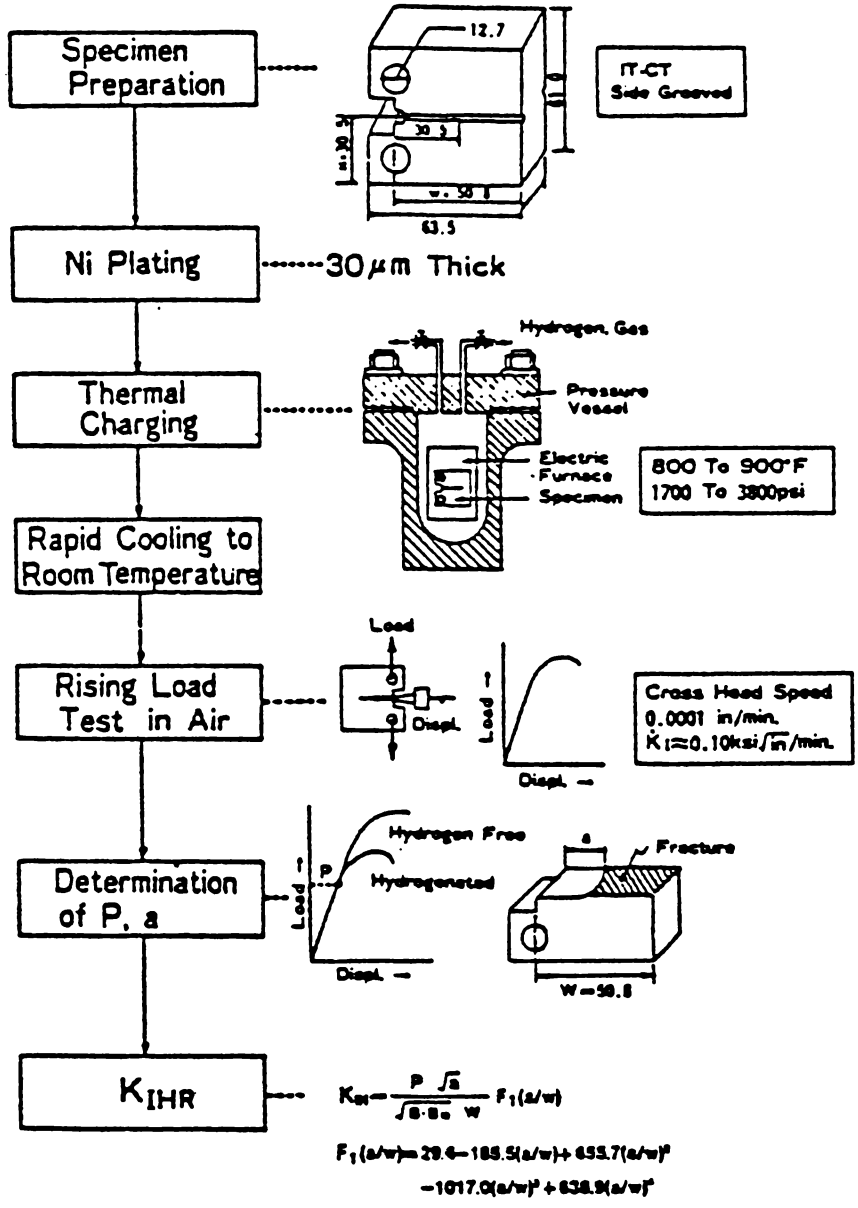


Figure 2.11 Flow-diagram of wedge-opening-loading test procedure [37].

remarkably. Metallographic examination showed intergranular cracks running primarily along the grain boundaries between ferrite and pearlite.

2.2.6 Dilatometric Swelling Testing

Dilatometric swelling tests involve the use of an in situ dilatometer to measure sample expansion induced by hydrogen attack as a function of time, temperature, and hydrogen pressure [16, 42]. Figure 2.12 schematically shows the dilatometric swelling test apparatus and specimen dimensions. This apparatus can be used to measure linear strain rates of about 10^{-7}/hr. in a 25 mm long sample. In this apparatus, a capacitance transducer consists of a dumbbell-shaped specimen, a fixed top electrode, and a cylindrical cage assembly as shown in the schematic. The top electrode and sample form a parallel plate capacitor which is electrically shielded by the surrounding cage. This transducer is fitted inside an austenitic stainless steel pressure vessel, which is externally heated by a resistance furnace.

As the sample is exposed to high temperature hydrogen, it begins to expand and thus decreases the gap between the capacitor plates and increases the capacitance between them. This increase is measured using a General Radio Model 1615-A capacitance bridge driven by a 1 kHz signal from the audio oscillator. The lock-in amplifier serves as the detector for the bridge. The output of the amplifier is fed to the strip-chart recorder. Specimen temperature is measured using a Type K thermocouple located inside the

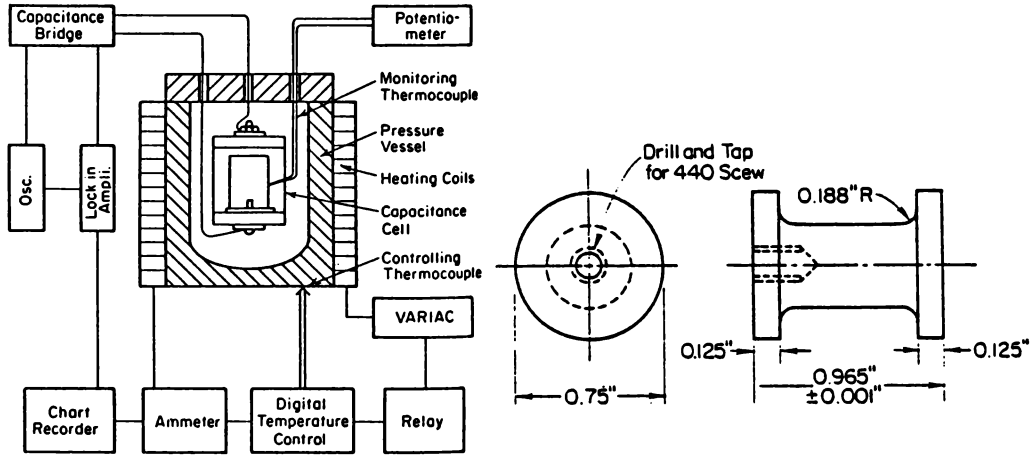


Figure 2.12 Schematic diagram of dilatometric apparatus and specimen [42].

transducer assembly adjacent to the sample.

Figure 2.13 presents a dilatometry swelling test result for A516 steel exposed to 4.4 MPa (0.6 ksi) hydrogen pressure at 455°C (850°F) [42]. It is evident that the specimen began to expand measurably after 20 hours. The expansion rate rapidly attained a nearly constant value and then the sample continued to expand at this slowly increasing rate for about 220 hours. After the specimen as undergone a total linear expansion strain of about 0.2% related to the incubation period, the expansion rate accelerated sharply, corresponding to rapid hydrogen attack. The swelling test results clearly show that bubble growth occurred during the constant expansion rate. The "rapid attack" corresponded to numerous intergranular cracks as well as discrete bubbles. The methane bubbles developed preferentially on or near cementite particles.

2.2.7 Nondestructive Examination of Hydrogen Attack

In API Publication 941, the importance of nondestructive examination (NDE) is addressed, such as using ultrasonic testing (UT) to detect hydrogen attack damage in reactor vessels and heat exchangers [23]. Quantitative evaluation using UT is recognized to be a major subject in assessing hydrogen attack damage in pressure vessels and piping [43-48]. In addition, acoustic emission and metallographic replica techniques are useful for inspecting hydrogen attack damage in steel components [49, 50].

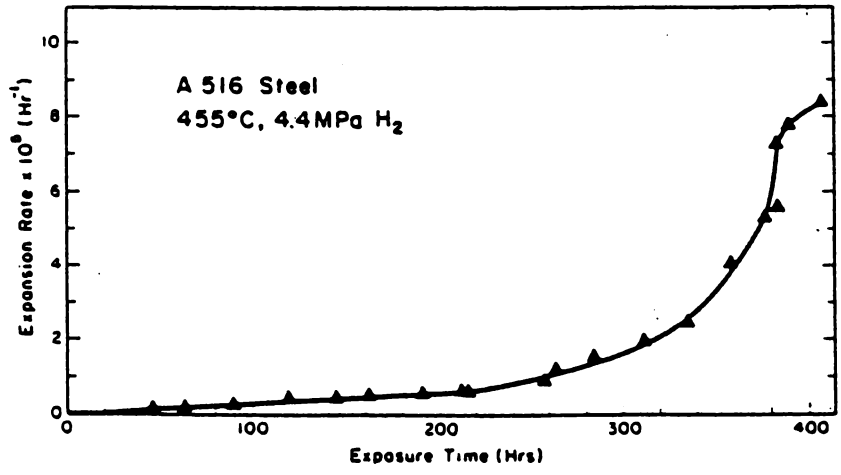


Figure 2.13 Dilatometric swelling test result for A516 steel exposed to 4.4 MPa (0.6 ksi) hydrogen pressure at 455°C (850°F) [42].

Kawano et al. [43] investigated the correlation between UT results and the hydrogen attack damage in service exposed C-0.5Mo pressure vessels. The wall thickness of the pressure vessels was in the range of 50 to 80 mm. Hydrogen attack damage and distribution through wall thickness were examined using four UT techniques: sound velocity, shear vs. longitudinal sound velocity ratio, attenuation, and backscattering techniques. In addition, metallographic examination and mechanical tests were conducted for the UT inspected samples. Hydrogen attack damage was detected at the inner side of the pressure vessels by using UT and confirmed by metallurgical examinations. An analytical interpretation showed that internal defects in steel affected the bulk modulus of elasticity and reduced the velocity of ultrasonic waves. Furthermore, the internal defects severely reduced the velocity of a longitudinal wave compared to that of a shear wave. These affects indicate the degree of internal hydrogen attack such as formation of methane bubbles, microcracks, and blisters, which can be characterized by measuring the ratio of a longitudinal wave velocity to a shear wave velocity. It was found that the damaged materials exhibited higher values of the wave velocity ratio (>0.55) while sound materials had a ratio below 0.54.

For inspection of hydrogen attack damage in weld HAZ, the contact focused angle beam S-wave and pitch-catch L-wave techniques were applied [44]. Authors stated that ultrasonic backscatter and velocity-ratio techniques were effectively applied to the inspection of hydrogen attack damage in base

metal, but they were not suitable for weld HAZ. Conventional shear wave examination was used for HAZ inspection. This method can detect large cracks but is not sensitive to detect microcracks produced by hydrogen attack. The contact focused angle beam S-wave and pitch-catch L-wave techniques were developed for detection of HAZ cracking type of hydrogen attack.

Hydrogen attack in pressure vessels and piping can be detected using a combination of backscatter and velocity-ratio techniques. Hydrogen attack related microcracks increased ultrasonic scattering and showed up as backscatter, while other sound modification sources, such as inclusion stringers, also produce backscatter. However, the backscatter from hydrogen attack had a certain pattern and was connected to the ID surface because hydrogen attack often occurs near ID surface. However, scattering from inclusion stringers is isolated and can occur anywhere in the metal thickness. Isolated noise signals on the baseline do not represent hydrogen attack. They are produced from inclusion stringers.

Acoustic emission (AE) is an in-situ measurement technique which can be used dynamically to monitor hydrogen attack. Takuichi et al invetigated hydrogen attack behavior using (AE) techniques [49]. Incubation of methane bubble initiation was monitored for different hydrogen pressures and temperatures as indicated in Figure 2.14. It was noticed that the incubation time of methane bubble formation is only few hours for the testing condition of 930°F-2.8 ksi. SEM examination confirmed acoustic emission results.

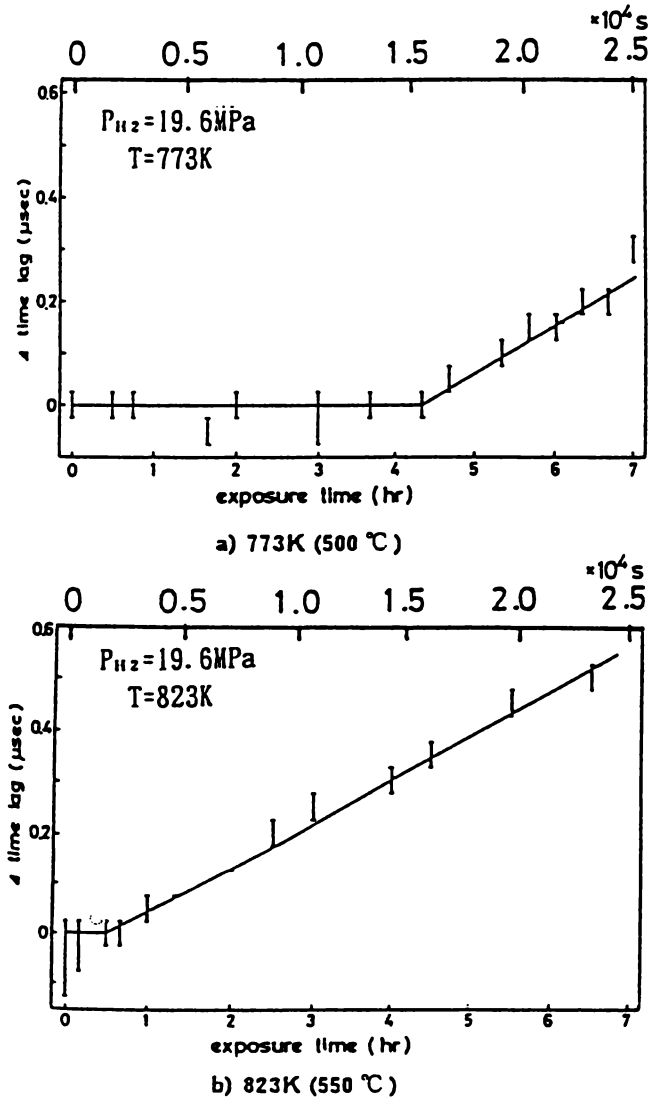


Figure 2.14 Acoustic emission time delay (time lag) as a function of exposure time (2.8 ksi H_2) [49].

2.3 Characteristics of Hydrogen Attack

2.3.1 Incubation

Hydrogen attack is caused by methane bubble nucleation, growth, and ultimate link-up to form cracks along grain boundaries [4, 51, 52]. Hydrogen attack is a diffusion controlled degradation process in which hydrogen damage is preceded by an "incubation period" during which mechanical properties are not significantly impaired. In the "incubation period", there is no deterioration of room temperature mechanical properties. After this initial period elapses, hydrogen attack damage can be detected by the results of mechanical properties deterioration, especially toughness and ductility. The "incubation period" varies with the type of steel and the severity of the exposure condition. It may be only a few hours under extreme conditions and become progressively longer at lower temperatures and hydrogen pressures. For some steels, the "incubation period" may extend for many years under a mild condition.

Numerous theories have been proposed to explain the "incubation period" [53-56]. During the "incubation period", hydrogen reacts with carbon and/or carbides to form methane and the methane gas pressure accumulates in submicroscopic voids. Initially, the methane pressure is balanced by surface tension and the voids can only grow slowly. When the void reaches a critical size, it grows more rapidly by a process of lattice-vacancy condensation. At a larger size, the void growth rate increases further as the controlling mechanism

becomes creep. With the growth of cavities to microscopically visible cracks, the effects on mechanical properties become significant. The incubation time depends on the type of steel, degree of cold working, hydrogen pressure, and exposure temperature. It is important to recognize that steels exposed to high pressure hydrogen at elevated temperature retain their initial strength only during the "incubation period".

However, the terminology of "incubation period" is not adequate based on the metallurgical concept of hydrogen attack as defined as a form of surface decarburization, internal decarburization, methane bubble formation, and cracking [6]. In fact, the methane bubble formation starts at the beginning of high temperature hydrogen exposure for the materials that is susceptible to hydrogen attack as shown in Figure 2.13 [42]. This early stage of hydrogen attack damage might not be detectable by some techniques, such as mechanical testing, UT, and OLM. High resolution techniques (SEM, TEM, dilatometric swelling testing) are required to reveal this early stage hydrogen attack damage.

2.3.2 Hydrogen Attack Damage Morphology

Hydrogen attack is caused by methane bubble nucleation, growth, and methane bubble coalescence to form intergranular microcracks. During the incubation stage of hydrogen attack, methane bubbles can not be observed under an optical light microscope. However, methane bubbles developed on grain boundaries in the incubation period can be resolved under a scanning

electron microscope (SEM) as shown in Figure 2.15 [54]. The methane bubbles grow and coalesce to form microcracks along the grain boundaries. These microcracks in turn link together and often vent methane to the surface. As long as the bubbles contain the equilibrium methane pressure, methane forms slowly and there is insignificant decarburization in the matrix. However, once the methane gas in cracks vents to the surface, methane forms as rapidly as carbon can diffuse to the cracking surfaces and decarburization of the regions on either side of the cracks proceeds rapidly. These decarburized regions increase in thickness and the entire surface layer may become cracked and decarburized [57, 58].

Hydrogen attack susceptibility can be influenced by chemical composition, heat treatment, cold working, and welding. If the occurrence of material microstructure is characterized by microstructural banding and/or inclusion stringers running beneath and parallel to the external surface, hydrogen attack cracks will generally be found to form parallel to the surface and often result in surface blisters [59, 60]. Figure 2.16 shows hydrogen attack cracking and internal decarburization in a service exposed heat exchanger. Blistering was observed on the ID surface and hydrogen attack cracks extended to a depth of 1/2 the wall thickness.

2.3.3 Heat Treatment Effect

Effects of heat treatment on hydrogen attack in C-0.5Mo steels were

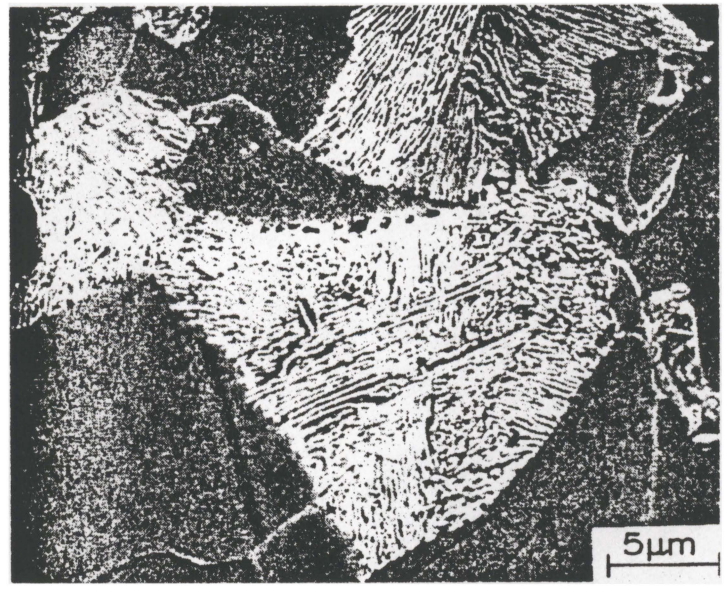


Figure 2.15 Typical methane bubbles in carbon steel after hydrogen exposure [54].



a



b

Figure 2.16 Intergranular cracking morphology of hydrogen attack with internal decarburization [59].

investigated at the Japan Steel Works [10, 59, 60]. In the 1980's, Chiba et al. [59, 60] assessed the effect of heat treatment on the hydrogen attack resistance of C-0.5Mo steels for pressure vessels, heat exchangers, and piping. Normalized only, normalized & tempered heat treatments and PWHT were conducted for two C-0.5Mo materials. Hydrogen exposure tests were performed for the heat-treated materials at temperatures of 320°C, 360°C, 400°C, 440°C (608°F, 680°F, 752°F, 860°F) and a hydrogen pressure of 9.81 MPa (1424 psi) for 300 hours. Hydrogen attack susceptibility was assessed by metallographic evaluation and hydrogen measurements. Hydrogen dissociated from methane at 900°C (1652°F) was analyzed. This hydrogen content is an indirect indication of hydrogen attack damage. The higher the hydrogen content, the greater the susceptibility to hydrogen attack. Furthermore, carbide types and chemistry were evaluated by using chemical analysis, EDS, and X-ray diffraction.

Figure 2.17 shows the hydrogen content in the normalized and tempered samples exposed to a hydrogen pressure of 9.81 MPa (1424 psi) at 400°C (752°F) and 440°C (860°F) for 300 hours [59]. As the tempering temperature is increased, the dissociated hydrogen content is reduced at the same hydrogen pressure. Figure 2.18 represents the hydrogen attack susceptibility of the PWHTed materials exposed at temperatures of 320°C (608°F) and 400°C (752°F) for 300 hours. Similar to the results for the tempered samples, hydrogen attack resistance is enhanced as the PWHT temperature increases.

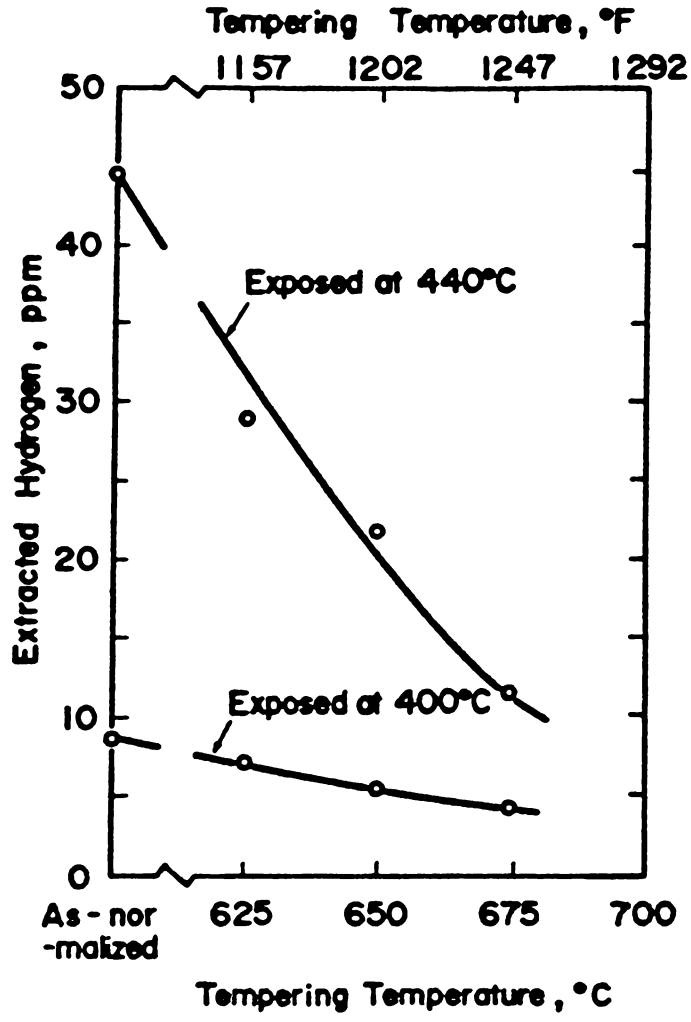


Figure 2.17 Effect of tempering temperature on the hydrogen content dissociated from methane gas [59].

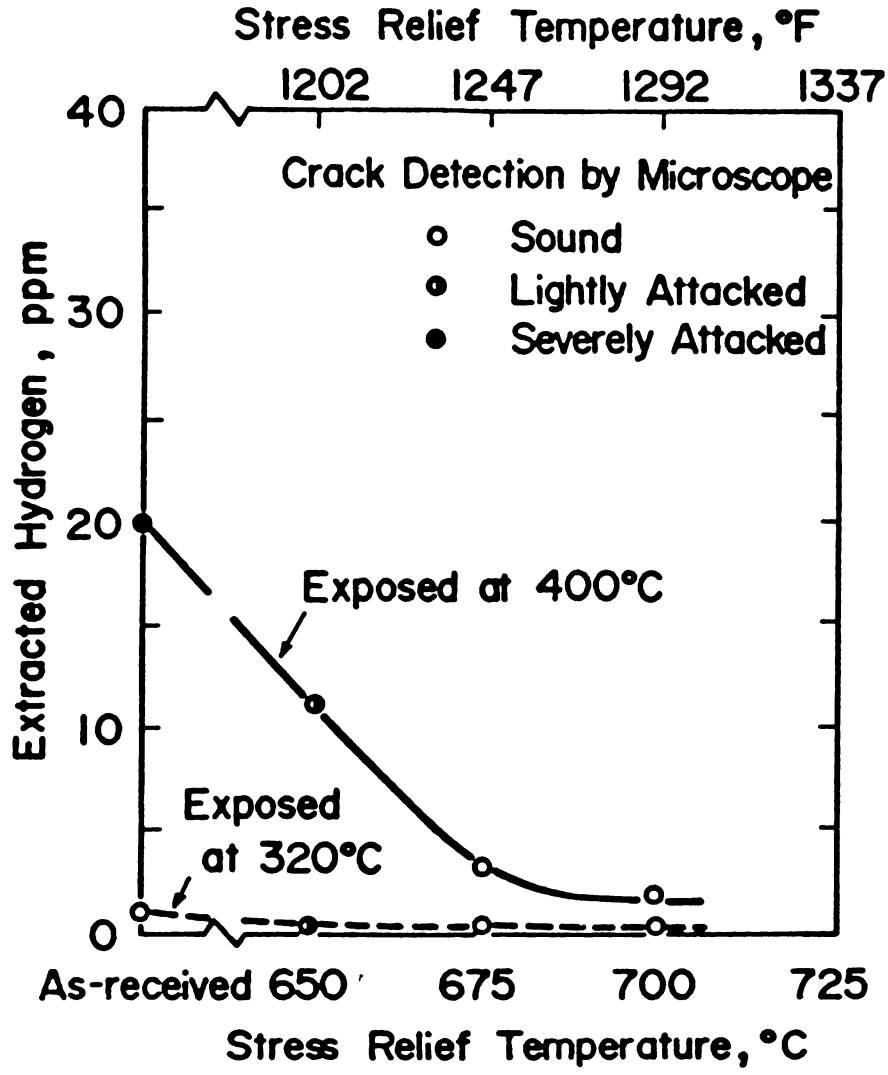


Figure 2.18 Effect of the PWHT temperature on the hydrogen content dissociated from methane gas [59].

The author considered that the resistance to hydrogen attack is attributable to the formation of more Mo rich stabilized carbides, such as $M_{23}C_6$ and Mo_2C in contrast to M_3C (in both tempered and PWHTed materials). The Mo concentration in M_3C carbides and the extracted residues was determined by using EDS and X-ray diffraction, respectively. The Mo content in carbides significantly increases with an increase in PWHT temperature for the materials with high Mo/C ratio (Mo/C = 4.42) in comparison to the materials with a lower Mo/C ratio (Mo/C = 2.21). A carbide evolution diagram was developed as a function of temperature and time. It recommends a temper or PWHT temperature above 650°C (1202°F) for preventing hydrogen attack in C-0.5Mo steel.

Furthermore, Chiba et al. studied the effect of autenization temperature, tempering condition, welds, and PWHT on hydrogen attack [60]. The microstructure was ferrite plus pearlite in the C-0.5Mo steel autenitized at 850°C (1562°F) and 900°C (1652°F) with a cooling rate of 25C°/hr. Bainite was formed after austenitizing at 950°C (1742°F) and 1000°C (1832°F) with a cooling rate of 200C°/hr. Grain coarsening occurred after austenizing at 1000°C (1832°F). The effect of austenitization temperature and the tempering parameter (Larson-Miller parameter) on carbides was investigated using X-ray diffraction. M_3C and $M_{23}C_6$ carbides were observed in the materials which were autenitized below 950°C (1742°F). Only M_3C was found in the material austenitized at or above 950°C (1742°F). Both $M_{23}C_6$ and M_3C type carbides

were observed in the material austenitized at 950°C (1742°F) and tempered at 650°C (1202°F) for 5 hours. High temperature hydrogen exposure tests show that the hydrogen attack susceptibility in the austenitized at or above 950°C (1742°F) condition is greater than that of the materials austenitized below 950°C (1742°F). Therefore, it was suggested that the austenitization temperature should be controlled (below 950°C/1742°F) to ensure securing hydrogen attack resistance in C-0.5Mo steel. $M_{23}C_6$ and Mo_2C carbides were found in the tempered materials austenitized below 950°C (1742°F). The stable $M_{23}C_6$ and Mo_2C carbides start to precipitate earlier in a ferritic/pearlitic microstructure than those in the ferritic/bainitic microstructure during tempering. In addition, the hydrogen attack susceptibility is greater in the HAZ in both as-welded and simulated HAZ conditions in contrast to the PWHT condition. Figure 2.19 shows the critical temperature as a function of the PWHT temperature. With an increase in PWHT temperature, the critical temperature increases. An optimum hydrogen attack resistance is achieved for the PWHT at 650°C (1202°F) for 5 hours and then declines when the PWHT temperature exceeds 650°C (1202°F) due to more carbides precipitated along grain boundaries.

In recent years, further study on the hydrogen attack in C-0.5Mo steel has been conducted at JSW [10, 11, 61]. A so-called "quasi-$M_{23}C_6$" carbide was found using X-ray diffraction in all hydrogen attacked samples. As a result of heat treatment study, the "quasi-$M_{23}C_6$" carbides were found at slow cooling

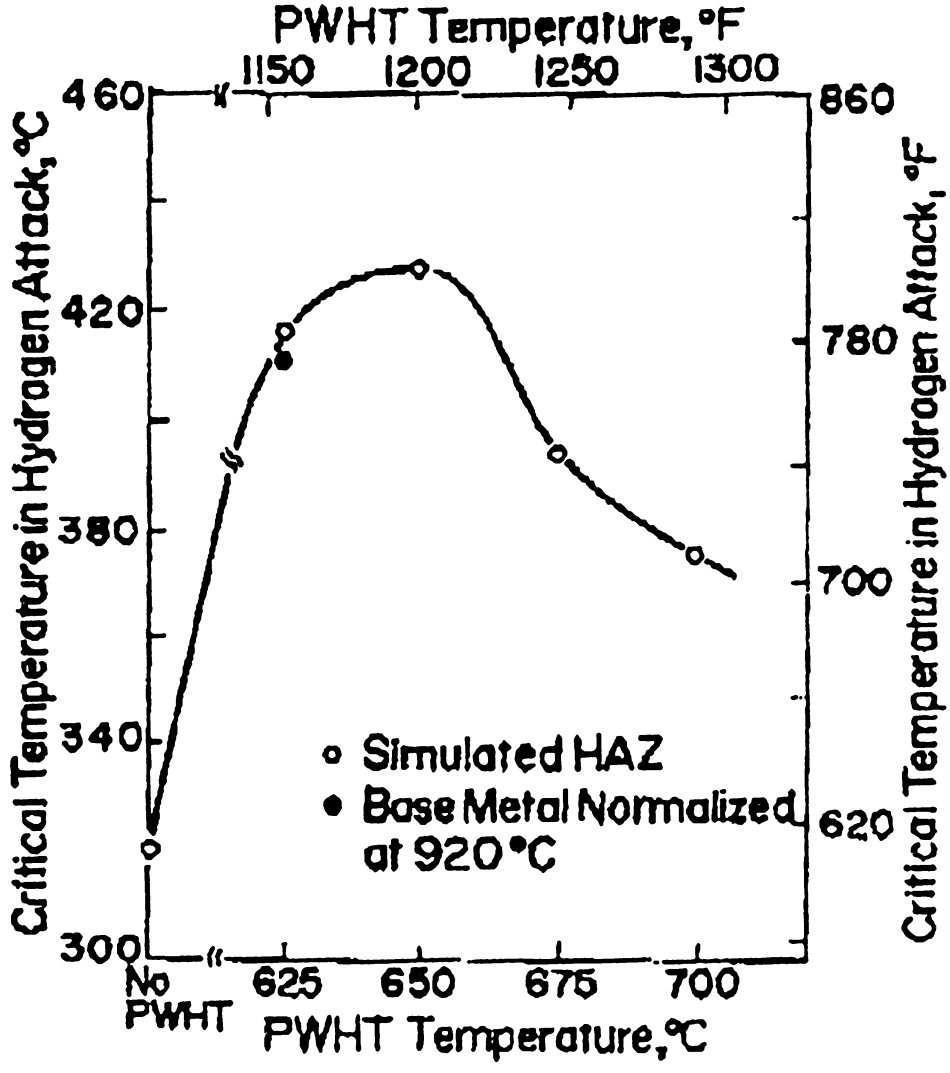


Figure 2.19 Hydrogen attack critical temperature as a function of the PWHT temperature for simulated HAZ and normalized base metal (C-0.5Mo) [60].

rates from the austenitizing temperature. Effects of tempering temperatures for normalized and annealed base metal as well as PWHT temperatures for heat affected zone (HAZ) on hydrogen attack were investigated using autoclave tests. The normalized samples showed less susceptibility to hydrogen attack than the annealed samples during tempering. PWHT improved the hydrogen attack resistance for the HAZ. It was concluded that methane bubbles initiated and grew at the interface between the globular "quasi-$M_{23}C_6$" carbide and matrix. In contrast, acicular bainitic microstructures always exhibited great hydrogen attack resistance. It is noted that these results and conclusions are contradictory to Chiba's results [59, 60].

The effect of heat treatment on the hydrogen resistance of 1.25Cr-0.5Mo was investigated [62]. The chemical composition is: 0.14%C, 1.39%Cr, 0.53%Mo, 0.55%Mn, 0.58%Si, 0.0055%P, 0.002%S, 0.050%Al, and 0.0011%B. After hot rolling, the steel plate was normalized at 930°C (1706°F) for 30 minutes and tempered at 520, 620, 670, and 710°C (968, 1148, 1238, and 1310°F) for 30 minutes with air cool. Samples were tested in two conditions: with and without hydrogen exposure. Hydrogen exposure was conduced at 18 MPa (2.6 ksi) hydrogen pressure and 520°C (968°F) for 1000 hours. Hardness measurements, tensile tests, metallographic and SEM observation were performed for both of the hydrogen exposed and unexposed conditions. Carbide morphology and types were quantitatively identified using TEM diffraction and EDS techniques.

Figure 2.20 presents the room temperature tensile test and hardness test results for the hydrogen exposed material (520°C/968°F-2.6 ksi H_2-1000 hrs.) compared with the unexposed material [62]. It is apparent that there exits a significant degradation of hardness, yield and tensile strength after hydrogen exposure for the material which had been tempered at 620°C (1148°F). However, there is little difference in the hardness, yield and tensile strength, and ductility between the hydrogen exposed and unexposed materials which had been tempered at 520, 670 and 710°C (968, 1238, and 1310°F). The influence of hydrogen elongation and reduction in area are not evident for all tested materials. Methane bubbles were observed only in the material tempered at 620°C (1148°F). Hydrogen attack was not observed in the materials tempered at 520, 670, and 710°C (968, 1238, and 1310°F). It was concluded that unstable M_3C carbides precipitated at a tempering temperature of 620°C (1148°) result in great hydrogen attack susceptibility. Hydrogen attack resistance was improved by tempering above 670°C (1238°F) for which there were more stable $M_{23}C_6$ carbides formed.

It is to be noticed that the material tempered at 620°C (1238°F) is more susceptible to hydrogen attack than that tempered at 520°C (968°F) [62]. Unstable M_3C carbides predominantly precipitated along the grain boundaries for both tempering conditions. It was explained that after tempering at 620°C (1148°F), a great number of M_3C carbides formed along the grain boundaries and increased the possibility of methane formation. On the other hand, all of the

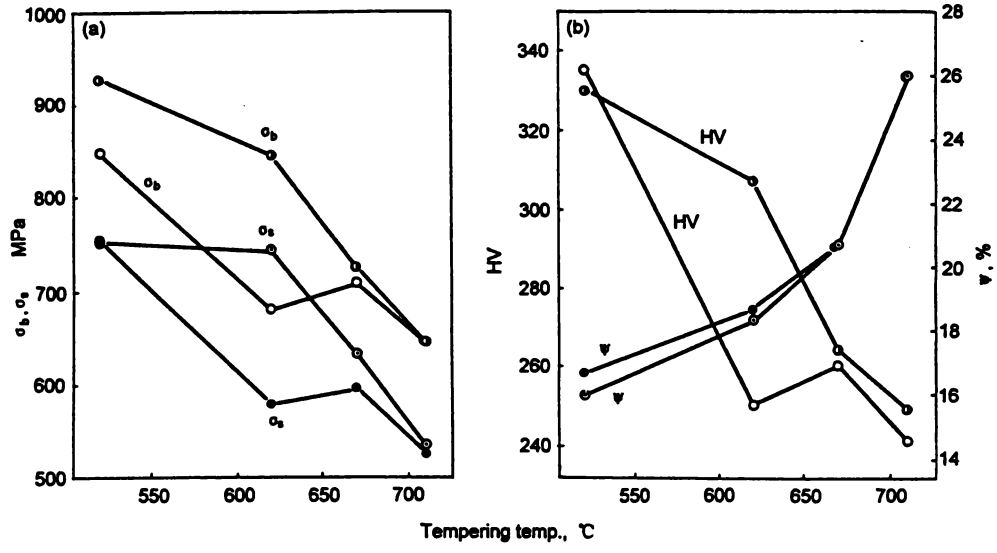


Figure 2.20 Room temperature tensile and hardness results for hydrogen exposed 1.25Cr-0.5Mo steel (520°C/968°F-2.6 ksi H_2-1000 hrs.) in comparison with unexposed condition [62].

carbides are M_3C after tempering at 620°C (1148°F) before hydrogen exposure. During the period of hydrogen exposure, a small amount of $M_{23}C_6$ carbides begin to precipitate along the grain boundaries. However, $M_{23}C_6$ carbides are evolved from the M_3C during hydrogen exposure. The formation of $M_{23}C_6$ requires more alloying elements but less carbon than the formation of M_3C when the alloy content is kept in the same level. Since the formation of $M_{23}C_6$ needs more alloying elements (especially Cr) than the formation of M_3C, an alloy element (major Cr) depleted and carbon enriched zone could form adjacent to the $M_{23}C_6$ carbides. As a consequence, hydrogen attack susceptibility would be increased.

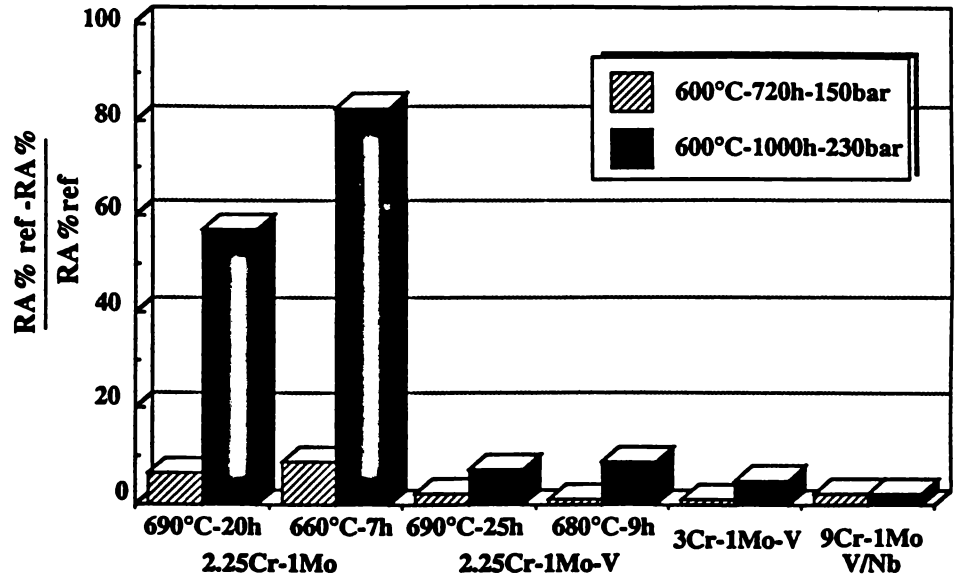
2.3.4 Alloying Element Effects

Since hydrogen attack involves the reaction of hydrogen and carbon and/or carbides in steels, alloying elements play a significant role in hydrogen attack resistance. Carbide-forming alloying elements can significantly increase the resistance to hydrogen attack in steels. The elements most commonly used for this purpose are Cr and Mo. Lowering carbon content is another approach for reducing hydrogen attack susceptibility. However, reducing carbon content is not a panacea since steels with only a few hundredths per cent of carbon are still attacked.

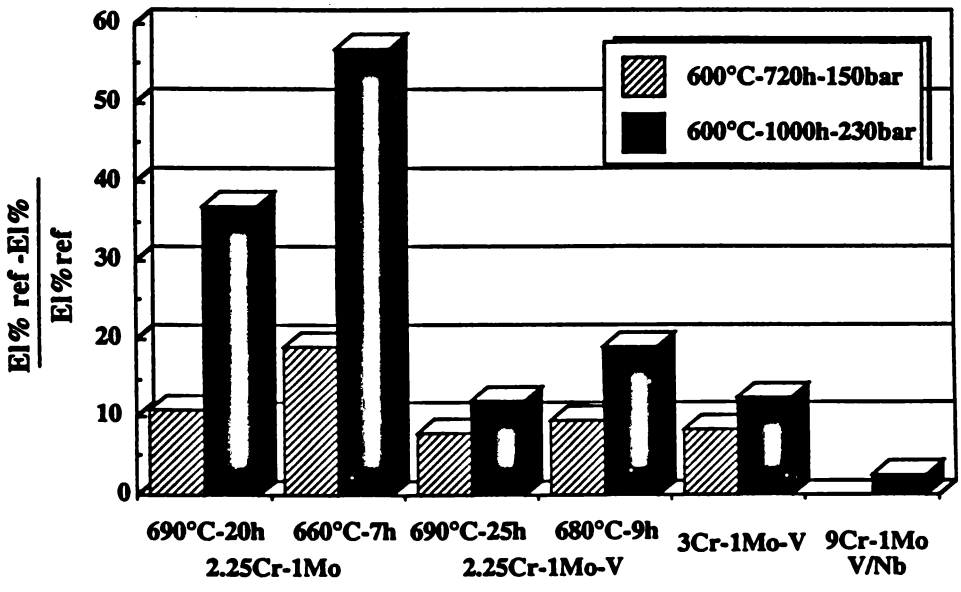
Carbide-stabilizing elements can increase the resistance to hydrogen attack in steel. As shown in Figure 1.1, the addition of Cr in steels significantly

increases the critical operating temperature and hydrogen pressure due to more stable $M_{23}C_6$ formation [6]. The increase in Mo content up to 0.5% enhanced the hydrogen attack resistance. In addition, the concept of a Mo equivalent (Mo + V + Ti + Nb + Cr/4) was applied to determine the effect of V, Ti, and Nb. An increase in the Mo equivalent improves the hydrogen attack resistance in C-Mo steels [20].

Berzolla et al investigated the hydrogen attack susceptibility of 2.25Cr-1Mo-0.25V, 3Cr-1Mo-0.25V-Ti-B, and 9Cr-1Mo-V-Nb steels using tensile tests [56]. Before testing, the samples were exposed to a hydrogen pressure of 150 bar (2.2 ksi) at temperature of 600°C (1112°F) for 720 hours and 230 bar (3.3 ksi) hydrogen at 600°C (1112°F) for 1000 hours. For comparison, an another set of samples was exposed to helium at the same pressure and temperature for an identical period. Figure 2.21 shows the effect of V in 2.25Cr-1Mo steel on the ductility degradation index in terms of the decreases of reduction in area and elongation after exposing at 600°C (1112°F) for 720 hours under 150 bar (2.2 ksi) hydrogen partial pressure and 600°C (1112°F) for 1000 hours under 230 bar (3.3 ksi) hydrogen partial pressure. The hydrogen attack resistance for modified 2.25Cr-1Mo-0.25V was improved significantly in contrast to the conventional 2.25Cr-1Mo in both exposed conditions. 3Cr-1Mo-0.25V-Ti-B and 9Cr-1Mo-V-Nb steels show less susceptible to hydrogen attack compared to 2.25Cr-1Mo and 2.25Cr-1Mo-0.25V.



a) INFLUENCE OF HYDROGEN ATTACK ON RA%



b) INFLUENCE OF HYDROGEN ATTACK ON El%

Figure 2.21 Influence of hydrogen attack on the ductility of 2.25Cr-1Mo, 2.25Cr-1Mo-V, 3Cr-1Mo-V, and 9Cr-1Mo-V/Nb steels [56].

Sakai et al studied the effect of carbide-forming elements on hydrogen attack in 2.25Cr-1Mo steel [63]. Autoclave exposure tests were performed at a hydrogen pressure of 4286 psi and a temperature of 1112°F. After autoclave exposure, the samples were assessed by measuring the methane bubbles on the polished and etched surface using SEM. Figure 2.22 presents number of methane bubbles per square millimeter as a function of alloying element content. It was concluded that the hydrogen attack resistance was improved by the addition of more than 0.2% V. The modified 2.25Cr-1Mo steels with less than 0.05% Nb, Ti, or Zr were demonstrated to be beneficial to hydrogen attack resistance. However, W shows little improvement on hydrogen attack. The susceptibility to hydrogen attack was increased by the addition of Ni (0.5%). The improvement of hydrogen attack resistance by the addition of the carbide-forming elements was contributed by the formation of fine and stable carbides such as VC, NbC, and TiC.

2.3.5 Hydrogen and Carbide Reaction

The equilibrium reaction between hydrogen and carbides can be written in a general form:

$$M_xC_y+2yH_2 = yCH_4+xM$$

where x is the number of metal atom (M) and y is the number of carbon atom (C) in the carbides. For Fe, Cr, Mo, Nb, V, and W containing carbides, the reactions are presented as follows (assuming carbides are pure alloying element

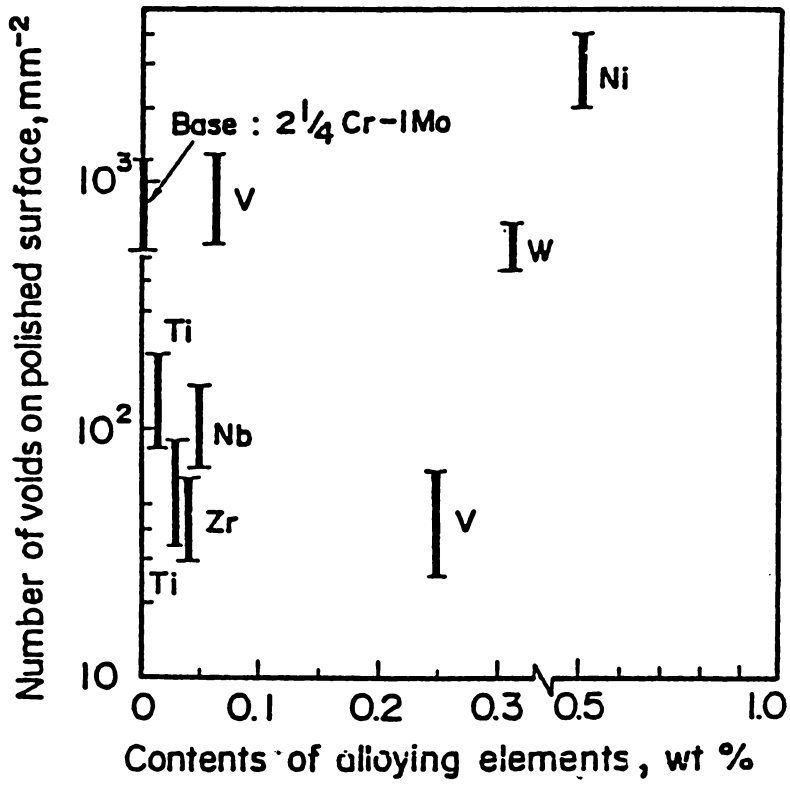


Figure 2.22 Effect of alloying elements on hydrogen attack in 2.25Cr-1Mo steel [63].

carbides, such as Fe_3C, $Cr_{23}C_6$, Mo_2C, NbC, VC, and WC):

$$Fe_3C+2H_2=CH_4+3Fe$$

$$Cr_{23}C_6+12H_2=6CH_4+23Cr$$

$$Mo_2C+2H_2=CH_4+2Mo$$

$$NbC+ 2H_2=CH_4+Nb$$

$$VC+ 2H_2=CH_4+V$$

$$WC+ 2H_2=CH_4+W$$

The types of carbides significantly influence hydrogen attack susceptibility of materials. Thermodynamically, the more stable the carbides, the less susceptible to hydrogen attack the material is. Figure 2.23 shows the free energy of formation ($\Delta G°$) for various carbides [64]. It is noted that Fe_3C is the least stable carbide compared with the Cr, Mo, Nb, V, and W carbides ($Cr_{23}C_6$, Mo_2C, NbC, VC, and WC). The free energy of M_6C carbide was not found in the available thermodynamic data sources. However, carbide evolution sequences were defined according to the carbide study for 2.25Cr-1Mo steel [65, 66]. The carbide evolution sequences are:

In bainitic region:

$$\begin{array}{lcccc} \varepsilon \text{ Carbide} & & & & \\ + & \rightarrow M_3C \rightarrow & M_3C & \rightarrow & M_7C_3 \\ M_3C & & + & & + \\ & & M_2C & & M_{23}C_6 \rightarrow M_6C \end{array}$$

In ferritic region:

$$M_2C \rightarrow M_6C$$

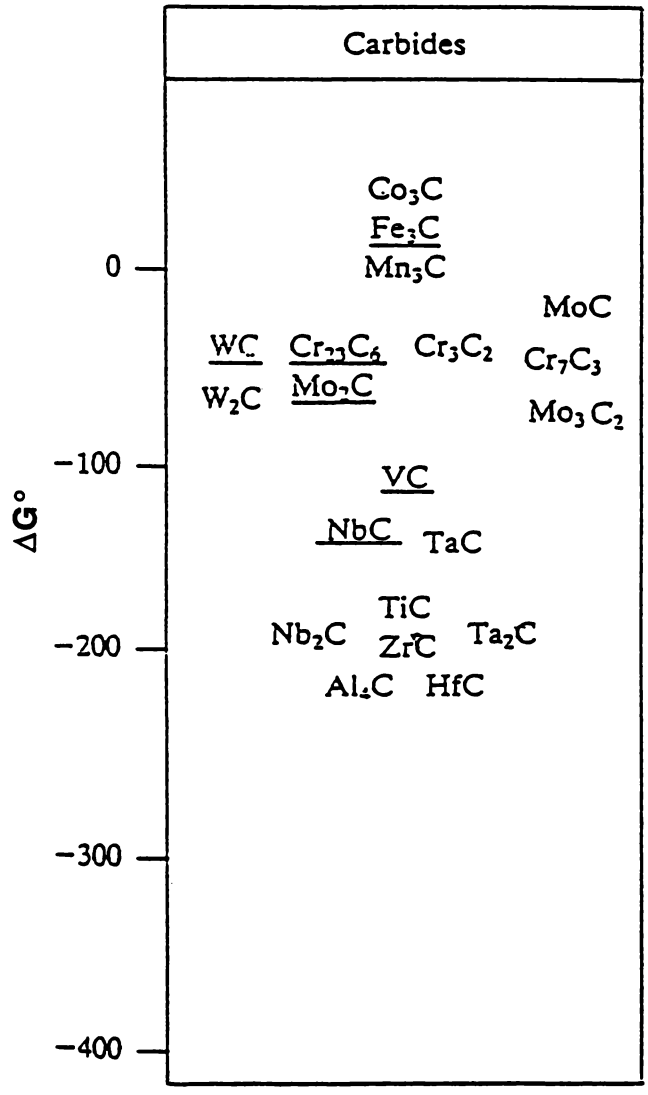


Figure 2.23 Standard free energy for carbide formation (ΔG°, KJ/mole) [64].

The carbide evolution sequence indicates that M_6C carbides are more stable than $M_{23}C_6$ and M_2C. Therefore, the free energy of formation of M_6C carbide should be less than that of $M_{23}C_6$ or M_2C.

The formation of methane gas is controlled by the reaction of hydrogen and carbon and/or carbides. The addition of carbide-stabilizing elements can form more stable carbides and reduce carbon activity [67]. Carbon activity can be determined using a thermodynamic methodology [68, 69]. The efficacy of alloying elements and impurities to inhibit hydrogen attack is summarized as follows [26]:

Inhibit hydrogen attack:	Cr, Mo, W, V, Nb, Ti, Zr, Ta, Mn, P
Enhance hydrogen attack:	C, Ni, Cu, S

Carbide evolution is dependent on tempering temperature and time [64, 70-75]. Figure 2.24 shows the effect of Mo content on the carbide evolution during tempering [70]. For C-0.5Mo steel, cementite forms first and then more stable carbides of Mo_2C and $M_{23}C_6$ occur [76]. Fe_3C is the predominant carbide in the normalized condition and it can contain a small amount Mo [77]. After a long time exposure at 530°C (986°F), Mo_2C carbides form and preferentially precipitate in the ferrite grain matrix. As a consequence, the Mo in solid solution is reduced in the ferrite grain matrix and thus reduces the strength of the grain matrix. Therefore, the formation of Mo_2C carbides coincides with a recovery of ductility. Mo_2C carbide was not observed after exposure at 450°C (842°F) for 13,470 hours. $(Fe_{21}Mo_2)C_6$ carbides begin to replace Fe_3C at 630°C (1166°F)

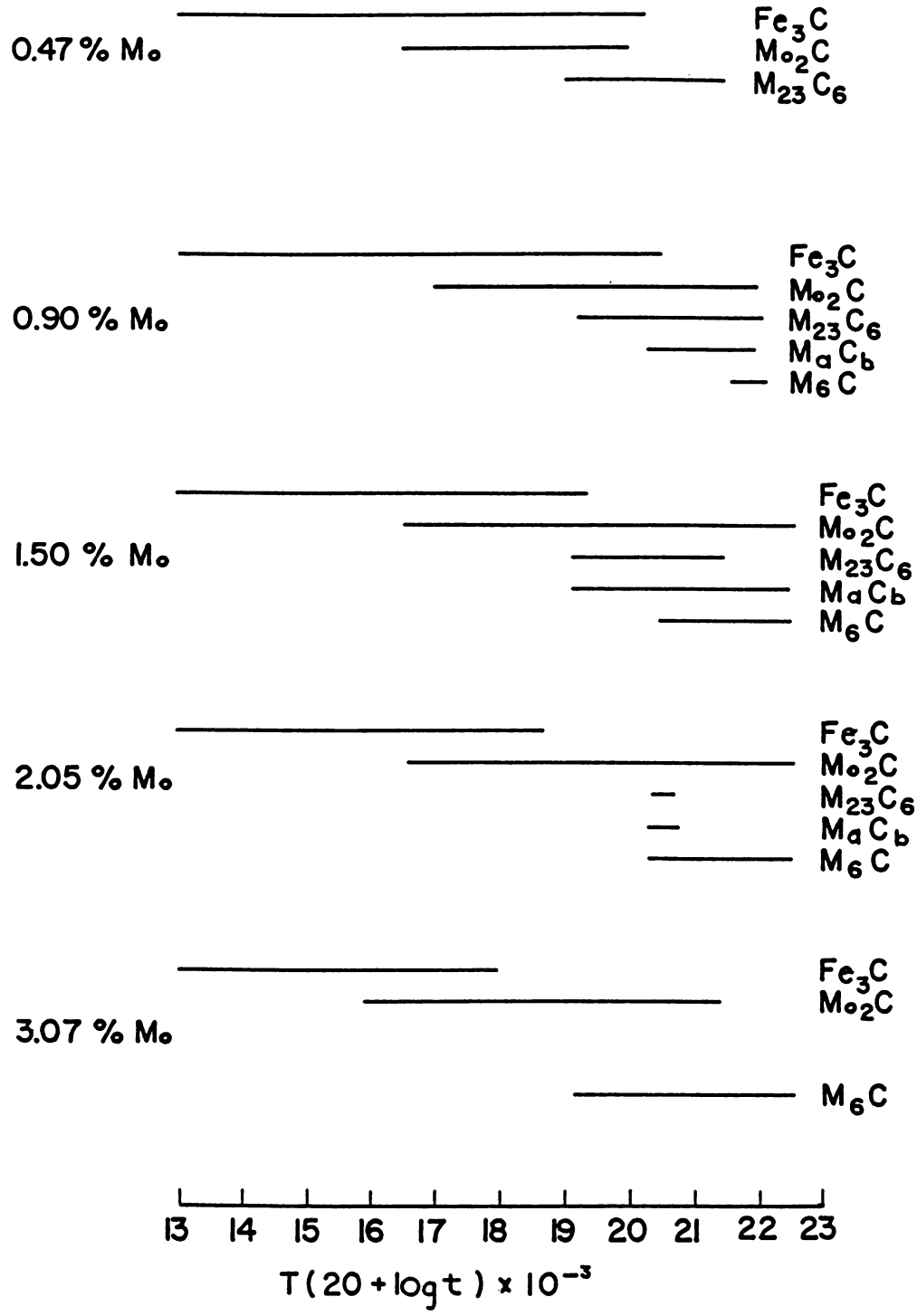


Figure 2.24 Effect of Mo on the carbide evolution during tempering [73].

and above. $(Fe_{21}Mo_2)C_6$ carbides are identifiable by its sooty black appearance on being etched by 4% nital, whereas Fe_3C remains relatively un-attacked. In addition, Fe_2MoC carbide with a crystal structure between Fe_3C and Fe_3Mo_3C was found in the reaction sequences where Fe_3C is initially present [78].

Shaw [74] studied the effect of Mo, Cr, Mn, Si, and C on the formation of carbides. It was found that the carbides on the grain boundaries are distinguishable from the those in the matrix. An increase for all the elements mentioned above promotes the evolution of stable M_6C carbides and reduces the amount of M_2C. Increase in Mo promotes the formation of Mo_2C. A carbide composition map was constructed using energy-dispersive spectroscopy (EDS). The chemical composition of the carbides is concluded as:

M_3C	Fe>60%
$M_{23}C_6$	Fe<60%
Mo_2C	70%<Mo<90%
M_6C	(a). 30%<Mo<60%
	(b). 5%<Si<12% (0<Si< is also found in Fe_3C)
M_7C_3	40<Cr<60%

An equilibrium precipitate frequently represents the final product of two or more transformations, for which two main mechanism were proposed. The intermediate precipitate can dissolve in the matrix, while the equilibrium precipitate nucleates separately from the solid solution. Alternatively, in-situ transformation can occur in the metastable precipitate by gradual inward

diffusion of solute. Raynor et al. [76] studied the early stages of the decomposition of martensite in an Fe-Mo-C alloy. The first precipitate observed was cementite, which was present even in the as-quenched state. Mo_2C carbides nucleated later at cementite/ferrite interfaces, in grain matrix, and at martensitic lath boundaries. The Mo_2C at the cementite/ferrite interface grows more rapidly than those in the grain matrix.

2.3.6 Hydrogen Attack Modeling

Hydrogen attack modeling has been approached at three levels: microscopic scale, mesoscopitc scale, and macroscopic scale [12-14, 31, 79-82]. For the microscopic scale, modeling involves the growth of a single cavity due to grain boundary diffusion and creep driven by the methane pressure and/or the local stress around the cavity. The model describes microvoid growth as a function of methane pressure, external stress, microvoid radius and spacing, as well as creep and diffusion parameters.

In the mescoscopic scale model, an aggregate of grains is considered [13, 14]. The effect of different methane pressure distribution on the hydrogen attack evolution and stress distribution was investigated. Two extreme cavitation modes were introduced: creep deformation mode and non-creep deformation mode. In the creep deformation mode, grains can deform significantly and cavities primarily form along grain boundaries perpendicular to maximum principal stress. In the non-creep deformation mode, creep

deformation was negligible and cavities could occur uniformly on all grain boundaries by the Fe atom diffusion.

In the macroscale, a continuum of damage was incorporated into a finite element model to calculate hydrogen damage evolution, stress distribution, and service life for steel components exposed to high pressure hydrogen at elevated temperature. Based on the models, the hydrogen attack rate in various conditions could be determined and Nelson Curves could be computed [83-85].

CHAPTER 3

MATERIALS AND EXPERIMENTAL PROCEDURES

3.1 Materials

Twenty six heats of C-0.5Mo steel were received from the petroleum refinery and petrochemical industry (Chevron, Shell Oil, BP Oil, Arco Oil, and Koch Petroleum Group) for hydrogen attack damage evaluation. 24 of these 26 heats were extracted from in-service pressure vessels, piping, reactors, and heat exchangers. In addition, Japan Steel Works (JSW) provided a heat of C-0.5Mo steel in the annealed and annealed & tempered condition. The influence of carbon and alloying elements on hydrogen attack susceptibility was investigated for these materials. Heat treatment in terms of normalizing, normalizing & tempering, annealing, and annealing & tempering was conducted to define an optimum heat treatment condition for improvement of hydrogen attack resistance.

The chemical composition of the materials is presented in Table 3.1. It is to be noted that primary alloying elements cover a wide range. Therefore, the research results and model developed represent the full range of hydrogen attack cases in industry and thus should provide an accurate fitness analysis of operating equipment. The major elements in the screened heats of C-0.5Mo steel are in the range of:

C:	0.11-0.26%
Mo:	0.41-0.57%

Table 3.1 Chemical composition of the received heats of C-0.5Mo steel for hydrogen attack evaluation (wt%).

Element	MPC-1	MPC-2	MPC-3	MPC-4	MPC-5	MPC-6	MPC-7	MPC-8	MPC-9*
C	0.22	0.20	0.21	0.18	0.16	0.16	0.19	0.17	0.11
Mn	0.75	0.79	0.86	0.67	0.71	0.70	0.78	0.58	0.64
P	0.004	0.004	0.005	0.013	0.020	0.021	0.004	0.008	0.007
S	0.016	0.015	0.022	0.030	0.034	0.034	0.012	0.016	0.007
Si	0.21	0.25	0.23	0.22	0.33	0.33	0.20	0.24	0.20
Ni	0.07	0.11	0.12	0.37	0.05	0.05	0.06	0.03	0.06
Cr	0.06	0.10	0.10	0.15	0.05	0.05	0.06	0.07	0.10
Mo	0.49	0.47	0.48	0.47	0.47	0.47	0.47	0.56	0.54
V	0.001	0.001	0.001	0.001	0.001	0.001	0.001	0.001	0.002
Nb	0.001	0.001	0.001	0.002	0.002	0.001	<0.001	<0.001	0.001
Ti	0.001	0.001	0.001	0.001	<0.001	<0.001	0.001	0.001	0.001
Co	0.008	0.009	0.010	0.016	0.019	0.019	0.008	0.052	0.018
Cu	0.06	0.10	0.26	0.24	0.09	0.09	0.08	0.01	0.13
Al	0.002	0.003	0.006	0.002	0.003	0.003	0.009	0.004	0.004
B	<0.001	<0.001	<0.001	<0.001	<0.001	<0.001	<0.001	<0.001	<0.001
W	<0.01	<0.01	<0.01	<0.01	<0.01	<0.01	<0.01	<0.01	<0.01
Sb	<0.002	<0.002	<0.002	<0.002	0.002	0.002	<0.002	<0.002	0.006
As	0.010	0.009	0.012	0.012	0.020	0.019	0.008	0.014	0.023
Sn	0.007	0.010	0.018	0.022	0.008	0.008	0.009	0.014	0.013
Zr	<0.001	<0.001	<0.001	<0.001	<0.001	<0.001	<0.001	<0.001	<0.001
N	0.007	0.006	0.006	0.005	0.007	0.006	0.006	0.008	0.011
O	0.004	0.005	0.004	0.007	0.008	0.009	0.005	0.003	0.012
Mo/C	2.23	2.35	2.29	2.61	2.94	2.94	2.47	3.29	4.91

* Hydrogen attacked during service.
Carbon content was determined at the OD location without hydrogen damage.

Table 3.1 Chemical composition of the received heats of C-0.5Mo steel for hydrogen attack evaluation (wt%, continued).

Element	MPC-10	MPC-11*	MPC-12	MPC-13	MPC-14	MPC-15*	MPC-16	MPC-17	MPC-18*
C	0.12	0.18	0.17	0.15	0.14	0.22	0.15	0.24	0.18
Mn	0.65	0.55	0.54	0.57	0.55	0.83	0.53	0.83	0.53
P	0.008	0.005	0.005	0.007	0.012	0.009	0.008	0.008	0.004
S	0.008	0.016	0.016	0.014	0.022	0.032	0.023	0.019	0.013
Si	0.20	0.11	0.11	0.33	0.26	0.23	0.23	0.32	0.24
Ni	0.06	0.08	0.07	0.04	0.02	0.13	0.08	0.09	0.09
Cr	0.10	0.07	0.07	0.17	0.04	0.17	0.09	0.05	0.06
Mo	0.55	0.48	0.46	0.57	0.53	0.50	0.55	0.45	0.43
V	0.002	0.001	<0.001	0.001	<0.001	0.002	<0.001	0.002	0.001
Nb	0.001	<0.001	<0.001	0.001	0.001	0.002	0.001	<0.001	<0.001
Ti	0.001	0.001	0.001	0.001	0.002	0.005	0.001	0.006	0.001
Co	0.018	0.008	0.008	0.007	0.002	0.011	0.006	0.010	0.008
Cu	0.13	0.11	0.11	0.08	0.02	0.17	0.04	0.14	0.17
Al	0.003	0.001	0.001	0.002	0.036	0.003	0.002	0.003	0.014
B	<0.001	<0.001	<0.001	<0.001	<0.001	<0.001	<0.001	<0.001	<0.001
W	<0.01	<0.01	<0.01	<0.01	<0.01	<0.01	<0.01	<0.01	<0.01
Sb	0.006	0.003	0.002	0.004	0.002	0.004	<0.002	0.004	0.002
As	0.025	0.007	0.007	0.007	0.002	0.013	0.007	0.015	0.009
Sn	0.015	0.011	0.010	0.010	0.003	0.023	0.005	0.015	0.010
Zr	<0.001	<0.001	<0.001	<0.001	<0.001	<0.001	<0.001	<0.001	<0.001
N	0.011	0.005	0.007	0.009	0.007	0.008	0.004	0.005	0.006
O	0.008	0.013	0.013	0.008	0.004	0.005	0.010	0.003	0.002
Mo/C	4.58	2.67	2.71	3.80	3.79	2.27	3.67	1.88	2.39

* Hydrogen attacked during service.
Carbon content was determined at the OD location without hydrogen damage.

Table 3.1 Chemical composition of the received heats of C-0.5Mo steel for hydrogen attack evaluation (wt%, continued).

Element	MPC-19*	MPC-20*	MPC-21	MPC-22*	MPC-23	MPC-24	MPC-25	MPC-26	MPC-27*
C	0.24**	0.22**	0.23**	0.26**	0.14	0.16	0.17	0.26	0.26
Mn	0.59	0.65	0.53	0.77	0.72	0.47	0.85	0.80	0.78
P	0.010	0.011	0.006	0.004	0.007	0.012	0.0087	0.007	0.009
S	0.028	0.021	0.018	0.019	0.003	0.009	<0.001	0.18	0.018
Si	0.24	0.18	0.23	0.32	0.22	0.17	0.23	0.22	0.25
Ni	0.13	0.16	0.15	0.09	0.14	-	0.03	0.07	0.08
Cr	0.07	0.13	0.16	0.08	0.11	-	0.04	0.32	0.32
Mo	0.41	0.48	0.51	0.54	0.50	0.50	0.56	0.54	0.53
V	0.002	0.003	0.001	0.001	0.001	-	<0.003	0.002	0.002
Nb	<0.001	0.001	<0.001	<0.001	0.001	-	<0.003	0.004	0.006
Ti	0.001	0.001	<0.001	0.001	-	-	<0.003	0.001	0.001
Co	0.008	0.009	0.011	0.008	-	-	-	0.010	0.011
Cu	0.14	0.13	0.13	0.12	0.14	-	0.02	0.14	0.13
Al	0.034	0.001	0.008	<0.001	0.021	-	0.005	0.001	0.002
B	<0.001	<0.001	<0.001	<0.001	-	-	<0.0003	0.001	0.001
W	<0.01	<0.01	<0.01	<0.01	-	-	-	<0.01	<0.01
Sb	0.003	<0.002	0.002	0.002	-	-	<0.002	<0.002	<0.002
As	0.008	0.01	0.008	0.007	-	-	<0.002	0.018	0.020
Sn	0.011	0.009	0.012	0.010	-	-	<0.001	0.017	0.018
Zr	<0.001	<0.001	<0.001	<0.001	-	-	-	0.001	0.001
N	0.005	0.005	0.006	0.006	-	-	0.0044	0.006	0.007
O	0.001	0.012	0.004	0.010	-	-	-	0.003	0.003
Mo/C	1.71	2.18	2.22	2.08	3.57	3.13	3.29	2.08	2.04

* Hydrogen attacked during service.
Carbon content was determined at the OD location without hydrogen damage.

** Carbon content was reported from manufacture.

Mn:	0.53-0.86%
Si:	0.11-0.33%
Mo/C:	1.71-4.91

The thickness of the screened components is in the range of 5/16" to 3 7/8".

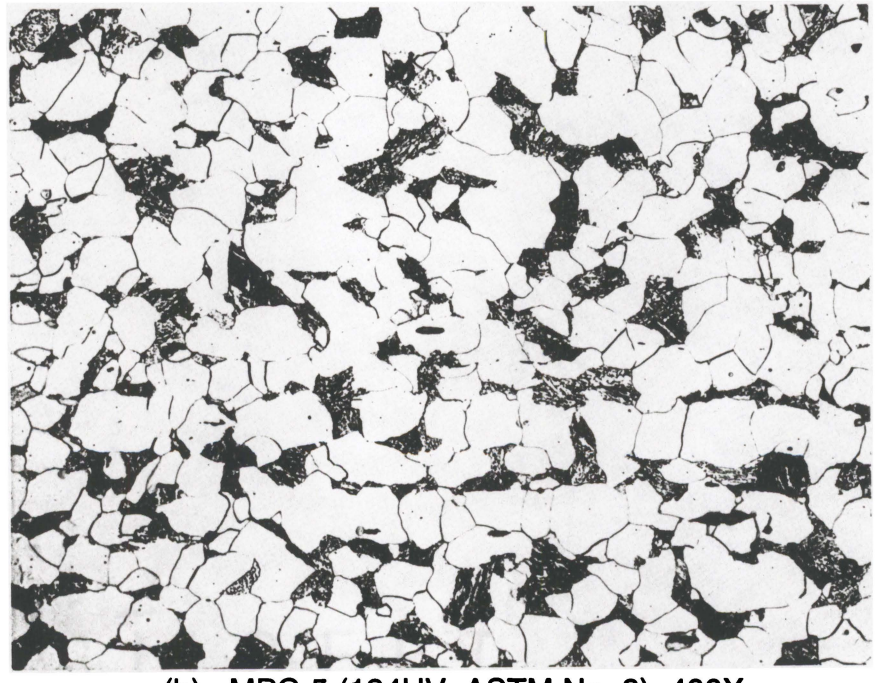
From the microstructural point of view, the grain size of the heats is in the range of ASTM No. 2 to 8. The microstructure is composed of bainite and ferrite for the majority of the heats. A mixture of pearlite, bainite, and ferrite was observed in a few heats. Figures 3.1 and 3.2 present typical microstructures, grain sizes, and hardness.

In addition, girth and longitudinal seam welds were examined for the many of the components. Hydrogen attack damage was evaluated in the weld metal and HAZ to define the most susceptible region. Shielded Metal arc welding (SMAW), Gas Tungsten arc welding (GTA), and Gleeble simulated HAZs were used to define the effects of welding and PWHT on the hydrogen attack susceptibility of welds.

Heat treatments were conducted to assess hydrogen attack susceptibility for the materials with different microstructures. MPC-3 was normalized at 1650°F-2 hrs. and tempered at 1250°F-1hr. (N&T) before hydrogen exposure. The N&T microstructure is a mixture of ferrite and tempered bainite. In addition, annealed (1652°F-3 hrs.) and annealed & tempered (1283°F-15 hrs and 1337°F-15 hrs.) heat treatments were conducted for MPC-3 and MPC-25 (received from JSW). The microstructure for the annealed-only is a mixture of ferrite and pearlite. Coarsened carbides were observed in the annealed and

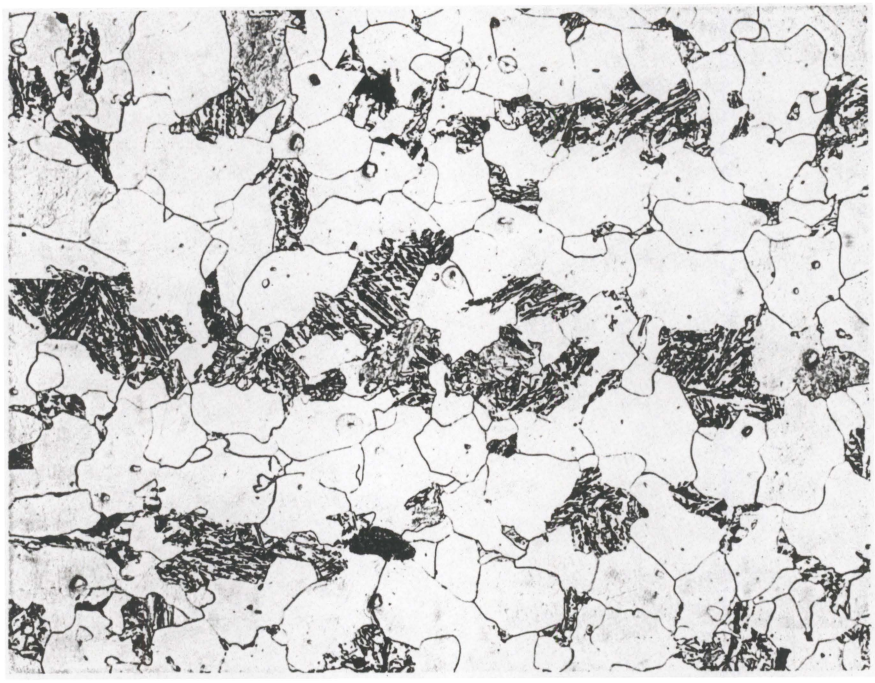


(a). MPC-4 (154HV, ASTM No. 2), 400X



(b). MPC-5 (124HV, ASTM No. 8), 400X

Figure 3.1 Typical microstructures of the received heats of C-0.5Mo steel.



(a). MPC-3 (151HV, ASTM No. 7), 400X



(b). MPC-8 (147HV, ASTM No. 6), 400X

Figure 3.2 Typical microstructures of the received heats of C-0.5Mo steel.

tempered materials (MPC-3 and MPC-25). Carbides were identified using TEM, EDS, and X-ray diffraction.

The influence of hot and cold work on hydrogen attack was studied. Hot and cold rolling processes were performed with plastic deformation of 5%, 10%, and 20%. Cold rolling was implemented at ambient temperature. An initial temperature of 1750°F was used for hot rolling.

3.2 Experimental Procedures

3.2.1 Hydrogen Service Exposure

Hydrogen attack damage was evaluated for the service exposed components. Available field operating conditions in terms of temperature, hydrogen partial pressure, and operating time were provided by the petroleum/chemical companies as presented in Table 3.2. It is to be noted that the operational temperatures and hydrogen partial pressures are in the range of 423-850°F and 100-2250 psi for periods of 13 to 32 years.

3.2.2 Hydrogen Autoclave Exposure

Autoclave hydrogen exposure tests were conducted for the study of hydrogen attack behavior in steels. Figure 3.3 schematically shows the autoclave apparatus used for high temperature and high hydrogen pressure exposure. Materials used for the autoclave exposure testing were selected from

Table 3.2 Available operational conditions for the received heats of C-0.5Mo steel.

Heats	Temperature (max.) °F	Hydrogen Pressure (max.) psi	Service Time Years
MPC-11	670	290	22
MPC-12	423	190	22
MPC-13	550	2250	13
MPC-14	850	190	16
MPC-15	770	550	30
MPC-16	600	450	32
MPC-17	770	550	30
MPC-18	580	950	28
MPC-19	500	950	28
MPC-20 (A)*	600	950	28
MPC-20 (B)*	700	100	28
MPC-21	530	950	28
MPC-22	500	950	28
MPC-26	700	500	25
MPC-27	700	500	25

* MPC-20 (A)-On Side A of tube sheet, MPC-20 (B)-On Side B of tube sheet.

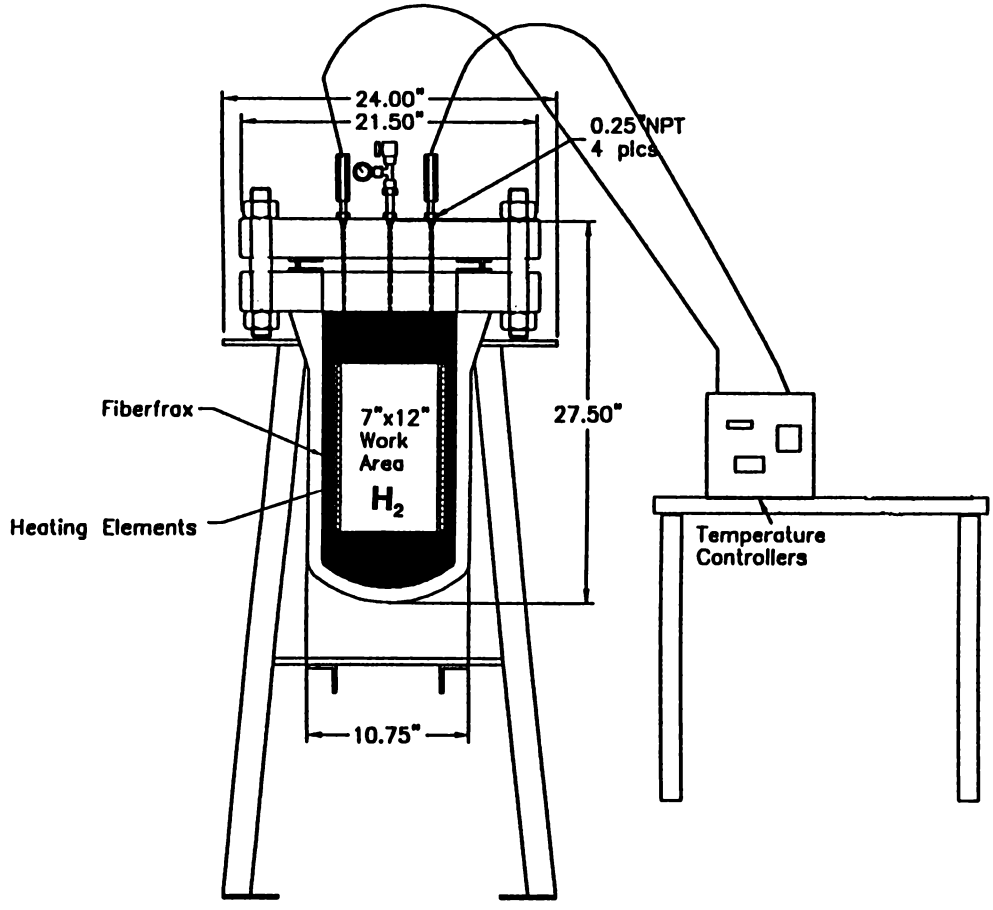


Figure 3.3 Schematic of the autoclave used for high temperature and high hydrogen pressure exposure testing.

the heats without hydrogen attack damage and re-normalized (1650°F-2 hrs.) and tempered (1150°F-2 hrs.) to remove the in-service effects. Samples were ground using 120 grit emery and cleaned in acetone using an ultrasonic cleaner. Different exposure temperatures (725 ~ 900°F) and hydrogen pressures (500 ~ 950 psi) were utilized to study methane evolution and the effects of carbon and alloying elements, cold and hot work, welding and PWHT on hydrogen attack susceptibility.

In practice, static autoclave exposure testing does not accurately simulate actual operating conditions encountered in pressure vessels and piping. Thus, in addition to the static autoclave exposure tests, a one-sided hydrogen exposure test was designed for this study. A differential of hydrogen partial pressure emerges from inside to outside of pressure vessels and pipes. A sustained hydrogen concentration gradient is established through wall thickness by a one-sided exposure.

To simulate practical operating condition for pressure vessels and piping, a box-like sample was assembled using MPC-3 and MPC-15 for one-sided hydrogen exposure testing. Figure 3.4 schematically shows the assembly and dimensions of the box-like sample. The two materials (MPC-3, MPC-15) used for the box-like sample were machined with sloping walls in order to include thicknesses from 1/4" to 2" to order to study a thickness effect on hydrogen attack (Figure 3.5). To prevent hydrogen leakage through the weld securing the box halves, the groove surfaces were buttered using gas tungsten arc welding

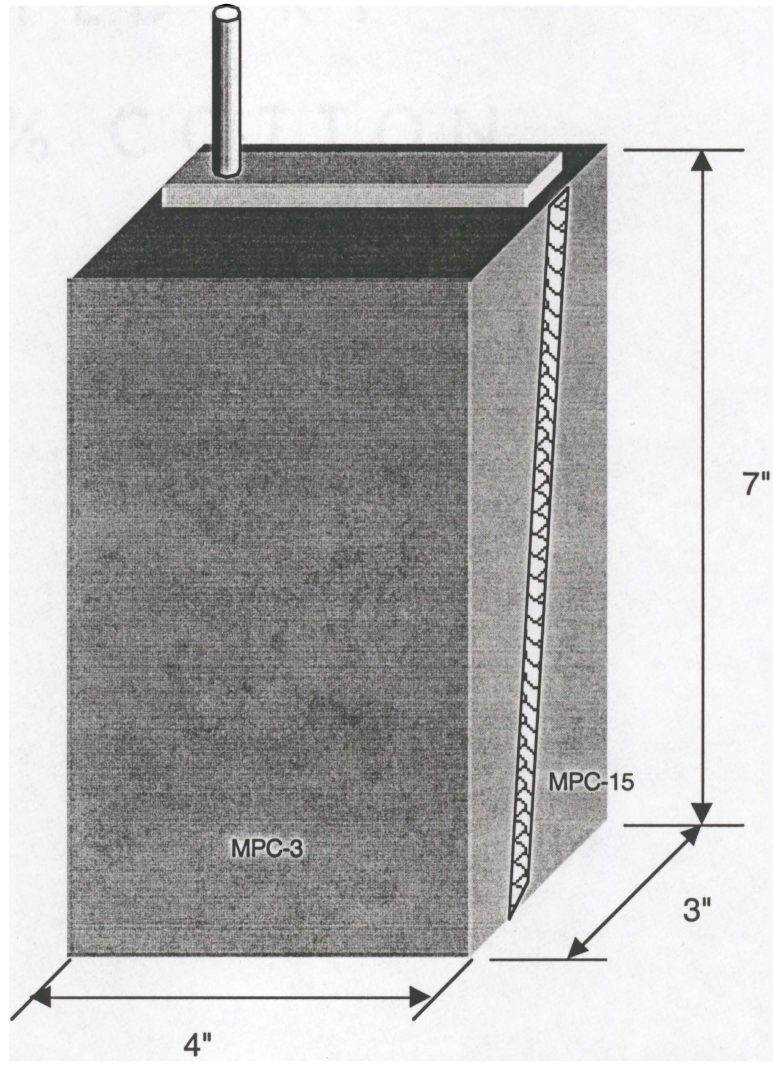


Figure 3.4 Schematic of the box-like sample for one-sided hydrogen exposure testing.

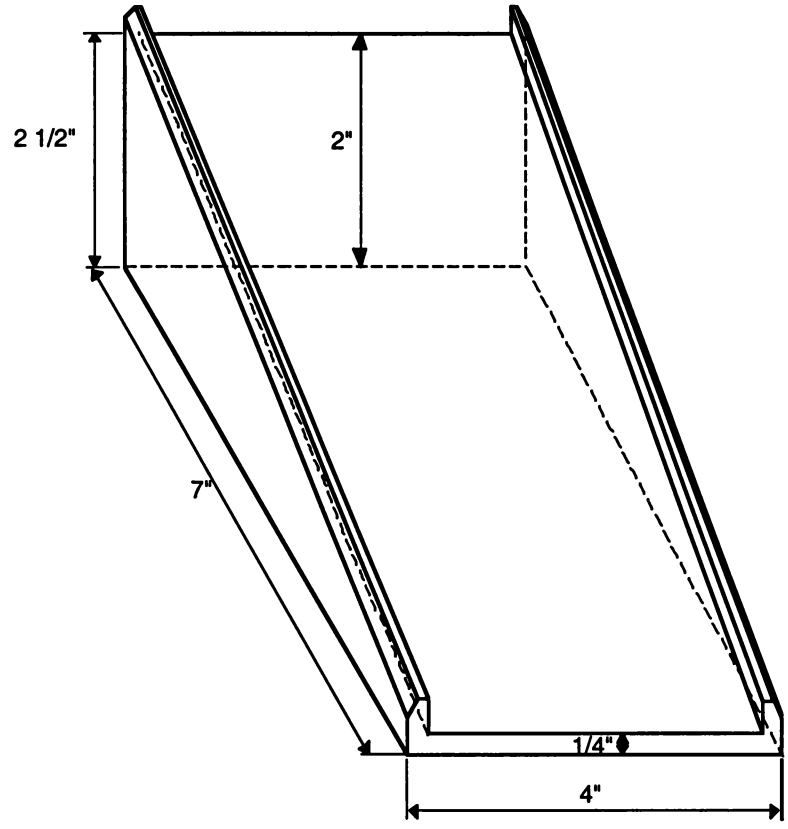


Figure 3.5 Dimensions of half part of the box-like sample with a sloping wall for one-sided hydrogen exposure testing.

(GTAW) with Inconel 82 filler metal (which has high resistance to hydrogen attack and low hydrogen diffusivity). After buttering, the two box halves were normalized at 1650°F for 2 hours to eliminate weld HAZ. Tempering heat treatment was conducted at 1150°F for 2 hours. The box-like sample was assembled using GTAW with Inconel 82 filler metal using a procedure that would not create a HAZ in the C-0.5Mo box halves. A stainless tube (AISI 304) was welded to one end of the box for venting the sample during hydrogen exposure testing. Pressure tests were performed for three times at air pressure of 75 psi for 20 minutes without leakage. Figure 3.6 shows a photograph of the box-like sample used of one-sided hydrogen exposure.

Figure 3.7 schematically shows the one-sided hydrogen exposure testing assembly. The box-like sample was placed in an autoclave at a controlled temperature and hydrogen pressure. The outside surfaces of the sample were exposed to hydrogen atmosphere and the inside is vented using a mechanical pump to maintain a differential of hydrogen pressure from outside to inside. A gradient of hydrogen concentration is anticipated through wall thickness. The box-like sample was exposed at 900°F-900 psi H_2 for 1248 hours and 950°F-900 psi H_2 for 288 hours. After autoclave exposure three sections were extracted from the MPC-3 material at locations with wall thicknesses of 44 mm (1.73"), 29 mm (1.14"), and 13 mm (0.51") for hydrogen attack damage evaluation using OLM, SEM, "Cryo-cracking", and gas chromatography.

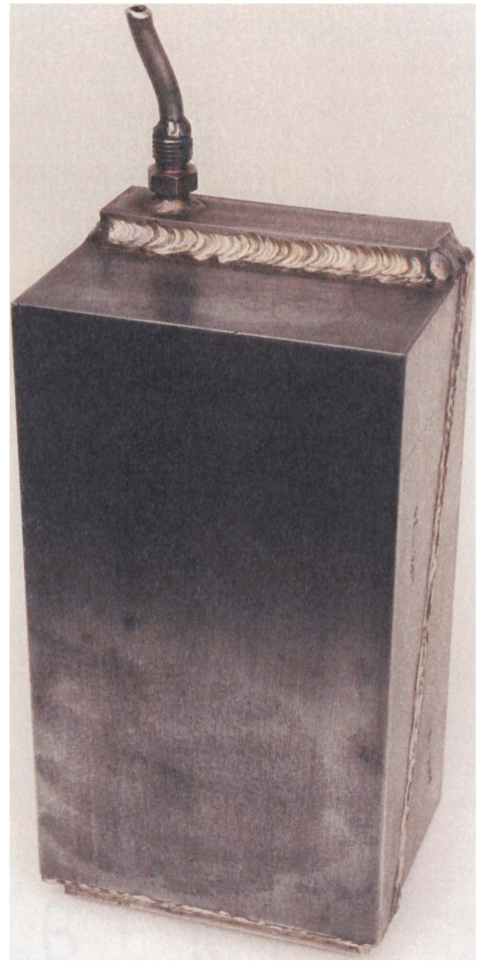


Figure 3.6 Photograph of the box-like sample for one-sided hydrogen exposure testing.

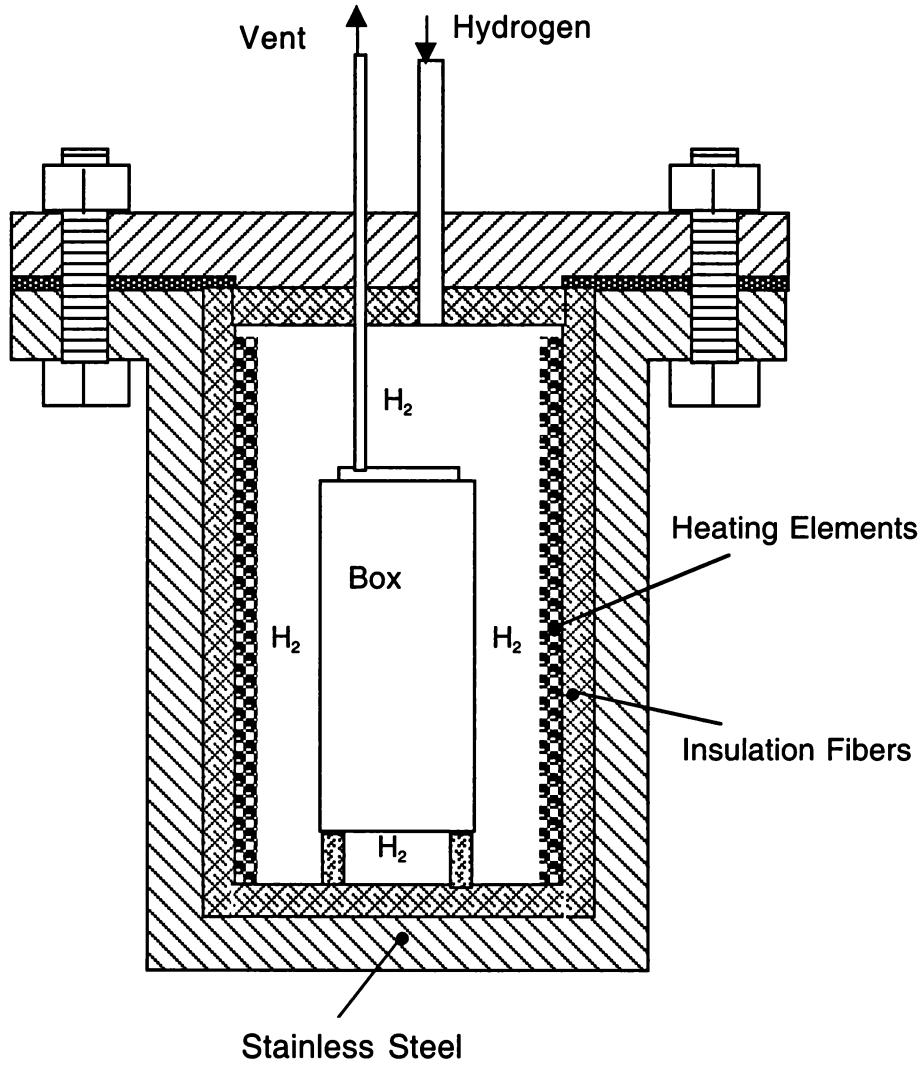


Figure 3.7 Schematic shown the assembly of one-sided hydrogen exposure testing.

3.2.3 Metallographic Evaluation

Hydrogen attack occurs in several stages after an "incubation" period: methane bubbles initiation, growth, and coalescence to form microcracks. The dimensions of hydrogen attack damage at each stage are visible for different scale examination. In the "incubation" stage, there is no visible evidence of hydrogen attack damage and mechanical property degradation. It was found that there are pre-existing microvoids at grain boundaries which provide nucleation sites for methane bubble formation [50, 86, 87]. The pre-existing microvoids can be grain boundary defects, incoherent carbide interface, and inclusion-matrix interfaces.

In the initiation stage, the size of the methane bubbles is too small to be resolved by using optical light microscopy (OLM). Therefore, scanning electron microscopy (SEM, Cambridge Instrument, Stereoscan 360) was utilized for examination. Quantitatively metallographic analysis was conducted to assess hydrogen attack damage using point counting methods and a computer image analysis software (NIH Image) [88-90]. The advantages of the NIH Image analysis software application are that the size and quantity of the methane bubbles or microcracks can be determined in an efficient way. Images can be manipulated in the aspects of sharpening, density slicing, and edge tracing to highlight microcracks for quantitative analysis. The fractions of hydrogen damaged grain boundary lengths (FL%) was defined as a parameter for

hydrogen attack damage evaluation. The FL% is determined by the damaged grain boundary length (L_D) divided by total grain boundary length (L_T):

$$FL\ (\%) = (L_D / L_T) \times 100$$

The value of FL% was averaged using three OLM images at magnifications of 400X as well as SEM images at magnifications of 1000X for polished and etched samples.

In addition, "Cryo-cracking," a technique that was developed for SEM fractographic examination, was utilized for hydrogen attack damage evaluation. The advantages of the "Cryo-cracking" technique are to reveal the extent of microstructural damage within materials and to preserve the damage morphology so as to show methane bubble morphology. In the preparation of specimens for "Cryo-cracking", a rectangular bar was extracted from the hydrogen damaged materials. A sharp circumferential notch was cut at the locations where evaluation was desired. The notched bar was submerged in liquid nitrogen for a minimum of 15 minutes. The bar was then placed in a vice and fractured. Immediately after fracture, the specimens were placed in methanol bath until the temperature reached ambient and then they were dried for SEM fractographic examination. The fraction of hydrogen damaged grain boundary area (FA%) was defined as a parameter for hydrogen attack damage evaluation. The FA% is the projection of damaged grain boundary area (A_D) divided by total examined area (A_T):

$$FA\ (\%) = (A_D / A_T) \times 100$$

The FA% value was averaged from three SEM images at a magnification of 1000X.

Carbide morphology, type, distribution, and composition strongly influence hydrogen attack susceptibility. SEM, transmission electron microscopy (TEM, Hitachi H-800), energy-dispersive spectroscopy (EDS), and X-ray diffraction (Rigaku) were utilized for carbide morphology examination, chemical composition determination, and carbide type. Carbon replicas extracted from polished and etched metallographic samples were used for TEM examination. Samples were mounted in cold setting epoxy with a wire welded to the back of the sample for electrolytic etching. The samples were polished and heavily etched using 2% nital to leave carbides in relief. A carbon film was deposited on the polished and etched surface using carbon evaporation (Benton Vacuum DV-515 Automatic Evaporator). An appropriate thickness of carbon film was controlled by observing the color change to dark brown on the sample surface. The region of interest was isolated by painting with insulating paint and the carbon film in this region was cut into grids (< 3x3 mm^2). Electrolytic etching in a 10% HCl methanol solution was then employed to dissolve the matrix and leave carbide particles attached to the carbon film. Then, the film contained carbide particles was placed on a TEM sample grid (200 mesh) for carbide examination.

3.2.4 Methane Determination

The reaction of hydrogen and carbides or carbon to form methane gas is the driving force for hydrogen attack in terms of bubble initiation and growth during high temperature and high hydrogen exposure. Therefore, the determination of methane concentration can provide important information for hydrogen attack assessment. Methane gas in bubbles and cracks is not diffusible and can not be measured directly. However, methane concentration can be indirectly determined by measuring hydrogen dissociated from methane gas. The dissociating temperature of methane gas can be estimated according to thermodynamic calculation [91]. For methane dissociation reaction

$$CH_4 = C + 2H_2$$

the standard free energy (cal./mole) is

$$\Delta G^\circ = 21550 - 26.16\ T$$

where T is absolute temperature in the range of 298°K to 2273°K (77°F to 3632°F). The dissociating temperature for methane was calculated to be above 824°K (1024°F). Experimental results showed that the methane gas in cavities or cracks was dissociated into hydrogen and carbon by heating to approximately 773°K to 873°K (932°F to 1112°F) for 6 hours [92].

For hydrogen measurements, service exposed or autoclave exposed samples were encapsulated in quartz tubes back-filled with high purity argon (99.9999%). The encapsulated samples were thermally treated at 1292°F (700°C) for 72 hours for complete methane gas dissociation. After heat

treatment, the encapsulated samples were placed in samplers of an Oerlikon-Yanaco Hydrogen Analyzer and filled with argon. The quartz capsules containing the samples were broken by shocking the sampler chambers. Therefore, any hydrogen in the capsules was released into the samplers and subsequently measured by the Hydrogen Analyzer. Figure 3.8 shows the apparatus of Hydrogen Analyzer, samplers, and a sample encapsulated in quartz tube. A bulk sample (minimum 6 grams) is required for hydrogen determination. Hydrogen concentration is measured in volume (mL) using Hydrogen Analyzer for the standard temperature and pressure (0°C-1 atm). Based on the methane dissociation reaction, 1 mole of CH_4 can dissociate to 2 moles of H_2 (1 ppm methane can dissociate 1/4 ppm hydrogen). Therefore, the methane concentration can be determined by hydrogen measurement.

In addition to Oerlikon-Yanaco Hydrogen Analyzer, hydrogen was analyzed using Leco high temperature fusion method at NSL Analytical Services Inc. for comparison.

3.2.5 Carbon Determination

Carbon is one of the major elements involved in methane bubble formation. Carbon content provides important evidence of hydrogen attack. Carbide dissociation as well as hydrogen and carbon diffusion in steels control methane reaction kinetics and result in internal decarburization. Because a differential of hydrogen partial pressure exists between inside and outside walls

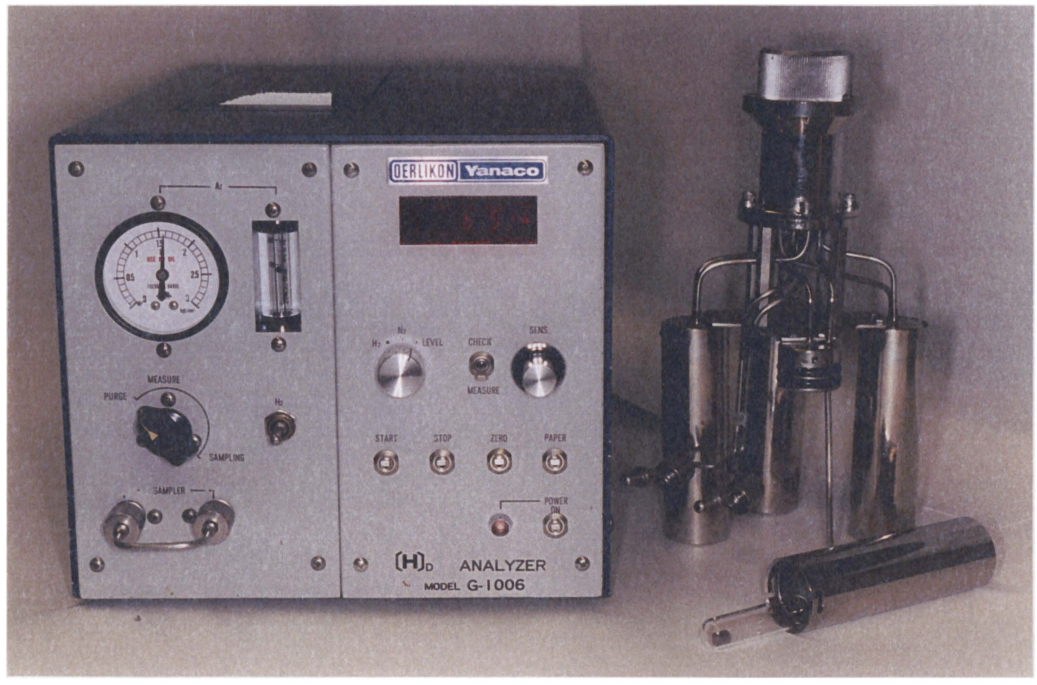


Figure 3.8 Oerlikon-Yanaco Hydrogen Analyzer, samplers, and samples encapsulated in quartz tubes for methane determination.

of a vessel or piping decarburization varies from inside to outside through wall thickness. Carbon concentration profiles through the wall thickness is an indirect indication of hydrogen attack damage distribution. Therefore, a decarburization index, DCI (%), was defined as:

$$DCI\ (\%) = (C_0 - C) / C_0$$

where C_0 is the carbon concentration before hydrogen exposure and C is the carbon concentration after hydrogen exposure.

3.2.6 Hardness Testing

Microhardness testing (Vickers, 0.5 kg) was used to evaluate hydrogen attack damage. A hardness degradation index (HDI) for hydrogen attack susceptibility was defined for hydrogen attack assessment:

$$HDI\ (\%) = (HV_0 - HV) / HV_0$$

where HV is the hardness after hydrogen exposure and HV_0 is the hardness after heat treatment at an identical temperature and time as the hydrogen exposed sample (without hydrogen). The greater the value of HDI is, the more severe hydrogen attack.

3.2.7 Gleeble Simulation and Dilatometry

Chemical composition, heat treatments, cooling rate, and carbide types and stability are strongly associated with hydrogen attack cracking susceptibility [7, 93, 94]. Therefore, phase transformations for C-0.5Mo steel were

investigated under heat treatment and welding conditions using Gleeble thermal simulation and high speed dilatometry techniques.

Two heats (MPC-3 and MPC-13) were applied to the development of CCT diagrams in the heat treatment and welding conditions. These two heats, representing high and low carbon contents (0.21% and 0.15%C, respectively), were selected so as to cover the hardenability range of C-0.5 Mo steel. In order to eliminate the influence of the service exposure, these two heats were re-normalized at 1650°F for 2 hours and tempered at 1150°F for 2 hours prior to sample machining. The samples used for CCT diagrams development are 0.25" diameter rods for the compatibility with the Gleeble dilatometry methodology.

For heat treatment CCT diagrams, the specimens were heated to 1670 °F and held for 15 minutes for complete austenitization and cooled at cooling rates of 1, 5, 10, 20, 300, 1000, and 6000 C°/min. Welding CCT diagrams were developed for the coarse grained HAZ (CGHAZ) at heat inputs of 12, 50, and 120 KJ/in ($t_{8/5}$: 3.5, 10, 20 seconds). Metallographic examination and hardness measurements were conducted to verify and supplement the dilatometry results.

3.2.8 Ultrasonic Testing

Hydrogen attack damage in the service exposed samples was inspected by a professional of Quality Consultants & Inspection, Inc. using advanced ultrasonic testing techniques (PortaScan007). Ultrasonic testing B-scan and C-

scan were applied to quantitatively reveal damaged depth profiles in cross section and damaged depth maps in the scanned area. The depth of damage was displayed as a computer image with a color scale or index number. Ultrasonic testing results were compared with the metallographic examination.

CHAPTER 4

EXPERIMENTAL RESULTS AND DISCUSSION

4.1 Hydrogen Attack Damage in Service Exposed Components

Evaluation of hydrogen attack damage was implemented for 24 service exposed heats. Hydrogen attack damage was found in 9 (MPC-9, 11, 15, 18, 19, 20, 21, 22, and 27) of the 24 service exposed heats using OLM, SEM, ultrasonic testing, and hydrogen measurement. Available operating temperatures and hydrogen partial pressures of the hydrogen attacked heats (MPC-11, 15, 18, 19, 20, 21, 22, and 27) were superimposed on the Nelson Curve as shown in Figure 4.1. It is to be noted that the operating conditions for the damaged heats are below the Nelson Curve for C-0.5Mo. One damaged heat (MPC-15) is directly situated on the Nelson Curve for C-0.5Mo. According to the experimental heat examination, hydrogen damage was characterized by internal decarburization, nucleation and coalescence of methane bubbles, and formation of cracks along grain/sub-grain boundaries. The extent of hydrogen attack damage is the greatest adjacent to inside surface and gradually decreases through wall thickness. A detailed evaluation of hydrogen attack damage was conducted for typical components as presented in the following sections.

4.1.1 Hydrogen Attack in Heat Exchanger (MPC-18, 19 & 20)

Samples were extracted from a service exposed heat exchanger channel (MPC-18), channel flange (MPC-19), and tube sheet (MPC-20) for hydrogen damage evaluation. The heat exchanger channel was operated from 500°F (adjacent channel flange) to 580°F (in the central portion of the channel) at a hydrogen partial pressure 950 psi. The operating temperatures and hydrogen partial pressures are approximately 600°F-950 psi for the tube sheet on one side (Side A, MPC-20) and 700°F-100 psi on the opposite other side (Side B, MPC-20). The heat exchanger channel (MPC-18), channel flange (MPC-19), and tube sheet (MPC-20) had operated for approximately 28 years. PWHT was implemented for the heat exchanger channel and flange at 1160°F for 3 hours after welding. The operating conditions of the channel, flange, and tube sheet are below the Nelson Curve for C-0.5Mo as shown in Figure 4.1.

Hydrogen attack damage was evaluated using UT, OLM, and "Cryo-cracking" SEM through the wall thickness of the channel and tube sheet. Several locations were examined along the channel cylinder to investigate the temperature gradient influence (580°F in the central portion and 500°F near the flange). A long seam weld in the channel was extracted for the evaluation of hydrogen attack behavior in the weld region in terms of weld metal and HAZ. The chemical composition of the long seam weld metal is presented in Table 4.1. A low carbon content (0.053%) was noted in the weld metal compared to the channel material (MPC-18, 0.18%C).

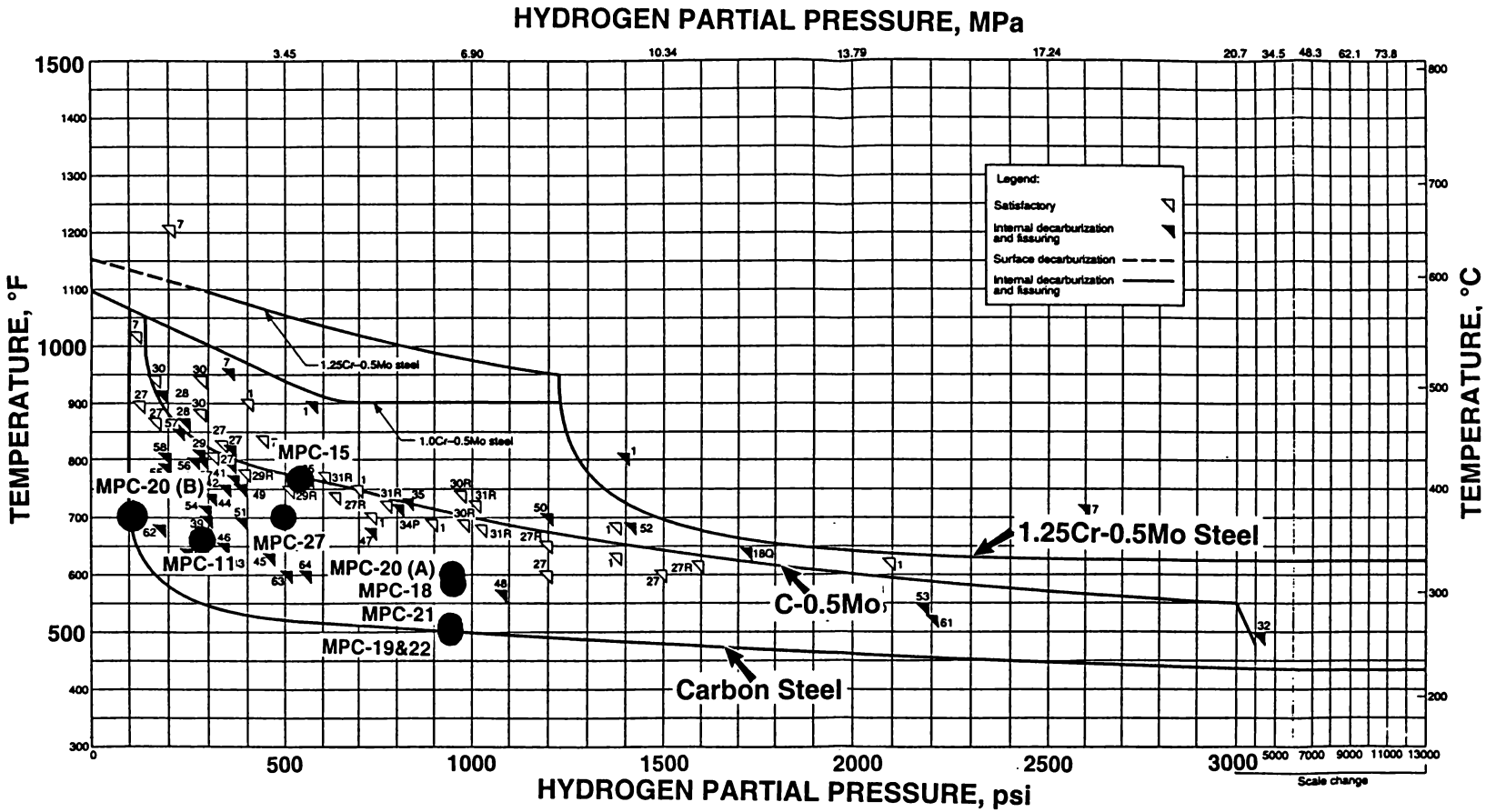


Figure 4.1 Operating conditions (temperatures and hydrogen partial pressures) for the service exposed heats superimposed on the Nelson Curve for C-0.5Mo steel.

Table 4.1 Chemical composition of a long seam weld metal in heat exchanger channel (MPC-18).

Elements	Weld Metal (wt%)
C	0.053
Mn	1.47
P	0.021
S	0.015
Si	0.49
Ni	0.04
Cr	0.05
Mo	0.44
V	0.005
Nb	0.005
Ti	0.003
Co	0.010
Cu	0.18
Al	0.006
B	<0.001
W	<0.01
Sb	-
As	0.018
Sn	0.006
Zr	0.002
N	0.004
O	0.064
Mo/C	8.30

4.1.1.1 Ultrasonic Inspection

Ultrasonic testing was implemented on a section of the heat exchanger channel (MPC-18) containing a long seam weld. This section was extracted from the central portion of the heat exchanger channel. The dimensions of the inspected sample are approximately 12 3/4" x 8" x 1". A computerized ultrasonic testing equipment (PortaScan 007) was applied to reveal hydrogen attack damage. Inspection was conducted over a 10" x 6" area from the OD surface including the seam weld as schematically shown in Figure 4.2.

Figure 4.3 shows a typical C-scan image with a color index. The X and Y scales indicate the scanned area and the color index displayed on the image indicates the depth of UT indications. The material thickness scale ranges from 0 to 1.25" corresponding to the color index to cover the entire wall thickness of the sample (1" thick). The wall thickness of the inspected sample was measured as 1" and the weld thickness was determined to be approximately 1.1", which corresponds to the blue color on the color scale. It is noted that the color in the C-scan image shows blue in the area of the weld, which indicates that the ultrasonic response was from the weld metal ID surface. Therefore, it was interpreted that there is no hydrogen damage in the weld metal. Figure 4.4 presents an enlarged view of the weld metal area with numerical values of the reflected depth. The reflection depth is in the range of 0.95" and 1.13" which is the approximate the weld thickness. In the base metal, the majority of the index color is in the range of green and yellow. The UT reflections from the hydrogen

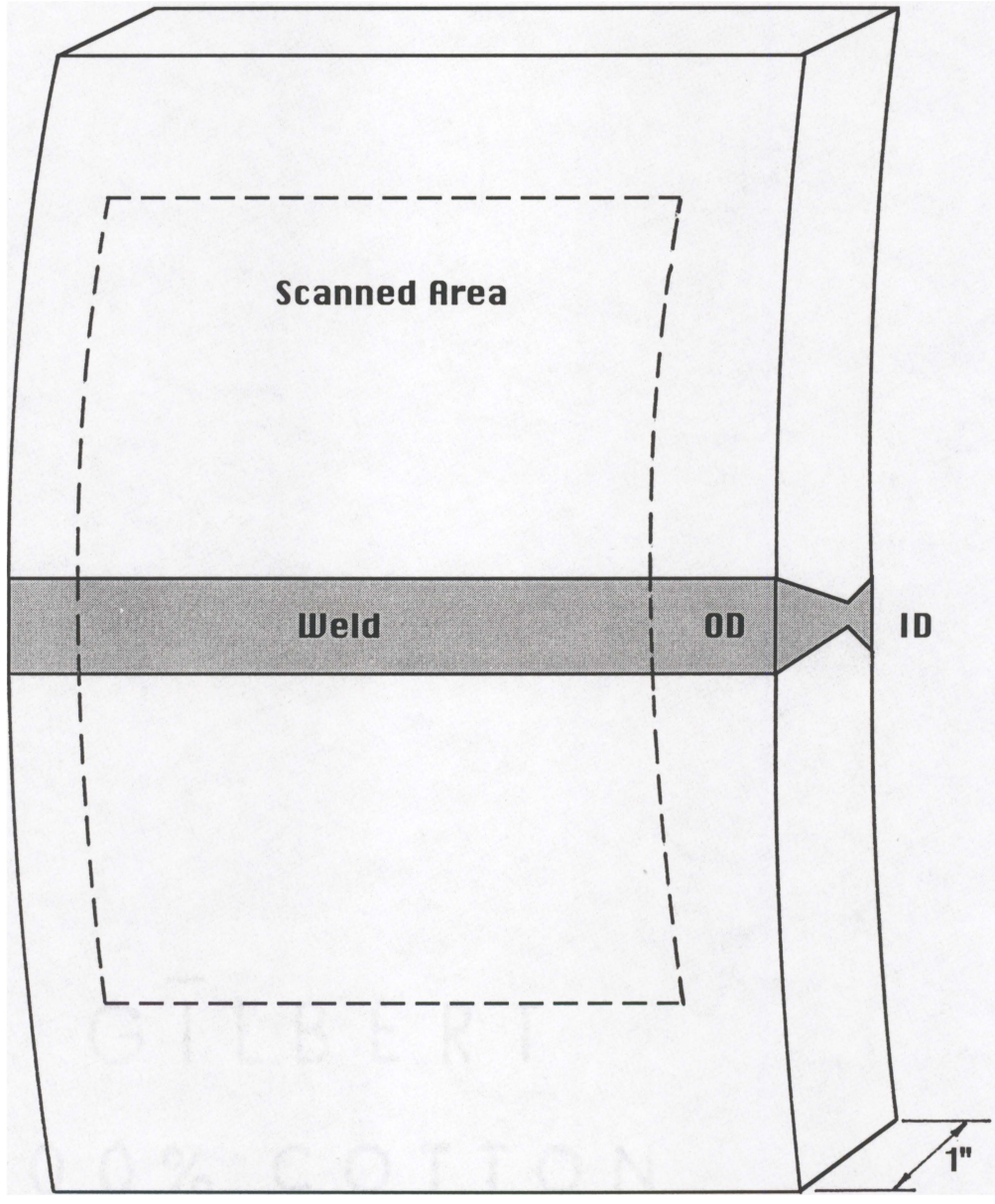


Figure 4.2 A schematic drawing of the sample with a long seam weld extracted from heat exchanger channel (MPC-18) for UT inspection.

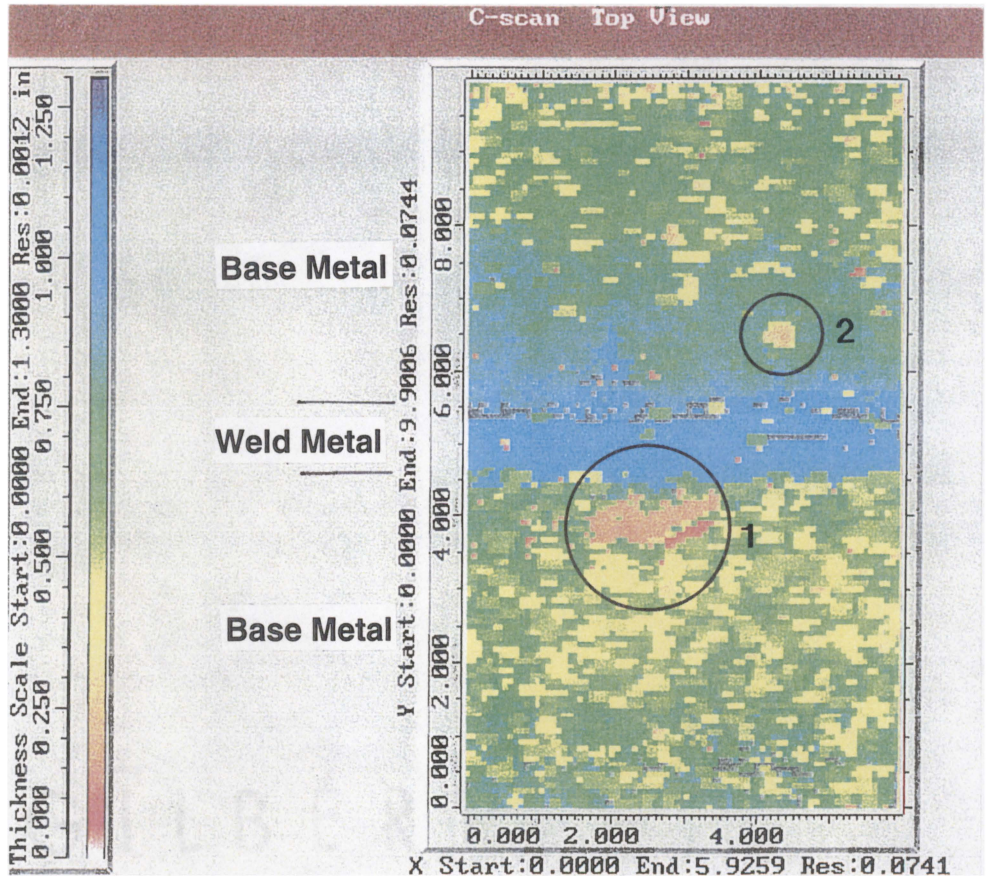


Figure 4.3 A typical UT C-scan image of the sample with a long seam weld extracted from heat exchanger channel (central portion, MPC-18).

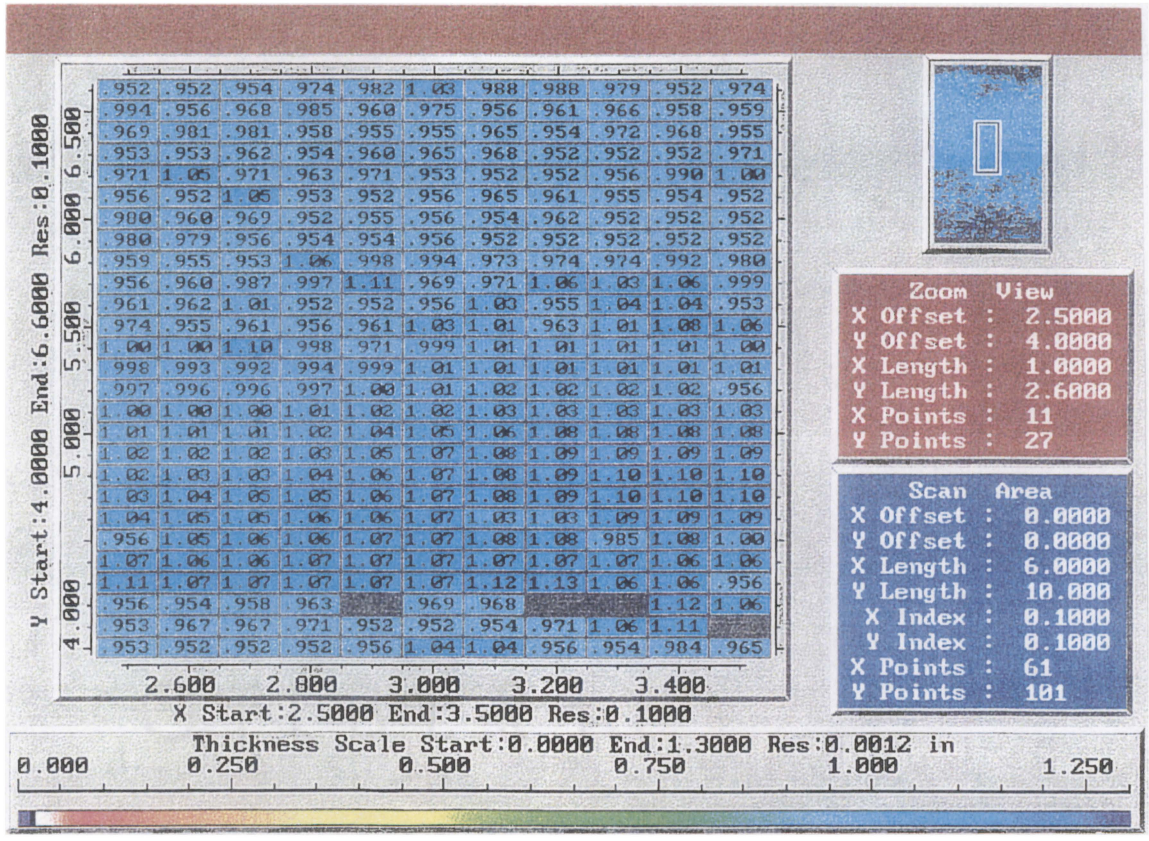


Figure 4.4 Enlarged view of the weld metal area with numerical values of the UT reflection depth (MPC-18).

attack cracks are approximately 0.5" to 0.75" in depth from the OD surface which indicates that the hydrogen attack damage extends to a maximum depth of 0.5" from the ID surface in the base metal.

From Figure 4.3, two indications are displayed as orange adjacent to the weld and are labeled as Locations 1 and 2. The indication at Location 1 is approximately 0.25" from the edge of the weld metal with maximum lateral dimensions of 1.8"X0.8". Figure 4.5 shows an enlarged view of Location 1 with a numerical index for the reflected depth. The indication at Location 1 is reflected from a depth of 0.15" to 0.17" from the OD surface. Figure 4.6 presents an enlarged view of Location 2. It shows that the reflection depth is approximately 0.22" to 0.26" from the OD surface. Based on the hydrogen attach characteristics, these two indications were not related to hydrogen attack.

Furthermore, Figure 4.7 shows the depth profiles for 2 cross-sections along A-A and B-B. Figure 4.8 is a 3-D representation of the reflection depth profile in the scanned area.

In summary, the UT inspection results show hydrogen attack damage was in the base metal to a depth of approximately 0.5" from the ID. There was no hydrogen damage in the weld metal.

4.1.1.2 Metallographic Examination

To supplement the UT inspection, metallographic examination was conducted on the cross sections of the base metal (MPC-18) and the long seam

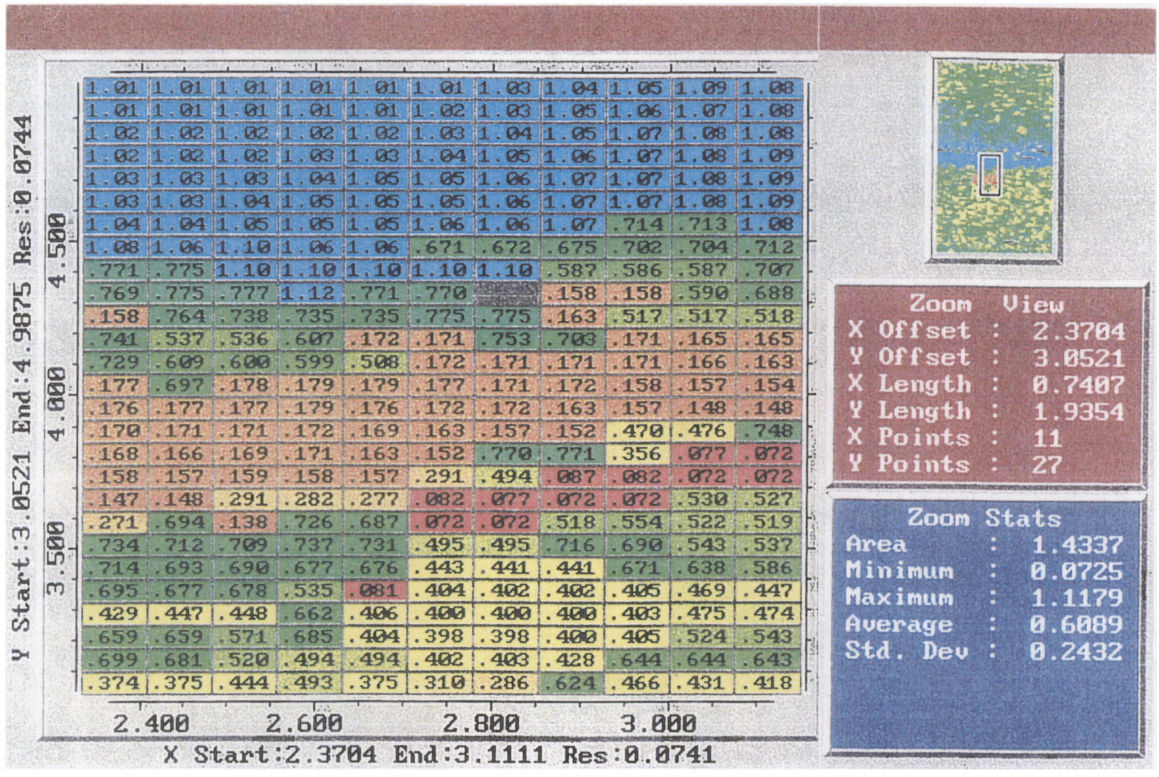


Figure 4.5 Enlarged view of the indication at Location 1 shown in Figure 4.3 (MPC-18).

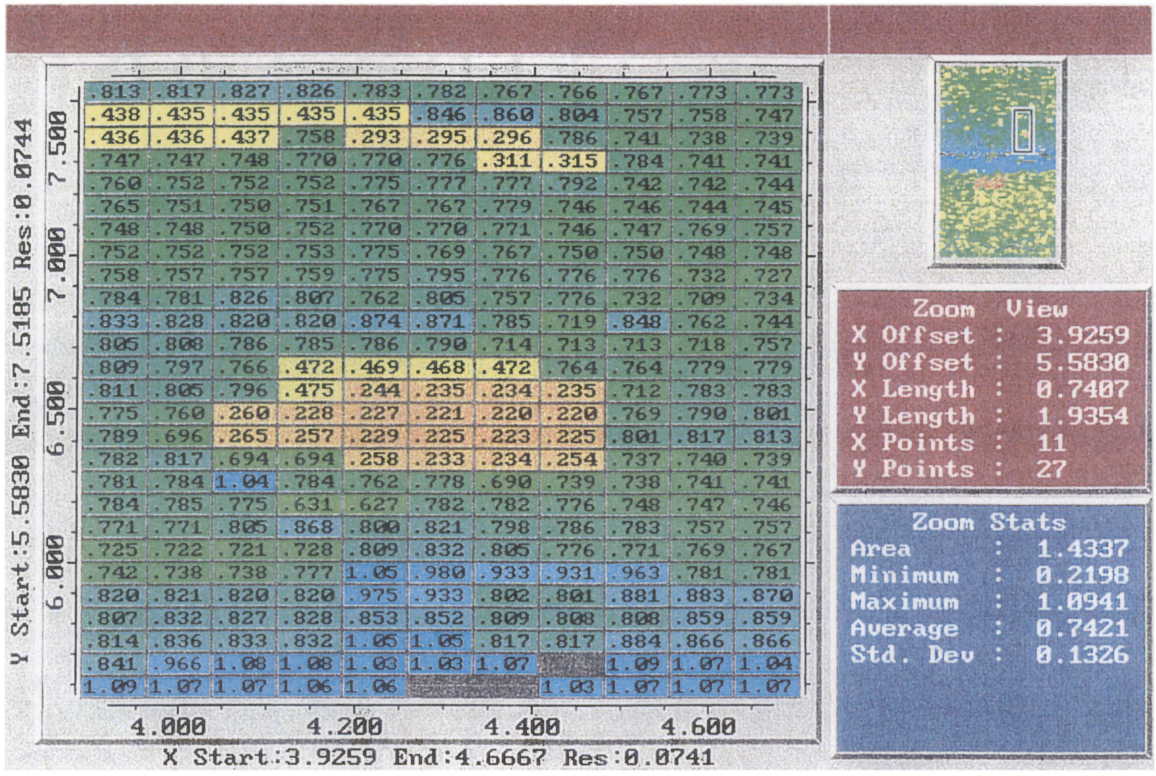


Figure 4.6 Enlarged view of the indication at Location 2 shown in Figure 4.3 (MPC-18).

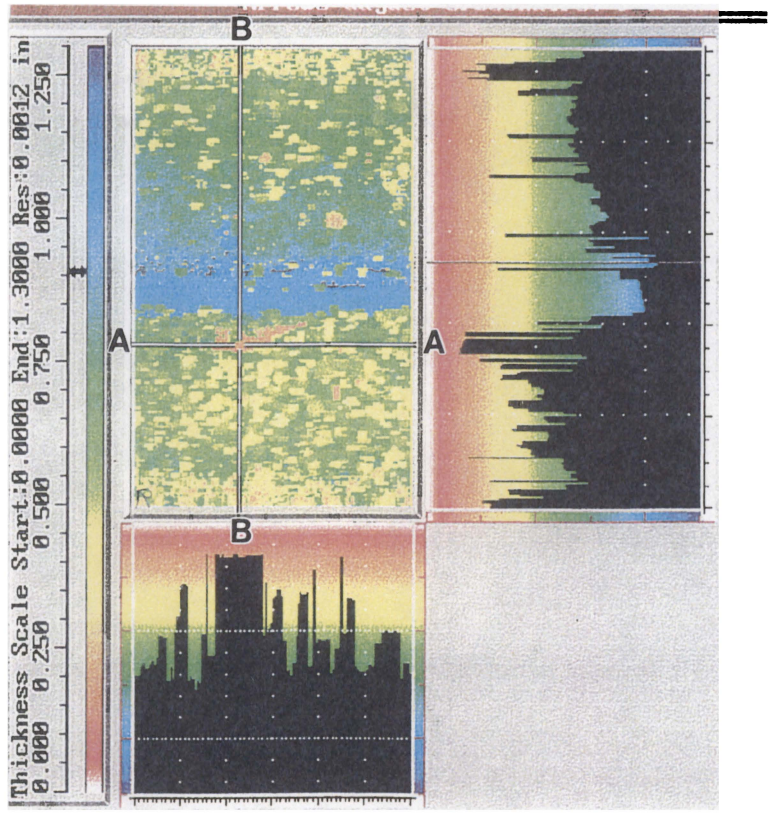


Figure 4.7 Cross section profiles of the reflection depth along A-A and B-B (MPC-18).

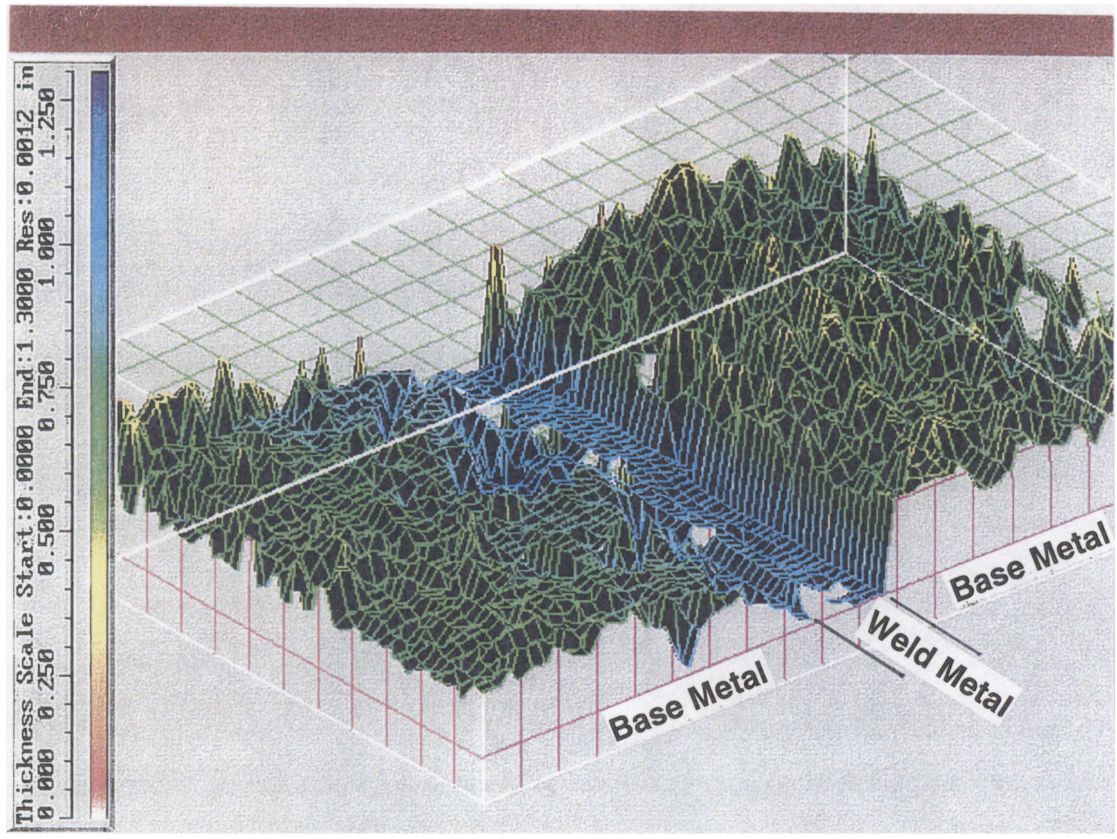
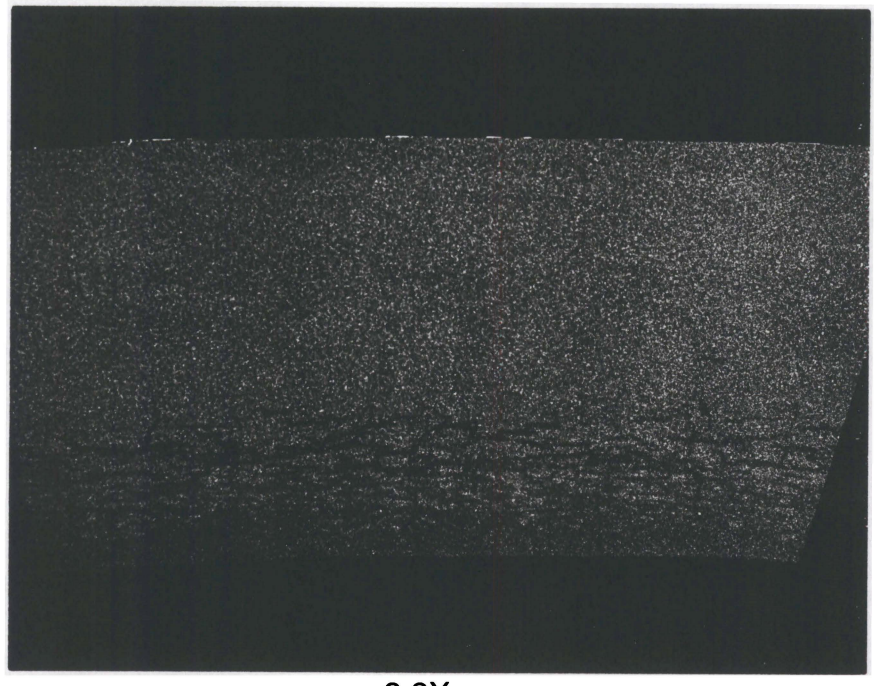


Figure 4.8 3-D presentation of the C-scan image of the sample with a long seam weld in heat exchanger channel (central portion, MPC-18).

weld using OLM and SEM. Figure 4.9 shows the cross section of the base metal with indication of hydrogen damage. Severe hydrogen attack damage occurs at the ID and extends to approximately half of the wall thickness (1" thick). The maximum damaged depth in the base metal was determined to be approximately 1/2" using OLM (1000X), which is consistent with the results determined by UT. Decarburization extends to a depth of approximately 300 μm from the ID surface.

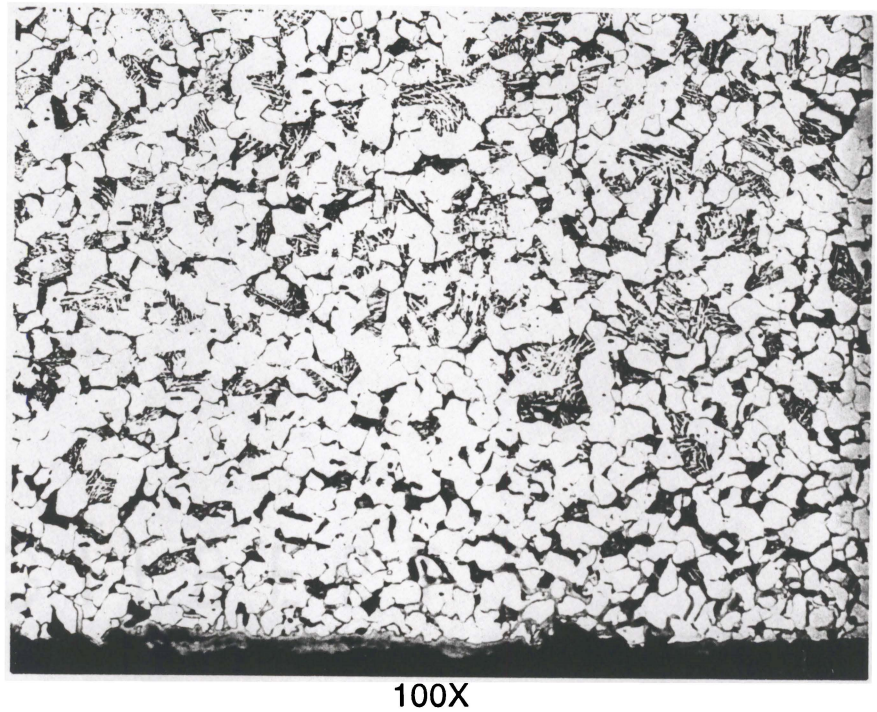
Figure 4.10 shows hydrogen attack cracks adjacent to the ID surface, which is characterized as intergranular cracking. The hydrogen attack damage gradually decreases from the ID surface to approximately 0.5" (13 mm) in depth through the wall thickness. This is reconcilable with the detectable depth by the UT. The morphology of hydrogen damage shows segregation related intergranular cracking (related to the rolling/banding direction) as shown in Figure 4.11. Internal decarburization adjacent to the cracks was observed in the bainitic regions. Hydrogen attack damage was not observed adjacent to the OD surface as shown in Figure 4.12. Therefore, the progression of hydrogen attack in terms of methane bubble initiation, growth, and coalescence to form cracks can be defined through the wall thickness by both OLM and UT.

Figure 4.13 is a photomacrograph of the cross section of the long seam weld. Hydrogen attack (cracking) was observed in the HAZ and base metal (MPC-18). Figure 4.14 shows the intergranular cracking in the CGHAZ. The prior austenitic grain size in the CGHAZ is ASTM No. 3. Internal

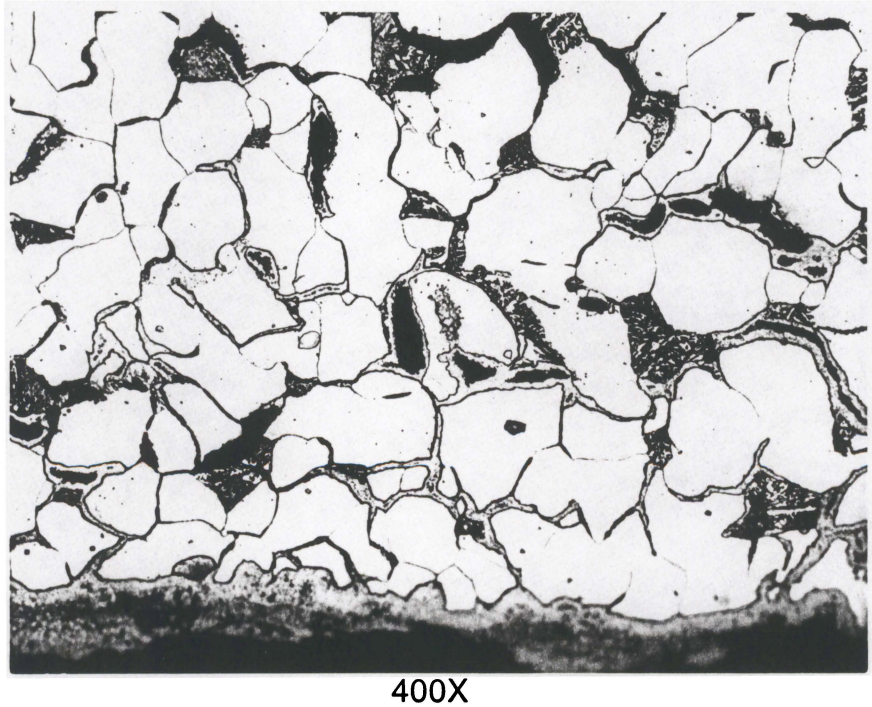


2.3X

Figure 4.9 Cross section of the base metal extracted from heat exchanger channel (central portion, MPC-18).

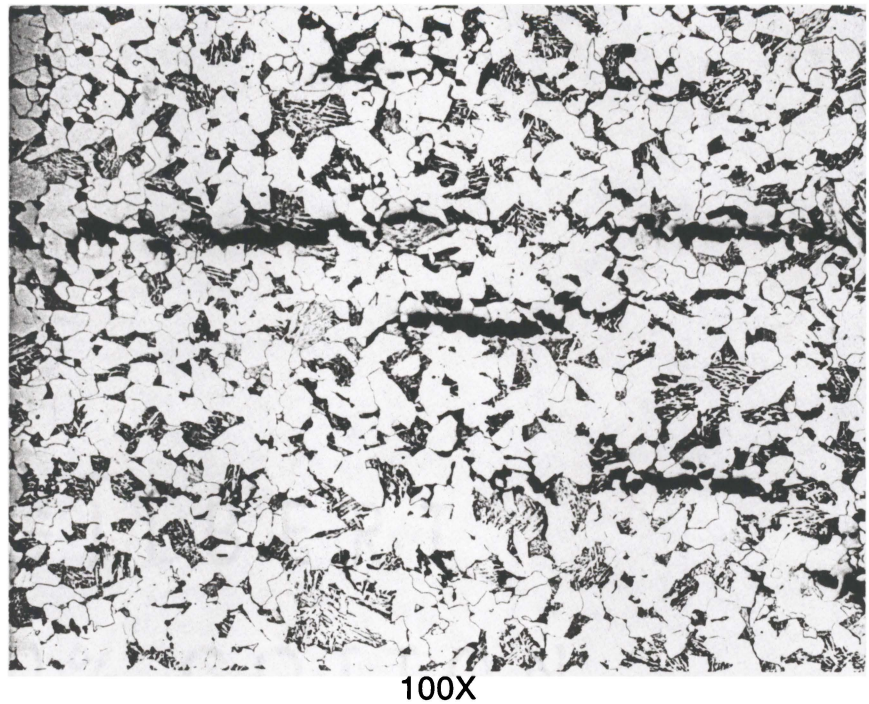


100X



400X

Figure 4.10 Hydrogen attack cracks adjacent to the ID surface of heat changer channel (central portion, MPC-18).

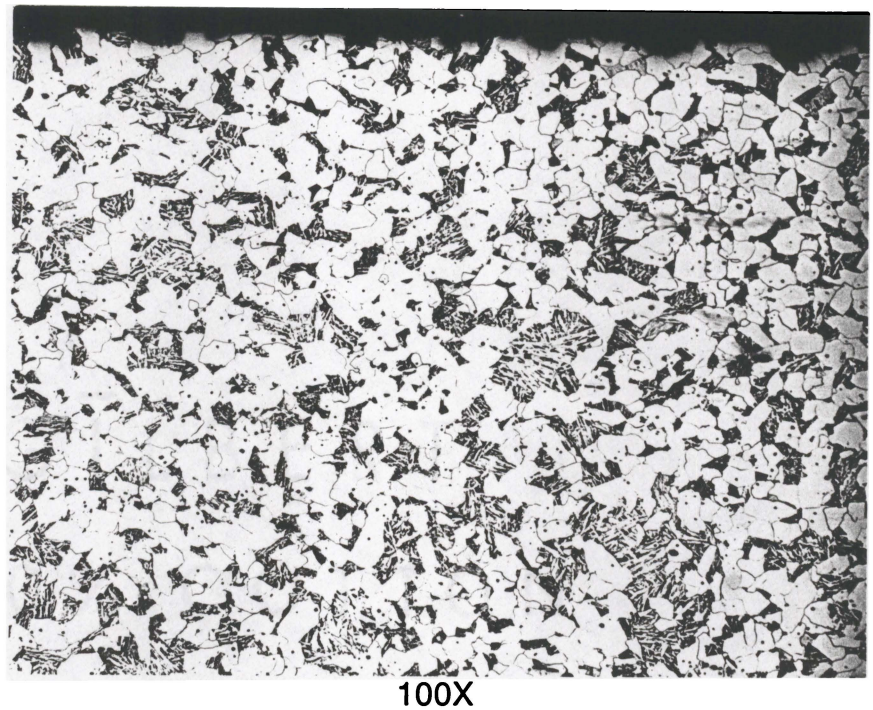


100X



400X

Figure 4.11 Hydrogen attack cracks at approximately 0.5" in depth from the ID surface of heat changer channel (central portion, MPC-18).

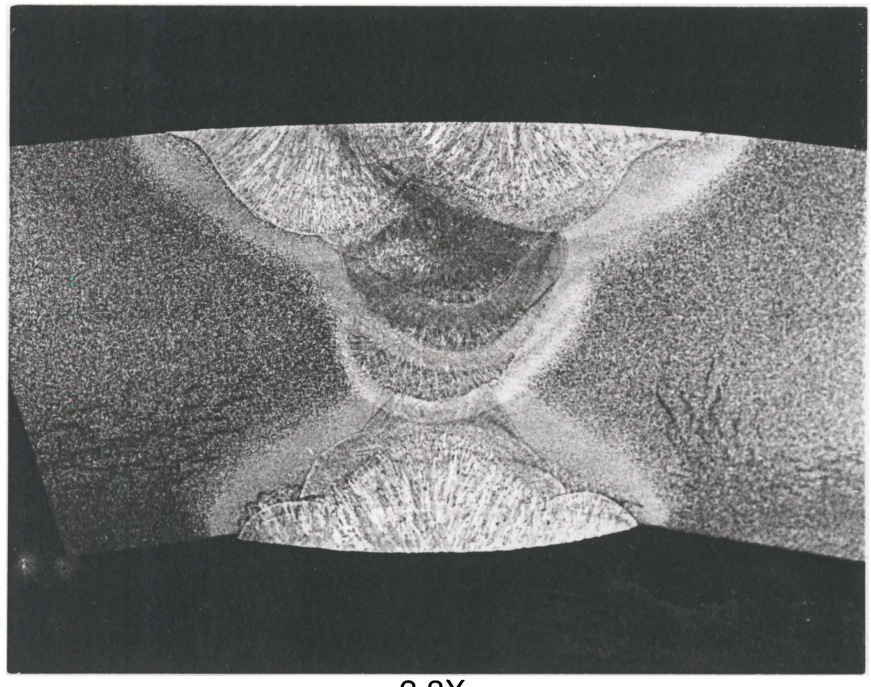


100X



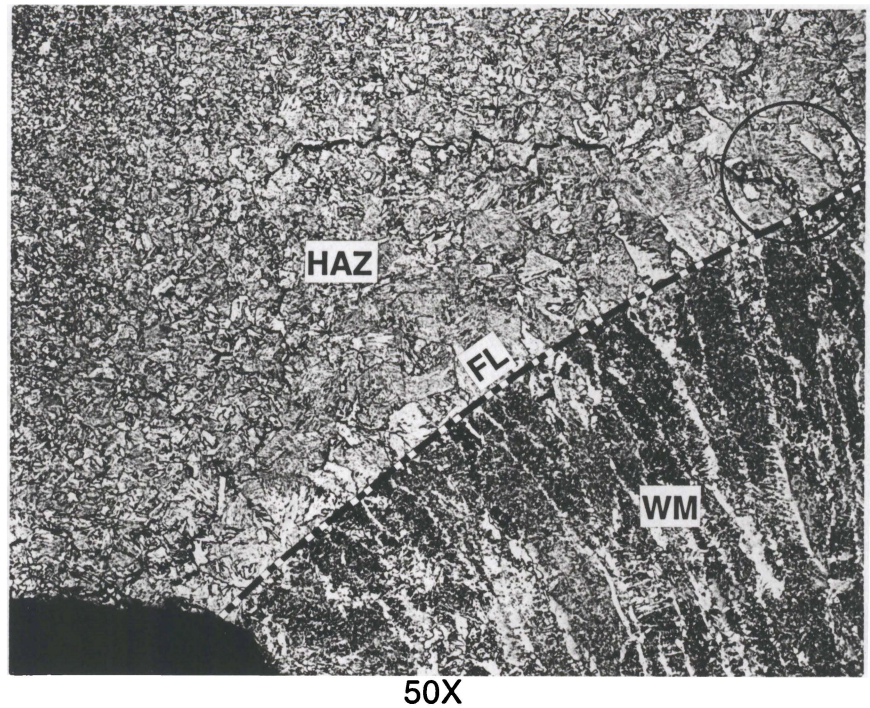
400X

Figure 4.12 No hydrogen attack damage adjacent to the OD surface of the heat changer channel (central portion, MPC-18).

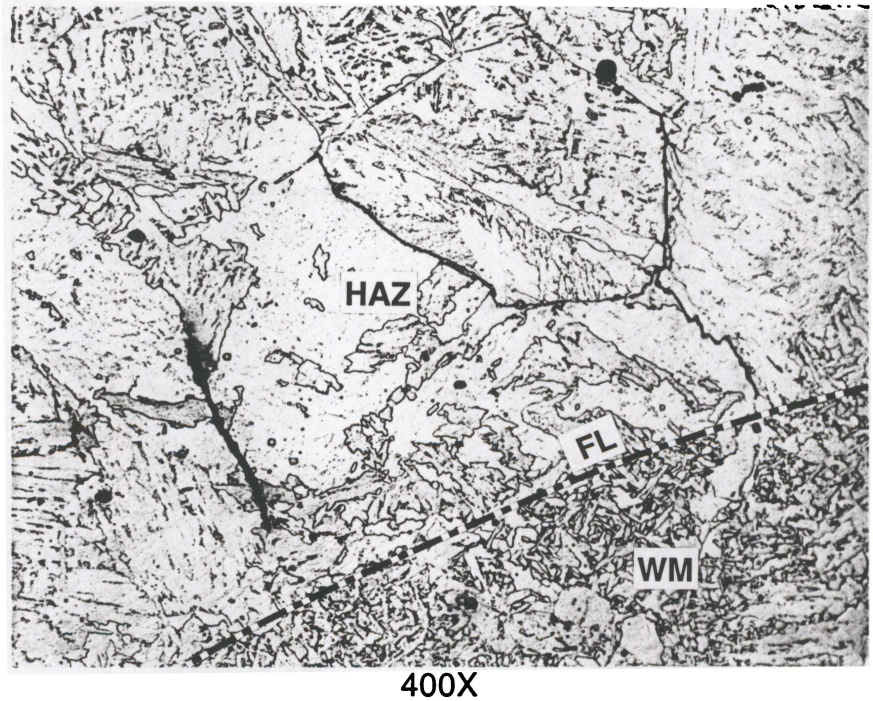


2.3X

Figure 4.13 Cross section of long seam weld extracted from the central portion of heat exchanger channel (MPC-18).



50X



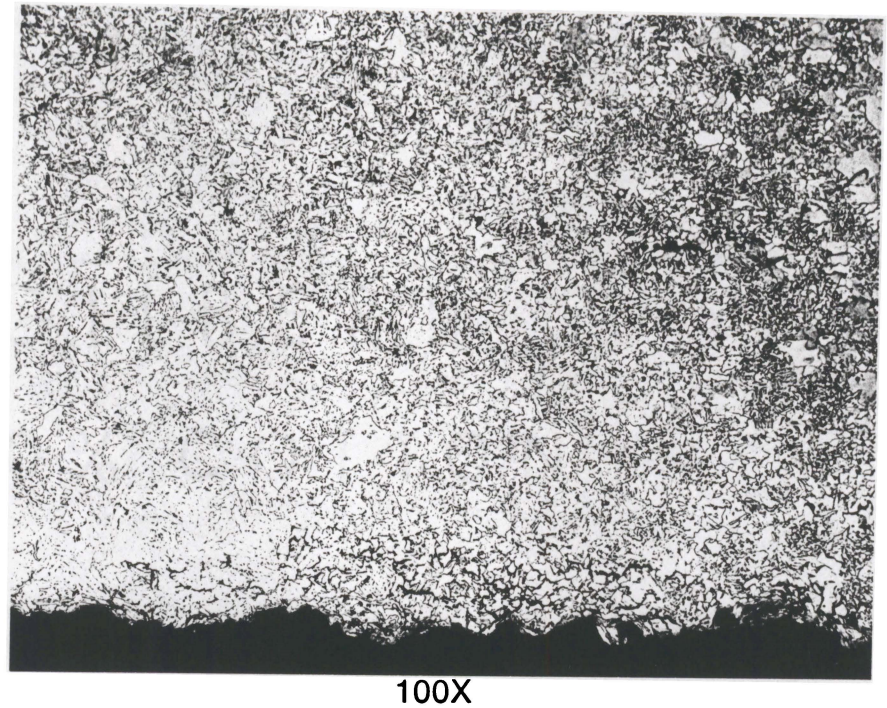
400X

Figure 4.14 Hydrogen attack cracks in the CGHAZ adjacent to the ID (central portion of heat exchanger channel, MPC-18).

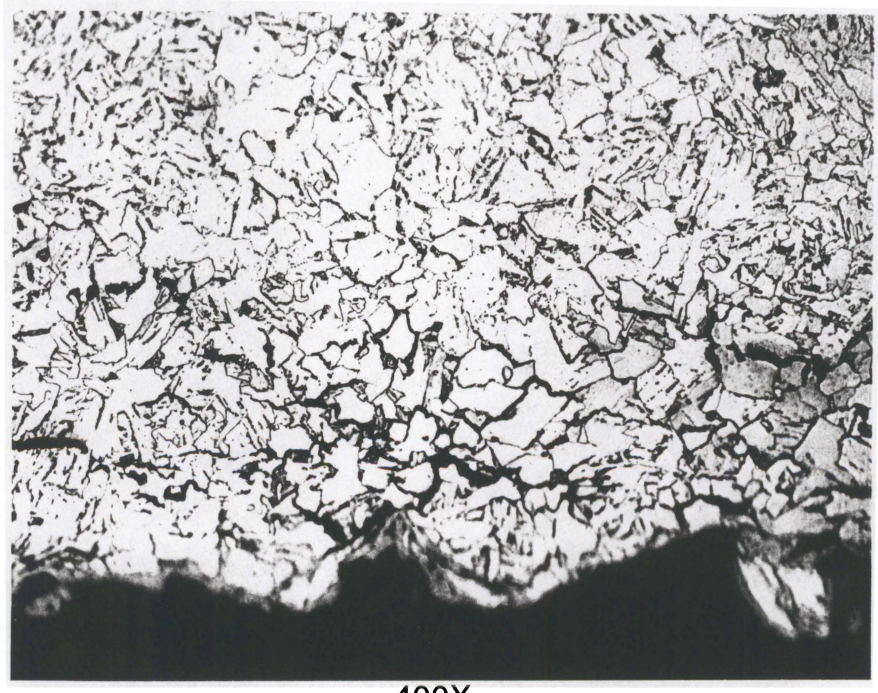
decarburization adjacent to the cracks resulted in the elimination of most bainitic and/or martensitic laths formed in the CGHAZ. The depth of hydrogen attack cracking is approximately 5 mm from the ID in the CGHAZ. The cracking was terminated at the overlapped region in the HAZ where the original CGHAZ grain size was refined from ASTM No. 3 to ASTM 10.

Hydrogen attack cracks were observed near the ID surface in the fine grained HAZ (FGHAZ) and they extended to a depth of 1.4 mm as shown in Figure 4.15. The depth of the hydrogen damage in the FGHAZ is less than that in the base metal (13 mm) and the CGHAZ (5 mm). The grain size in the FGHAZ was determined as ASTM No. 10, which is finer than that of the base metal (ASTM No. 5) and the CGHAZ (ASTM No. 3). Hydrogen damage was not found in the weld metal as shown in Figure 4.16, which is consistent with the UT inspection results. The microstructure of the weld metal is fine acicular ferrite and grain boundary ferrite. It is demonstrated that the refined microstructure in the FGHAZ and low carbon (0.053%) in the weld metal enhance the resistance to hydrogen attack compared with the base metal and the CGHAZ.

In addition to the samples extracted from the central portion of the heat exchanger channel, metallographic samples extracted along the channel and flanges were examined. It was found that the hydrogen attack damage decreased as the channel flanges were approached compared with the central portion of the channel. The hydrogen attack depth near the flange extends approximately 9 mm from the ID surface.

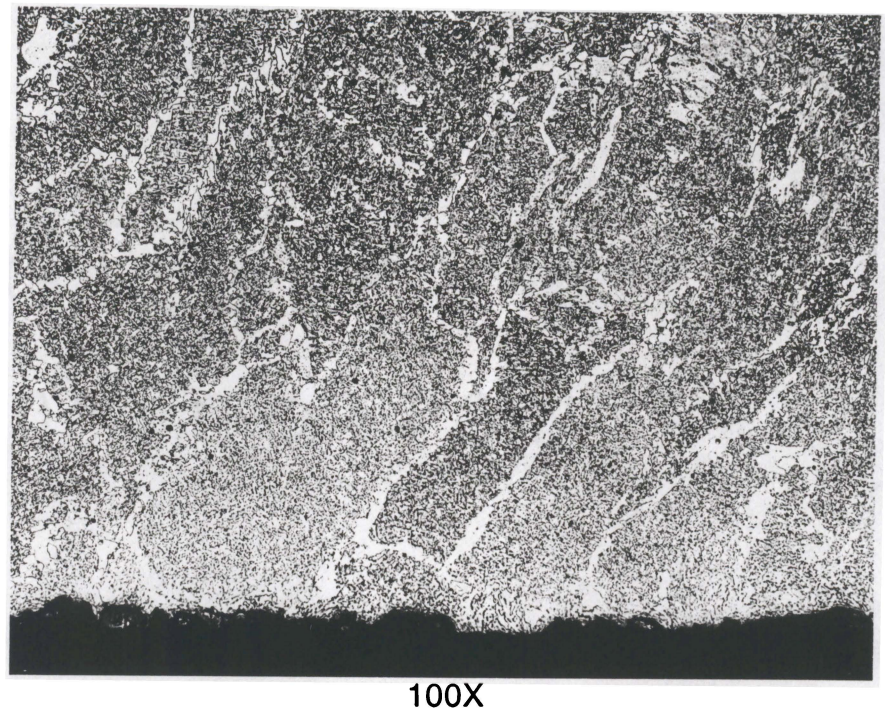


100X

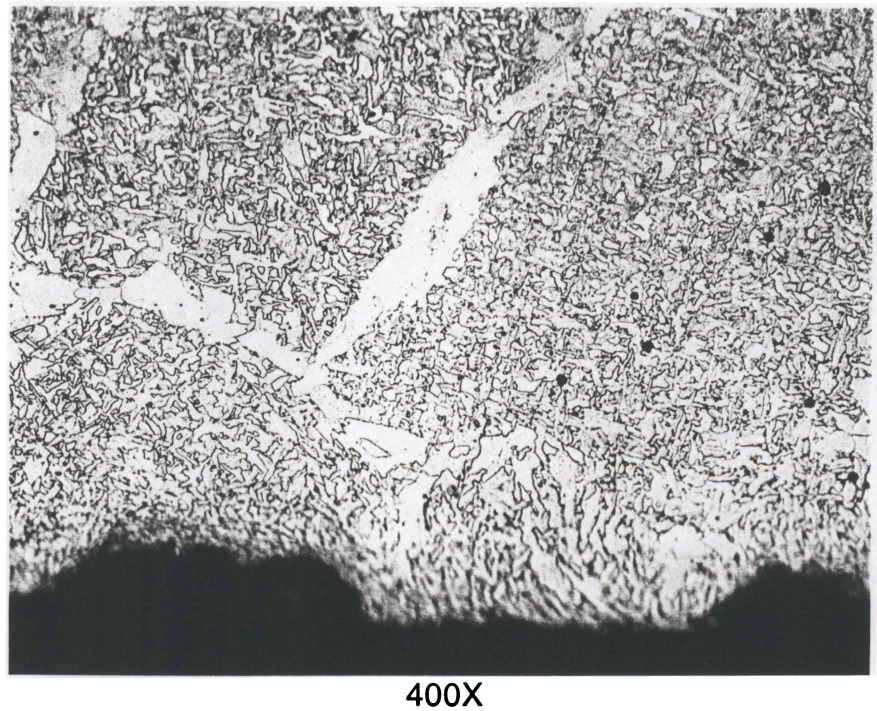


400X

Figure 4.15 Hydrogen attack cracks in the FGHAZ adjacent to the ID (central portion of heat exchanger channel, MPC-18).



100X



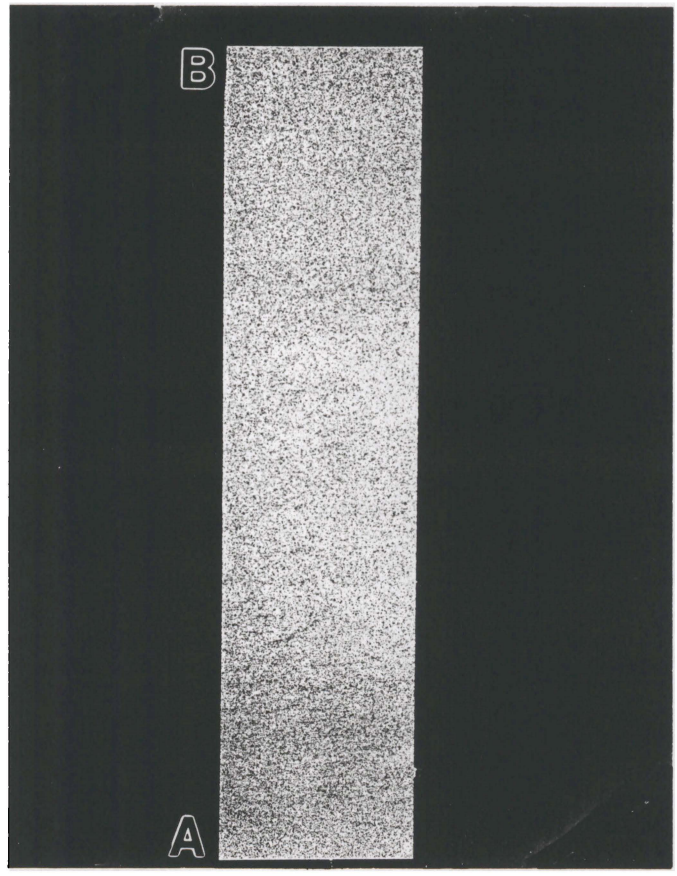
400X

Figure 4.16 No hydrogen attack crack in the long seam weld metal adjacent to the ID (central portion of heat exchanger channel, MPC-18).

Metallographic evaluation was implemented for the heat exchanger tube sheet (MPC-20). Figure 4.17 shows the cross section of the tube sheet. The tube sheet face and the opposite face were labeled as Side A and Side B, respectively. The thickness of the tube sheet is 3-3/4". The operating temperature and hydrogen partial pressure are 600°F-950 psi for Side A and 700°F and 100 psi for Side B, both of which are below the Nelson Curve for C-0.5Mo steel as depicted in Figure 4.1. Because both surfaces of the tube sheet were exposed to hydrogen, hydrogen attack damage was observed through the entire wall thickness (3-3/4"). Figures 4.18 through 4.20 present representative photomicrographs of hydrogen attack cracking at the locations adjacent to the tube sheet face (Side A), at 1 7/8" deep from the tube sheet face, and adjacent to the surface opposite to the tube sheet face (Side B). Intergranular cracking occurred at both bainite/ferrite and ferrite/ferrite grain boundaries. Hydrogen attack cracking is more extensive near Side A that was exposed to higher hydrogen pressure (950 psi at 550°F) compared to Side B (100 psi at 700°F).

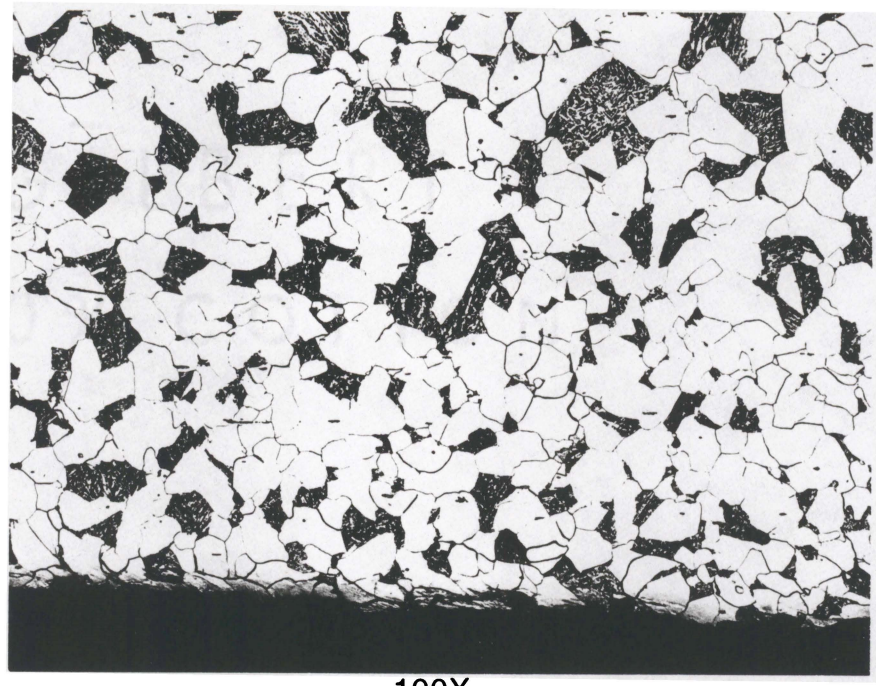
4.1.1.3 Quantification of Hydrogen Damage

Hydrogen attack damage through the wall thickness was quantified for the metallographic samples (MPC-18) extracted from the central portion of the channel cylinder and adjacent to the flange using quantitative metallographic analysis. The fraction of damaged grain boundary length (FL%) was applied as a parameter for hydrogen damage evaluation. Optical light micrographs were

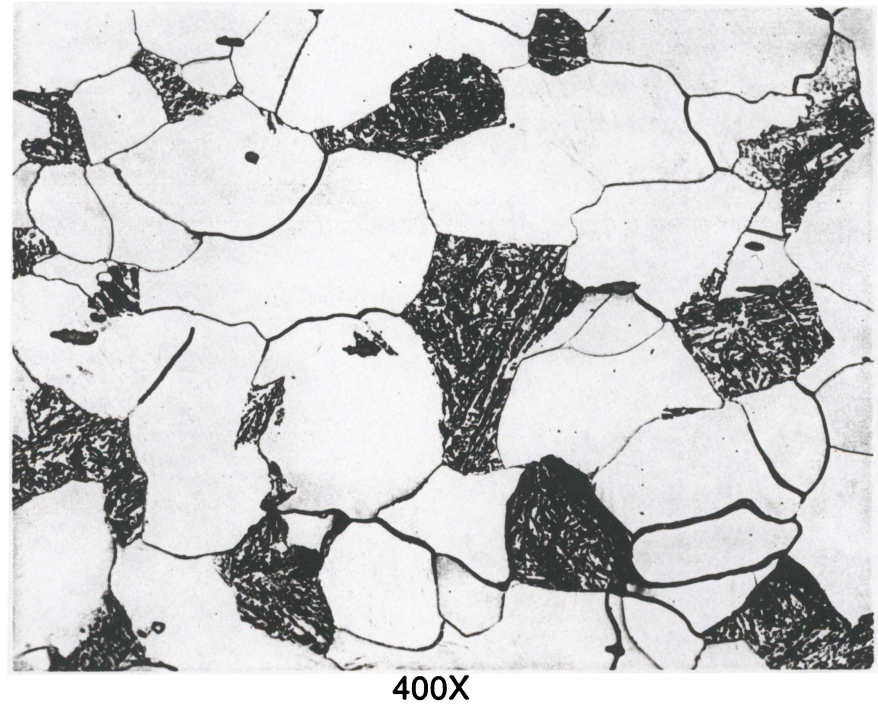


1.1X

Figure 4.17 Cross section of the tube sheet for hydrogen attack damage evaluation.

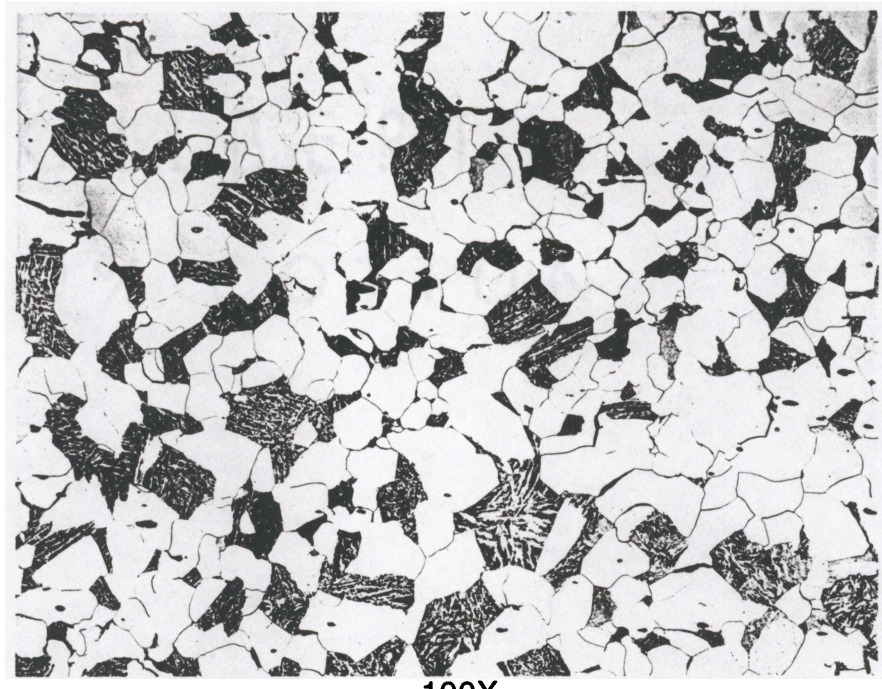


100X

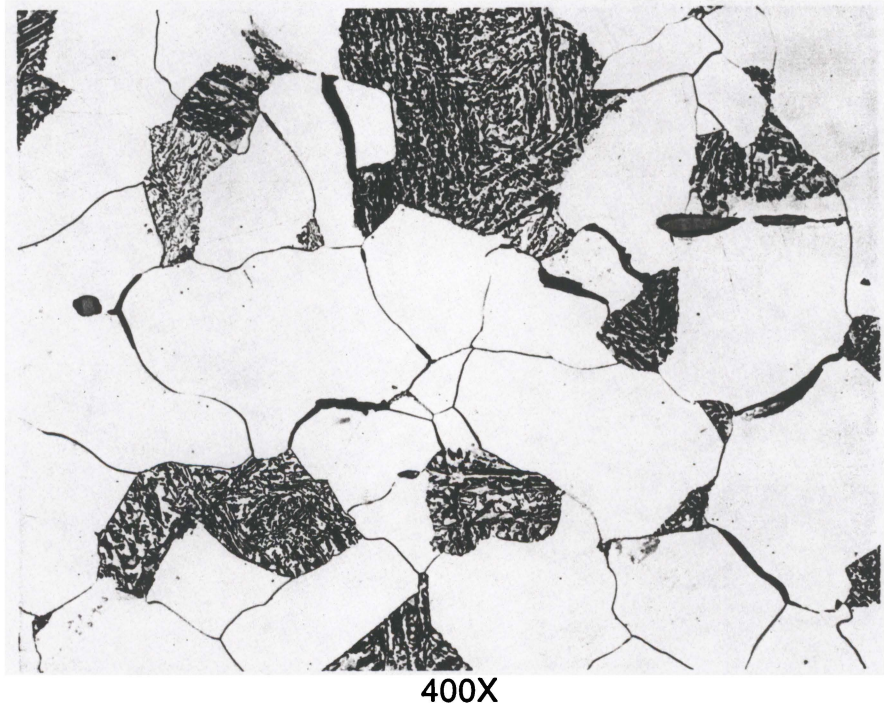


400X

Figure 4.18 Hydrogen attack cracks adjacent to the surface of Side A (tube sheet, MPC-20).

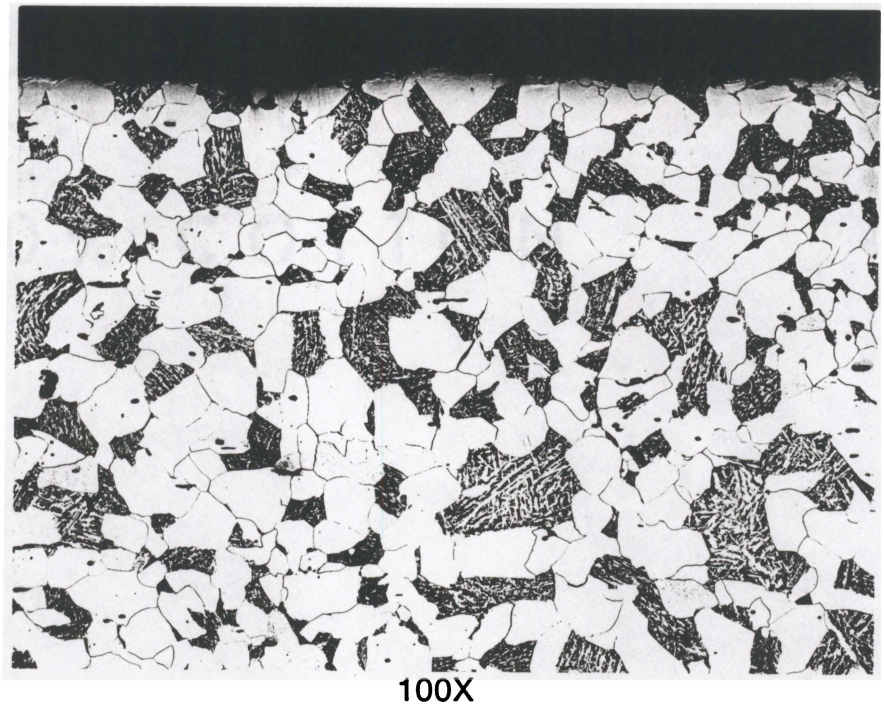


100X

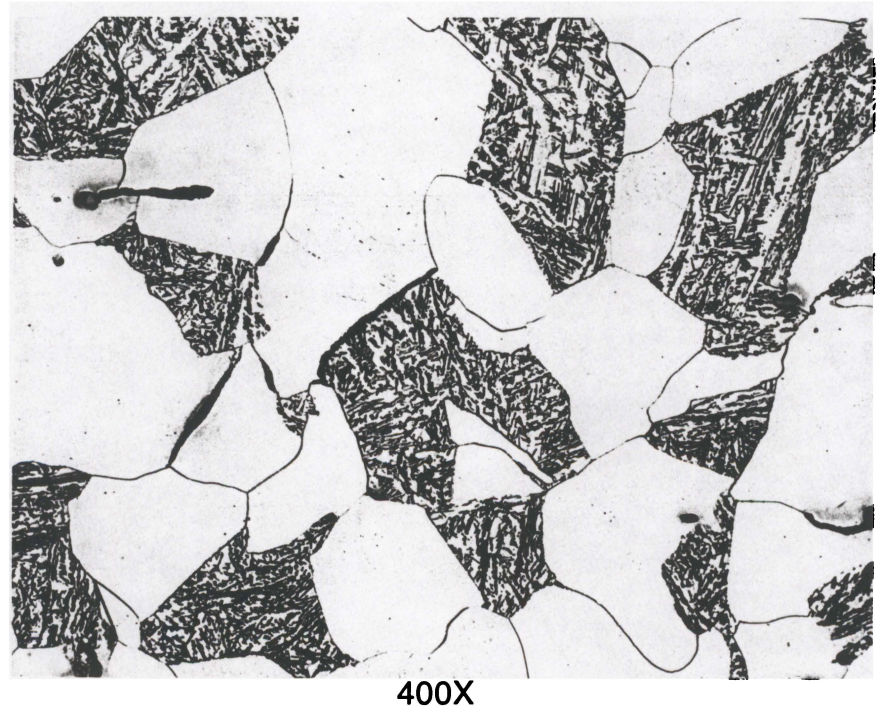


400X

Figure 4.19 Hydrogen attack cracks at the location of 1 7/8" deep from the surface of Side A (tube sheet, MPC-20).



100X



400X

Figure 4.20 Hydrogen attack cracks adjacent to the surface of Side B (tube sheet, MPC-20).

obtained from different depths in the wall thickness from the ID surface through the entire wall. Three photomicrographs were taken at each depth as depicted in Figure 4.21. The OLM photomicrographs at magnification 400X were used to determine the fraction of damaged grain boundary length (FL%) using NIH Image analysis software. Figure 4.22 shows a typical NIH image of hydrogen attack cracks compared with the original photomicrograph.

Figure 4.23 presents the fraction of damaged grain boundary length though the wall thickness in the central portion of the channel and near the flange. The fraction of damaged grain boundary length decreases in an exponential manner from the ID to the OD, which indicates that the hydrogen attack is controlled by the mechanism of hydrogen diffusion and solubility. In the central portion of the channel, approximately 60% of the grain boundaries are damaged adjacent to the ID surface in the form of intergranular cracking. Hydrogen attack damage extends to approximately 13 mm (1/2 t) in depth from the ID surface, which indicates that 50% of the wall thickness has been damaged by cracking. Near the flange, the severity of hydrogen attack damage is less compared to the central portion. The fraction of damaged grain boundary length was determined as 22% adjacent to the ID surface and the hydrogen damage extended to approximately 25% of wall thickness from the ID surface near the flange. The difference in the hydrogen attack damage in the central portion and near the flange might be caused by the temperature gradient along the heat exchanger channel.

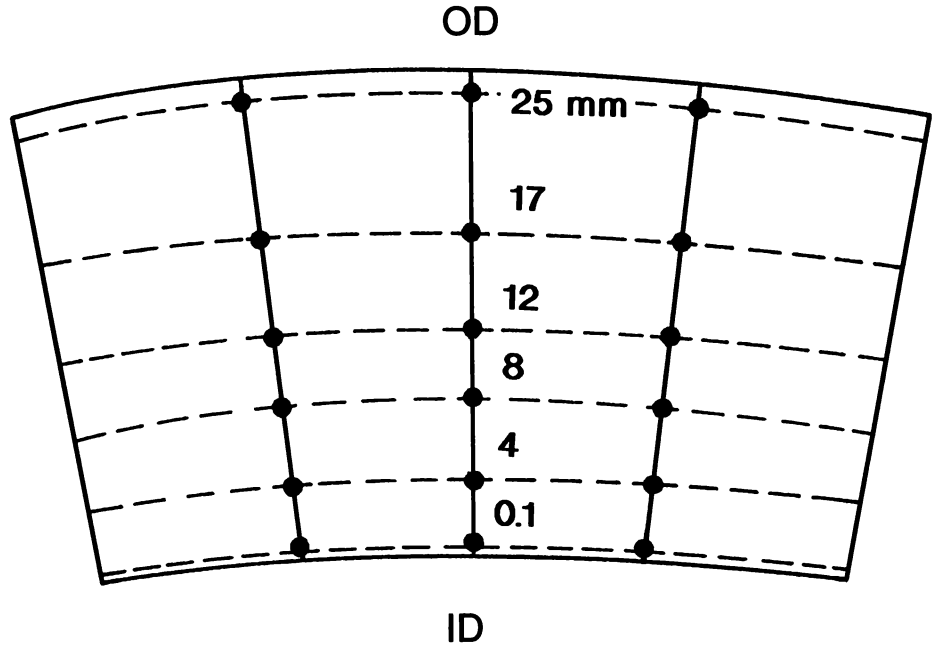
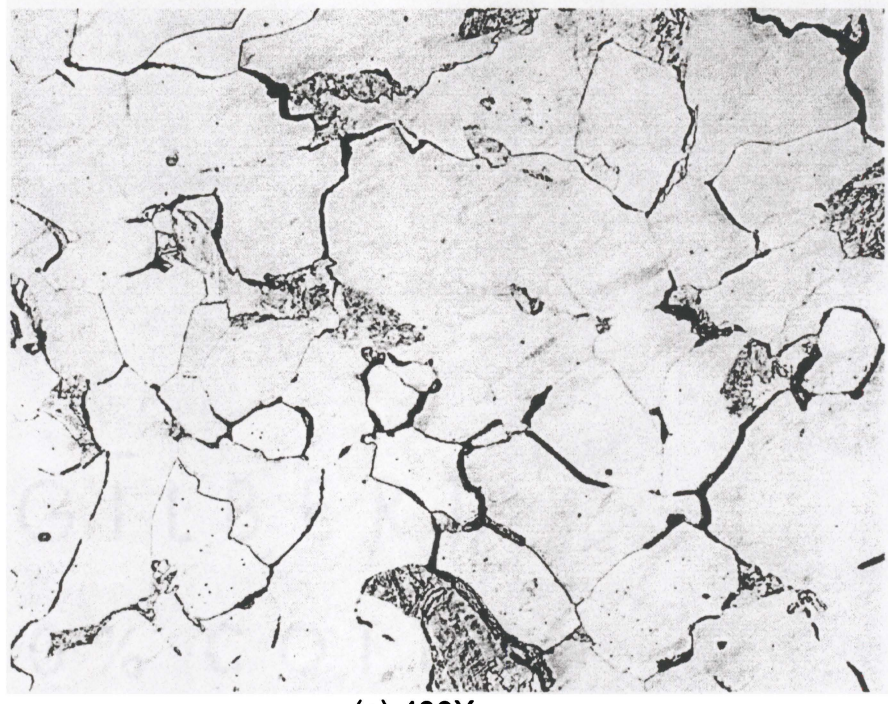


Figure 4.21 Schematic to depict the locations where photomicrographs were taken for hydrogen attack damage quantification through wall thickness of heat exchanger channel (MPC-18).



(a) 400X



(b) 400X

Figure 4.22 Comparison of original photomicrograph (a) and enhanced NIH image (b) of hydrogen attack cracks.

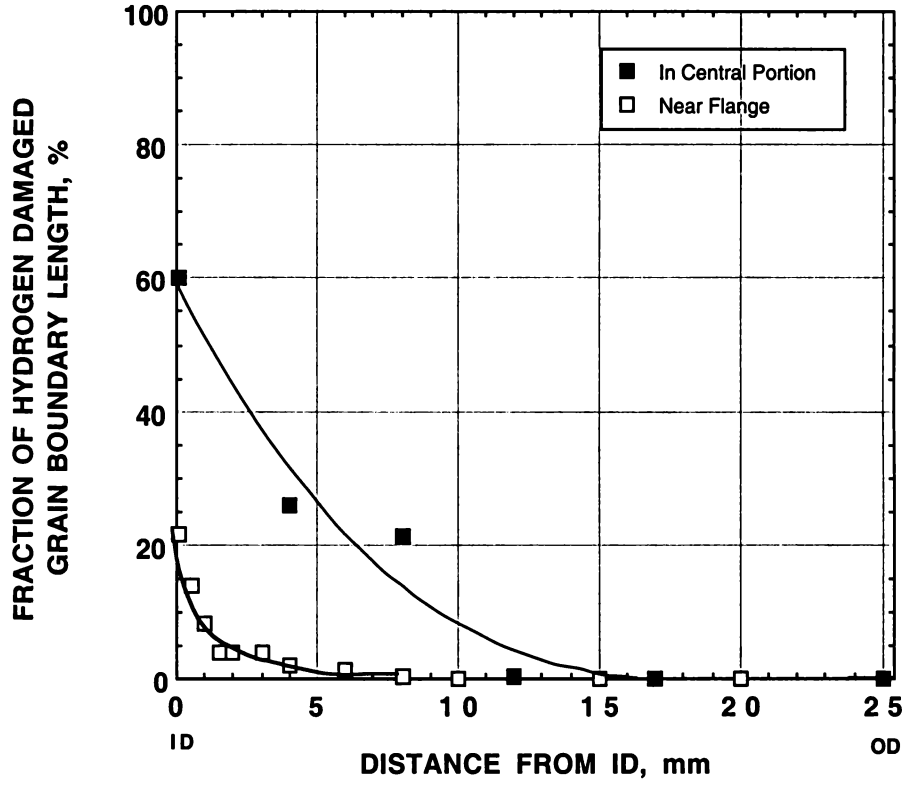


Figure 4.23 Hydrogen attack damage profiles (FL%) within the wall (central portion and near flange, MPC-18).

In addition to OLM, SEM was utilized to evaluate hydrogen damage in the channel and tube sheet using "Cryo-cracking" samples and polished and etched metallographic samples. "Cryo-cracking" samples were extracted from the central portion and adjacent to the flange of the channel. Coupons were sectioned (2"x1/4"x1") through the full wall thickness. The coupon was notched through the wall and the ID surface was preserved for observation of hydrogen attack damage as depicted in Figure 4.24. The notched bars were submerged in liquid nitrogen for a minimum of 15 minutes and then quickly placed in a vice and fractured. Immediately after fracture, the specimens were submerged in methanol bath till the specimen temperature was raised to ambient and then dried. Examination was implemented through the wall thickness using scanning electron microscopy.

The same basic damage levels were found on the fracture surface as using OLM. Hydrogen attack damage gradually decreases from the ID to the OD. However, hydrogen damage was observed to a greater depth by using SEM for both "Cryo-cracking" and metallographic samples compared to OLM. For the sample extracted from the central portion of the channel, hydrogen attack damage was found in a depth of 19 mm (75% of wall thickness) from the ID surface using SEM in contrast to 13 mm (50% of wall thickness) in depth observed using OLM. Representative fractographs are presented in Figures 4.25 through 4.27 corresponding to the locations adjacent to the ID, 6 mm, and 19 mm in depth from the ID surface for the central portion of the channel.

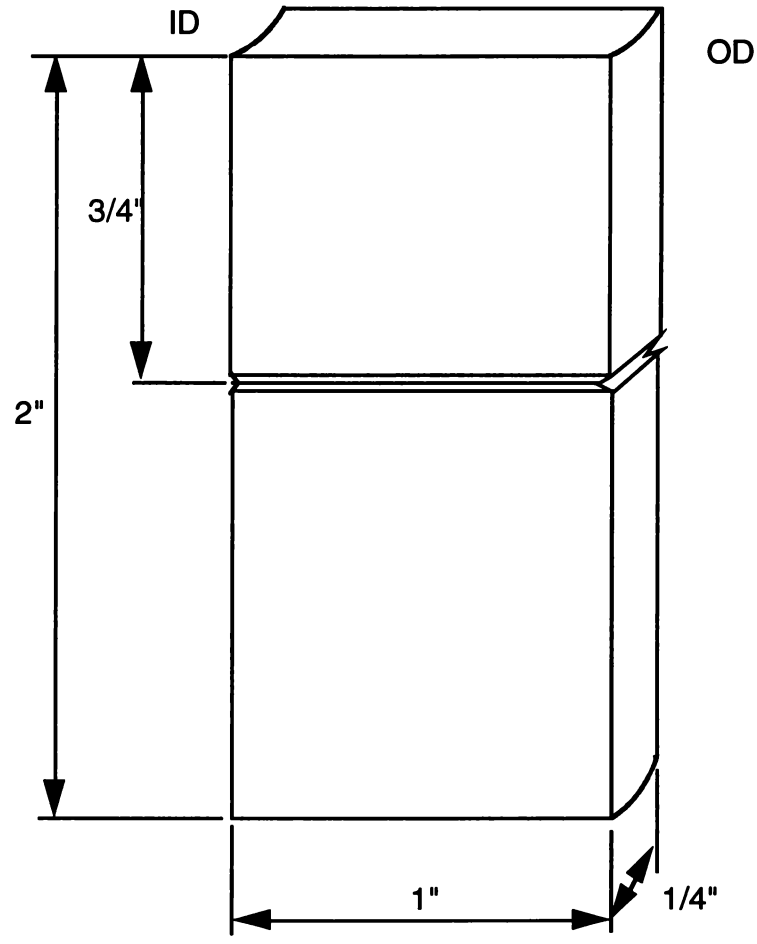
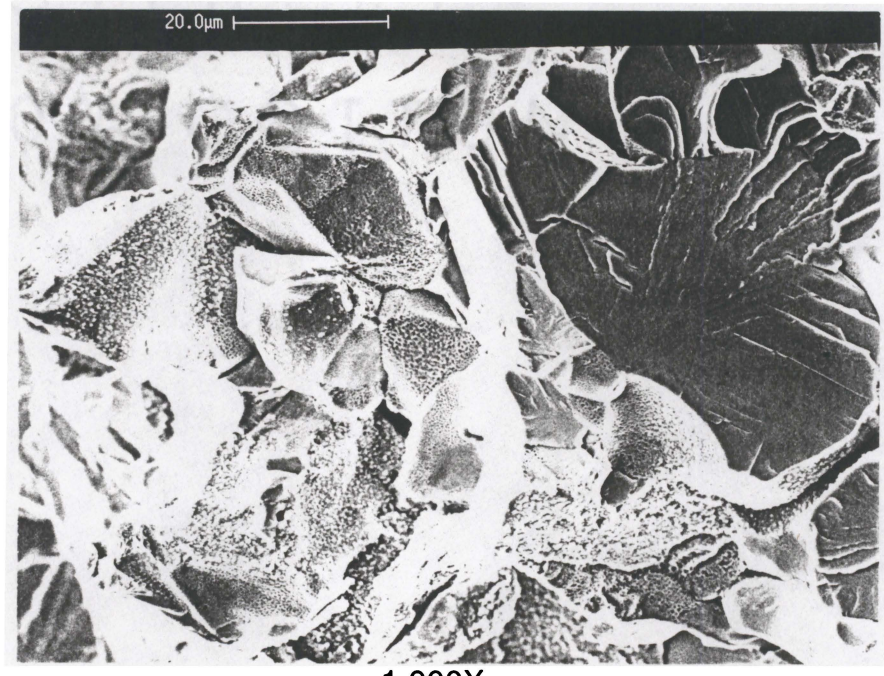
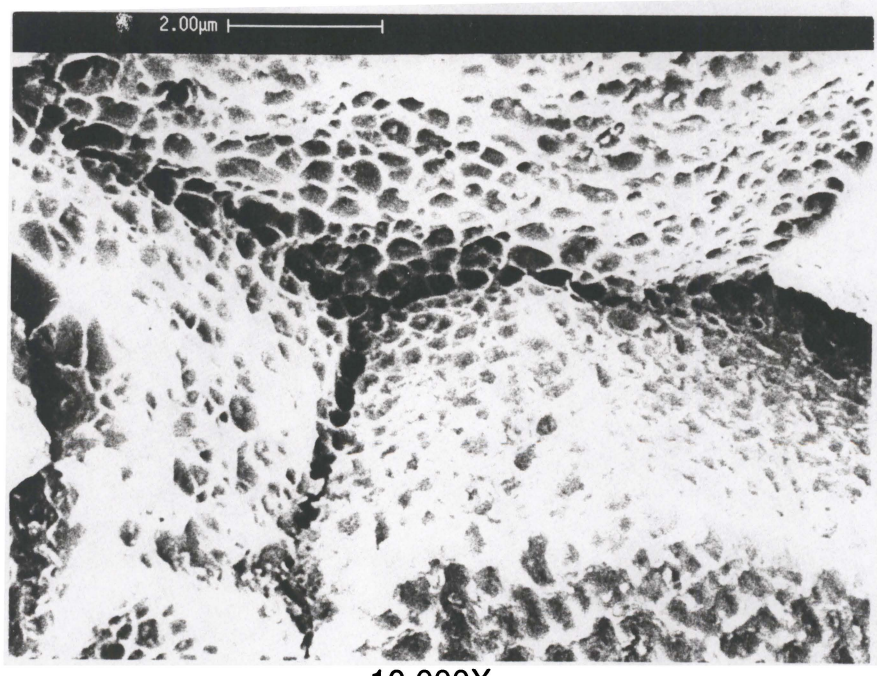


Figure 4.24 SEM "Cryo-cracking" sample preparation for hydrogen attack evaluation.

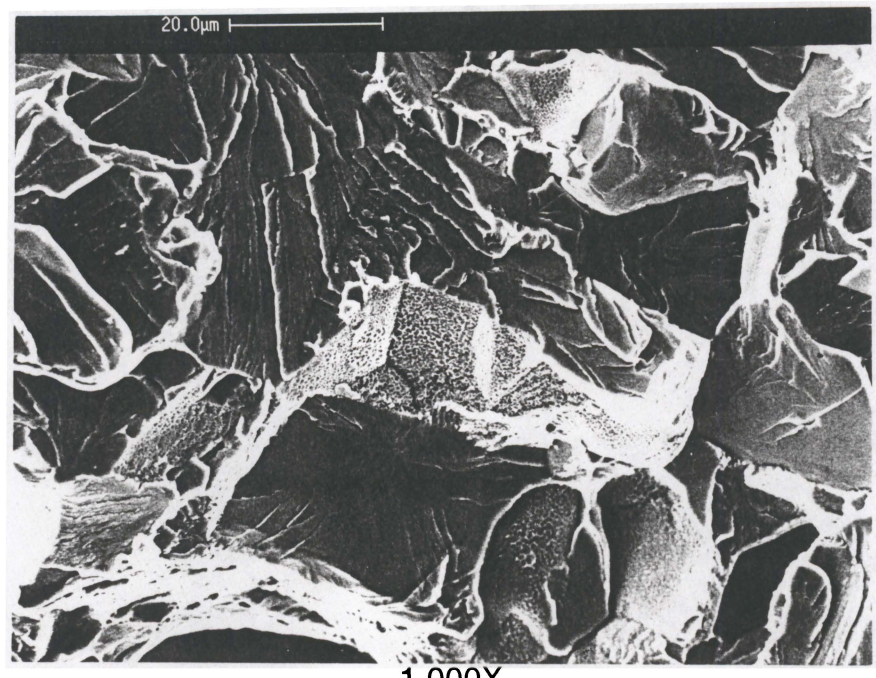


1,000X

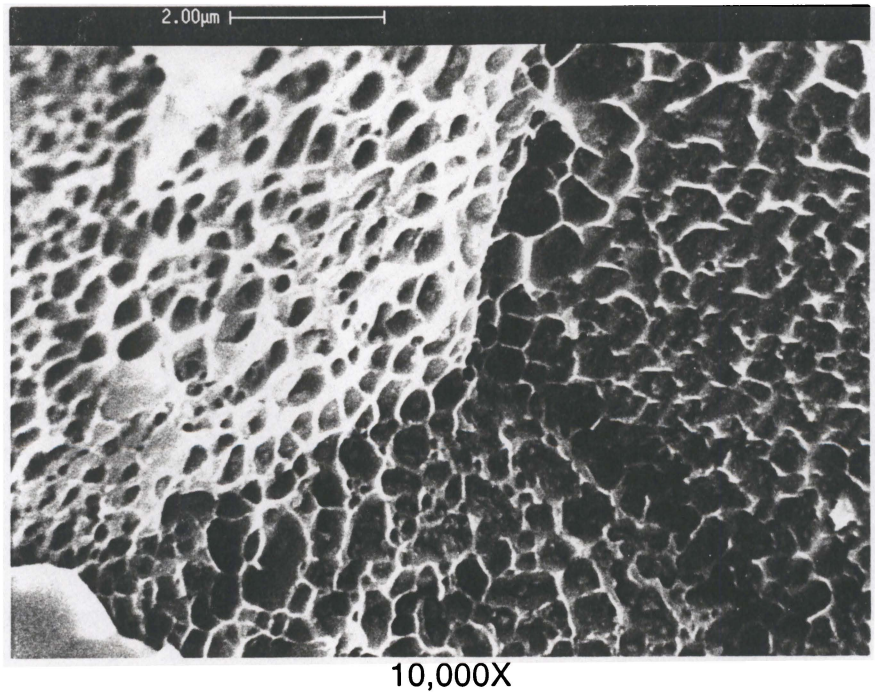


10,000X

Figure 4.25 SEM images of hydrogen attack damage with coalesced methane bubbles on the grain boundaries adjacent to the ID surface (central portion of the channel, MPC-18).

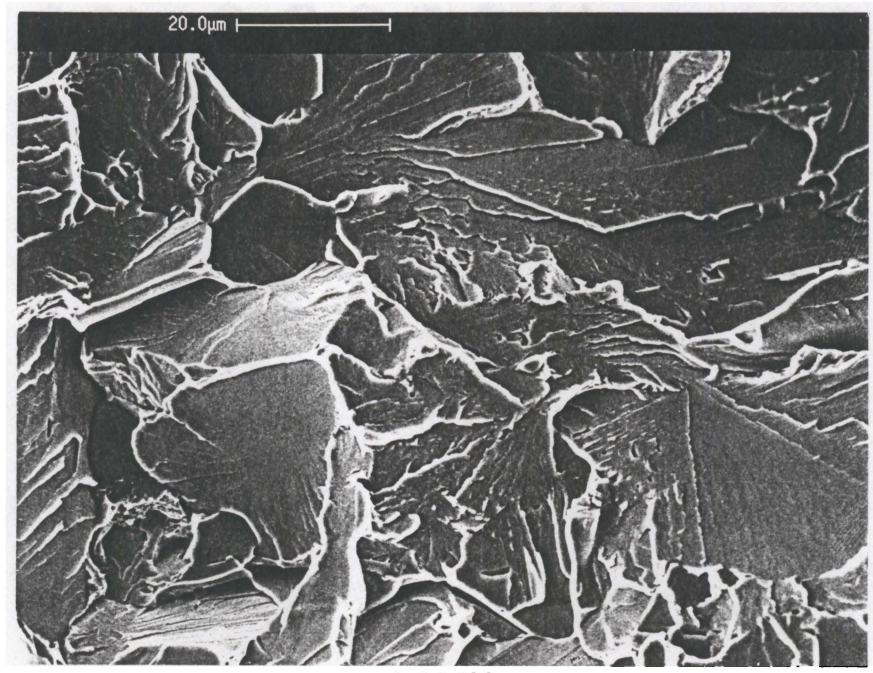


1,000X



10,000X

Figure 4.26. SEM images of hydrogen attack damage with coalesced methane bubbles on the grain boundaries at the location of 6 mm deep from the ID surface (central portion of the channel, MPC-18).



1,000X



10,000X

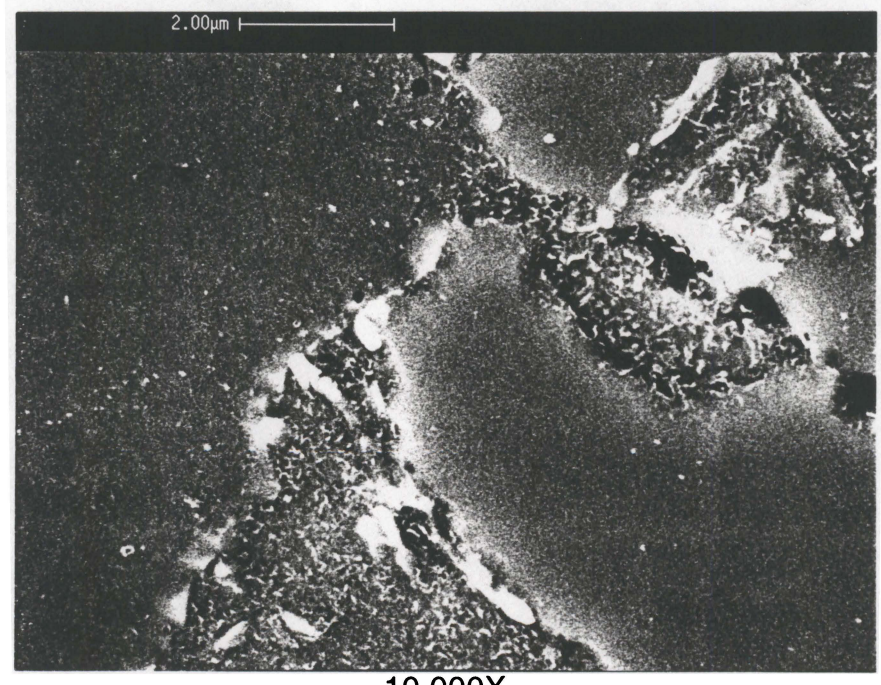
Figure 4.27 SEM images of hydrogen attack damage with methane bubbles along grain boundaries at the location of 19 mm deep from the ID surface (central portion of the channel, MPC-18).

Figures 4.28 through 4.30 show the SEM images of hydrogen attack cracks and methane bubbles at different depths (adjacent to the ID, 6 mm, and 19 mm in depth from the ID) on the polished and etched sample. Intergranular cracks and methane bubbles are observed along both ferrite/bainite and ferrite/ferrite boundaries. The early stages of methane bubble initiation are revealed in the form of isolated bubbles at the 19 mm depth location as shown in Figures 4.27 and 4.30.

The fraction of hydrogen damaged grain boundary area (FA%) was determined to quantify the severity of hydrogen damage. The hydrogen damaged area was measured from the SEM images of the "Cryo-cracking" samples in three fields at a magnification of 1,000X. Methane bubble sizes were also measured from the SEM image of the "Cryo-cracking" samples at a magnification of 10,000X through the wall thickness. The fraction of hydrogen damaged grain boundary area through the wall thickness is presented in Figure 4.31. The fraction of damaged grain boundary area exponentially decreased from the ID to the OD in the same manner as the fraction of damaged grain boundary length (FL%) using OLM. The fraction of damaged area at the ID is approximately 60% and the maximum damaged depth is 19 mm from the ID. To compare with the OLM results, the fraction of damaged grain boundary area is superimposed on the fraction of damaged grain boundary length (FL%) as represented in Figure 4.32. The fraction of damaged grain boundary area (SEM) is consistent with the fraction of damaged grain boundary length (OLM)

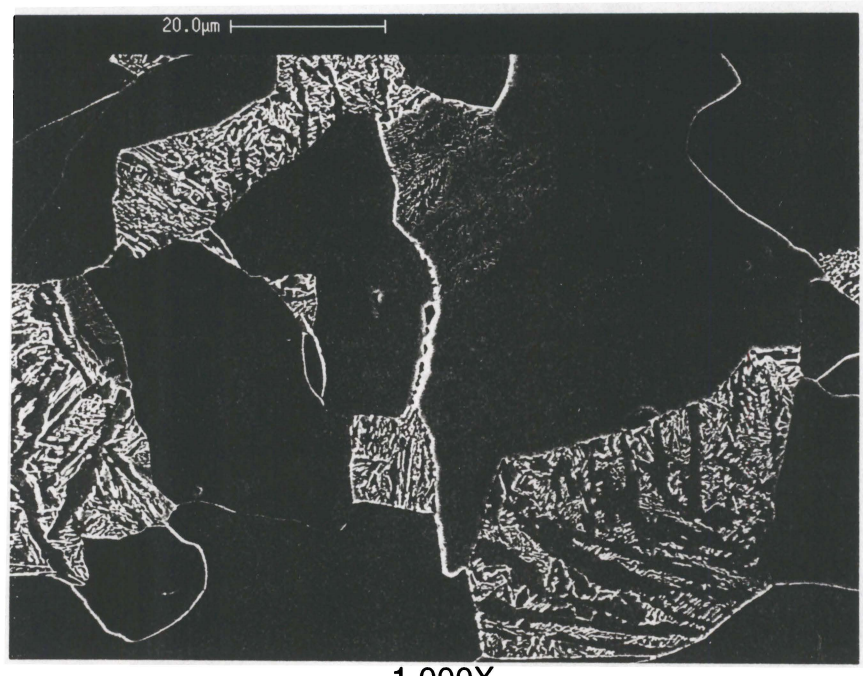


1,000X

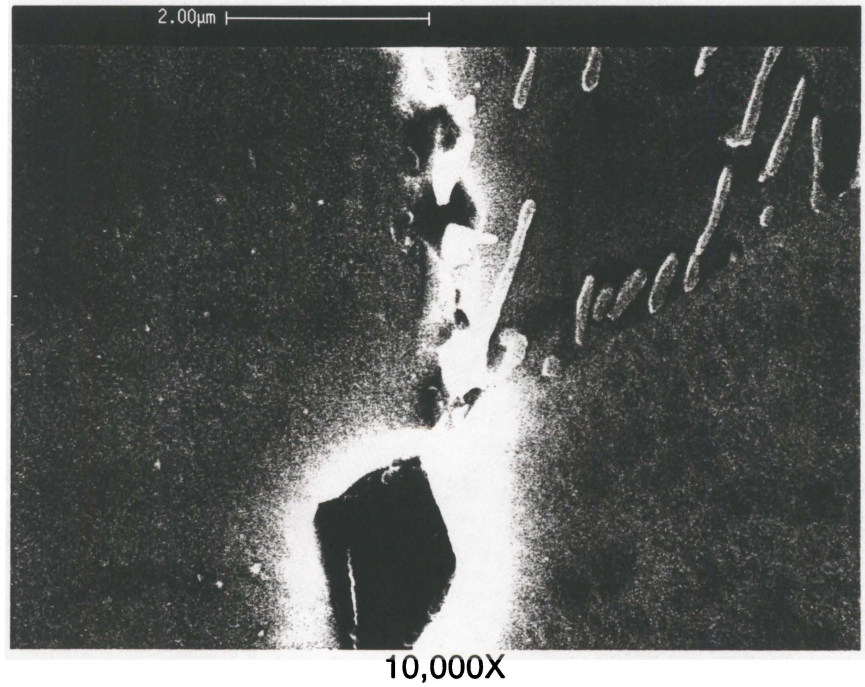


10,000X

Figure 4.28 Hydrogen attack cracking and methane bubbles along grain boundaries on the polished and etched sample adjacent to the ID (central portion of the channel, MPC-18).

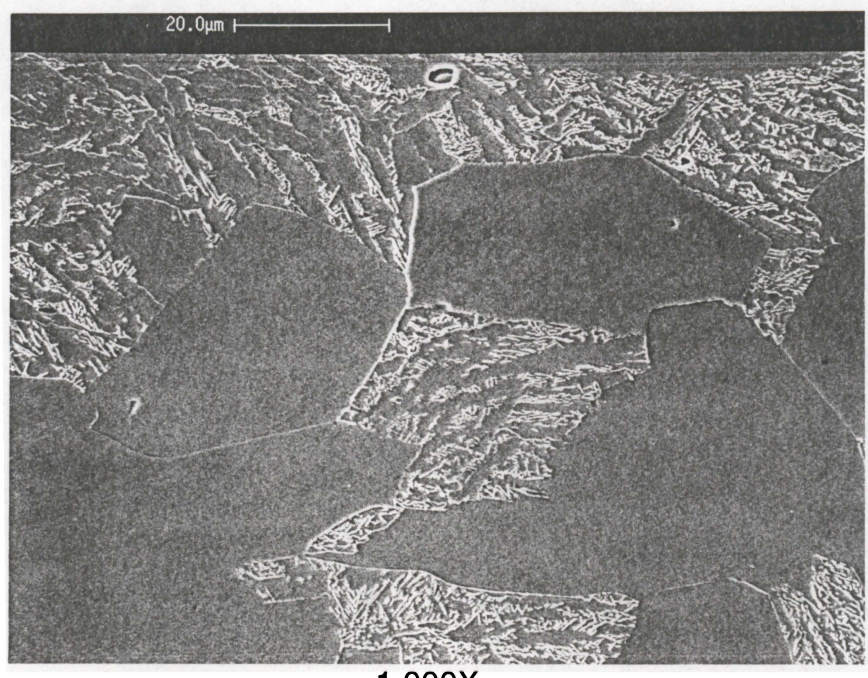


1,000X

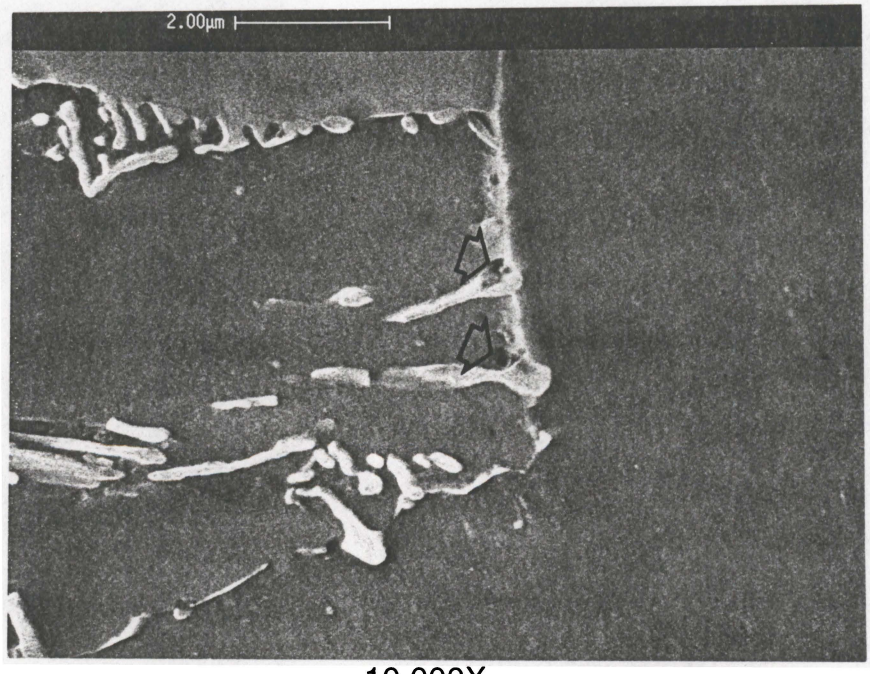


10,000X

Figure 4.29 Coalesced methane bubbles along grain boundaries on the polished and etched sample at the location of 6 mm deep from the ID (central portion of the channel, MPC-18).



1,000X



10,000X

Figure 4.30 Isolated methane bubbles along grain boundaries on the polished and etched sample at the location of 19 mm deep from the ID (central portion of the channel, MPC-18).

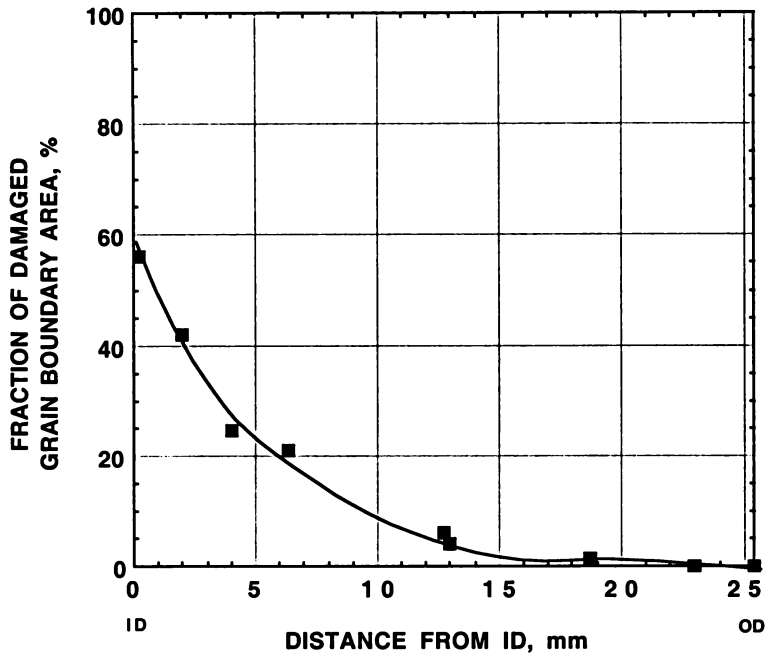


Figure 4.31 Hydrogen damage profile (FA%) through the wall of the heat exchanger channel (central portion, MPC-18).

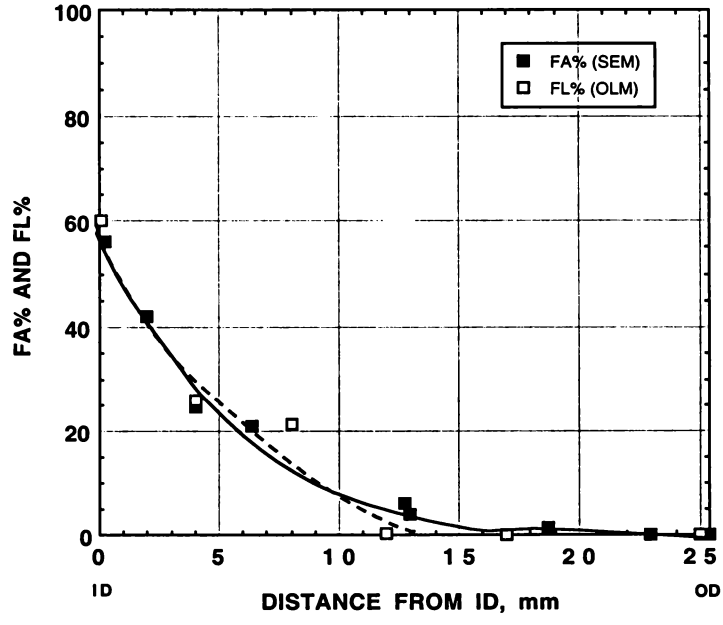


Figure 4.32 Comparison of FL% (OLM) and FA% (SEM) used to quantify hydrogen damage through the wall of the heat exchanger channel (central portion, MPC-18).

for the hydrogen damage evaluation of the channel material (central portion). It is to be emphasized that the maximum damaged depth determined by using SEM is greater than that by using OLM because of the higher resolution of SEM. It was observed using SEM that the hydrogen attack damage is in the form of isolated bubbles beyond a 13 mm depth. These aligned or isolated bubbles could not be detected by using OLM (1000X). OLM can effectively resolve hydrogen attack cracks. SEM is necessary to define the early stages of hydrogen attack in the form of aligned or isolated bubbles at a high magnification (above 5000X).

Methane bubble sizes (diameter) were measured from the SEM "Cryo-cracking" images at a magnification of 10,000X. A profile of the methane bubble sizes through wall thickness is shown in Figure 4.33. Methane bubble size is constant at approximately 0.45 μm to a depth of 13 mm from the ID and then the size decreases. The morphology of hydrogen attack damage is characterized as coalesced methane bubbles on an entirely damaged grain boundary from the ID to 13 mm in depth. Beyond 13 mm, the damage is in the form of aligned or isolated methane bubbles as shown in Figures 4.27 and 4.30.

These results indicate that hydrogen attack occurred with the initiation of small size methane bubbles on grain boundaries. With the growth of methane bubbles, more bubbles were continuously formed on the remaining sound grain boundaries. Once the methane bubbles grew to certain sizes, they reached each other and coalesced to form cracks.

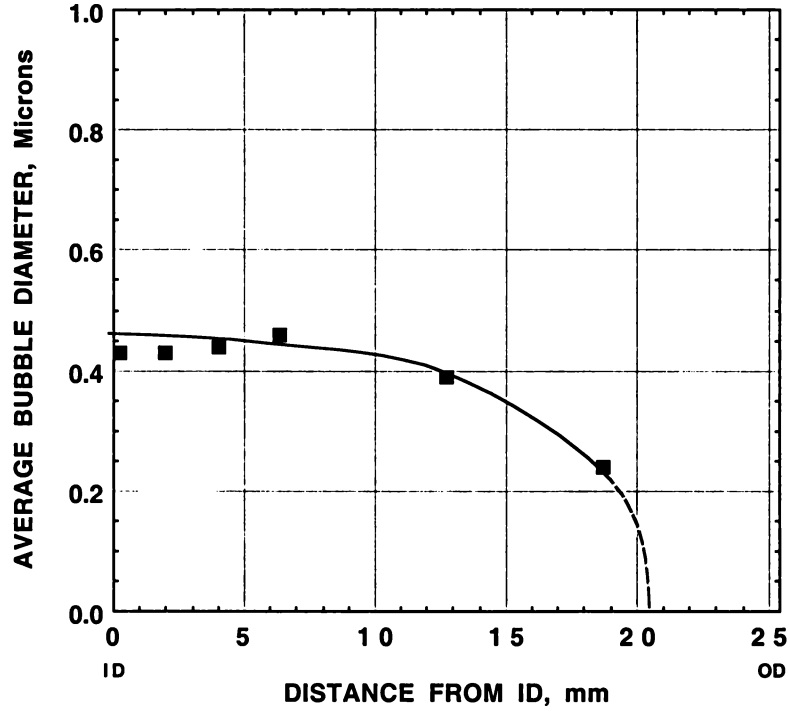


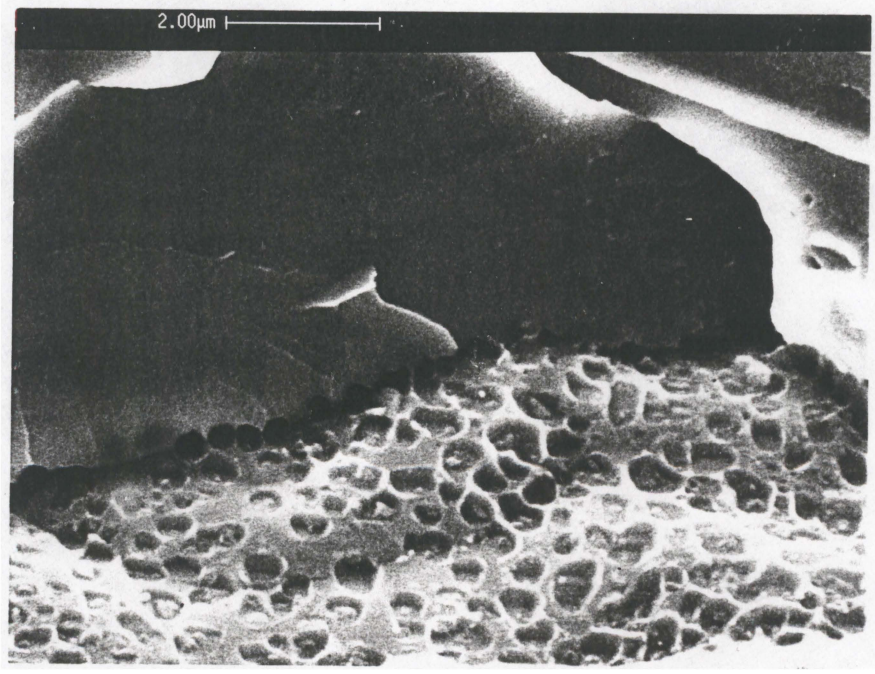
Figure 4.33 Profile of bubble diameters through the wall of the heat exchanger channel (central portion, MPC-18).

For the sample extracted from the channel near the flange, the depth of the hydrogen damage extended to approximately 10 mm from the ID surface according to the SEM observation (4 mm deeper than OLM resolved depth). Figures 4.34 and 4.35 show the hydrogen attack damage morphology at locations adjacent to the ID surface and 5 mm deep, respectively. The profile of hydrogen damage in terms of fraction of damaged grain boundary area (FA%) is presented in Figure 4.36. The maximum damaged grain boundaries are approximately 25% adjacent to the ID surface. Methane bubble sizes were determined as shown in Figure 4.37. The methane bubble size measured adjacent to the ID surface is approximately 0.4 μm. Figures 4.38 and 4.39 present the hydrogen attack cracks and methane bubbles initiated along grain boundaries in the polished and etched sample. The hydrogen damage morphology is characterized as coalesced bubbles, aligned bubbles, and isolated bubbles from the ID towards to the maximum damaged depth. Figure 4.40 show a comparison of hydrogen attack damage profiles through wall of the channel cylinder in the central portion and near the flange. Hydrogen attack damage is greater in the central portion than that near the flange.

A relationship of the fraction of hydrogen damaged grain boundaries (FA% and FL%) area and methane bubble size is shown in Figure 4.41. With an increase in the fraction of damaged grain boundaries, the methane bubble size increases. As the fraction of damaged grain boundaries reaches approximately 10%, the methane bubble size begins to level off (approximately 0.35 μm)

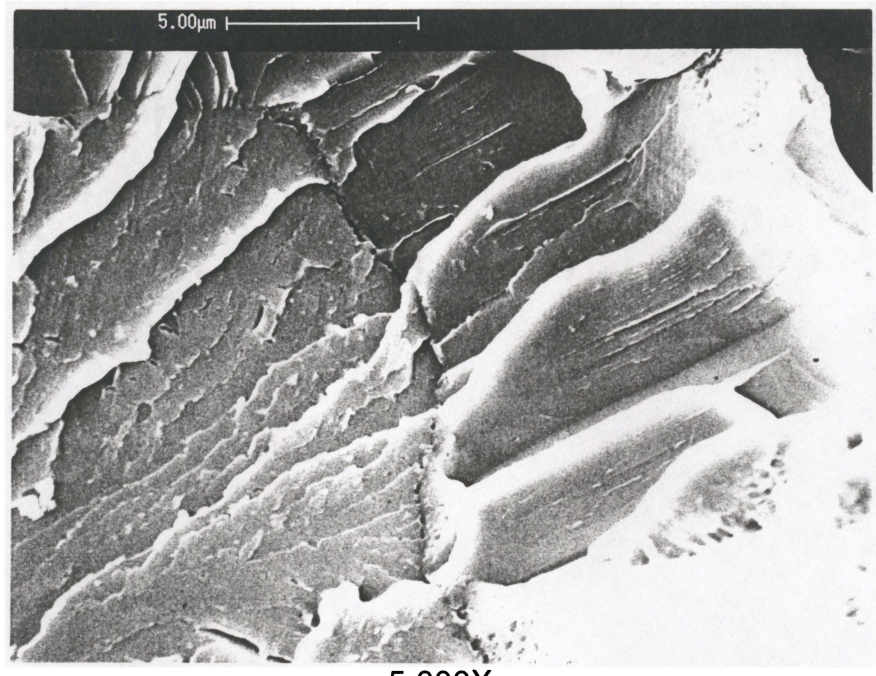


1,000X

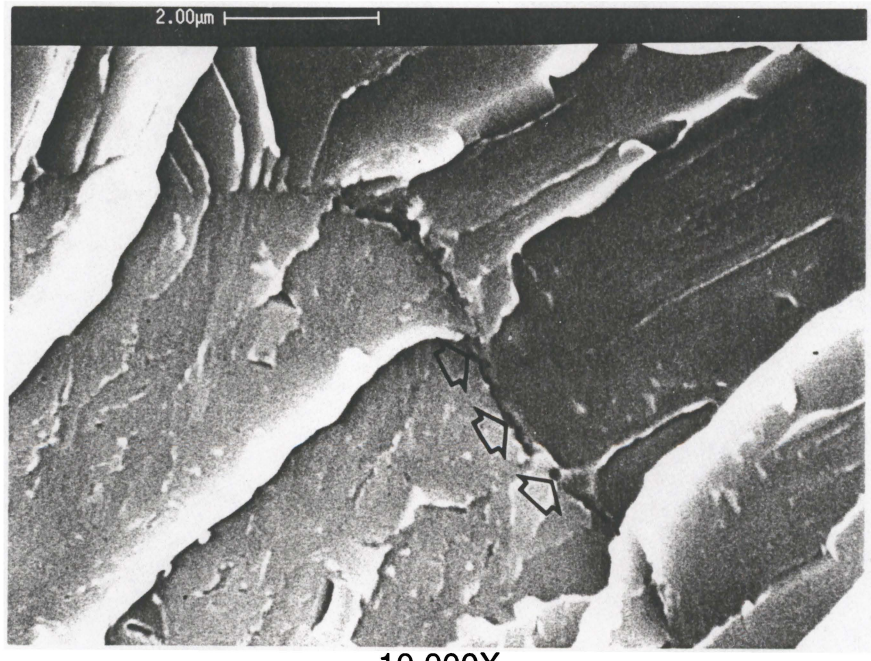


10,000X

Figure 4.34 Coalesced methane bubbles on the grain boundaries adjacent to the ID surface (near flange, MPC-18).



5,000X



10,000X

Figure 4.35. Methane bubbles along the grain boundaries at the location of 5 mm deep from the ID surface (near flange, MPC-18).

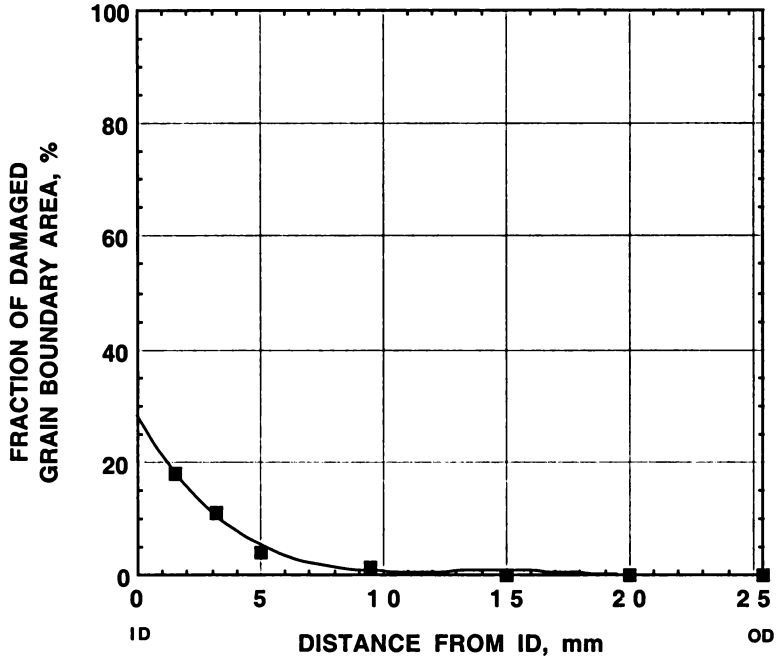


Figure 4.36 Hydrogen damage profile (FA%) through wall thickness of heat exchanger channel (near flange, MPC-18).

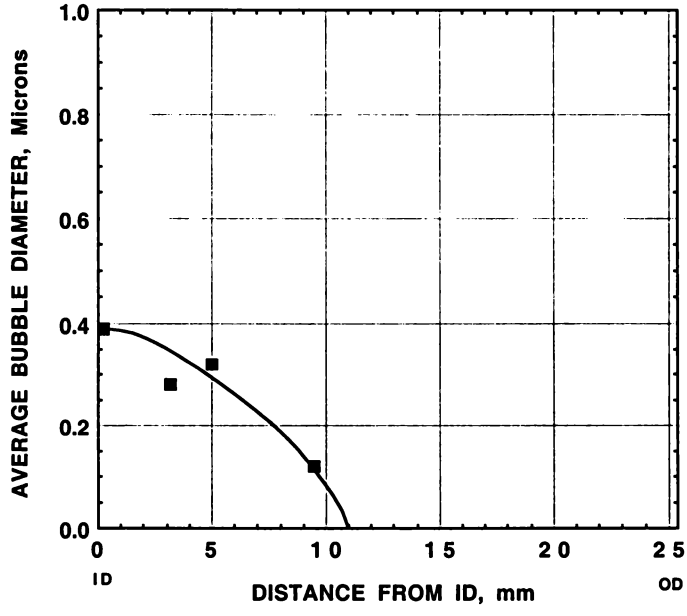
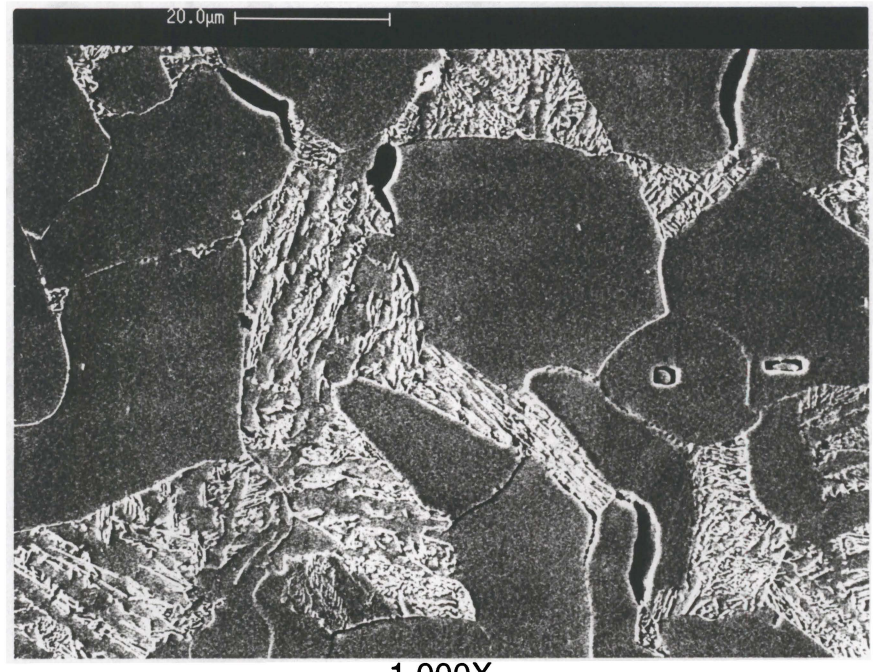
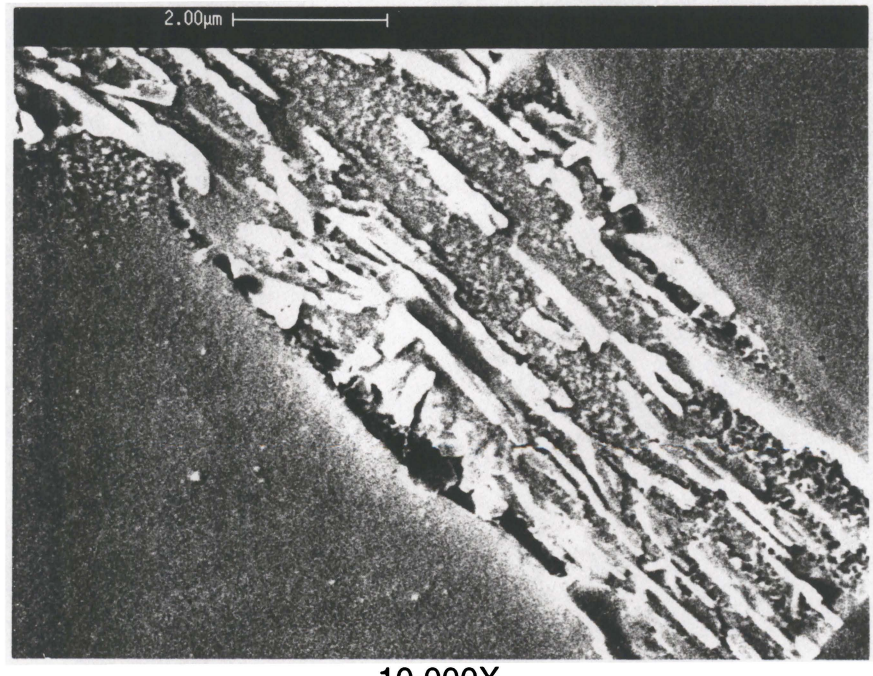


Figure 4.37 Profile of average bubble diameter through wall thickness of the heat exchanger channel (near flange, MPC-18).

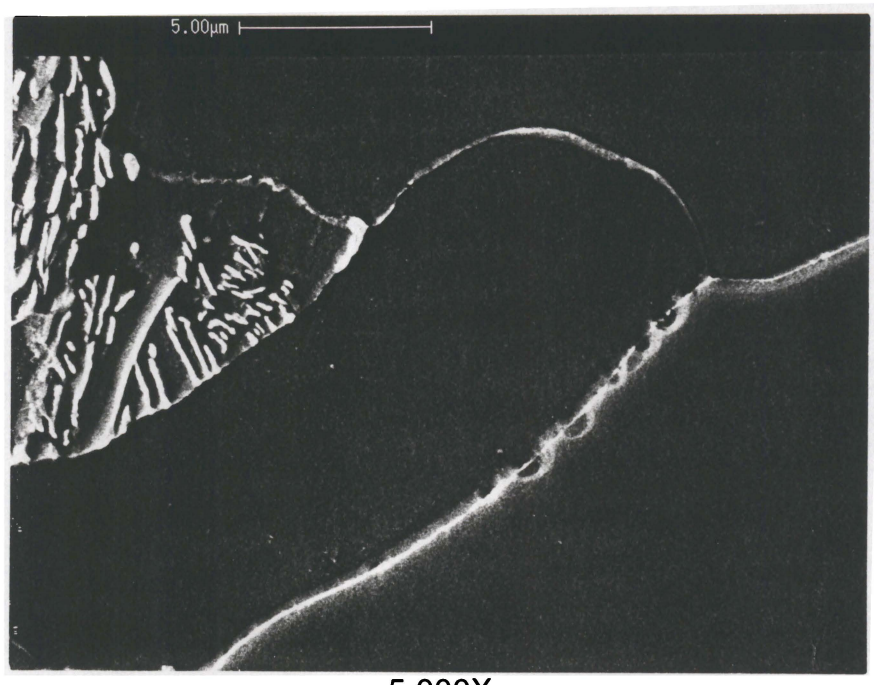


1,000X

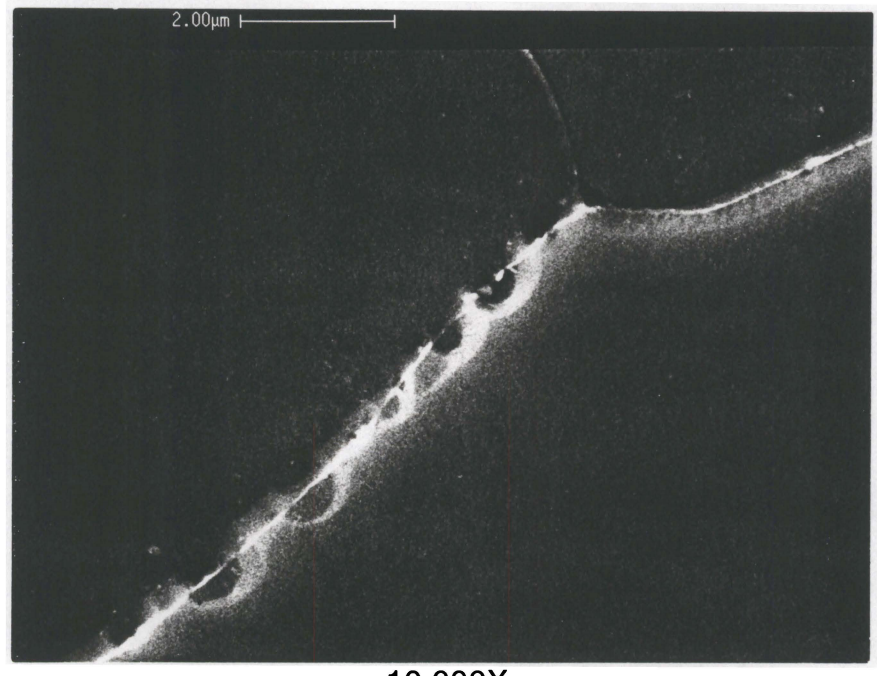


10,000X

Figure 4.38 Hydrogen attack cracks at grain boundaries in polished and etched sample adjacent to the ID (near the flange, MPC-18).



5,000X



10,000X

Figure 4.39 Methane bubbles initiated at grain boundaries at the location of 5 mm deep from the ID surface in the polished and etched sample (near flange, MPC-18).

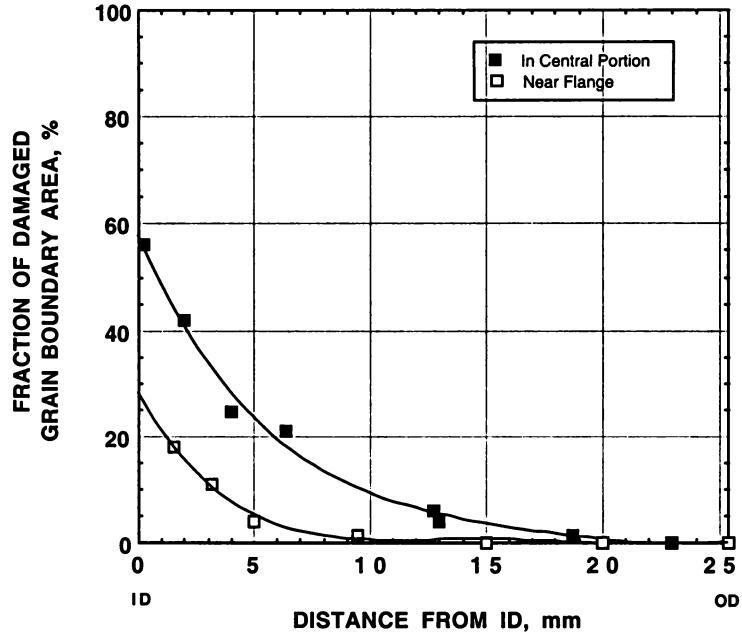


Figure 4.40 Comparison of hydrogen attack damage profiles (FA%) within the wall of heat exchanger channel in the central portion and near the flange (MPC-18).

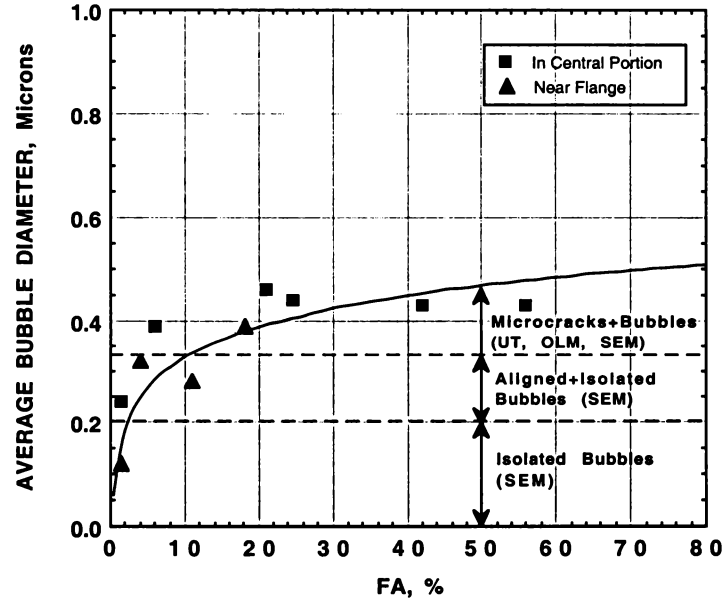


Figure 4.41 Correlation of methane bubble size and the fraction of damaged area (FA%, MPC-18).

and thus corresponds to the change of methane bubble coalescence. Metallographic examination shows that the maximum damaged depth along the exchanger channel is greater in the central portion than that near the flanges. This indicates that higher operating temperature in the central portion (580°F) promotes more severe hydrogen attack compared to the location near the flanges that are at a lower operating temperature (500°F).

The fractions of damaged grain boundary length and area were quantitatively determined through the wall of the tube sheet (MPC-20) using both OLM and SEM images. Figure 4.42 shows the profiles of hydrogen attack damage in terms of fraction of damaged grain boundary length from the Side A to Side B of the tube sheet using OLM. The fraction of damaged F/F, F/B, and total damaged grain boundaries was quantified. A gradient of hydrogen attack damage was observed decreasing from Side A to Side B. The fraction of total damaged grain boundaries was determined as approximately 38% adjacent to Side A and 3% adjacent to Side B. There are more damaged F/F grain boundaries than damaged F/B grain boundaries. A flat portion revealed on the plots (Figure 4.42) can be related to the interaction of different temperatures and hydrogen pressures on Sides A and B. Similar consistent results of the hydrogen damage in the tube sheet was obtained using SEM "Cryo-cracking" technique as presented in Figure 4.43 in comparison to the OLM results. Figures 4.44 and 4.45 show the representative SEM images of damaged F/F and F/B grain boundaries, respectively. The damaged F/F grain boundaries are

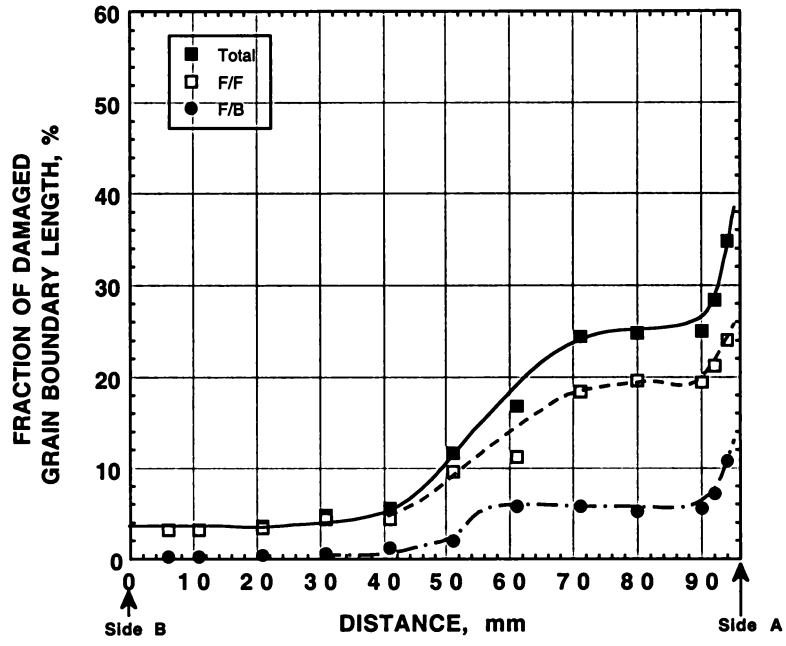


Figure 4.42 Hydrogen damage profiles in terms of damaged F/F, F/B boundaries and total damaged boundaries (FL%) within the wall of tube sheet (MPC-20).

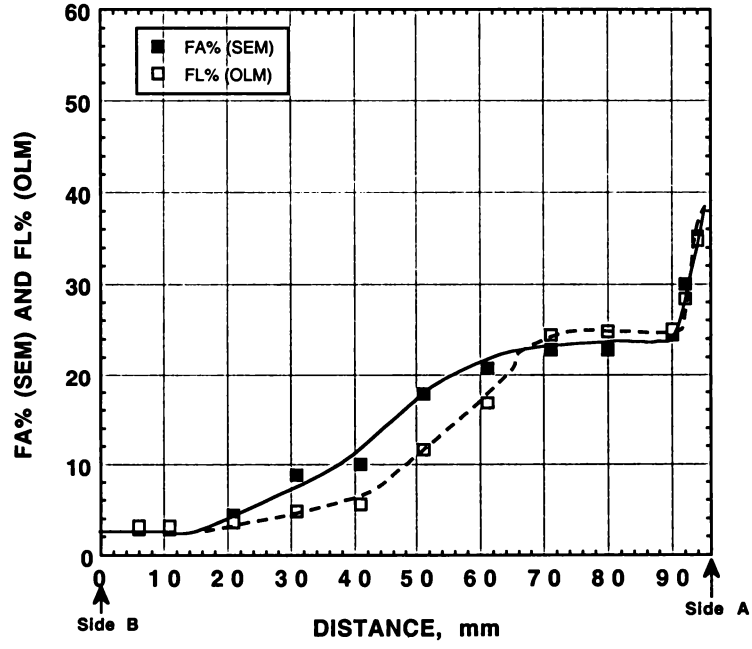


Figure 4.43 Comparison of hydrogen damage profiles of FA% (SEM) and FL% (OLM) within the wall of tube sheet (MPC-20).

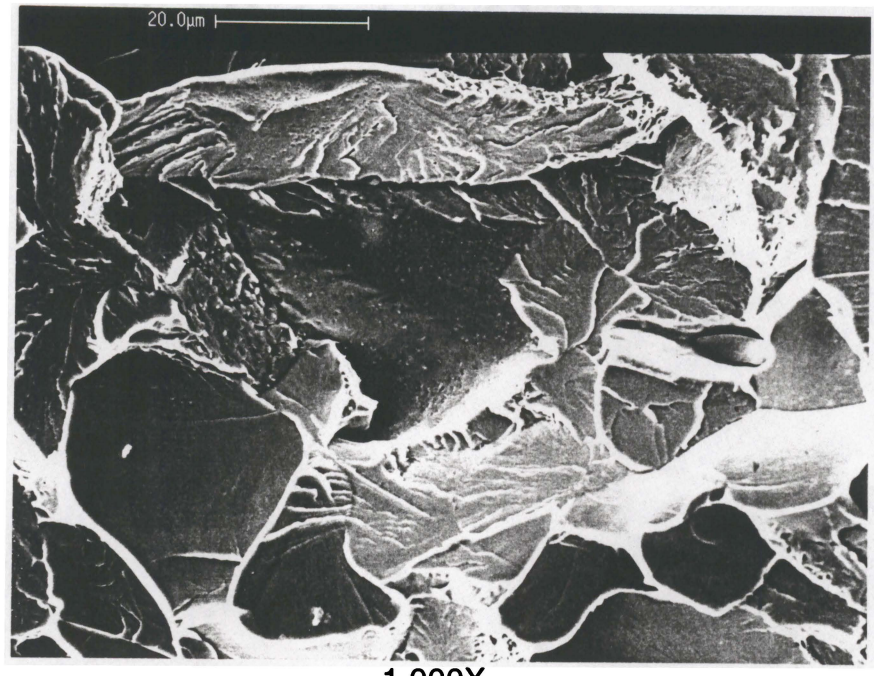


1,000X

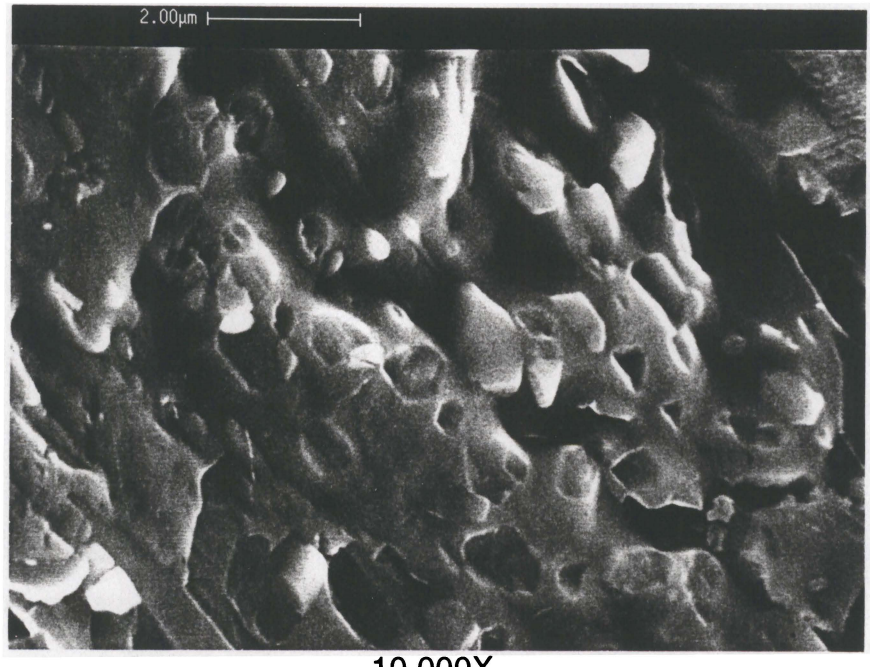


10,000X

Figure 4.44 Typical hydrogen damaged F/F boundaries with methane bubbles and carbides (16 mm from Side A, tube sheet, MPC-20).



1,000X



10,000X

Figure 4.45 Typical hydrogen damaged F/B boundaries with methane bubbles and carbides (45 mm from Side A, tube sheet, MPC-20).

characterized as smooth grain boundary facets and/or grain boundary facets with distant bubbles and fine carbides (Figure 4.44). In contrast to the damaged F/F grain boundaries, more bubbles were observed on the damaged F/B grain boundary facets with or without retained carbides (Figure 4.45).

4.1.1.4 Methane Determination

Samples for methane determination were extracted from the central portion and adjacent to the flange of the heat exchanger channel (MPC-18). Figure 4.46 shows the sample extraction at different depths through the wall thickness in the central portion of the channel. The samples were cleaned using acetone and methanol to remove any contamination on surfaces. Hydrogen dissociated from methane was measured using both Oerlikon-Yanaco Hydrogen Analyzer and Leco fusion method. Methane concentration was determined based on the measured hydrogen concentration.

Figure 4.47 presents the hydrogen concentration through the wall (central portion of the channel). High hydrogen concentration was determined as approximately 80 ppm adjacent to the ID. Then the hydrogen concentration exponentially decreases from the ID through wall thickness. It is to be noted that the hydrogen measurement results using Oerlikon-Yanaco Hydrogen Analyzer are consistent with the results using Leco fusion method. The measuring repeatability using Oerlikon-Yanaco Hydrogen Analyzer was verified using multiple samples as demonstrated in Figure 4.47. According to "Cryo-

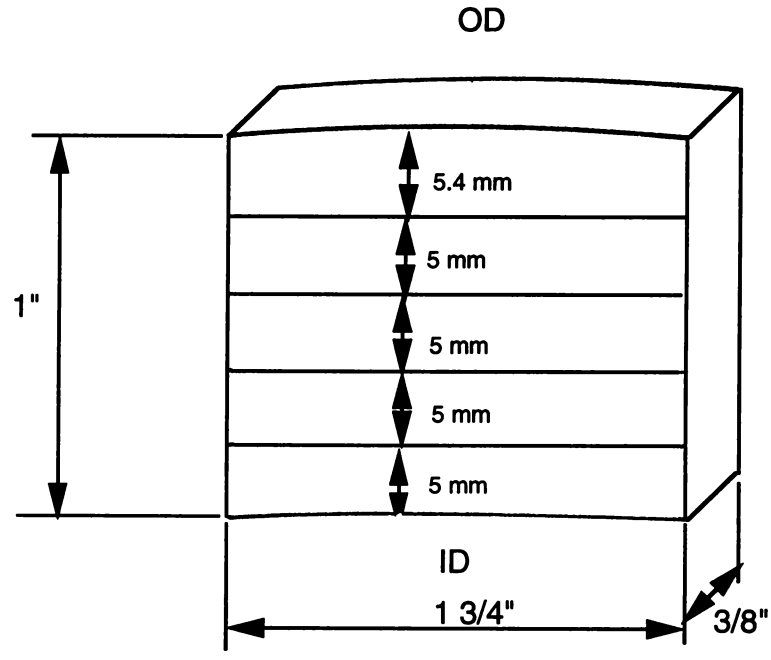


Figure 4.46 Sample extraction in different depths through the wall thickness of heat exchanger channel for methane determination (MPC-18).

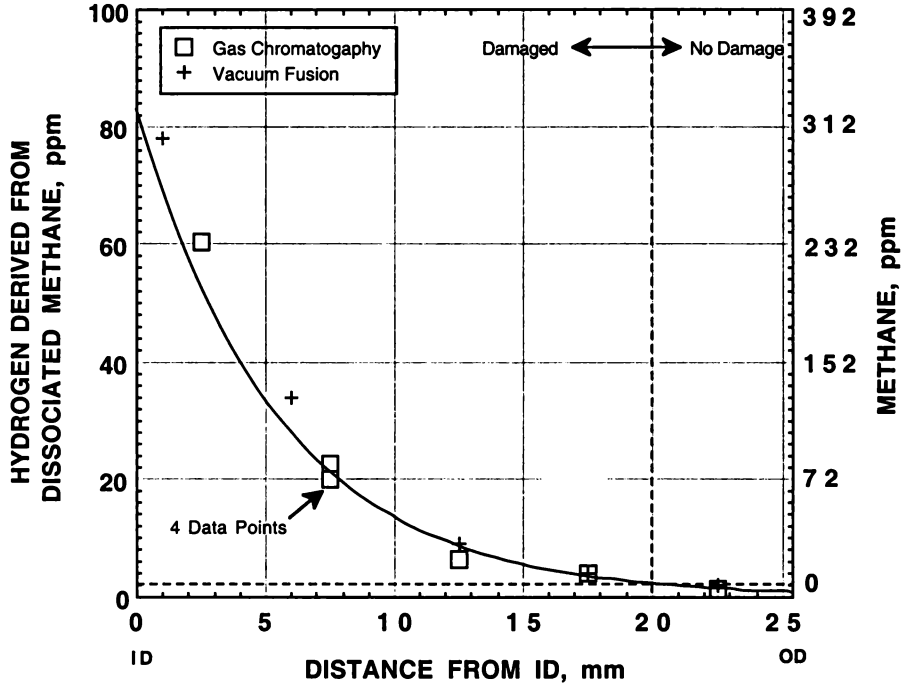


Figure 4.47 Methane concentration (hydrogen dissociated from methane) profiles within wall thickness of the exchanger channel (central portion, MPC-18).

Table 4.2 Hydrogen content in the materials without hydrogen exposure.

Un-exposed Material	H_2, ppm Gas Chromatography	H_2, ppm Leco Fusion Method
C-0.5Mo (N&T)	2	2
1.25Cr-0.5Mo (N&T)	1	2
2.25Cr-1Mo (N&T)	2	2
A710 (Q&T)	2	-

cracking" observation results, the maximum depth of the hydrogen attack damage is approximately 20 mm from the ID in the central portion of the exchanger channel as shown in Figure 4.31. Therefore, the hydrogen concentration corresponding to the cut-off line of hydrogen attack/no hydrogen attack observed by using SEM was defined as approximately 2 ppm as shown in Figure 4.47, above which hydrogen attack occurred.

In fact, hydrogen concentration is measured for methane determination. The measured hydrogen is a total hydrogen content which is attributed by the hydrogen dissociated from methane, trapped hydrogen, and hydrogen in solid solution. However, the hydrogen in traps and solid solution is a small fraction of the total hydrogen content [95]. To define the hydrogen in traps and solid solution, hydrogen content was determined for the materials without hydrogen exposure including C-0.5Mo (N&T), 1.25Cr-0.5Mo (N&T), 2.25Cr-1Mo (N&T), and A710 (Q&T) using both gas chromatography and Leco vacuum fusion method. The hydrogen results are presented in Table 4.2. The hydrogen content in the un-exposed materials is approximately 2 ppm, which is consistent

with the 2 ppm hydrogen content at the cut-off line above which hydrogen attack damage was observed in the heat exchanger channel as shown in Figure 4.47.

In accordance with an assumption of the background hydrogen content of 2 ppm (in solution and traps), the methane concentration (C_{CH4} ppm) can be determined by hydrogen measurement using

$$C_{CH4}\ (ppm) = 4\ (C_{H2} - 2)$$

where C_{H2} is the total measured hydrogen content. The methane concentration profile was determined within the wall of the heat exchanger channel (central portion) as shown in Figure 4.47. The methane concentration is approximately 312 ppm adjacent to the ID surface the heat exchanger channel (central portion).

Methane concentration profile was determined for the exchange channel near the flange as shown in Figure 4.48. The methane concentration is approximately 150 ppm near the ID, which is less than that in the central portion of the exchanger channel (312 ppm). The cut-off line for hydrogen attack/no hydrogen attack is 15 mm in depth from the ID based on the "Cryo-cracking" observation. The hydrogen concentration corresponding to the cut-off line is approximately 2 ppm as shown in Figure 4.48, which is accord with the results determined for the central portion of the exchanger channel. Figure 4.49 shows the comparison of the methane concentration in the heat exchanger channel in the central portion and near the flange.

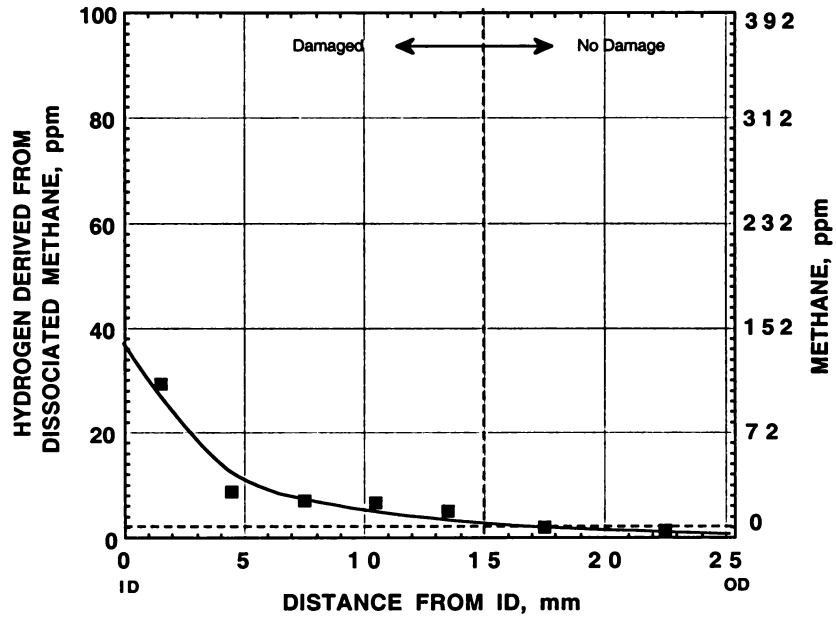


Figure 4.48 Methane concentration (hydrogen dissociated from methane) profiles within wall thickness of the exchanger channel (near flange, MPC-18).

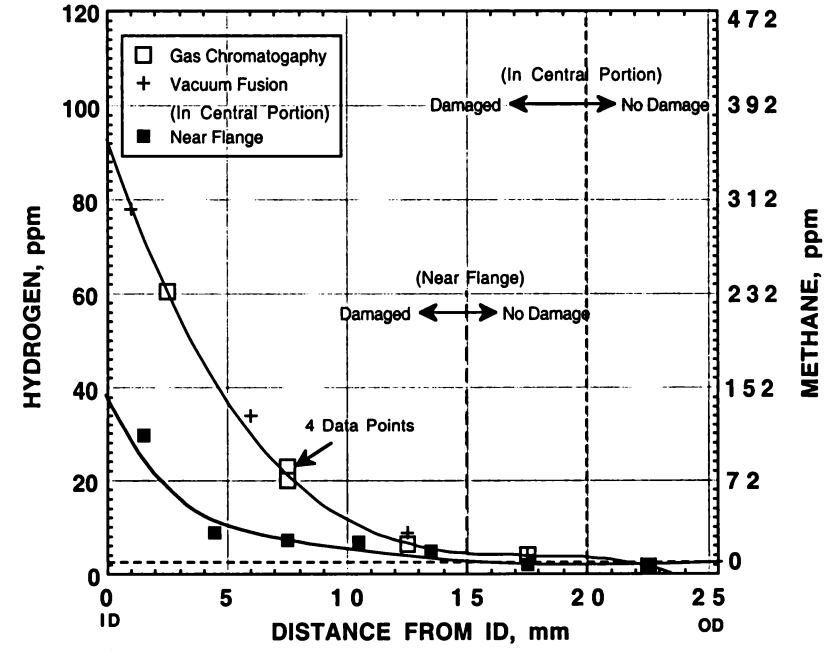


Figure 4.49 Comparison of methane concentration (hydrogen dissociated from methane) profiles within the wall thickness of heat exchanger channel in the central portion and near the flange (MPC-18).

Hydrogen attack damage (FA%, FL%) as a function of methane concentration (or hydrogen concentration) was derived in accord with the quantitative metallographic analysis and hydrogen measurements for the heat changer channel (MPC-18) as presented Figure 4.50. A linear relationship of hydrogen damage and methane concentration (or hydrogen concentration) was found on the basis of the experimental data. A critical hydrogen content was determined as approximately 2 ppm by extrapolating the plot. This critical hydrogen content accommodates the cut-off line of the hydrogen concentration profiles (Figures 4.47 and 4.48), below which hydrogen attack damage was not found using SEM. The development of a master curve of the hydrogen damage as a function of hydrogen concentration is significant for quantitative evaluation of hydrogen damage and fitness-for-service assessment using a small size sample and simple hydrogen measurement methods.

4.1.1.5 Carbon Concentration and Hardness

Carbon concentration and decarburization index profiles through the wall thickness were measured to assess the hydrogen attack damage in the central portion of the heat exchanger channel (MPC-18). According to the heat exchanger fabrication documents, the carbon content of the channel was 0.18% before hydrogen service. The decarburization index (DCI%) was computed by using the initial carbon content (0.18%) in comparison to the measured results of carbon determination through the wall. Figure 4.51 shows the carbon

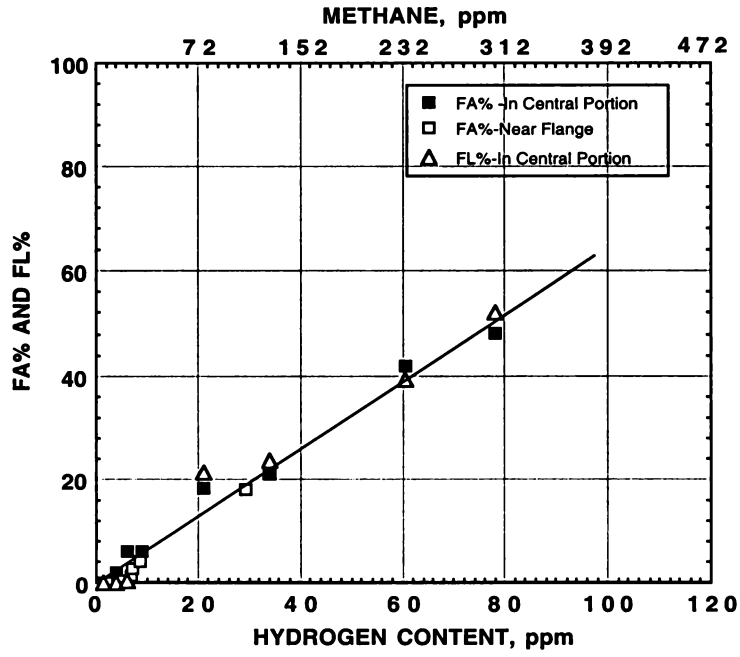


Figure 4.50 Relationship of the fraction of damaged grain boundaries (FA%, FL%) and the methane concentration determined by hydrogen measurements.

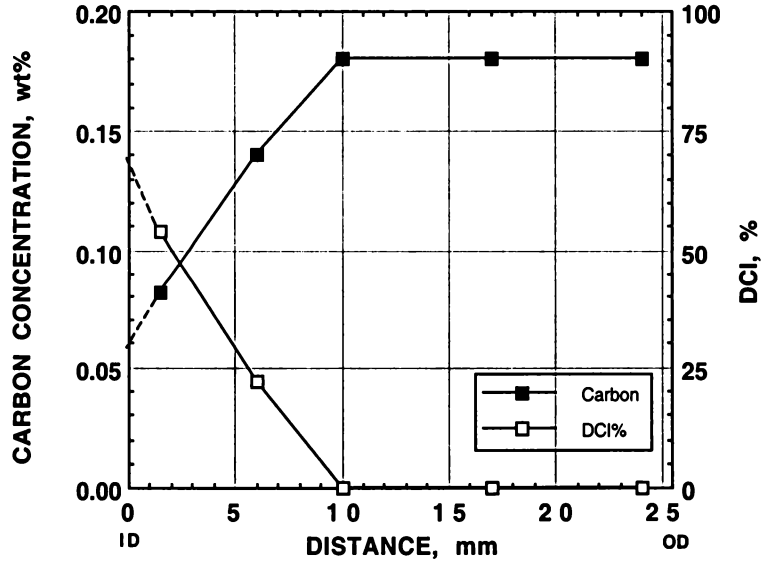


Figure 4.51 Carbon concentration and DCI profiles within the wall thickness of the exchanger channel (central portion, MPC-18).

concentration and decarburization index profiles through the wall thickness. Decarburization occurs and extends to approximately 10 mm deep from the ID surface. The maximum value of DCI was estimated as 65% by the extrapolation of the plot at the ID. Comparing Figure 4.51 with Figure 4.32, it is evident that the maximum depth of the hydrogen damage defined by using SEM "Cryo-cracking" technique is greater than that determined by using carbon concentration measurements.

Hardness was determined for base metal, CGHAZ, and weld metal of the long seam weld of the channel material (MPC-18). Because the heat exchanger channel was insulated during operation, the temperature from the ID to OD is assumed to be uniform and thus the material experienced the same thermal history through the wall. Therefore, the hardness difference between the ID and the OD is an indication of hydrogen attack. The decrease in hardness for the ID compared to the OD was attributed to hydrogen attack in terms of decarburization. Figure 4.52 shows the hardness of base metal, the CGHAZ, and weld metal. A decrease in hardness was observed for the base metal and the CGHAZ that has shown hydrogen attack damage based on the metallographic examination. Degradation of hardness did not occur for the weld metal in which hydrogen attack damage was absent in accord with the metallographic examination. The hardness degradation index numbers are approximately 7% for base metal, 13% for CGHAZ, and 0% for weld metal. However, the fraction of damaged length and area determined using

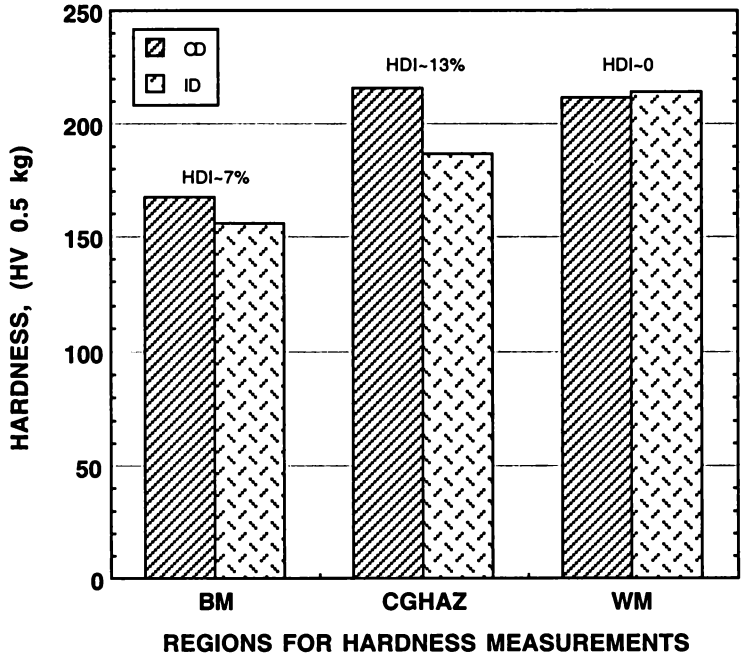


Figure 4.52 Hardness and HDI for the base metal, CGHAZ, and weld metal of the long seam weld (central portion of the channel, MPC-18).

quantitative image analysis is approximately 60% adjacent to the ID surface. Therefore, the hardness degradation index for hydrogen damage assessment is not as sensitive as the fraction of damaged length and area determined by using metallography and "Cryo-cracking" techniques.

4.1.1.6 Stress Assessment

Pressure vessels applied to the petroleum industry are designed in accordance with ASME Code for pressure vessel (Section VIII, Division I). Allowable design stresses were specified for carbon, C-0.5Mo, Cr-Mo, and stainless steels in the ASME Boiler and Pressure Vessel Code, Section VIII, Division 1 or 2 [96, 97]. For elevated temperature application, the allowable stresses are defined to be no higher than the lowest of the following:

(1). 1/4 of the specified minimum tensile strength at room temperature

(2). 1/4 of the tensile strength at elevated temperature

(3). 2/3 of the specified minimum yield strength at room temperature

(4). 2/3 of the yield strength at elevated temperature

(5). 100% of the stress to produce a creep rate of 0.01% in 1000 hr. (or 10^{-5} %/hr.)

(6). 67% of the average stress or 80% of the minimum stress to produce creep rupture in 100,000 hr. as determined from extrapolated data.

The allowable stress for C-0.5Mo steel (SA-204 B) is 17,500 psi in temperature range of 200°F to 850°F [96, 97]. A hoop stress (σ_h) in the exchanger channel (MPC-18) can be computed based on

$$\sigma_h = PR / t$$

where P is the operating pressure in the exchanger channel (1000 psi), R is the mean radium of the channel (14"), and t is the wall thickness. Because of the hydrogen damage in the wall, a concept of effective wall thickness is introduced for stress calculation. The effective thickness of the exchanger channel is defined as the original thickness minus the maximum depth of hydrogen damage. As discussed above, the maximum depth of hydrogen damage in the exchanger channel was determined as 0.5" by OLM and ultrasonic inspection. The hoop stress in the exchanger channel was computed as 28000 psi, which exceeds the allowable stress of 17500 psi. For safety concern, this exchanger channel should be replaced. It should be addressed that this is an approximate stress calculation. In fact, there exits a strength distribution within the hydrogen damaged wall of the heat exchanger channel. The determination of strength distribution within the wall is required for an accurate stress calculation to establish a criterion for fitness service evaluation.

In summary, hydrogen attack occurred in the heat exchanger channel (MPC-18), flange (MPC-19), and tube sheet (MPC-20) that had been operated in a condition below the Nelson Curve for C-0.5Mo steel. Hydrogen attack damage was quantitatively determined through the wall thickness of the heat

exchanger channel (MPC-18) and tube sheet (MPC-20). Consistent results were demonstrated by using UT inspection, metallographic evaluation, hydrogen determination, decarburization assessment, and hardness measurements. Hydrogen attack damage in different stages (methane bubbles and microcracks) was defined using SEM, methane determination, OLM, carbon and hardness measurements. A refined microstructure in the FGHAZ and low carbon weld metal enhanced the resistance to hydrogen attack.

4.1.2 MPC-9

4.1.2.1 Metallographic Evaluation

A section of a service exposed C-0.5Mo steel component, identified as MPC-9, was received from Shell Oil Company. The operating condition is not available. The wall thickness was measured as 2-11/16" (68.3 mm). The OD surface was machined and attested by the appearance of machined marks. Therefore, the original wall thickness and the OD surface condition are unknown. The chemical composition of MPC-9 is shown in Table 3.1. It is to be noted that the carbon content was determined at the OD location.

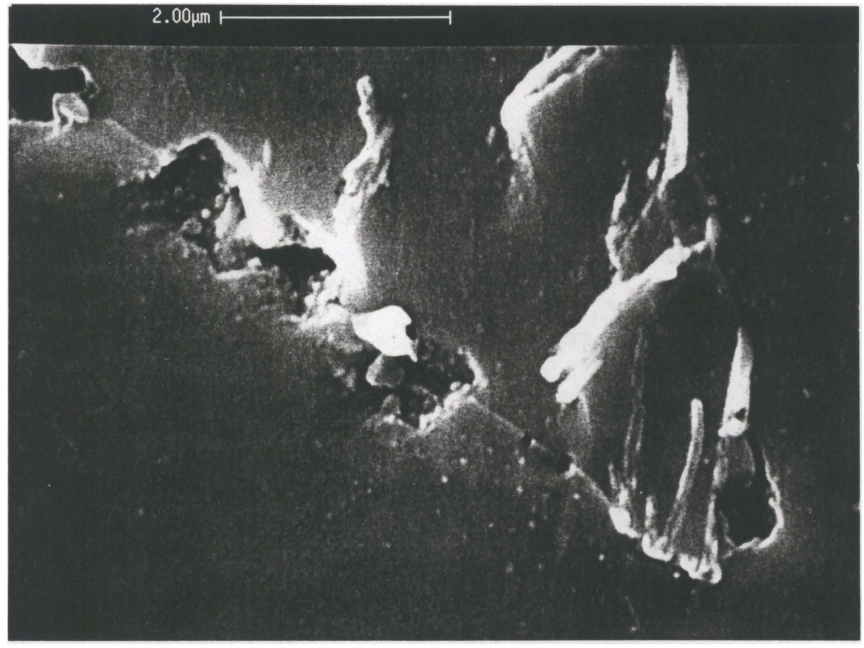
The microstructure of this service exposed heat is ferrite and bainite. Hydrogen attack damage was evaluated through wall thickness by using OLM and SEM. Hydrogen damage in terms of intergranular cracking along the ferrite/bainite (F/B), ferrite/ferrite (F/F) boundaries, and in the bainitic regions gradually decreases from the ID through the wall thickness. Internal

decarburization was observed adjacent to the damaged grain boundaries in the bainitic regions. A polished and etched specimen was examined using SEM. Figures.4.53 and 4.54 present typical SEM images of hydrogen damage between F/B interface and in bainitic region. Aligned and coalesced methane bubbles were observed at the leading edge of the primary crack. The smallest methane bubble size was determined as 0.06 μm at the F/B grain boundaries measured at a magnification of 15000X. In bainite region as shown in Figure 4.54, multiple bubbles initiated and coalesced along the bainitic sub-grain boundaries. Figure 4.55 presents typical SEM images of hydrogen damage along the F/F grain boundaries. Grain boundary carbides are evident in the bubbles at the triple point of the grain boundary intersection.

"Cryo-cracking" specimens were prepared for SEM examination through wall thickness. Figure 4.56 represents SEM images of hydrogen damage on the F/B grain boundaries. The hydrogen damage is characterized as intergranular separation (cracks) with bubbles and carbides on the grain boundaries, which can be distinguished from the cleavage fracture facets caused by low temperature fracture during sample fracture at liquid nitrogen temperature. The F/B grain boundary damage appears with dense and coarse carbides related to the methane bubbles. The carbide sizes are in the range of 0.1 ~ 1.0 μm and the bubble sizes were measured as in the range of 0.1 ~ 0.6 μm on this F/B boundary. Figure 4.57 shows the morphology of hydrogen damage on the F/F boundaries. Methane bubbles are evident on the F/F grain

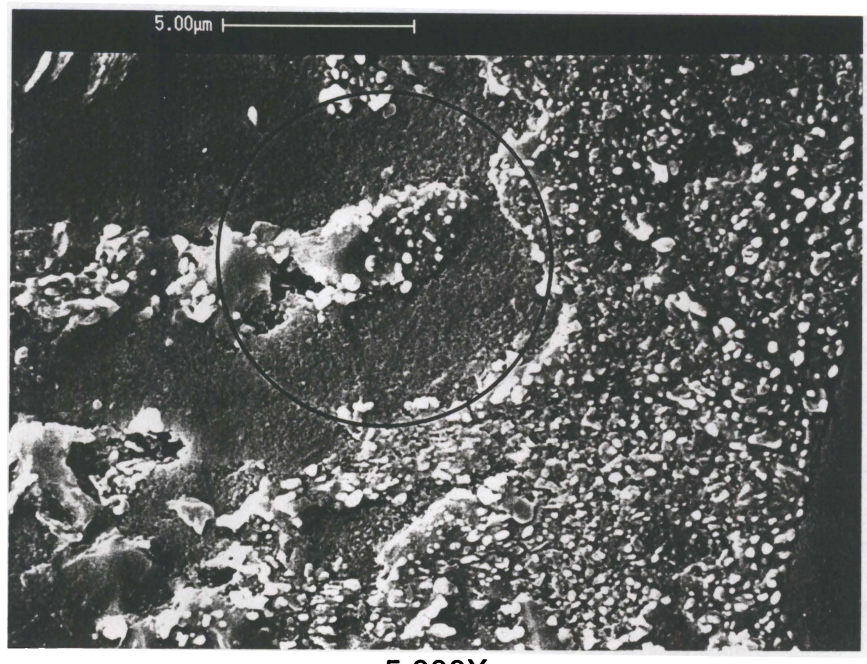


5,000X

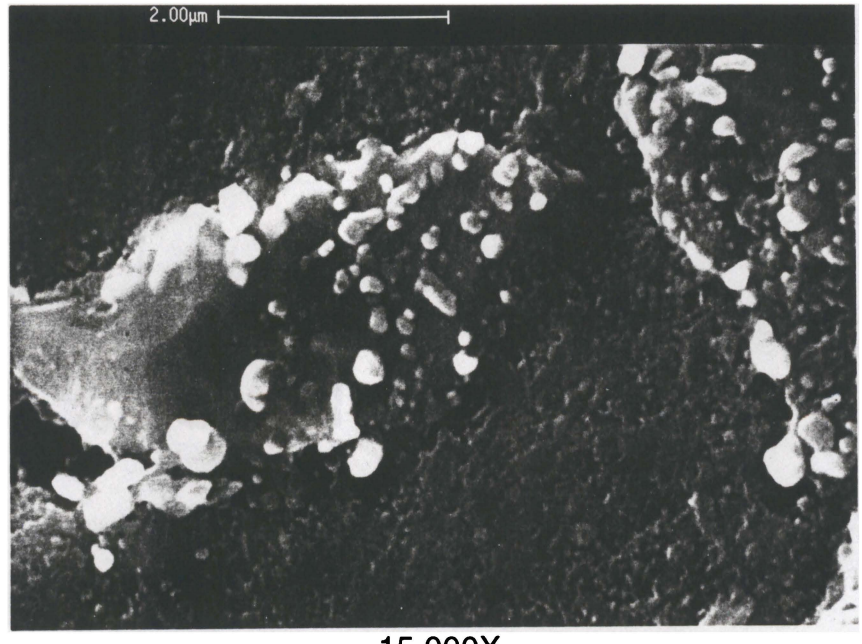


15,000X

Figure 4.53 Hydrogen attack crack and methane bubbles along F/B grain boundary (MPC-9).

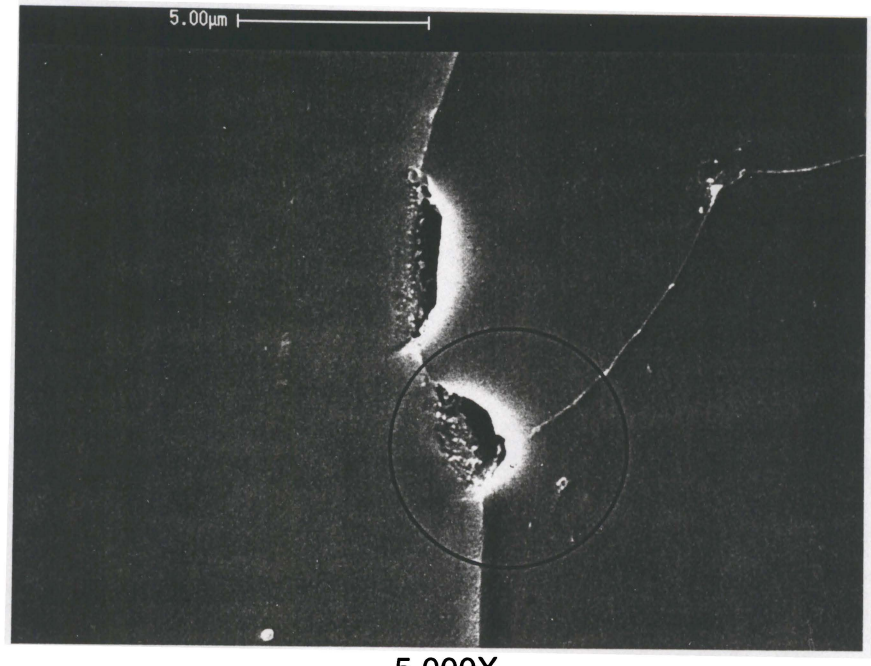


5,000X

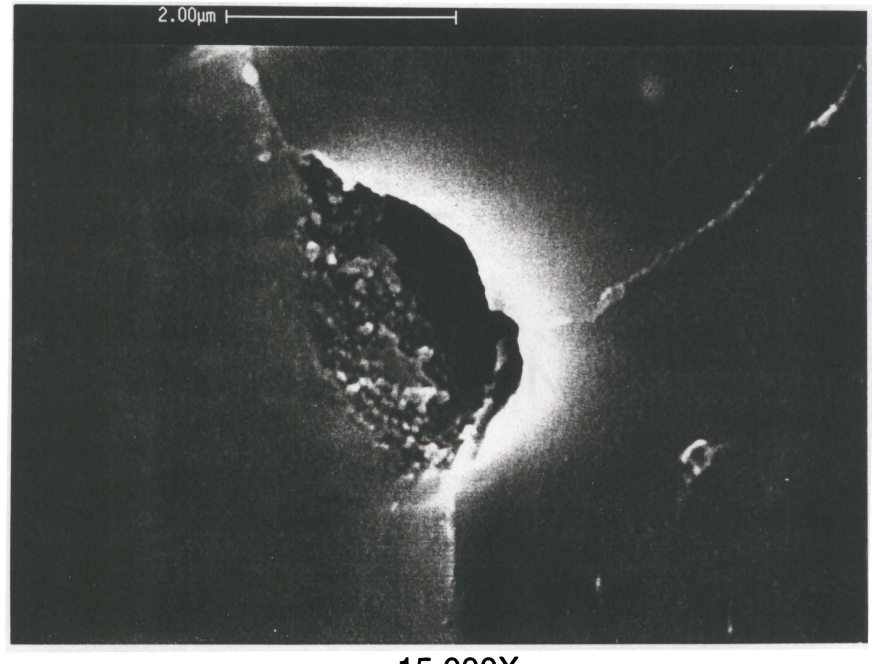


15,000X

Figure 4.54 Methane bubbles formed at sub-grain boundaries in bainitic region (MPC-9).



5,000X

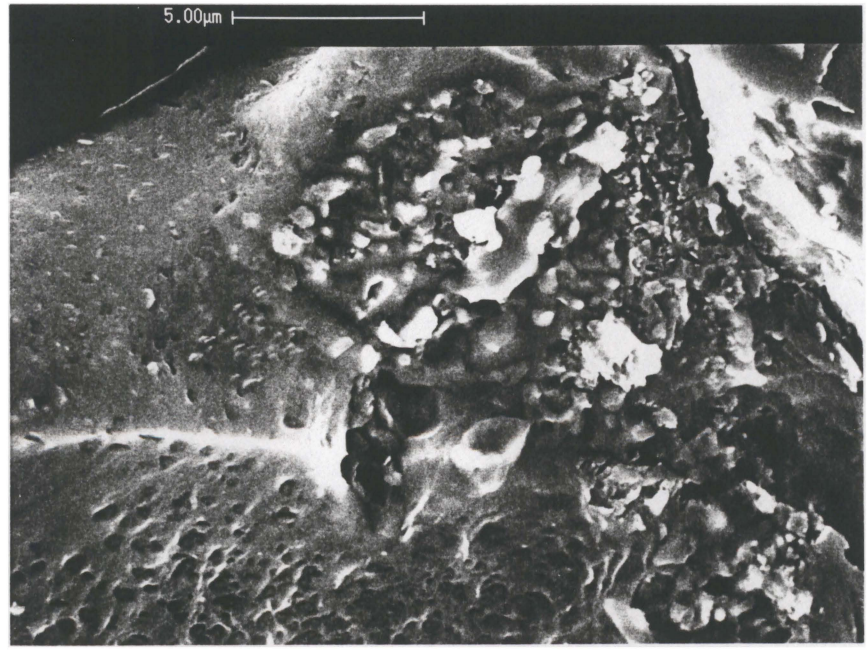


15,000X

Figure 4.55 Methane bubbles along F/F grain boundaries (MPC-9).

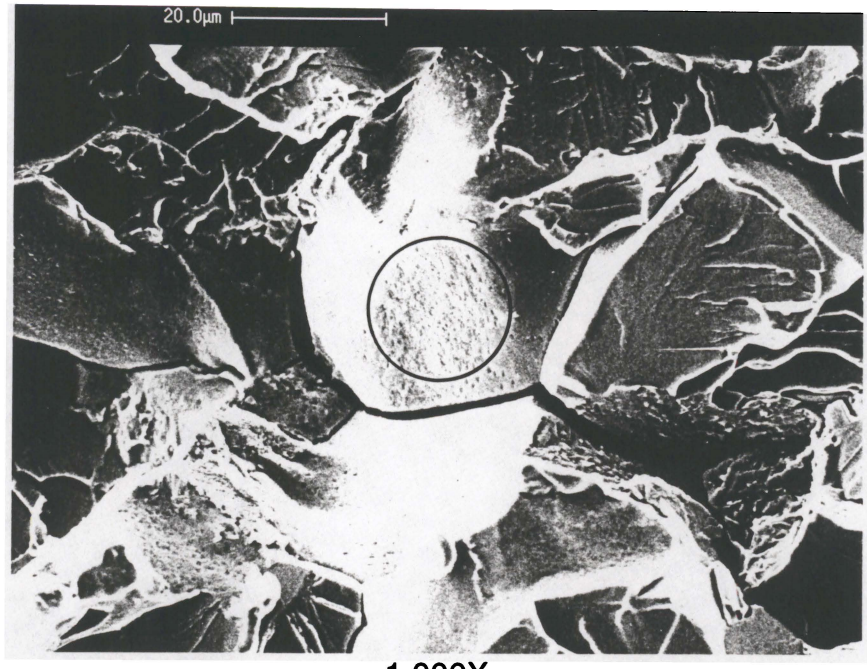


1,000X



5,000X

Figure 4.56 Typical SEM images of methane bubbles and carbides on F/B grain boundaries (MPC-9).



1,000X



5,000X

Figure 4.57 Typical SEM images of methane bubbles on F/F grain boundaries (MPC-9).

boundaries with less carbide remnants in comparison with the F/B boundaries.

4.1.2.2 Hydrogen Damage Quantification

Hydrogen attack damage was quantified through the wall thickness using OLM and SEM images. Figure 4.58 presents the profiles of the fraction of hydrogen damaged grain boundaries (FA% and FL%) through the wall thickness. The fraction of hydrogen damaged grain boundaries decreases in an exponential manner from the ID to the OD surface, which is caused by the differential of hydrogen pressure between the ID and the OD surfaces. Approximately 60% of the grain boundaries were damaged in the form of intergranular cracks and methane bubbles adjacent to the ID surface. Hydrogen damage extends through the entire wall thickness. The fraction of hydrogen damage determined by using SEM is consistent with the OLM results.

Methane bubble size (average diameter) was measured from the SEM images as a function of wall thickness. The bubble size and damaged grain boundary area for MPC-9 was superimposed on the database established from the examination of hydrogen attack in the heat exchanger (MPC-18, MPC-20, Figure 4.41) as shown in Figure 4.59. The bubble size was determined in the range of 0.10 to 0.45 μm at a magnification of 10,000X. The correlation of methane bubble size and the fraction of damaged grain boundary area for MPC-9 is accord with the results of MPC-18. With an increase in methane bubble size, the fraction of hydrogen attack damaged area increases. The SEM

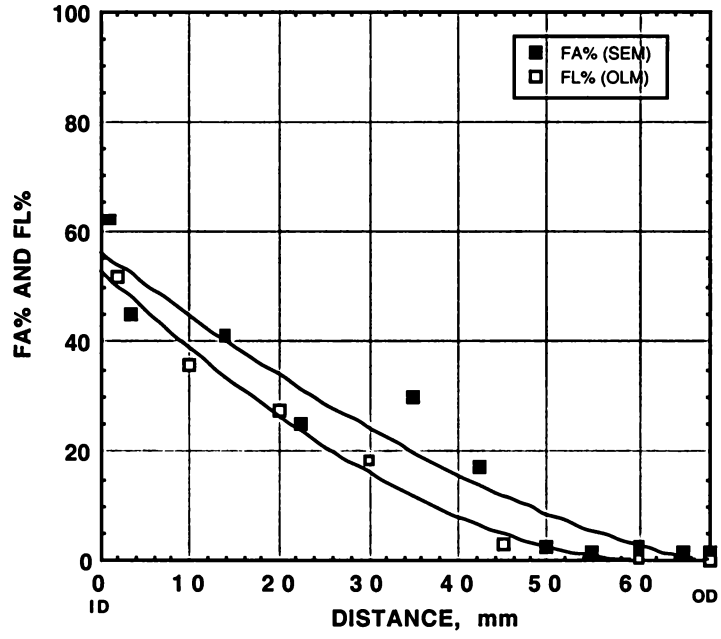


Figure 4.58 Hydrogen damage profiles (FA%, FL%) through wall thickness (MPC-9).

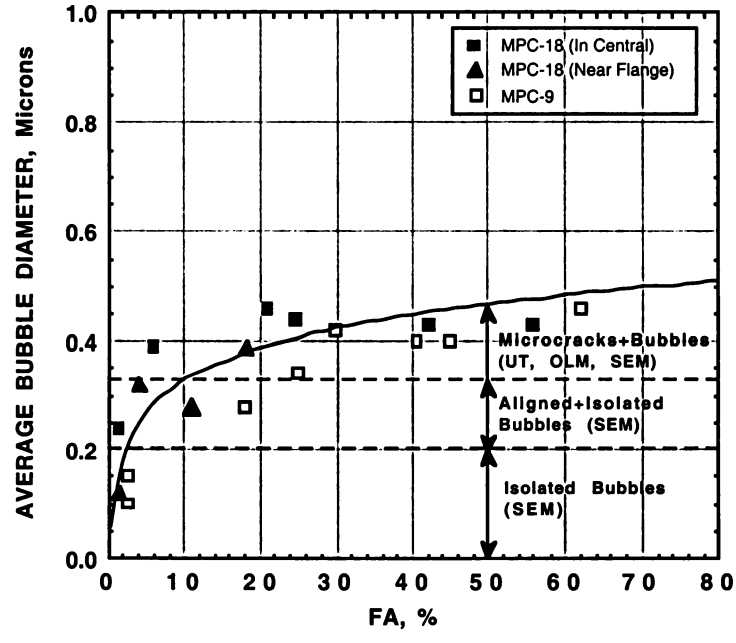


Figure 4.59 Correlation of methane bubble diameter and fraction of hydrogen damage (FA%, FL%, MPC-9, MPC-18).

examination demonstrated that hydrogen damage is in the form of isolated bubbles when the damaged area fraction is approximately less than 3%. Methane bubble coalescence to form cracks was observed when the fraction of damaged grain boundary area is approximately greater than 10%.

Methane concentration was determined for the locations near the ID and OD surface. The methane contents are 420 ppm and 2 ppm corresponding to the damaged grain boundary area of 62% and 2%, respectively. These data satisfy with the relationship of hydrogen damage and hydrogen content as shown in Figure 4.60.

4.1.2.3 Carbon Concentration

Figure 4.61 presents the carbon concentration and the decarburization index profiles through the wall thickness (68 mm). The depth of decarburization extended approximately 30 mm from the ID surface, which is less than the maximum depth of hydrogen damage determined by using OLM (60 mm) and SEM (68 mm). Therefore, the decarburization index has less resolution than the metallographic techniques such as OLM and SEM "Cryo-cracking".

In summary, hydrogen attack damage in MPC-9 was characterized as methane bubble initiation, growth, coalescence, and cracking along F/F and F/B grain boundaries and bainitic sub-grain boundaries. Internal decarburization was observed in bainitic region. Hydrogen attack damage was quantified through the wall thickness using OLM and SEM image analysis. The results of

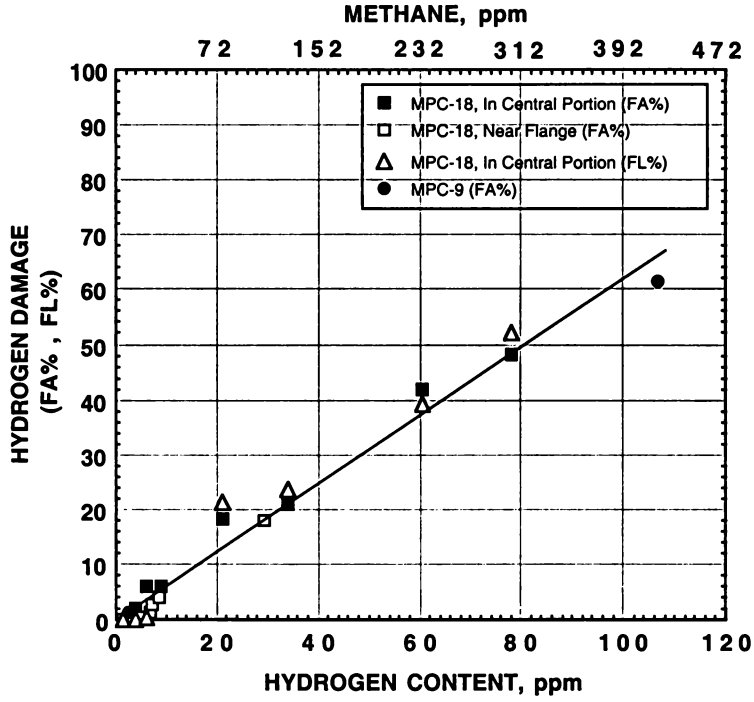


Figure 4.60 Relationship of hydrogen attack damage (FA%, FL%) and methane content (or hydrogen content, MPC-9; MPC-18).

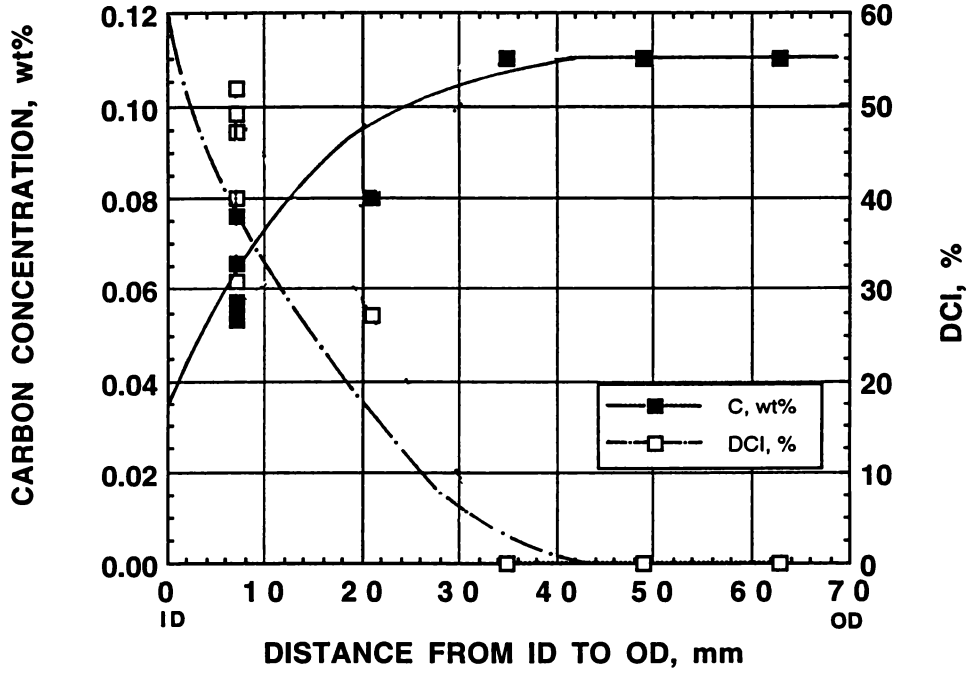


Figure 4.61 Profiles of carbon concentration and decarburization index (DCI%) through wall thickness (MPC-9).

hydrogen damage determined by using both SEM and OLM are consistent. Hydrogen damage is extensive near the ID with the fraction of damaged grain boundaries of 62% and decreases toward the OD. The maximum depth of hydrogen attack damage was determined as 60 mm from the ID surface using OLM. SEM "Cryo-Cracking" technique shows that hydrogen attack damage occurs through the entire wall thickness. As anticipated, the resolution for SEM is greater than OLM for hydrogen damage examination. The average bubble diameter increases with an increase in the fraction of damaged grain boundary area (FA%). SEM examination demonstrated that hydrogen damage is in the form of isolated bubbles when the damaged area fraction was approximately less than 3%. Methane bubble coalescence to form cracks was observed when the fraction of damaged area was approximately greater than 10%. Decarburization was evident near the ID and gradually decreased toward the OD. The maximum decarburized depth was determined to be approximately 30 mm from the ID.

4.1.3 MPC-11

4.1.3.1 Ultrasonic Inspection

The MPC-11 material was extracted from a service exposed heat exchanger shell with 5/8" (16 mm) thick wall. Chemical composition of MPC-11 is presented in Table 3.1. The carbon content and Mo/C of MPC-11 material are 0.18%C and 2.67, respectively. This heat exchanger shell was operated at

a temperature 670°F and a hydrogen partial pressure 290 psi for approximately 22 years.

Ultrasonic inspection was implemented in an area of 4"x3" for hydrogen damage. Figures 4.62 is a 3-D presentation of the C-scan image of the scanned area. It is evident that hydrogen damage is detectable in the entire scanned area. A zoom view with digital index numbers as shown in Figure 4.63 indicates that the major reflections came from a depth of 0.4" from the OD surface. Therefore, the depth of hydrogen damage is approximately 0.25" from the ID. Figure 4.64 shows the B-scan images in which hydrogen damage profiles are revealed in cross section.

4.1.3.2 Hydrogen Damage Quantification

Hydrogen attack damage was defined through the wall thickness by quantitatively metallographic analysis. Hydrogen content dissociated from methane was determined using gas chromatography. Figure 4.65 shows a cross section of the sample with a fillet joint attached on the OD surface. Hydrogen attack damage is macrographically evident in the form of segregation related cracks. In this photomacrograph, hydrogen attack cracks penetrated to a depth of 0.25" from the ID surface, which is consistent with the depth detected by ultrasonic testing.

The hydrogen attack cracking is characterized as intergranular cracks along segregation rolling bands. Internal decarburization was observed as

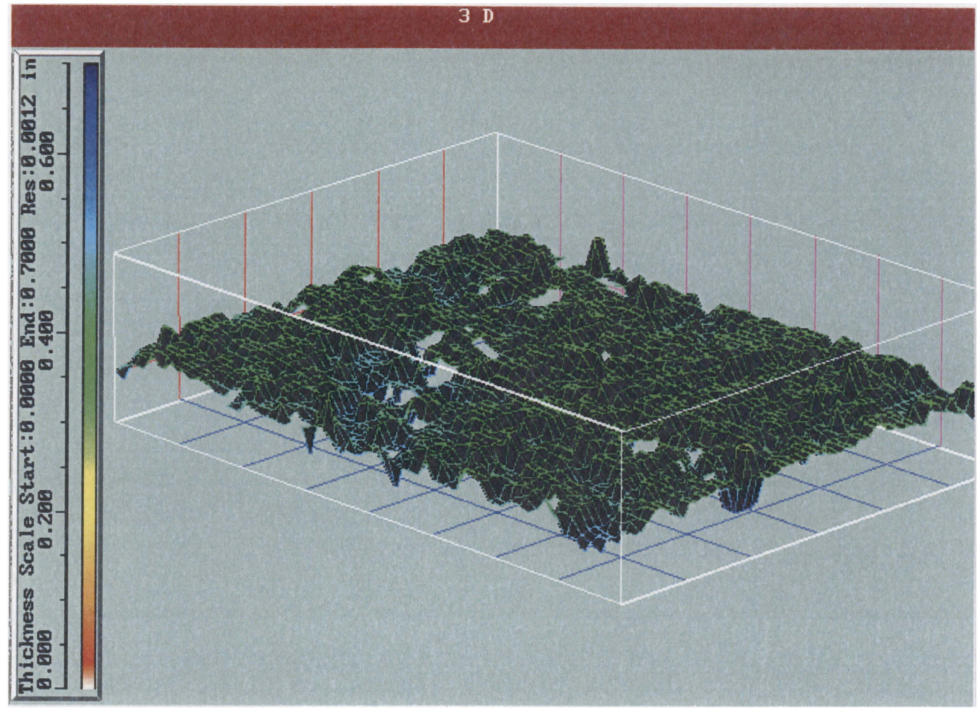


Figure 4.62 3-D presentation of ultrasonic testing C-scan image of hydrogen damage (MPC-11).

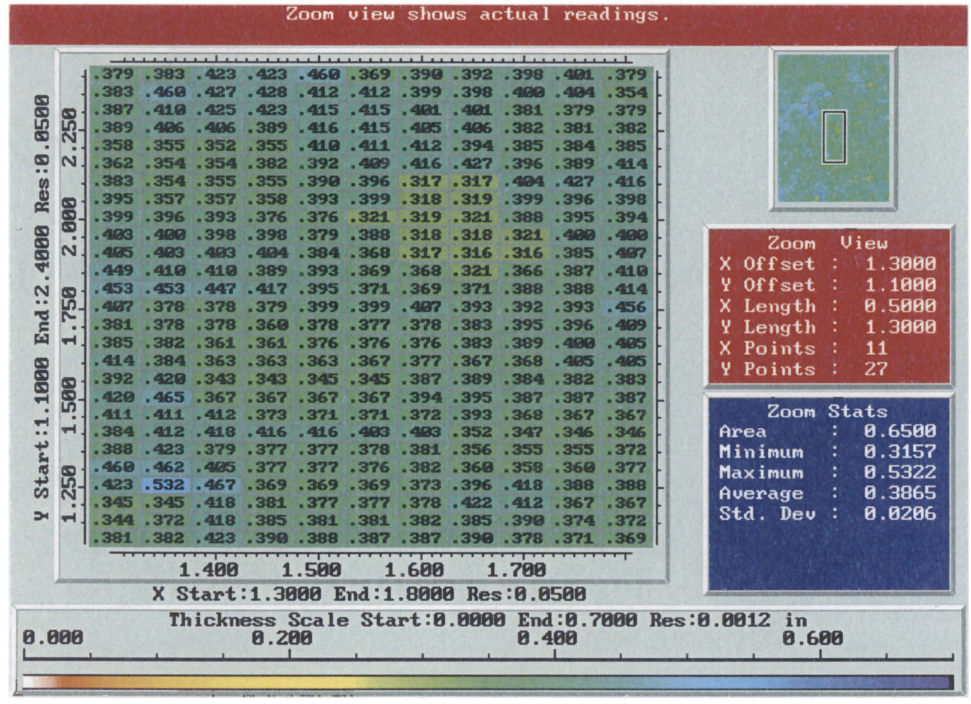


Figure 4.63 Numerical index of the reflection depth from OD surface in a zoom view area (MPC-11).

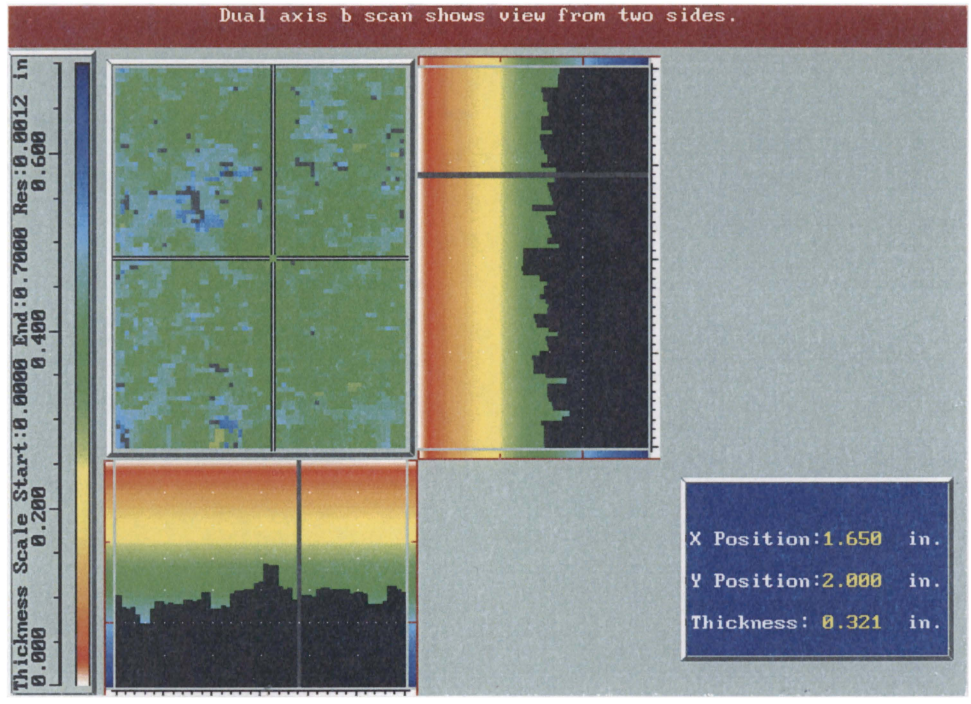
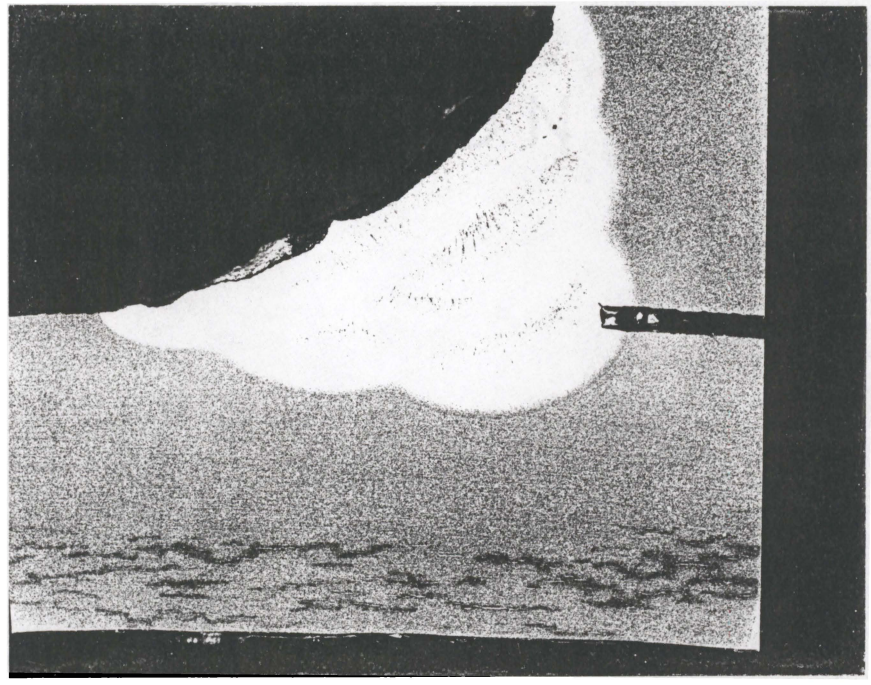


Figure 4.64 Ultrasonic testing B-scan images of hydrogen damage in two cross sections (MPC-11).



3X

Figure 4.65 Hydrogen attack cracks in the heat exchanger shell material (MPC-11).

shown in Figure 4.66. Extensive damage occurred near the ID surface and gradually decreased toward the OD surface. Quantitative image analysis was implemented through the wall thickness as shown in Figure 4.67. The fraction of hydrogen damaged grain boundaries is approximately 13% adjacent to the ID surface. The maximum depth of the damage was determined as approximately 11 mm (0.4") according to metallographic examination.

Methane content was determined at four locations through the wall. The methane contents are 48.0, 20.0, and 4.4 ppm (hydrogen content: 14.0, 7.0, and 3.1 ppm) corresponding to the values of the damaged grain boundary fraction of 11.0%, 0.5%, 0.8%, respectively. These data are superimposed on Figure 4.60 in which the correlation between hydrogen attack damage and methane content is established. Figure 4.68 presents the updated plot to show the relationship of hydrogen damage and methane content.

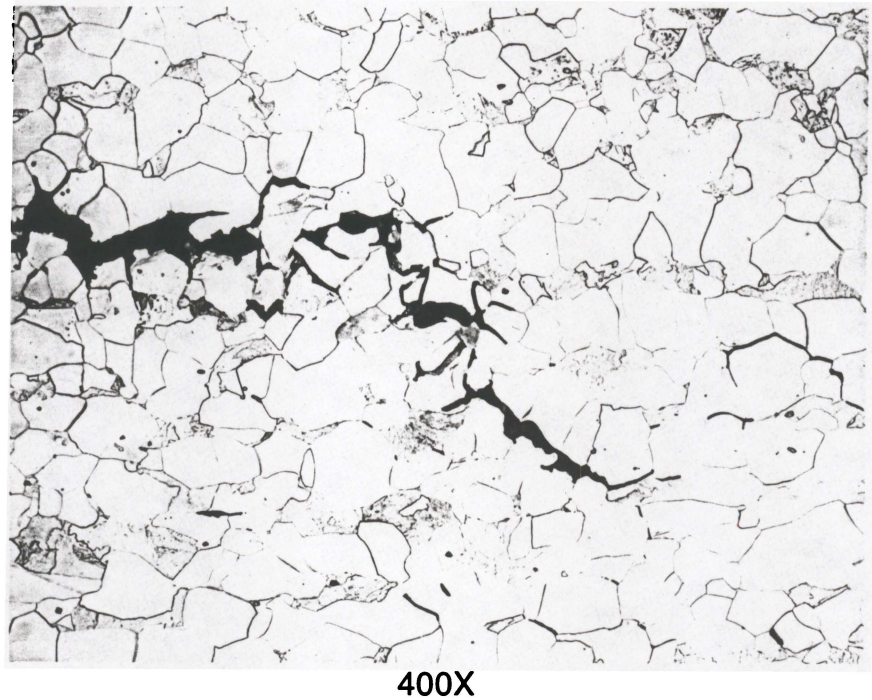
Linear curve fitting was implemented for Figure 4.68 and an experimental equation expresses the fraction of hydrogen damaged grain boundaries (FA% or/and FL%) as a function of hydrogen content:

$$\text{FA\% or/and FL\%} = 0.66\, C_{H2} - 1.32$$

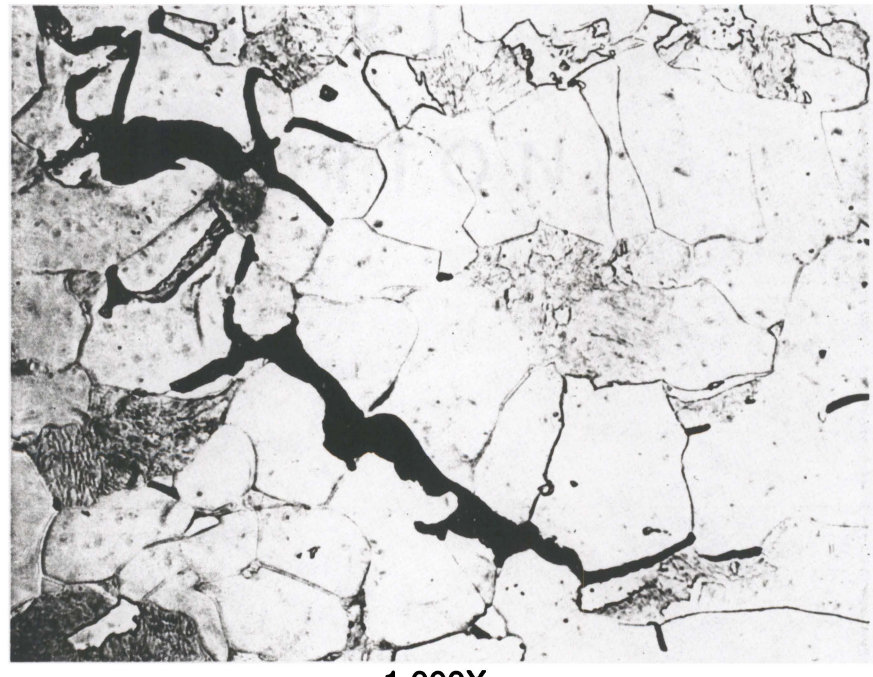
where C_{H2} is total measured hydrogen in ppm. In accord with the relationship of Methane (C_{CH4}, ppm) and hydrogen:

$$C_{CH4} = 4\,(C_{H2} - 2)$$

The correlation between the fraction of hydrogen damaged grain boundaries (FA% or/and FL%) can be expressed as



400X



1,000X

Figure 4.66 Hydrogen attack cracks and internal decarburization in MPC-11.

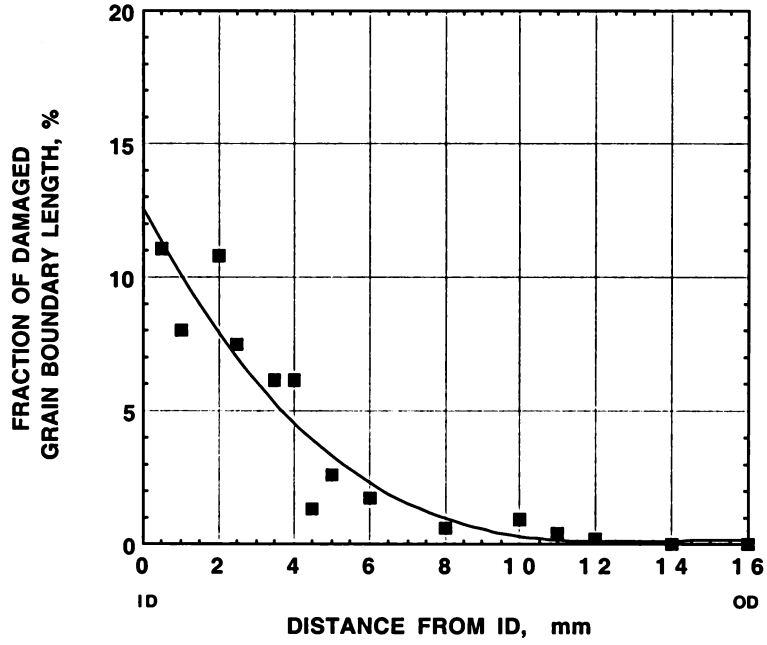


Figure 4.67 Hydrogen damage profile (FL%) through wall thickness (MPC-11).

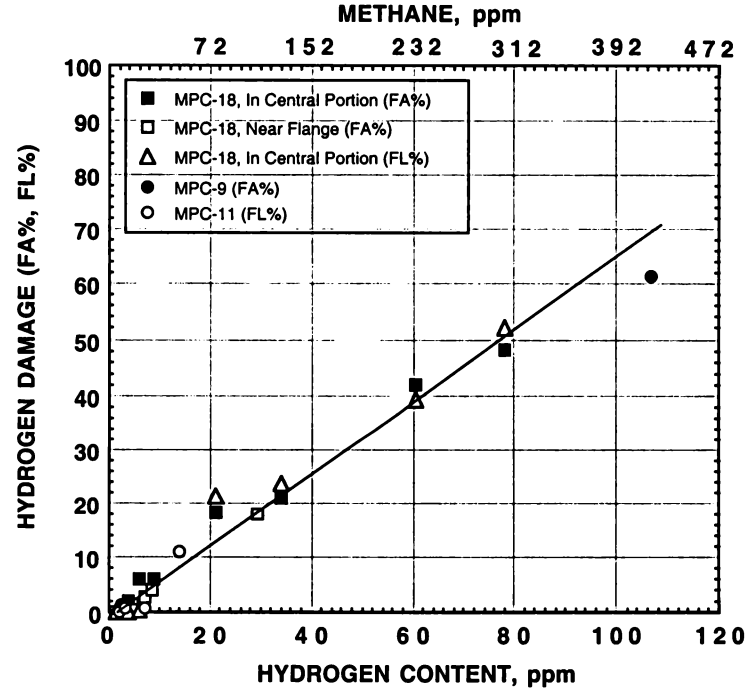


Figure 4.68 Relationship of hydrogen attack damage (FA%, FL%) and methane content.

$$FA\% \text{ or/and } FL\% = 0.17\ C_{CH4}$$

These equations can be applied to determine hydrogen attack damage by hydrogen measurement using a relatively small sample.

4.1.4 MPC-21 and MPC-22

MPC-21 and MPC-22 materials were extracted from another heat exchanger channel and tube sheet provided by Equilon Enterprises LLC (Shell and Texaco Oil Companies) for hydrogen damage evaluation. The heat exchanger channel (MPC-21) was postweld heat treated at 1160°F for 3 hours before service. The wall thickness is 1-1/8" (28.6 mm) for the exchanger channel and 3-7/8" (98.4 mm) for the tube sheet. The operating temperature and hydrogen partial pressure are 530°F and 950 psi for the heat exchanger channel (MPC-21) and 500°F and 950 psi for the tube sheet (MPC-22). Both the heat exchanger channel and tube sheet had been operated for 28 years before they were replaced. It is to be noticed that the operating temperature and hydrogen partial pressure is below the Nelson Curve for C-0.5Mo steel (on the carbon steel Nelson Curve) as shown in Figure 4.1. The chemical composition of MPC-21 and MPC-22 is presented in Table 3.1. Hydrogen attack damage was evaluated using UT, OLM, SEM, and hydrogen measurements.

Hydrogen attack damage was not detected for either exchanger channel (MPC-21) or tube sheet (MPC-22) using ultrasonic testing and OLM (1000X).

Methane determination on the exchanger channel shows that the maximum methane concentration was determined as approximately 8 ppm near the ID surface and decreased toward the OD as presented in Figure 4.69. The methane concentration is about 0 to a depth of 12 mm from the ID surface. In accord with the correlation of hydrogen damage and hydrogen content as shown in Figure 4.68, it is suggested that hydrogen attack should have occurred in a depth of 12 mm from the ID. Furthermore, the hydrogen damage should be in the form of methane bubbles based on the correlation of hydrogen damage and methane bubble size as presented in Figure 4.59. The fraction of hydrogen damaged grain boundaries was estimated at less than 2% near the ID surface in MPC-21 in accord with the experimental equation of hydrogen damage as a function of methane.

SEM was used for hydrogen damage examination in the exchanger channel material (MPC-21) and tube sheet (MPC-22). Hydrogen damage was observed in the form of isolated bubbles in both MPC-21 and MPC-22 materials. Figures 4.70 and 4.71 presents typical SEM images from the polished and "Cryo-cracking" samples to show the methane bubbles at the interface of carbides and ferrite and on the grain boundary in the exchanger channel material (MPC-21). The fraction of hydrogen damaged grain boundary length was determined as 1.8% using quantitative image analysis which is consistent with the computed result (< 2%).

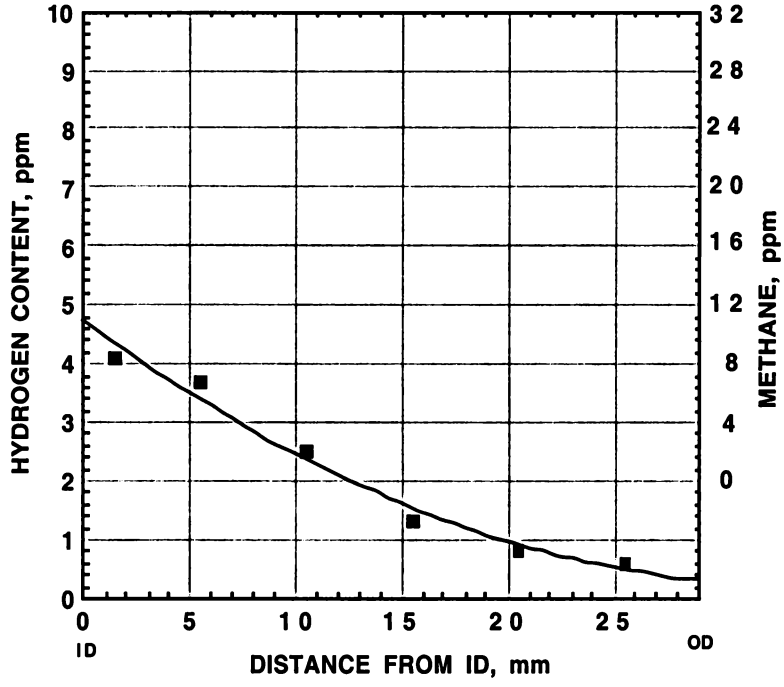
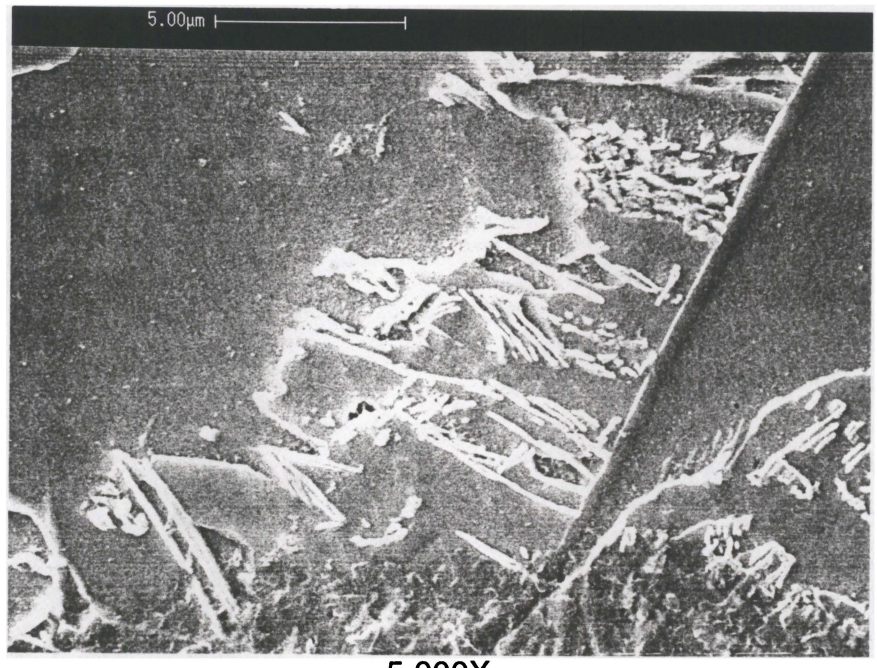


Figure 4.69 Methane concentration through the wall thickness of heat exchanger channel (MPC-21).

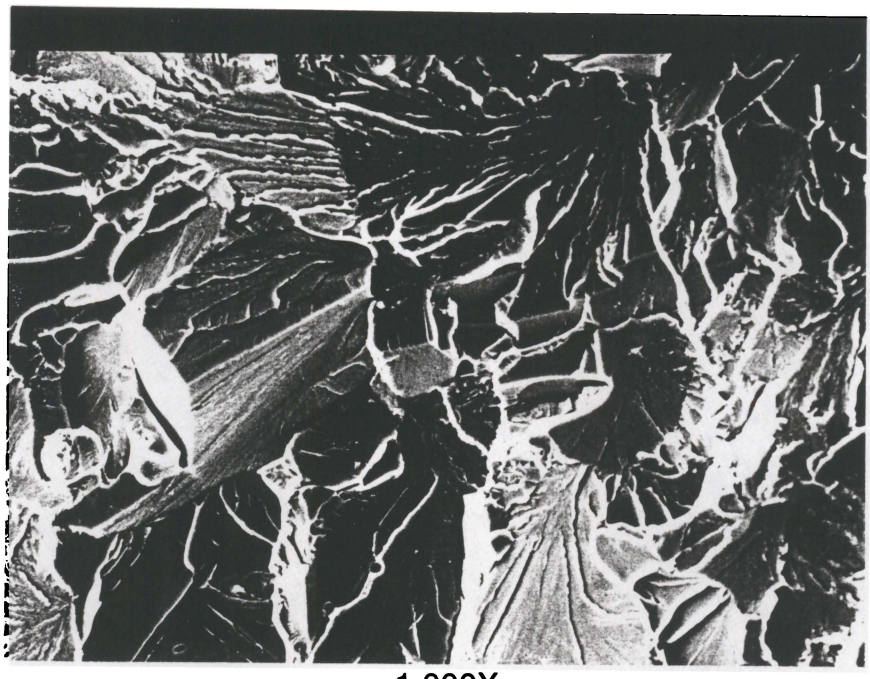


5,000X

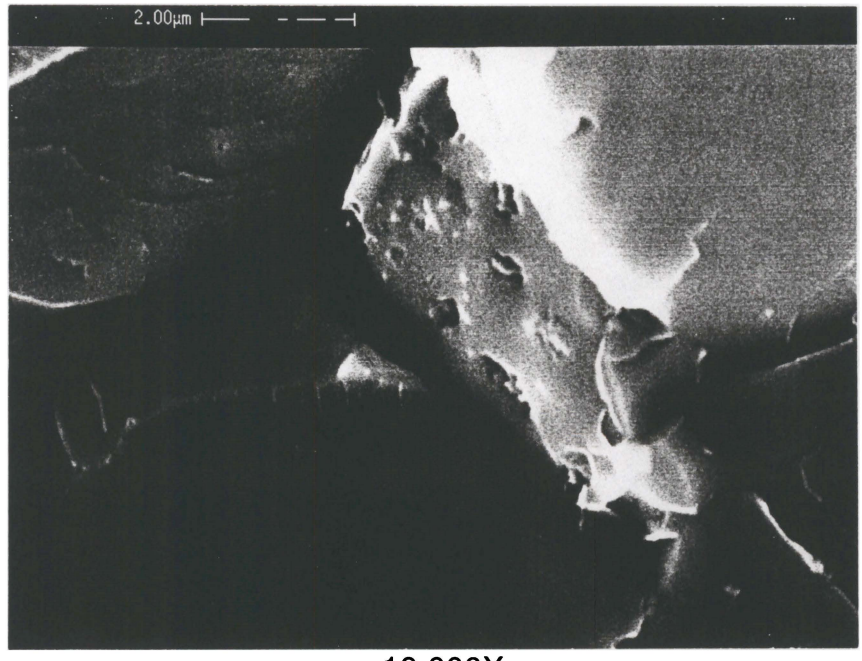


20,000X

Figure 4.70 Methane bubbles at the interface of carbides and ferrite matrix (MPC-21).



1,000X



10,000X

Figure 4.71 SEM images of hydrogen attacked grain boundary in the tube sheet (MPC-22).

In summary, hydrogen attack was not found in the heat changer channel (MPC-21) and tube sheet (MPC-22) by using both ultrasonic testing and OLM since their delectability limitation. However, the occurrence of hydrogen damage in the exchange channel (MPC-21) was predicted by using methane determination and the correlation of damage and methane content. Hydrogen damage was demonstrated in the exchanger channel (MPC-21) and tube sheet (MPC-22) by using SEM on the polished and etched samples and the "Cryo-cracking" samples. Hydrogen attack damage is in the form of isolated bubbles with a low level of damage. The fraction of hydrogen damage grain boundaries was determined as less than 2% near the ID surface of the exchanger channel. Therefore, SEM is required for the examination of minimal hydrogen damage.

4.1.5 MPC-26 and MPC-27

A boat sample was received from Koch Petroleum Group, Corpus Christi Refinery. The boat sample was removed from the inside surface of C-0.5Mo pressure vessel with 410 stainless steel cladding. The boat sample contained a girth weld. This pressure vessel was operated at 700°F and 500 psi hydrogen partial pressure for approximately 25 years. The operating condition is below the Nelson Curves for C-1/2Mo as shown in Figure 4.1.

The dimensions and photomacrograph of the boat sample are presented in Figures 4.72 and 4.73. Sides A and B are designated as MPC-26 and MPC-27 to distinguish each side of the material in the boat sample with a weld.

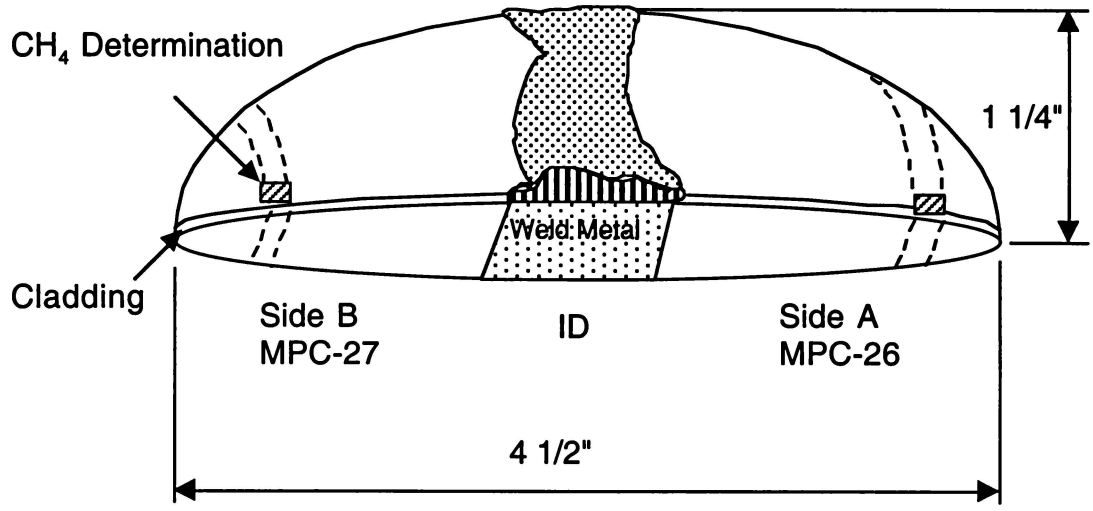
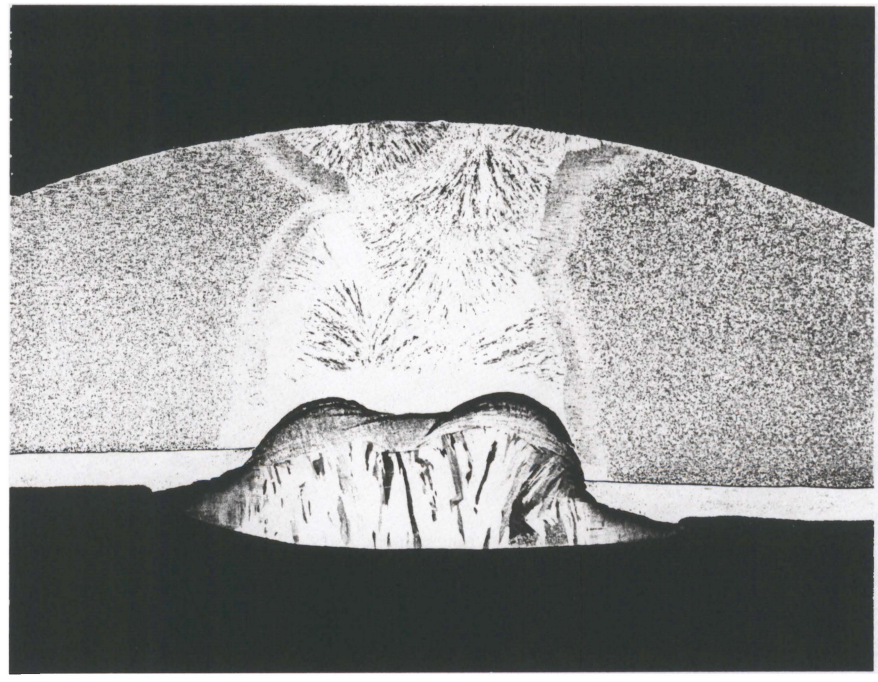


Figure 4.72 Schematic of the boat sample for hydrogen damage evaluation (MPC-26 and 27).



2.7X

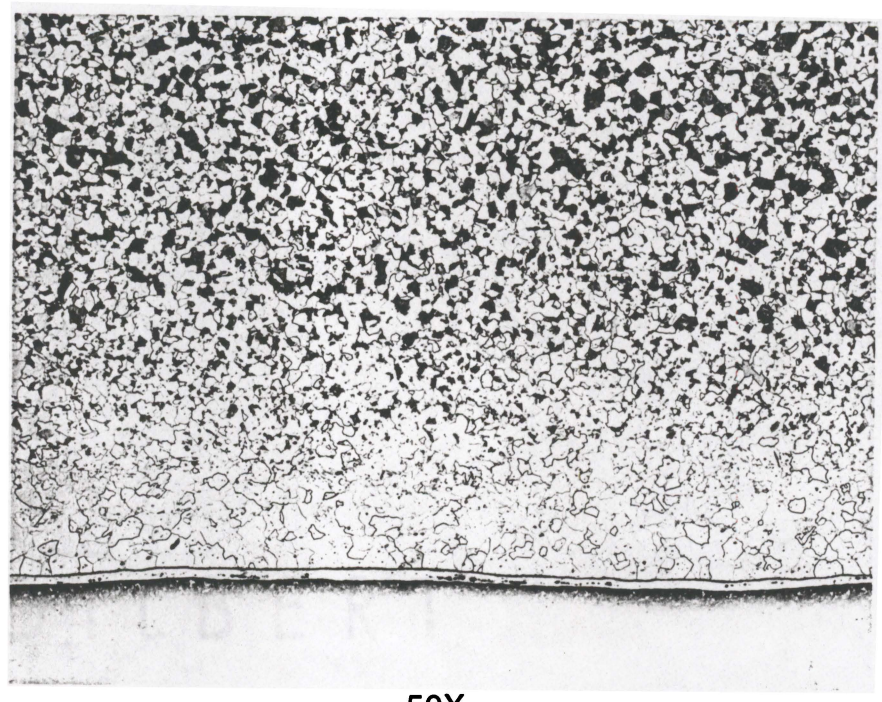
Figure 4.73 Cross section of the boat sample with 410 stainless steel cladding.

Samples were extracted for chemical analysis, metallographic examination, and hydrogen determination.

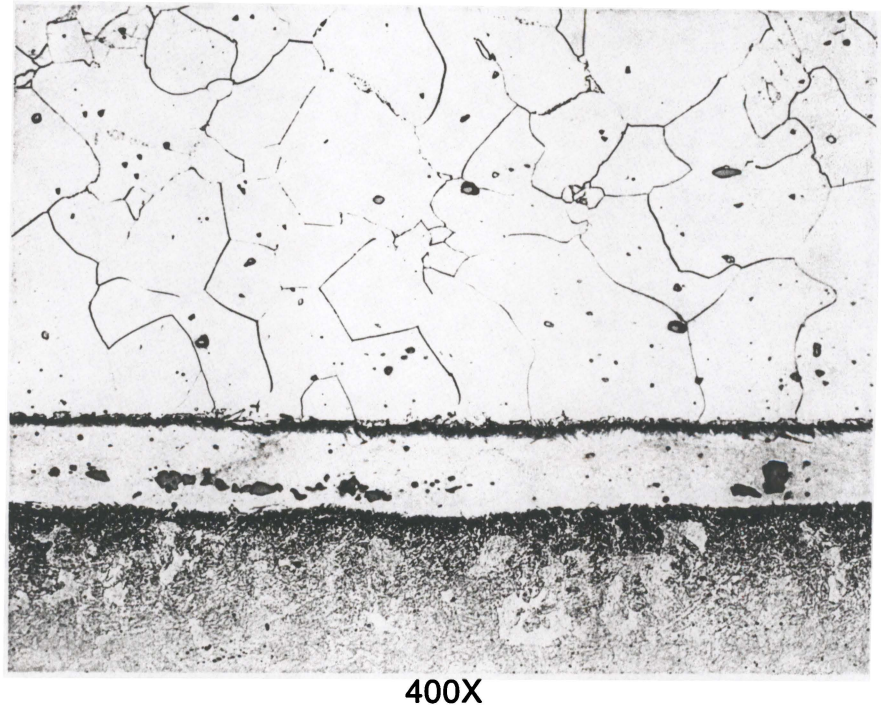
Chemical composition of C-1/2Mo material at both sides of the boat sample is presented in Table 3.1. The chemical composition is similar for both sides of the weld with Mo/C of 2.08 and 2.04 for MPC-26 and MPC-27, respectively.

Metallographic examination was implemented using OLM and SEM. Figure 4.73 shows the transverse section of the boat sample weld. The thickness of the 410 stainless steel cladding was determined as 2 mm for both sides. The weld metal of the ID cap pass is different from the weld metal under the cap pass revealed by different etching effects using Vilella's enchant. An interlayer is observed between the 410 stainless steel cladding and C-0.5Mo steel as shown in Figure 4.74. The interlayer is approximately 30 μm thick and was identified as Ni using EDS. A complete decarburized region occurred in the C-0.5Mo material adjacent to the interface. The depth of the complete decarburized region is approximately 40 μm. Remote from the decarburized region, the microstructure is a mixture of ferrite and bainite.

Hydrogen attack damage in terms of isolated methane bubbles was observed in the partially decarburized region of MPC-27, which is approximately 40-80 μm from the interface of interlayer and C-0.5Mo. Figures 4.75 and 4.76 show the methane bubbles at the F/B and F/F boundaries by using SEM. The average

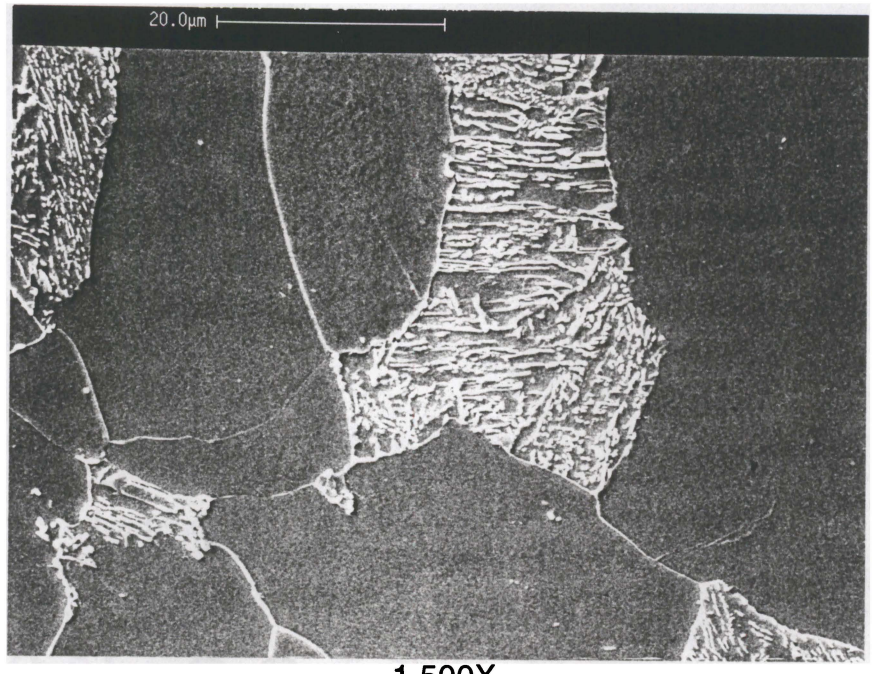


50X



400X

Figure 4.74. Completely decarburized region adjacent to the interfaces between Ni interlayer and C-0.5Mo steel (MPC-27).

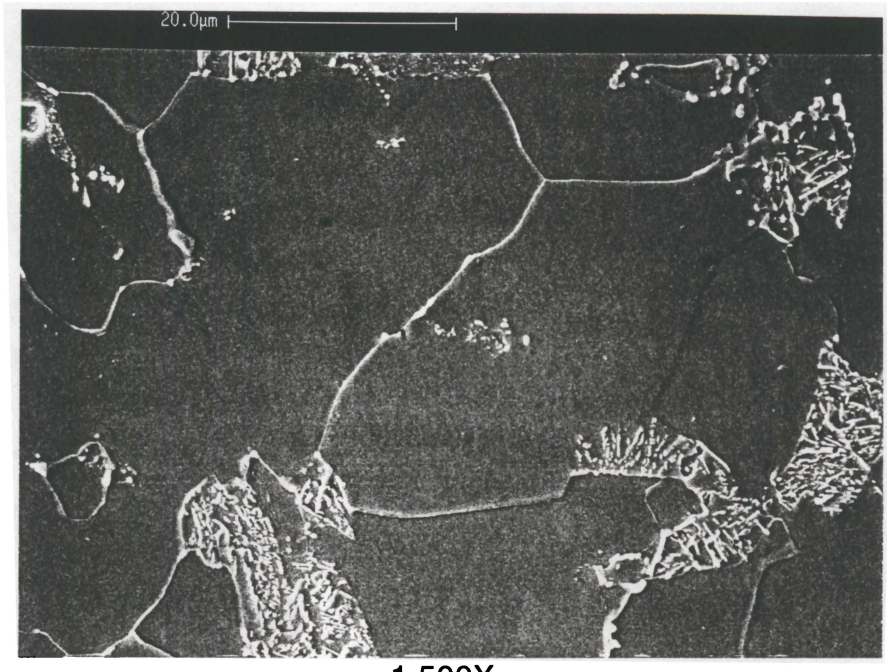


1,500X

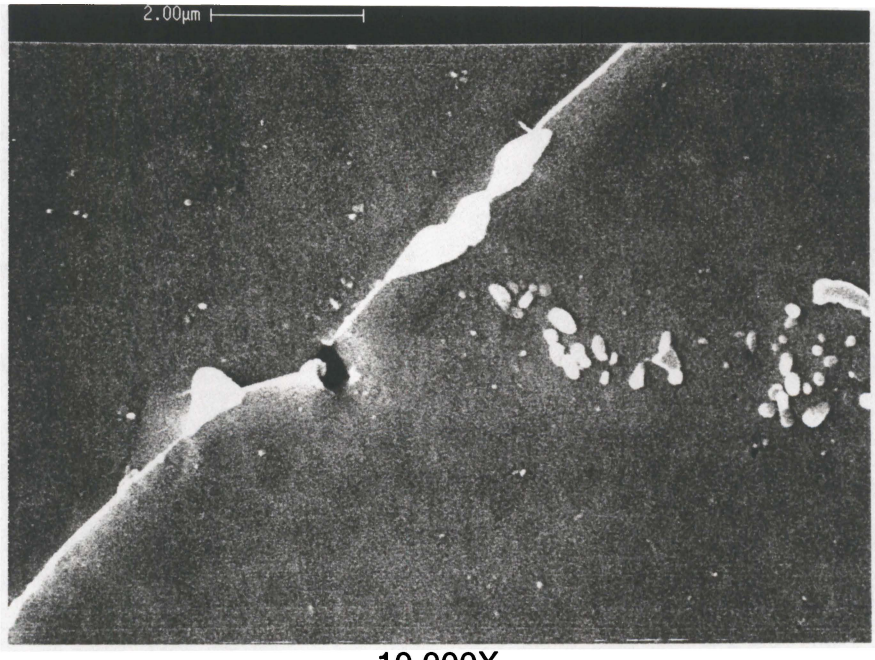


10,000X

Figure 4.75 Isolated methane bubbles at F/B boundary in MPC-27.



1,500X



10,000X

Figure 4.76. Isolated methane bubble at F/F boundary in MPC-27.

methane bubble diameter was determined as 0.2 μm. The fraction of damaged grain boundaries is approximately 1%. No methane bubbles were found in the completely decarburized region. Hydrogen attack damage was not observed in the weld metal and MPC-26 at a magnification of 10,000X. Hydrogen measurements were implemented by using gas chromatography. Samples were extracted from the C-0.5Mo material adjacent to the interface between the Ni interlayer and C-0.5Mo steel. The hydrogen contents for MPC-26 and MPC-27 were determined as 1 ppm and 2 ppm, respectively. The hydrogen content in MPC-27 is equal to the critical hydrogen content (2 ppm) for hydrogen attack as defined in the early sections of this theory.

In conclusion, minor hydrogen attack damage in terms of isolated methane bubbles was found in MPC-27. Hydrogen attack was not found in the weld metal and MPC-26 material.

4.1.6 Summary of Service Exposed Component Evaluation

24 heats of service exposed C-0.5Mo steel were received from petroleum refineries for evaluation of hydrogen attack damage. Hydrogen damage was found in 9 heats (MPC-9, 11, 15, 18, 19, 20, 21, 22, and 27) out of the 24 service exposed heats using ultrasonic testing and metallographic examination. In accord with the available operating conditions, the hydrogen damaged heats were operated below the Nelson Curve of C-0.5Mo steel with the exception of MPC-15 which was at the Nelson Curve.

Ultrasonic testing revealed hydrogen attack damage in the base metal of heat exchangers (MPC-18 and 11). Maximum depths of the hydrogen damage were defined as 0.5" for MPC-18 (1" thick) and 0.33" for MPC-11 (0.625" thick) from the ID surfaces in accord with the UT imaging. Hydrogen damage was not found in the long seam weld metal (MPC-18), MPC-21 and MPC-22 materials using ultrasonic testing.

OLM examination substantiated the UT results in terms of maximum depth of hydrogen damage. Hydrogen attack cracking was observed in the base metal and the CGHAZ of the heat exchanger channel (MPC-18). Hydrogen damage was significantly lesser in the fine grained HAZ region (FGHAZ) with a maximum damage depth of 0.039" from the ID surface in comparison with the base metal (0.5") and the CGHAZ (0.2") for the same exposure condition. Hydrogen attack cracking was found at the ID in the CGHAZ and was terminated by the overlapped regions where the initial coarse grains were refined by the following welding thermal cycle. It is noteworthy that hydrogen damage was not found in the weld metal with low carbon content (0.053%) even though extensive hydrogen damage occurred in the base metal (FA%~60% near the ID) and the CGHAZ (MPC-18).

The fractions of damaged grain boundary area (FA%) and grain boundary length (FL%) were denoted to quantify the hydrogen damage by using quantitative metallographic analysis. The extent of the hydrogen damage is extensive in proximity to the ID surfaces and decreases within the wall. The

fraction of the damage grain boundaries at the ID surface is in the range of 1% (MPC-27) to 60% (MPC-18 and 9) for the 9 damaged heats. The progression of hydrogen attack in terms of methane bubble nucleation, growth, coalescence, and cracking was revealed by the examination through the walls.

The SEM "Cryo-cracking" technique was demonstrated to be a unique method for hydrogen damage evaluation (FA%) and methane bubble size determination. As anticipated, SEM is required for minor hydrogen damage definition in the form of isolated and aligned methane bubbles. A correlation of the bubble size and the fraction of damaged boundaries was established. The average bubble diameter increases with increase in the fraction of damaged grain boundaries. Only isolated bubbles were observed when the fraction of damaged grain boundaries was less than 3%. When the hydrogen damage is greater than 10%, methane bubbles coalesced to form microcracks.

Methane concentration was determined by hydrogen measurements in the service exposed samples using gas chromatography and checked by the Leco vacuum fusion method. The methane gas in the bubbles and cracks is completely dissociated into hydrogen by heating a sample encapsulated in a quartz tube to 700°C (1290°F) for 72 hours. Recall that methane (ppm) is 4 times of the dissociated hydrogen (ppm). The profiles of the methane concentration through wall demonstrates that the methane concentration is greatest adjacent to the ID surface and decreases through the wall of the service exposed components. The methane concentration profile is similar to

the metallographic damage profiles (FA% and FL%). The cut-off hydrogen damage / no hydrogen damage was determined as 2 ppm hydrogen below which hydrogen damage was not found.

It is to be noted that below the 2 ppm hydrogen level there is a residual in un-exposed hydrogen content. This in effect indicates that the hydrogen attack damage producing methane is "0" when the measured hydrogen is below 2 ppm. It was demonstrated that the hydrogen content in the un-exposed materials was measured as approximately 2 ppm, which was considered to be the hydrogen in solution and traps (not from dissociated methane). Therefore, methane can be determined by hydrogen measurement (ppm):

$$C_{CH4} \text{ (ppm)} = 4 (C_{H2} - 2)$$

If the calculated C_{CH4} is less than zero, it is to be considered that there is no methane in materials.

A relationship between hydrogen damage and methane content (ppm) was established as:

$$\text{FA\% or/and FL\%} = 0.17\ C_{CH4}$$

These two equations can be used to determine the hydrogen damage by methane determination using a small amount of materials.

Decarburization and reduction in hardness were observed in the hydrogen damaged regions in comparison with un-damaged region. As anticipated, the measurement of carbon content and hardness are less sensitive than OLM and SEM for hydrogen damage evaluation.

4.2 Evaluation of Hydrogen Attack in Autoclave Exposed Samples

4.2.1 Hydrogen Attack Damage in One-Side Exposed Assembly

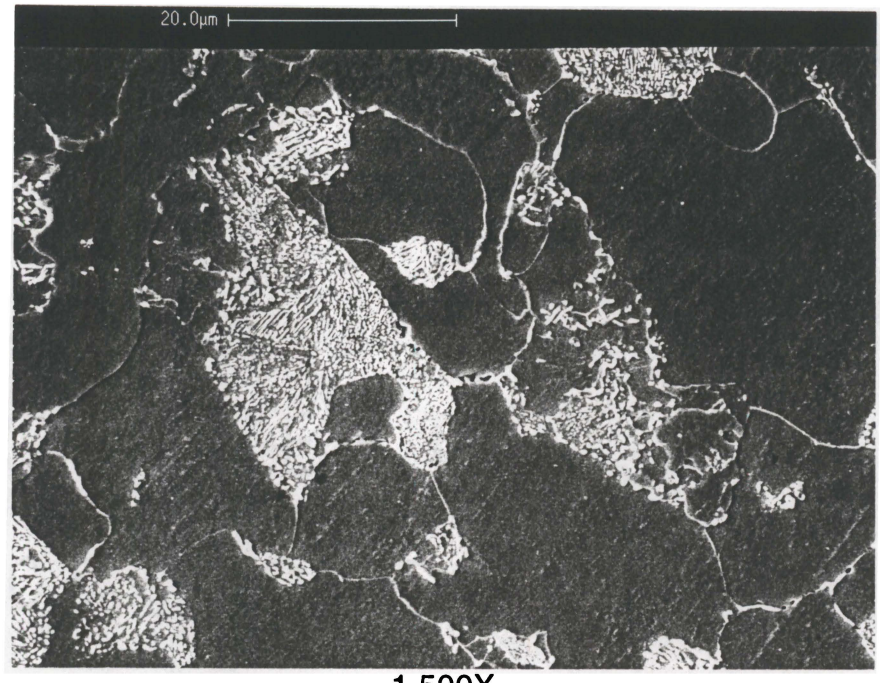
Autoclave exposure testing using static hydrogen pressure with or without applied stress is most commonly used for hydrogen attack studies [24, 26]. However, static hydrogen exposure testing does not simulate the actual operating conditions in pressure vessels and piping. For practical operating conditions, pressure vessels or piping are exposed to high pressure hydrogen on one-side and thus a differential of hydrogen pressure exists from inside to outside. In order to obtain a better understanding of the hydrogen attack mechanism, one-side hydrogen exposure testing was implemented in this study.

The one-side exposure assembly was illustrated and discussed in Chapter 3. MPC-3 and MPC-15 were selected for the one-side exposure testing. The chemical composition of these two materials is presented in Table 3.1. After the hydrogen exposure at 900°F-900 psi for 1248 hours plus 950°F-900 psi for 288 hours, hydrogen attack damage was evaluated through the wall thickness at the 44 mm (1.73"), 29 mm (1.14"), and 13 mm (0.51") locations by quantitative image analysis and hydrogen measurements. It is to be noted that the outside surface was exposed to the hydrogen atmosphere for this one-side exposure testing.

4.2.1.1 Metallographic Evaluation

Hydrogen attack damage was examined on the polished & etched metallographic samples and "Cryo-cracking" samples for MPC-3 using OLM and SEM. Hydrogen damage was not resolved by using OLM at a magnification of 1000X. Therefore, SEM was used for the examination of hydrogen damage on the polished & etched metallographic samples and "Cryo-cracking" samples. Hydrogen attack damage is characterized as aligned methane bubbles and isolated methane bubbles along the B/F and F/F boundaries as well as in the bainite regions. It was observed that the hydrogen damage was most extensive in proximity to the outside surface and decreased through the wall based on the observation of samples with thickness of 44 mm, 29 mm, and 13 mm.

Figures 4.77 through 4.79 show the hydrogen damage in the form of aligned and isolated bubbles at depths of 1, 18, and 28 mm from the outside surface of the 44 mm wall thickness sample. It is evident that the amount and size of the methane bubbles is reduced proceeding from outside surface toward the ID surface. The profile of the hydrogen damage within the wall was quantified by using the quantitative image analysis software (NIH Image) as shown in Figure 4.80. The fraction of damaged grain boundaries is approximately 10% in proximity to the outside surface. The maximum depth was determined as 28 mm from the outside surface at a magnification of 10,000X. Figure 4.81 is a presentation of hydrogen damage as a function of the



1,500X



10,000X

Figure 4.77 Aligned and isolated bubbles adjacent to the outside surface of one-side exposed assembly (44 mm thick, MPC-3).



1,500X



10,000X

Figure 4.78 Isolated bubbles at depth of 18 mm from the outside surface of one-side exposed assembly (44 mm thick, MPC-3).



1,500X



10,000X

Figure 4.79 Isolated bubbles at depth of 28 mm from the outside surface of one-side exposed assembly (44 mm thick, MPC-3).

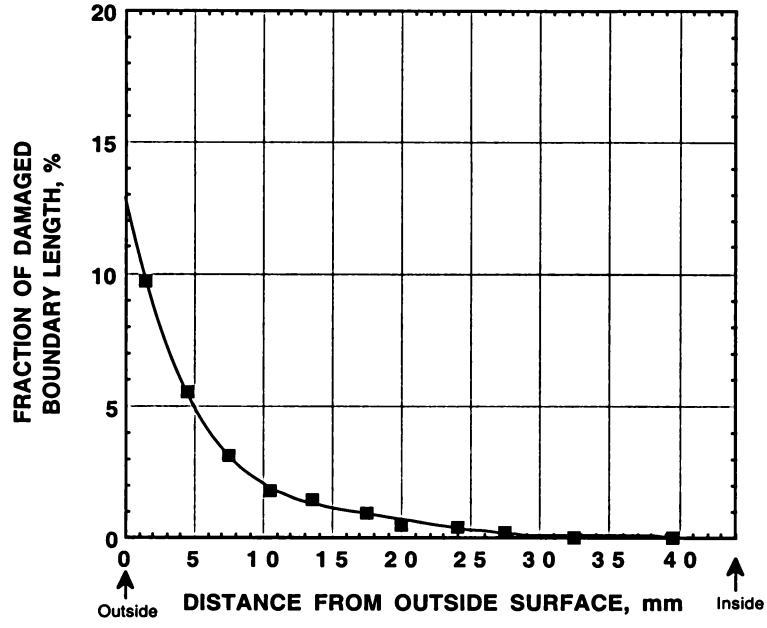


Figure 4.80 Hydrogen damage profile through the wall of one-side exposed assembly (44 mm thick, MPC-3).

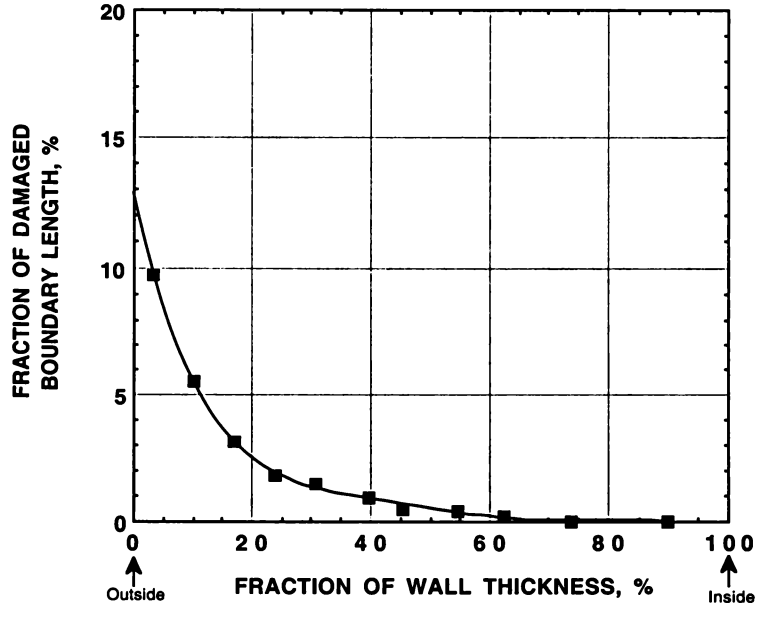


Figure 4.81 Hydrogen damage as a function of fraction of wall thickness of one-side exposed assembly (44 mm thick, MPC-3).

fraction of wall thickness. Approximately 60% of the wall thickness were damaged in this section (44 mm). Figure 4.82 shows the profile of the average bubble diameter within the wall. The average bubble diameter is 0.3 μm adjacent to the outside surface and sharply decreases to 0.13 μm at a depth of 10 mm. Comparing the profiles of the bubble size in the one-side exposed assembly to the service exposed pressure vessels (Figures 4.33 and 4.37), it is apparent that the methane bubbles in the one-side exposed assembly were in the processes of initiation and growth. Data for the fraction of damaged boundaries and bubbles sizes for the one-side exposed assembly (44 mm thick) are superimposed to the database for the service exposed samples as shown in Figure 4.83. It is demonstrated that the test results for the one-side exposed assembly are comparable with hydrogen damage and average bubble diameter established from the database for the service exposed heats. The morphology of the methane bubbles was characterized as aligned and isolated bubbles within the damaged depth of the one-side exposed assembly. The shape for the hydrogen damage profiles in the one-side exposed assembly is similar to the ones observed in the service exposed pressure vessels and piping. Therefore, it is concluded that the one-side exposure testing can be used to simulate the operating condition of pressure vessels for hydrogen attack evaluation.

Figures 4.84 through 4.87 show the profiles of the hydrogen damage within the 29 mm and 13 mm thick samples. Similar to the 44 mm thick sample,

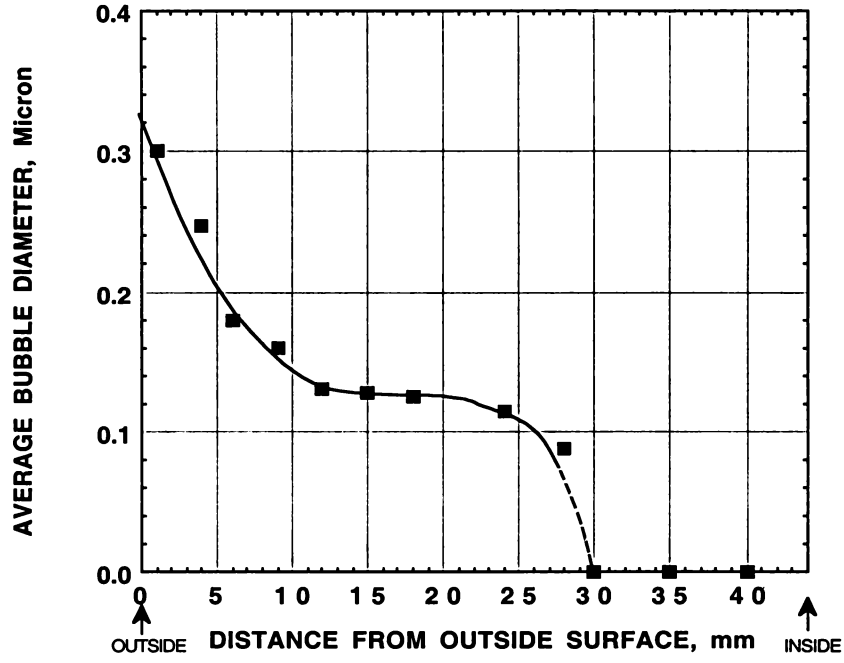


Figure 4.82 Profile of the average bubble diameter through the wall of one-side exposed assembly (44 mm thick, MPC-3).

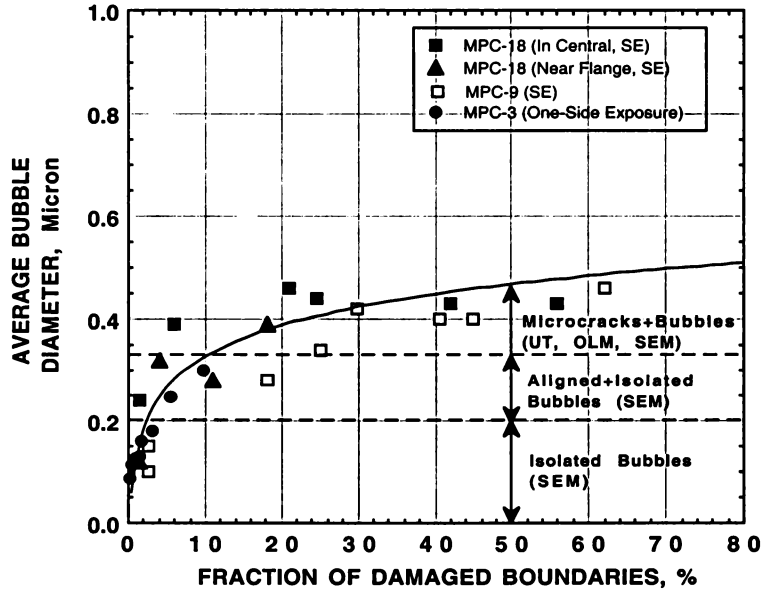


Figure 4.83 Correlation between hydrogen attack damage (FA% and FL%) and average bubble diameter for service exposed and one-side exposed assembly.

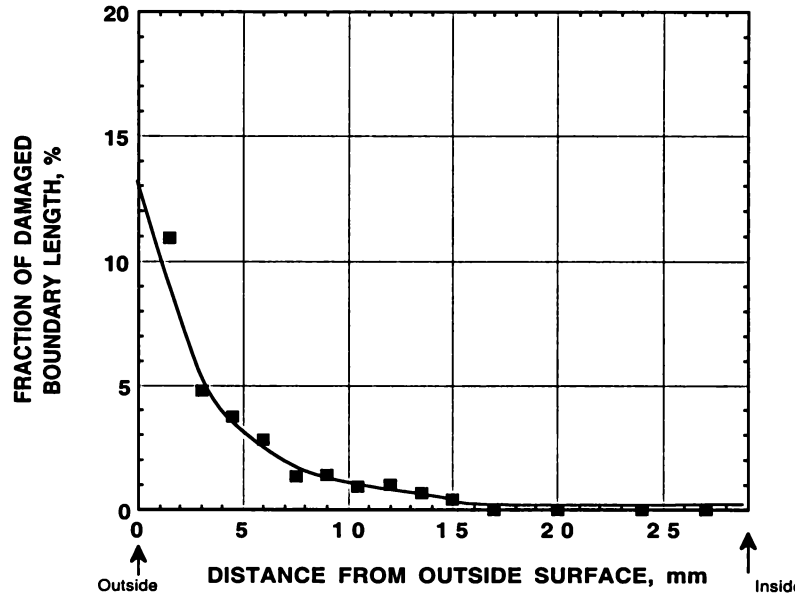


Figure 4.84 Hydrogen damage profile through the wall of one-side exposed assembly (29 mm thick, MPC-3).

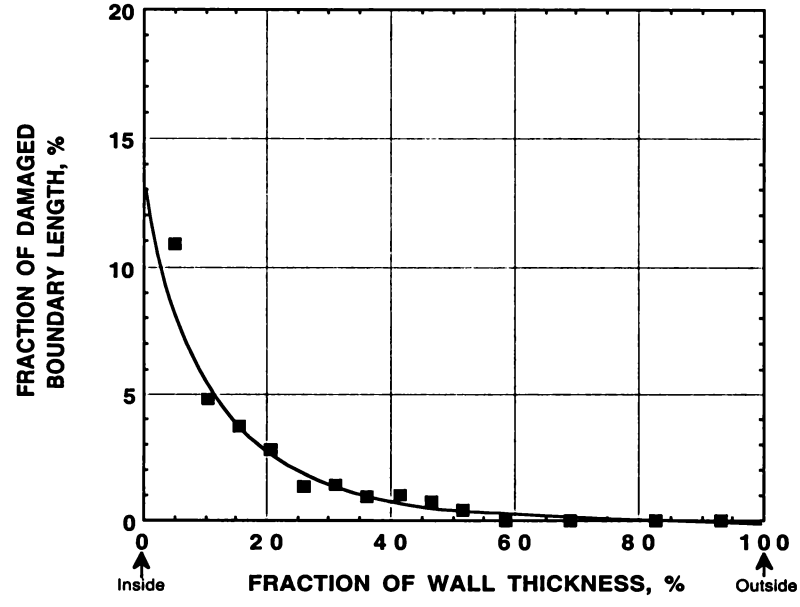


Figure 4.85 Hydrogen damage as a function of fraction of wall thickness of one-side exposed assembly (29 mm thick, MPC-3).

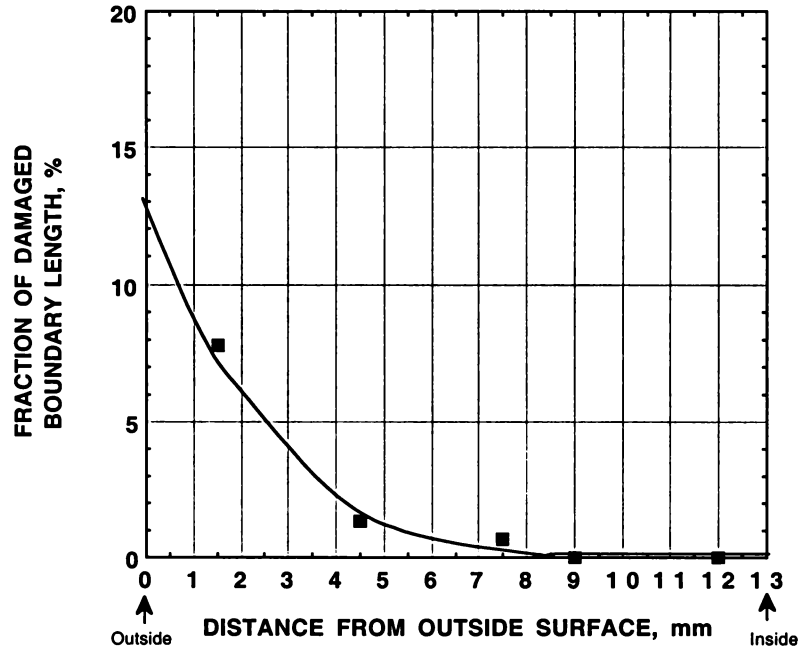


Figure 4.86 Hydrogen damage profile through the wall of one-side exposed assembly (13 mm thick, MPC-3).

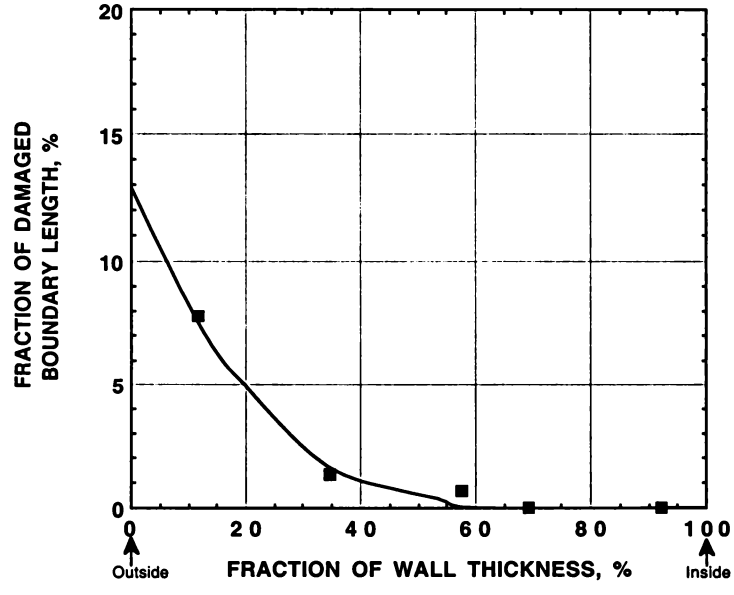


Figure 4.87 Hydrogen damage as a function of fraction of wall thickness of one-side exposed assembly (13 mm thick, MPC-3).

the hydrogen damage was found greatest near the outside surface and decreased through the wall. The maximum values of the damaged boundaries was determined as 11% and 8% near the outside surface for the 29 mm and 13 mm thick samples, respectively. The maximum depths of hydrogen damage are 17 mm and 8 mm from the outside surface for the 29 mm and 13 mm thick samples, respectively. The fraction of damaged wall thickness is approximately 60% as revealed in Figures 4.85 and 4.87. The fraction of damaged wall thickness was defined by the maximum damaged depth normalized by the wall thickness. It is noteworthy that the fraction of damaged boundaries near the outside surface and the fraction of maximum damaged wall thickness are approximately same regardless of the difference in the wall thickness (44, 29, 13 mm).

The fraction of damaged boundary length (FL%) plotted as a function of the fraction of wall thickness for these three samples (44 mm, 29 mm, and 13 mm) is presented in Figure 4.88. The hydrogen damage profiles are the same for these three samples. This indicates that the degree of hydrogen damage adjacent to the outside surface and the fraction of maximum damaged wall depth are independent of the wall thickness when they are exposed to the same conditions. In other word, hydrogen damage is dependent on the hydrogen concentration within the wall. The maximum damaged depth is determined by a critical hydrogen concentration within the wall, above which hydrogen damage occurs.

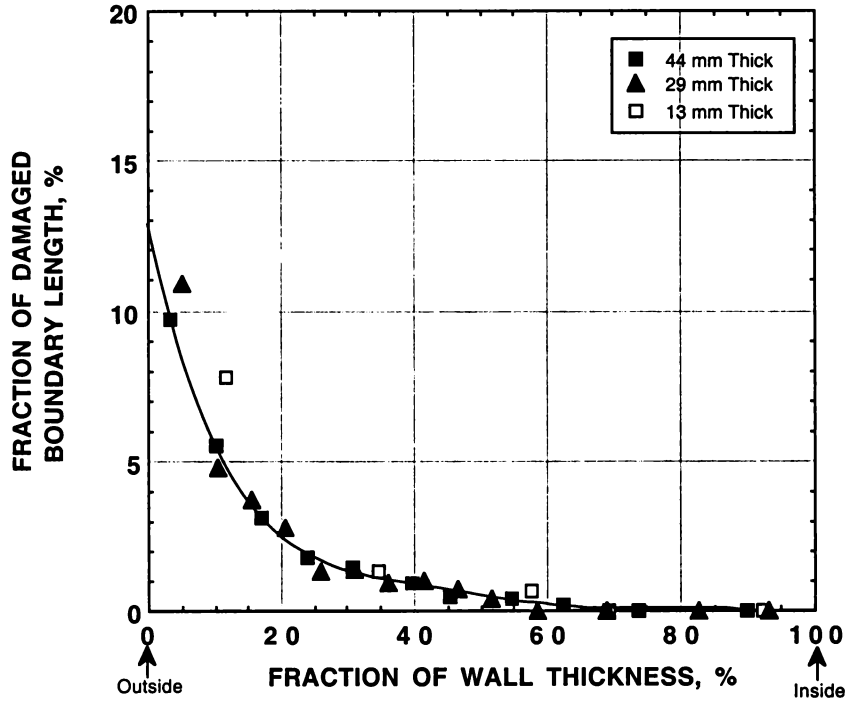


Figure 4.88 Hydrogen damage as a function of the fraction of wall thickness for three samples (13, 29, and 44 mm thick, MPC-3).

4.2.1.2 Methane Determination

Hydrogen concentration derived from the dissociated methane was measured using gas chromatography. The hydrogen concentration within the walls (44, 29, 13 mm) was determined as shown in Figures 4.89 through 4.94. Methane concentration is approximately 52 ppm near the outside surface (exposed to hydrogen) and decreases through the wall. In comparison with the profiles of hydrogen damage, a cut-off line of hydrogen attack/no hydrogen attack is defined as approximately 2 ppm hydrogen (C_{CH4} = 0) for these samples, which is consistent with the critical hydrogen concentration derived from the service exposed materials as discussed in the previous sections.

The methane concentration was plotted as a function of fraction of wall thickness for the three sections of the one-side exposed assembly as presented in Figures 4.90, 4.93, and 4.94. The maximum depth, at which the methane concentration is 0, is approximately 60% of wall thickness for all three locations. The methane concentration profile is plotted as a function of the fraction of wall thickness for these three locations as shown in Figure 4.95. Similar to the hydrogen damage profiles, methane concentration for the three sections are included the same profile and thus is independent of the wall thickness.

The hydrogen damage in terms of fraction of damaged boundary length and hydrogen concentration are superimposed on the database developed from the hydrogen damage evaluation for service exposed heats as shown in Figure 4.96. The results of the one-side exposed assembly are virtually

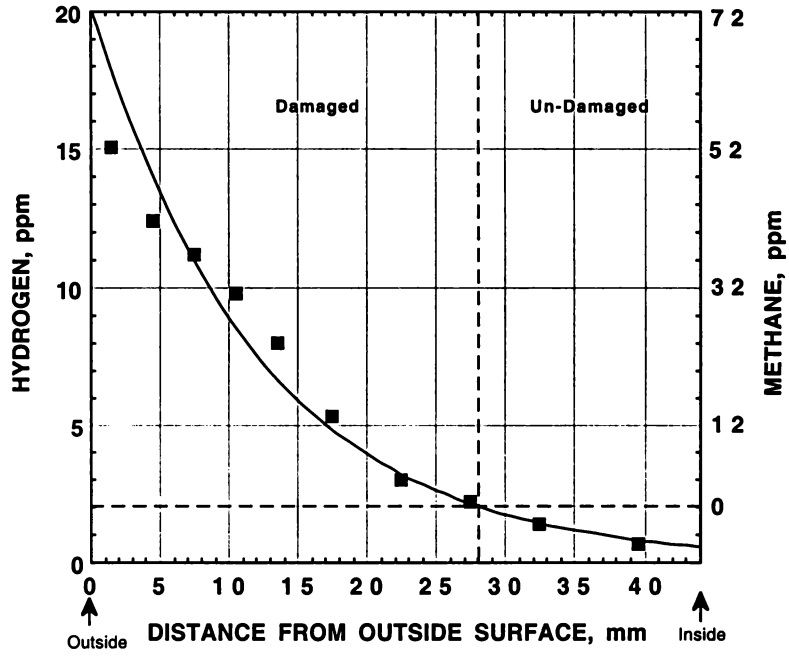


Figure 4.89 Methane concentration profile through the wall of one-side exposed assembly (44 mm thick, MPC-3).

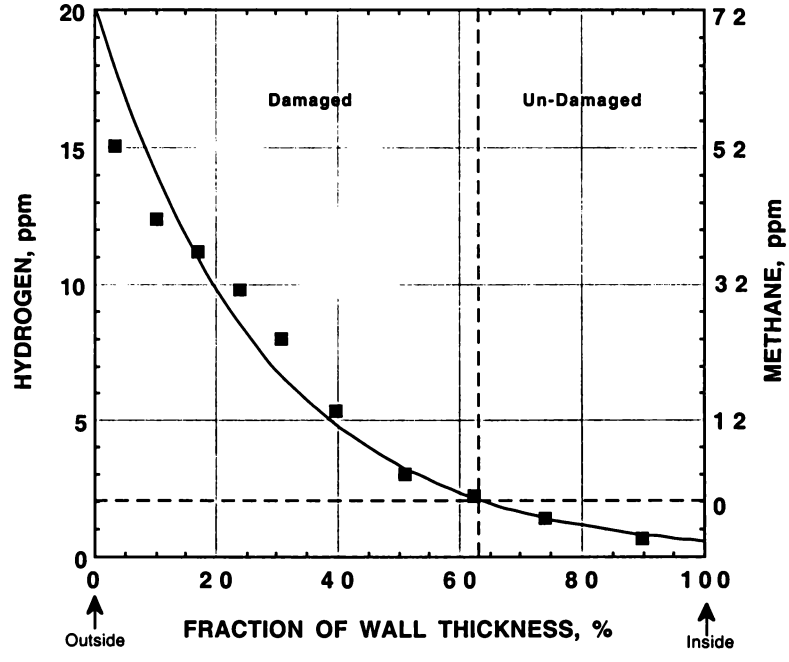


Figure 4.90 Methane concentration as a function of fraction of wall thickness of one-side exposed assembly (44 mm thick, MPC-3).

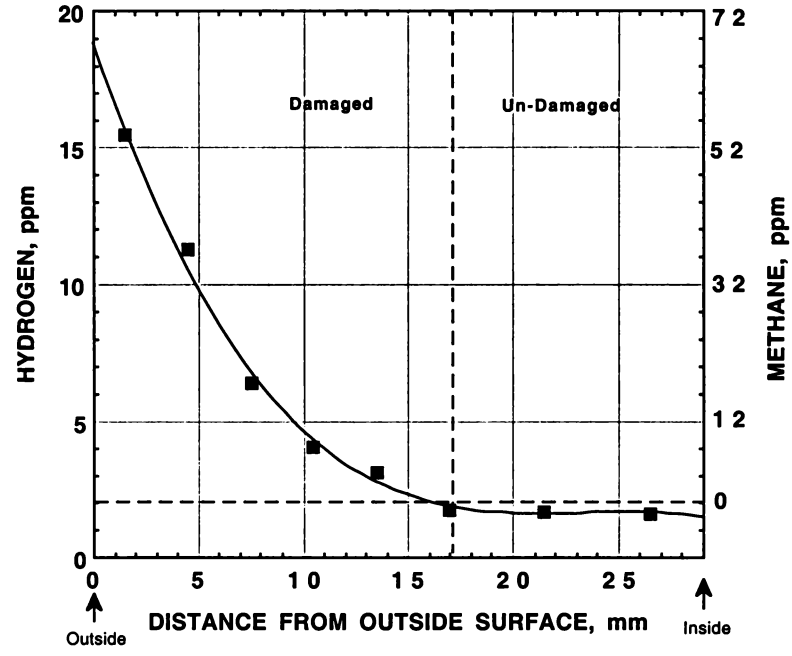


Figure 4.91 Methane concentration profile through the wall of one-side exposed assembly (29 mm thick, MPC-3).

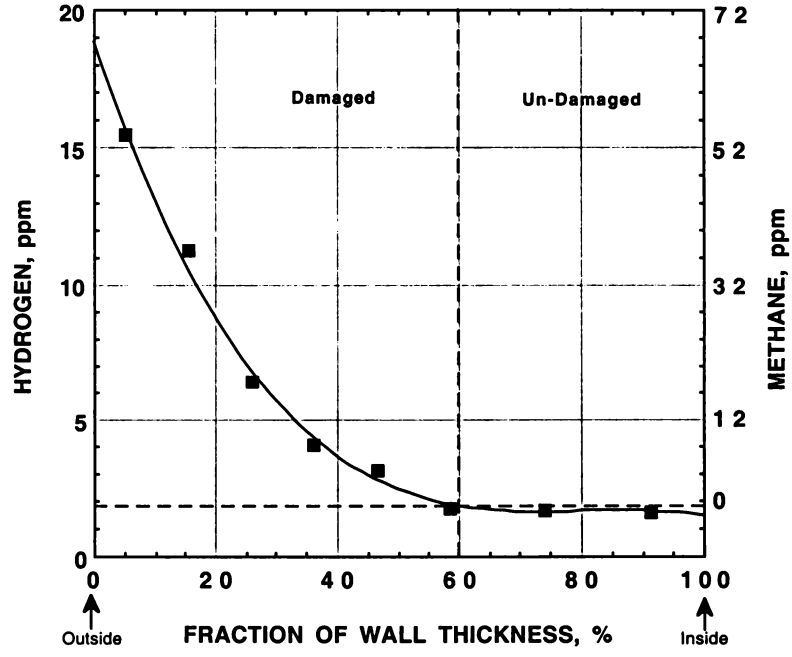


Figure 4.92 Methane concentration as a function of fraction of wall thickness of one-side exposed assembly (29 mm thick, MPC-3).

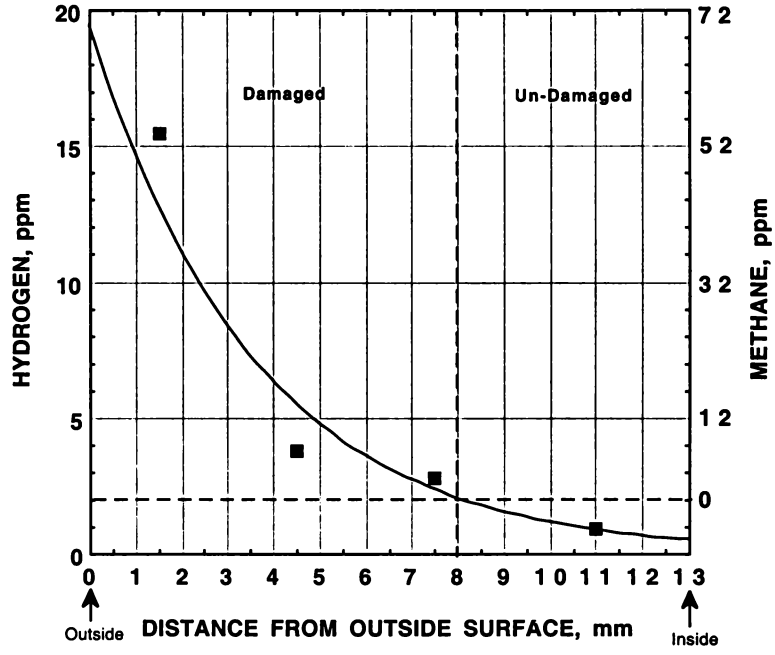


Figure 4.93 Methane concentration profile through the wall of one-side exposed assembly (13 mm thick, MPC-3).

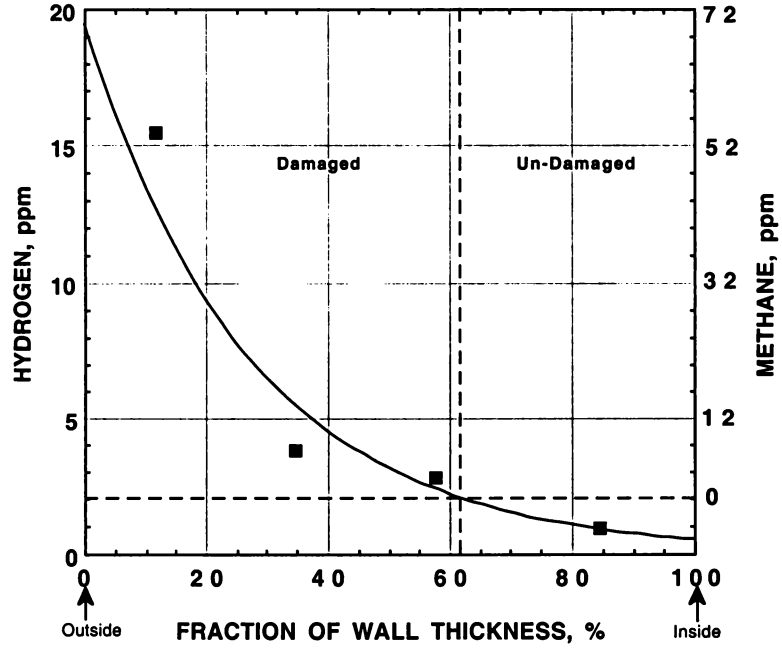


Figure 4.94 Methane concentration as a function of fraction of wall thickness of one-side exposed assembly (13 mm thick, MPC-3).

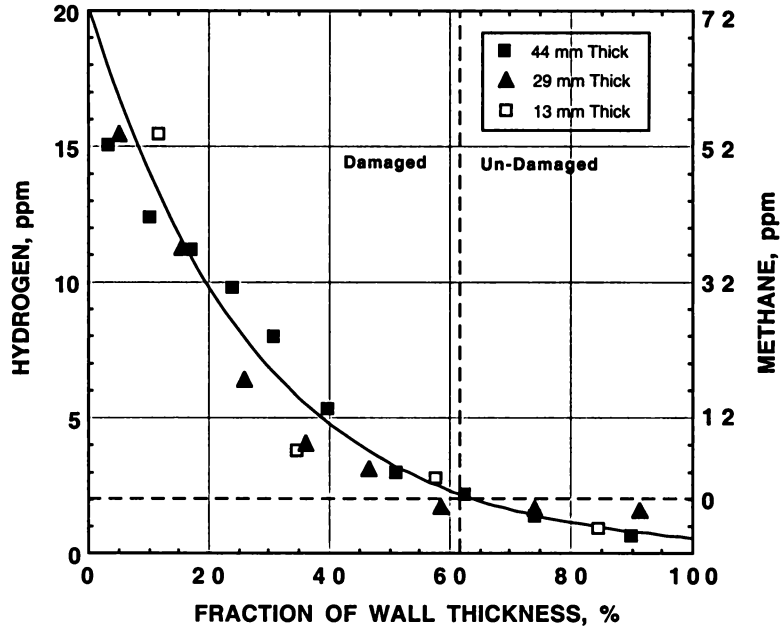


Figure 4.95 Hydrogen concentration as a function of fraction of wall thickness of the three sections (13, 29, 44 mm thick, MPC-3).

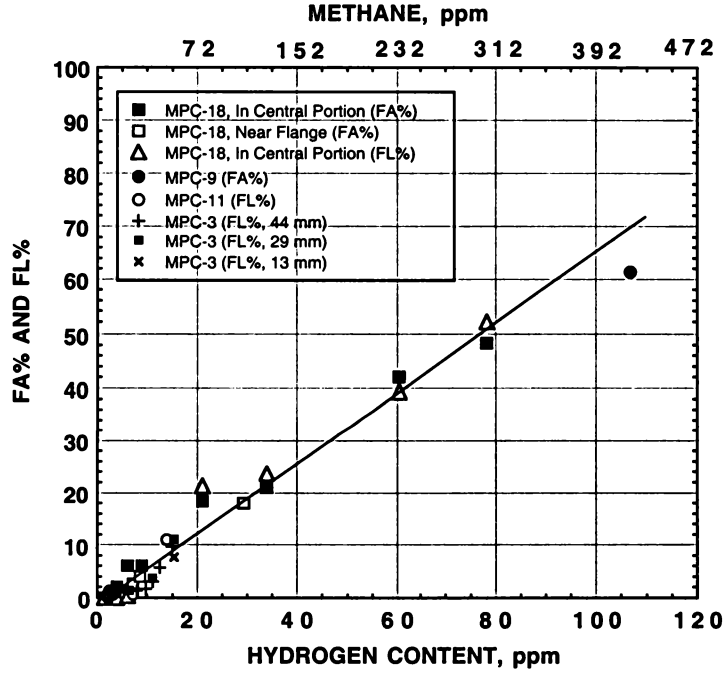


Figure 4.96 Relationship of the fraction of damaged grain boundaries (FA%, FL%) and the methane concentration in accordance with the service exposure and one-sided exposure database.

identical to the hydrogen damage as a function of methane content derived from the database for service exposed heats.

In summary, the one-side hydrogen exposure testing successfully simulated the hydrogen attack behavior in pressure vessel and piping. A gradient of hydrogen damage was observed within the wall by using SEM and gas chromatography. The fraction of damaged depth is approximately 60% of the wall thickness for three locations with different wall thickness (44 mm, 29 mm, and 13 mm). It is found that the fraction of damage depth is independent of the wall thickness if the exposure condition is the same. This phenomenon implies that hydrogen attack is controlled by the hydrogen concentration established within the wall of pressure vessel or piping. According to SEM observations and hydrogen concentration measurements through the wall, a critical hydrogen content can be assessed to be approximately 2 ppm above which hydrogen attack occurs within the wall.

4.2.2 Effects of Carbon and Alloying Elements

The effect of carbon and alloying elements on hydrogen attack was investigated for C-0.5Mo materials with low and high Mo/C ratio (MPC-3, Mo/C: 2.29; MPC-13, Mo/C: 3.80). In addition, carbon steel (SA-516-70), C-Mn-0.5Mo (SA-508, SA-533), and 1.25Cr-0.5Mo steels were utilized to study the effect of alloying elements on the hydrogen attack susceptibility. The chemical composition of carbon steel, C-Mn-0.5Mo, and 1.25Cr-0.5Mo materials is

Table 4.3 Chemical composition of carbon steel (SA-516-70) and C-Mn-0.5Mo (SA-508, SA-533), 1.25Cr-0.5Mo materials (wt%).

Element	SA-516-70	SA-508	SA-533	1.25Cr-0.5Mo
C	0.21	0.26	0.21	0.19
Mn	0.97	0.75	1.38	0.58
P	0.007	0.010	0.010	0.009
S	0.002	0.014	0.014	0.003
Si	0.20	0.26	0.18	0.63
Ni	0.05	0.81	0.48	0.05
Cr	0.04	0.45	0.17	1.05
Mo	0.01	0.61	0.47	0.48
V	0.002	0.05	-	0.006
Nb	0.002	-	-	0.00011
Cu	0.06	-	0.12	0.01

presented in Table 4.3. Comparing with the chemical composition of C-0.5Mo (MPC-3 and 13) in Table 3.1, the SA-508 contains higher Mo (0.61%) and V (0.05%); the SA-533 has higher Mn (1.38%); and 1.25Cr-0.5Mo is higher in Cr (1.05%). The carbon steel was in normalized condition and C-Mn-0.5Mo materials are water quenched (from 1650°F) and tempered (1250°F). 1.25Cr-0.5Mo steel is in normalized and tempered condition.

Static autoclave exposure testing was performed at 775°F-900 psi H_2-300 hours and 725°F-900 psi H_2-300 hours. After exposure, hydrogen dissociated from methane was determined for hydrogen attack evaluation. Figure 4.97 shows the methane contents in MPC-3 and MPC-13 materials for two exposure conditions. As anticipated, the heat of MPC-3 with low Mo/C ratio (2.29) is more susceptible to hydrogen attack than MPC-13 with high Mo/C ratio (3.80). The methane contents in MPC-3 and MPC-13 were measured as 14

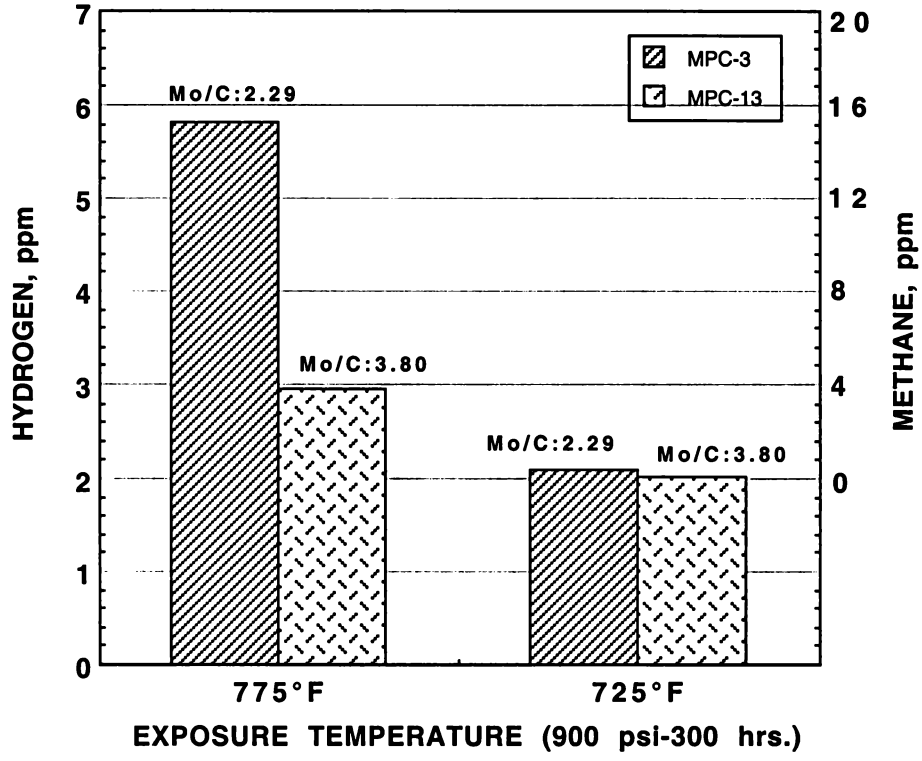


Figure 4.97 Effect of Mo/C ratio on hydrogen attack susceptibility of C-0.5Mo.

ppm and 4 ppm, respectively, for the exposure condition of 775°F-900 psi H_2-300 hours. In accord with the empirical relationship of hydrogen damage as a function of methane content, it indicates that hydrogen attack occurred in both heats exposed at 775°F-900 psi H_2 for 300 hours. The fraction of damaged boundaries is estimated less than 5% for both heats. Hydrogen damage morphology is predicted as isolated bubbles, which can not be resolved by OLM. There is little difference in methane concentrations in MPC-3 and MPC-13 exposed at 725°F-900 psi H_2 for 300 hours. Methane content is approximately 0 ppm for both heats.

Figure 4.98 shows the hydrogen attack susceptibility of different steels. It is apparent that carbon steel is the most susceptible to hydrogen attack compared to other steels according to methane determination. Methane contents in C-0.5Mo steel (MPC-3, MPC-13) are greater than that in SA-508, SA533 and 1.25Cr-0.5Mo steels for both exposure conditions. This demonstrates that the alloying elements of Mn, V, and Cr in steels enhances the resistance to hydrogen attack because Mn, V, and Cr are carbide forming elements and reduce carbon activity to inhibit methane formation in steels [67].

4.2.3 Heat Treatments

The influence of heat treatment in terms of normalized & tempered, annealed only, and annealed & tempered conditions on hydrogen attack susceptibility was investigated using static autoclave exposure testing. MPC-3

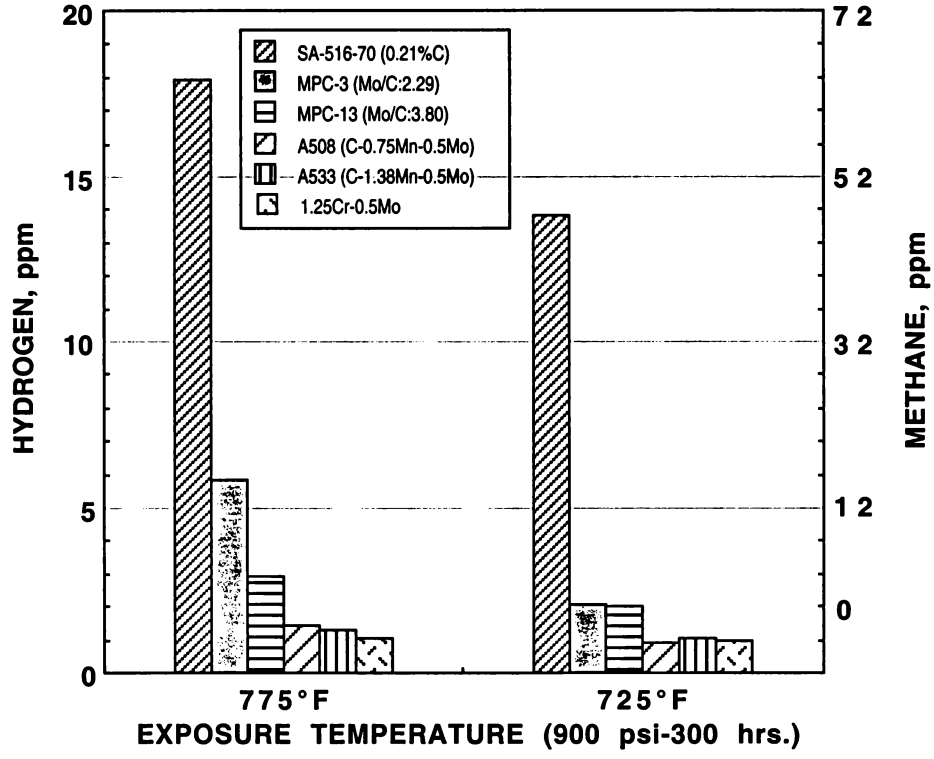
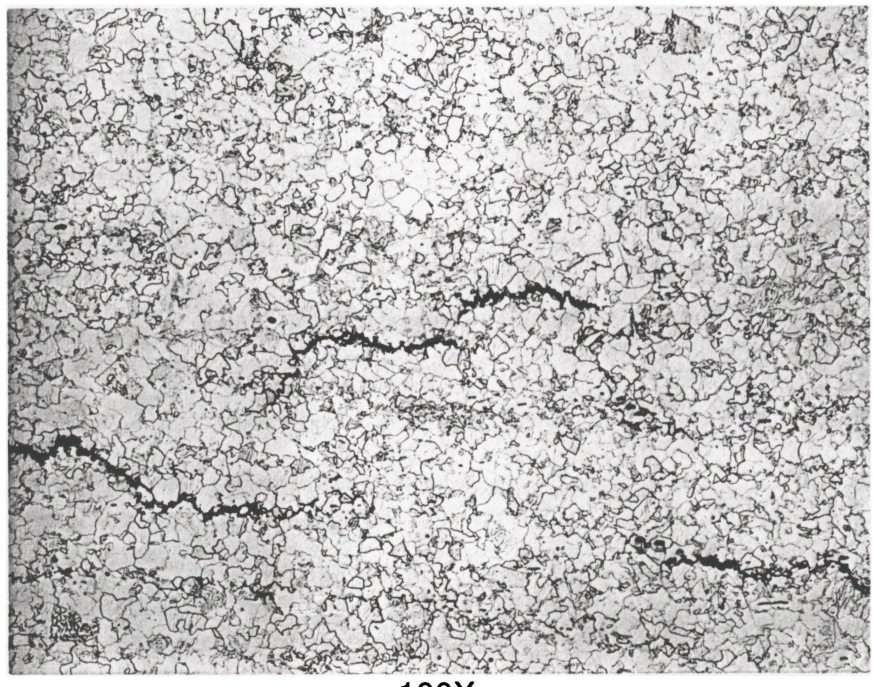


Figure 4.98 Hydrogen attack susceptibility of carbon steel, C-0.5Mo, C-Mn-0.5Mo, and 1.25Cr-0.5Mo materials.

material was normalized (1650°F-2 hrs.) and tempered (1250°F-1hr.) before hydrogen exposure. The microstructure of the N&T MPC-3 material is a mixture of ferrite and bainite. In addition, annealed (1652°F-3 hrs.) and annealed & tempered (1283°F-15 hrs and 1337°F-15 hrs.) heat treatments were conducted for materials MPC-3 and MPC-25. The microstructure is a mixture of ferrite and pearlite in the annealed condition and ferrite & coarsened carbides in the annealed & tempered condition.

Static hydrogen autoclave exposure testing was conducted at 900°F-900 psi-1248 hrs. plus 950°F-900 psi-288 hours. This testing condition is above the Nelson Curve for C-0.5Mo steel. Metallographic examination was conducted to evaluate the hydrogen attack damage. Figure 4.99 shows typical photomicrographs of the hydrogen attack damage in the normalized and tempered material (MPC-3). Hydrogen attack cracking and internal decarburization occurred in the N&T material.

Figures 4.100 through 4.102 present the typical photomicrographs of the hydrogen attack damage in the annealed only and annealed & tempered materials (MPC-3). Hydrogen attack cracking and internal decarburization occurred in both annealed only and annealed & tempered materials after exposure at 900°F-900 psi for 1248 hours plus at 950°F-900 psi for 288 hours. Hydrogen attack cracking is associated with rolling bands. It is noted that the entire pearlite constituent was virtually eliminated by extensive decarburization in the annealed only material (MPC-3). The degree of hydrogen attack damage

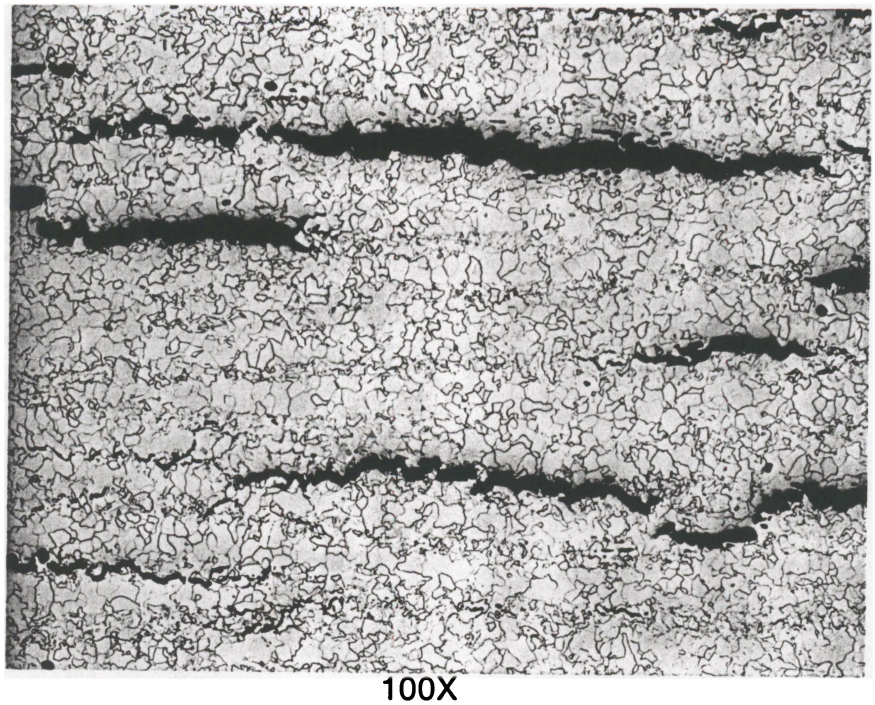


100X



1,000X

Figure 4.99 Hydrogen attack cracking in N&T material (MPC-3, 1650°F-2 hrs. & 1150°F-2 hrs.) after hydrogen exposure at 900°F-900 psi-1248 hrs.+950°F-900 psi-288 hrs..

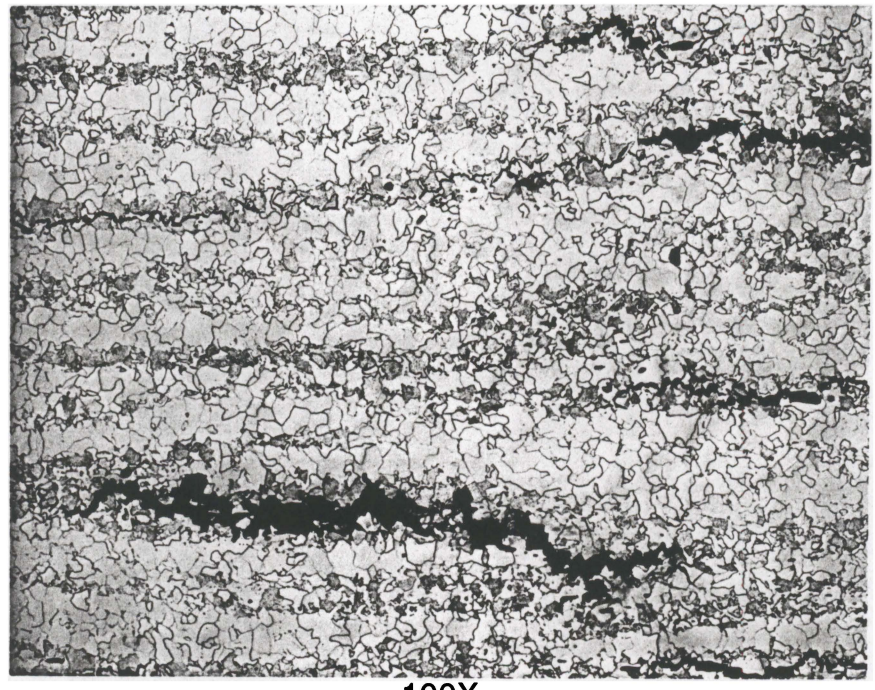


100X

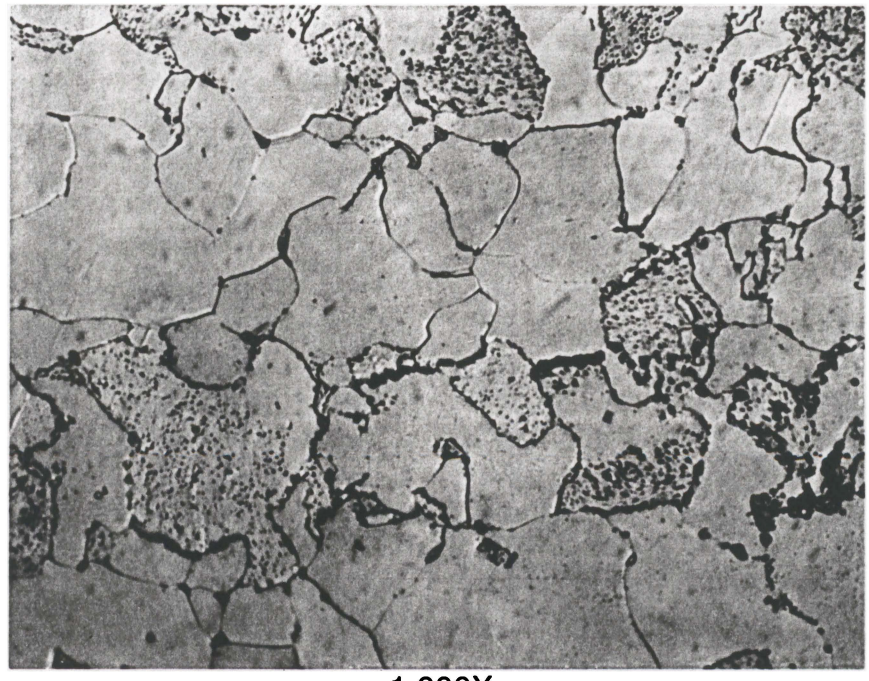


1,000X

Figure 4.100 Hydrogen attack cracking in annealed only material (MPC-3, 1652°F-3 hrs.) after hydrogen exposure at 900°F-900 psi-1248 hrs.+950°F-900 psi-288 hrs.

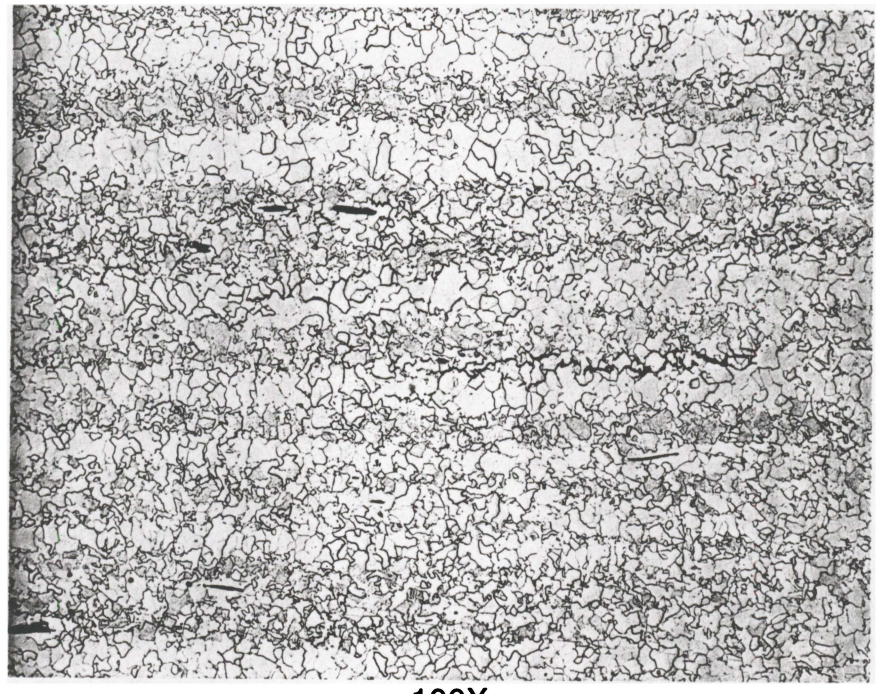


100X

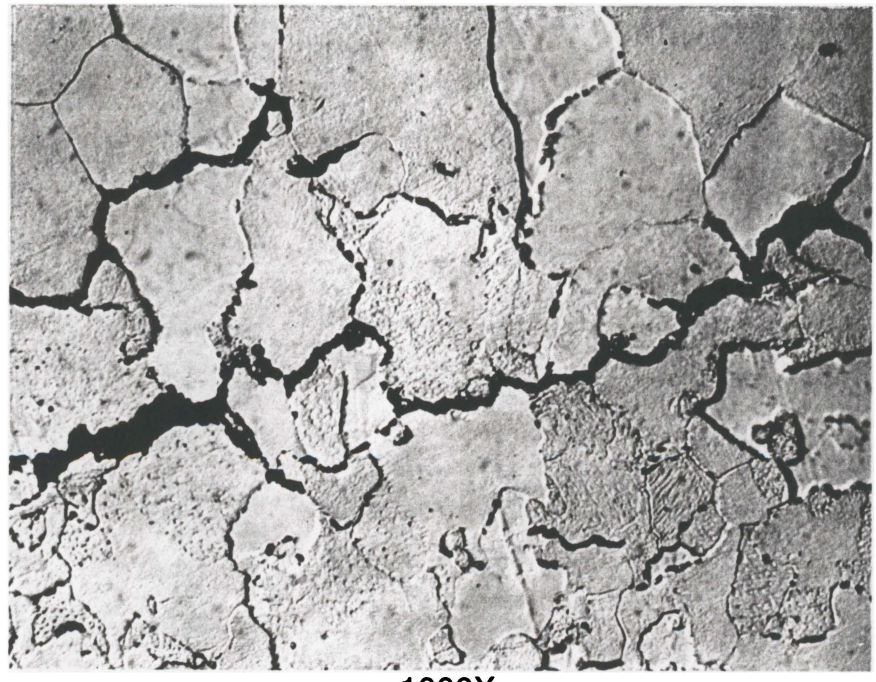


1,000X

Figure 4.101 Hydrogen attack cracking in annealed & tempered material (1283°F-15 hrs., MPC-3) after hydrogen exposure at 900°F-900 psi-1248 hrs.+950°F-900 psi-288 hrs..



100X



1000X

Figure 4.102 Hydrogen attack cracking in annealed & tempered material (1337°F-15 hrs., MPC-3) after hydrogen exposure at 900°F-900 psi-1248 hrs.+950°F-900 psi-288 hrs..

decreased with the increase in tempering temperature for both MPC-3 and MPC-25 compared with the annealed only condition as presented in Figures 4.100 through 4.102.

In comparison with the annealed only and annealed & tempered materials, the degree of hydrogen damage in the N&T material was ranked similar to the annealed and tempered material (1283°F for 15 hours). In conclusion, tempering heat treatments can enhance the resistance to hydrogen attack by the formation of stable carbides.

4.2.4. Welding and PWHT

Effects of welding processes and postweld heat treatment (PWHT) on hydrogen attack in C-0.5Mo steel were investigated. Bead-on-plate welds were prepared on MPC-3 and MPC-15 materials by applying both Shielded Metal-arc welding (SMAW) using E7018-A1 electrodes and Gas Tungsten-arc welding (GTAW). The welding heat inputs are 100 KJ/in and 35 KJ/in for SMAW, 26 KJ/in and 7 KJ/in for GTAW. The CGHAZ samples of MPC-3 and MPC-13 were simulated at heat inputs of 100 KJ/in and 30 KJ/in by using the Gleeble thermal simulation technique. After the Gleeble simulation, PWHT was conducted at 1150°F-4 hrs., 1200°F-4 hrs., and 1250°F-4 hrs..

After static autoclave exposure, metallographic examination was implemented for hydrogen attack assessment. Hydrogen attack cracking was observed in the as welded CGHAZ (MPC-3) after exposed to 850°F-500 psi H_2

for 88 hours, at which hydrogen attack did not occur in the base metal, FGHAZ, and a weld metal. Therefore, the CGHAZ is most susceptible to hydrogen attack in weldment. The weld with low heat input (35 KJ/in, SMAW) shows more extensive hydrogen attack cracking in the CGHAZ than the weld with high heat input (100 KJ/in, SMAW) as shown in Figure 4.103 for an exposure condition of 900°F-900 psi H_2-1248 hrs. plus 950°F-900 psi H_2-288 hrs..

Hydrogen attack susceptibility in the CGHAZ is reduced by postweld heat treatments. Hydrogen attack cracks were observed in the as-simulated CGHAZ (100 KJ/in, MPC-3) exposed to 850°F-500 psi H_2 for 88 hours but were not found in the PWHTed CGHAZ (100 KJ/in, 1150°F-4 hrs., MPC-3) after exposure to 850°F-500 psi H_2 for 110 hours as shown in Figure 4.104. The CGHAZ experiences a high peak temperature during welding. Carbides the CGHAZ dissociate and dissolve into matrix during their high temperature thermal cycle. Because of the rapid cooling, the dissolved carbon saturates the matrix and forms martensite upon cooling. Saturated carbon has high carbon activity and tends to readily react with hydrogen to form methane during hydrogen exposure. After PWHT, the formation of stable carbides decreases carbon activity and enhances hydrogen attack resistance.

Hydrogen attack damage was not found in the weld metal and fine-grained HAZ regions (FGHAZ) in the SMAW welds (MPC-3 and MPC-15, with or without PWHT) exposed to 900°F-900 psi H_2-1248 hrs. plus 950°F-900 psi H_2-288 hrs, at which extensive hydrogen damage occurred in the base metals and



35 KJ/in, 400X



100 KJ/in, 400X

Figure 4.103 Hydrogen attack cracks in the CGHAZ of SMAW weld (MPC-15) at heat inputs of 35 KJ/in and 100 KJ/in exposed to 900°F-900 psi H_2-1248 hrs. + 950°F-900 psi H_2-288 hrs..



As-simulated CGAHZ, 850°F-500 psi H_2-88 hrs., 400X



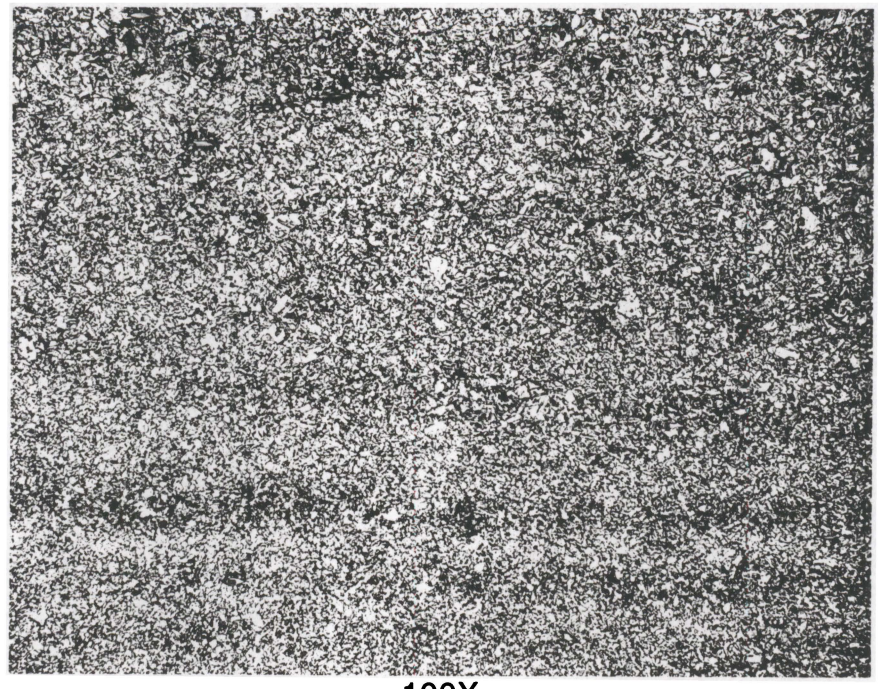
PWHTed CGHAZ, 850°F-500 psi H_2-110 hrs., 400X

Figure 4.104 Effect of PWHT (1150°F-4hrs.) on hydrogen attack in the CGHAZ (MPC-3).

the CGHAZ. Figure 4.105 shows representative photomicrographs of the FGHAZ of SMAW with a heat input of 100 KJ/in for MPC-15 material after hydrogen exposure. These observations are consistent with the results found in the service-exposed welds (e.g. long seam weld of heat exchanger channel, MPC-18). These results demonstrate that the application of the tempered-bead technique to the solution of hydrogen attack in the CGHAZ is a possibility. However, hydrogen attack cracking was found in the as welded autogenous GTAW fusion zone (MPC-15) in comparison with the SMAW weld metal which shows no hydrogen attack as presented in Figure 4.106. This can be explained by the fact that the carbon content in the autogenous GTA weld is equal to the base metal of MPC-15 (0.22%C) in contrast to a 0.04%C level in the SMAW weld. Therefore, the autogenous GTA fusion zone (with high carbon content) is more susceptible to hydrogen attack than the SMAW weld metal with low carbon content.

4.2.5. Hot and Cold Working

Hot and cold rolling was conducted with plastic deformation levels of 5%, 10%, and 20% for the MPC-3 material. The cold rolling was implemented at room temperature. The initial temperature for hot rolling was 1750°F. Samples were exposed to 900°F-900 psi H_2-1248 hours plus 950°F-900 psi H_2-288 hours. After the static autoclave exposure, metallographic evaluation was conducted to define the effect of cold and hot working on hydrogen attack.



100X



400X

Figure 4.105 No hydrogen attack damage in the FGHAZ of SMAW with heat input of 100 KJ/in after hydrogen exposure (900°F-900 psi-1248 hrs. + 950°F-900 psi-288 hrs.).



Autogenous GTAW, 400X



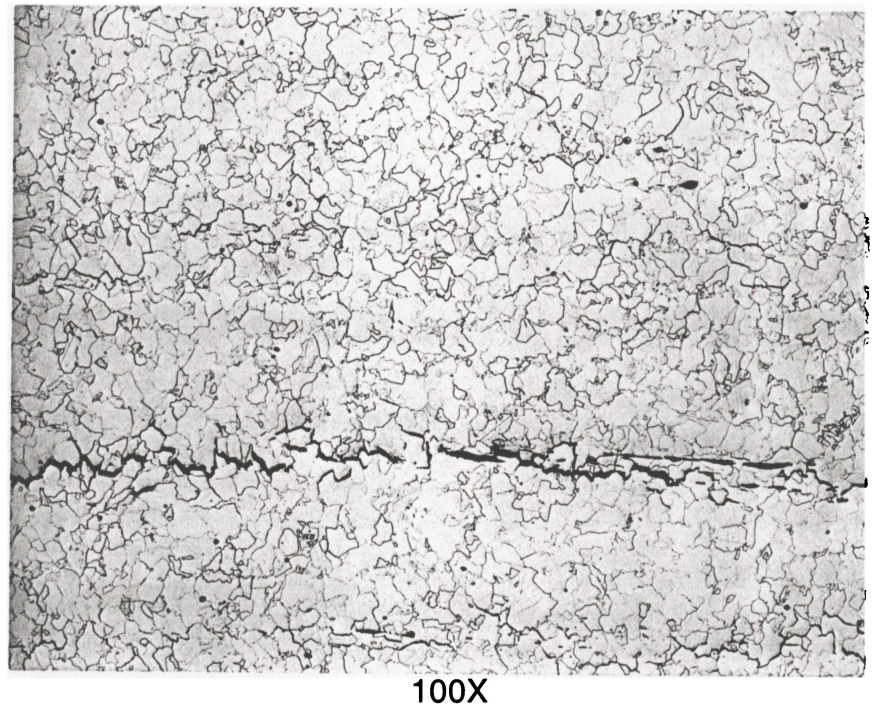
SMAW, 400X

Figure 4.106 Comparison of hydrogen attack susceptibility of autogenous GTAW fusion zone (26 KJ/in) and SMAW weld metal (100 KJ/in) after hydrogen exposure (900°F-900 psi-1248 hrs. + 950°F-900 psi-288 hrs.).

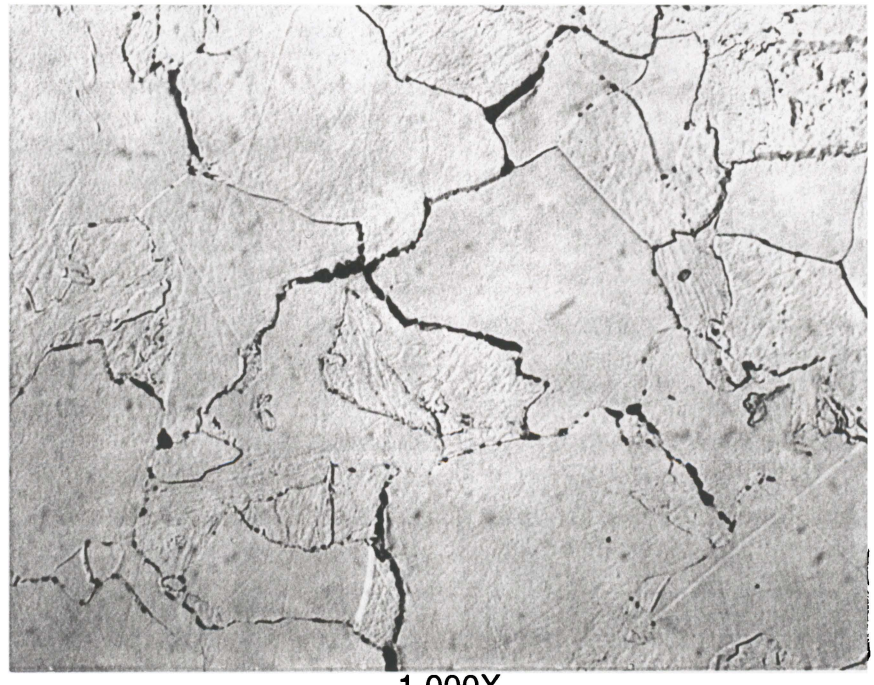
Figures 4.107 through 4.109 represent the photomicrographs of hydrogen attack damage in the cold rolled material (MPC-3). Extensive hydrogen attack damage occurred in all cold rolled material in terms of complete internal decarburization and intergranular cracking. As the cold work deformation increases, the extent of hydrogen attack cracking is promoted. The acceleration of hydrogen attack in cold worked material can be explained by the ferrite deformation around carbides to introduce localized residual stresses [50, 98] and to form microvoids [99]. The occurrence of localized residual stress and microvoids enhances methane bubble nucleation and growth.

Figures 4.110 through 4.112show the hydrogen attack damage in the hot rolled material (MPC-3). Hydrogen attack cracks were observed in all the hot rolled material. The extent of decarburization and hydrogen attack cracking decreases as the hot working deformation increases. The hydrogen attack damage is more extensive in the cold worked material than the hot worked material with the same plastic deformation.

Hydrogen attack susceptibility was ranked for the materials in the N&T, annealed only, annealed & tempered, hot and cold worked conditions based on the metallographic examination. It was demonstrated that the cold worked and annealed only materials are the most susceptible to hydrogen attack. The material annealed & tempered at 1337°F-15 hours is improved in comparison to the material annealed & tempered at 1283°F-15 hours. The hydrogen attack susceptibility for the annealed & tempered, N&T, and hot worked materials is



100X



1,000X

Figure 4.107 Hydrogen attack damage in cold rolled material (MPC-3, 5%, 900°F-900 psi H_2-1248 hrs. + 950°F-900 psi H_2-288 hrs.).

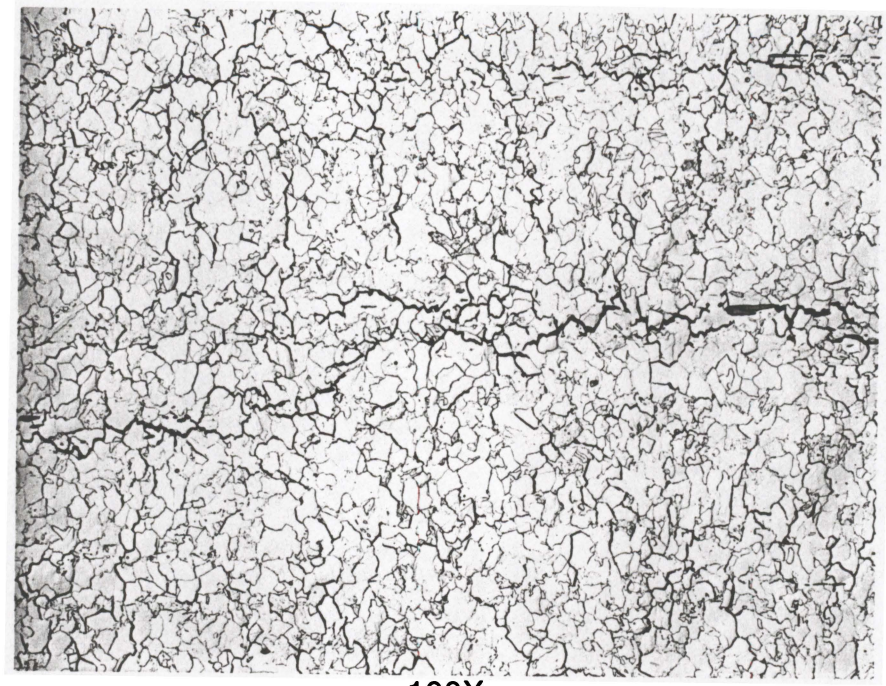


100X

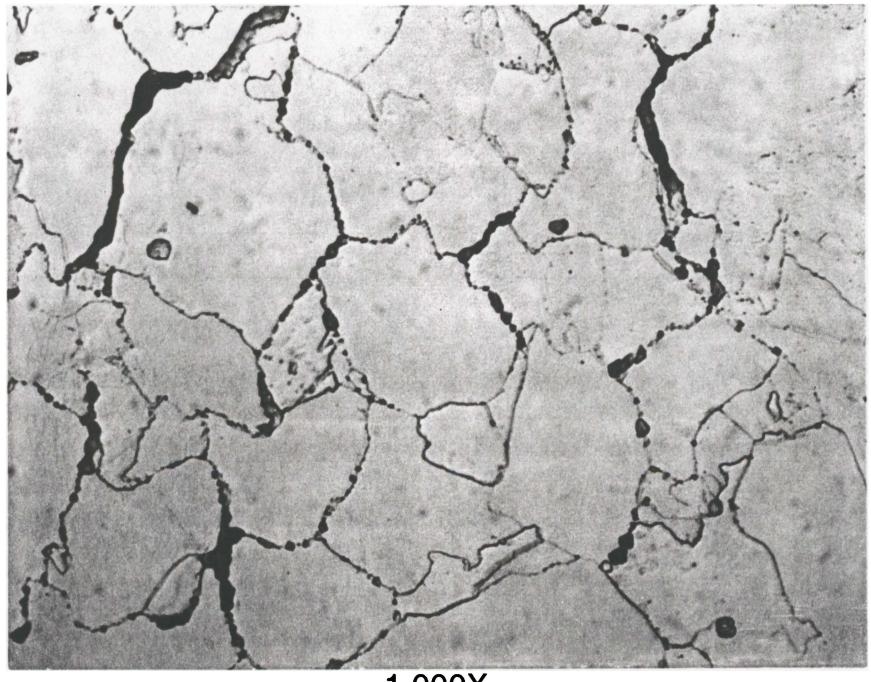


1,000X

Figure 4.108 Hydrogen attack damage in cold rolled material (MPC-3, 10%, 900°F-900 psi H_2-1248 hrs. + 950°F-900 psi H_2-288 hrs.).

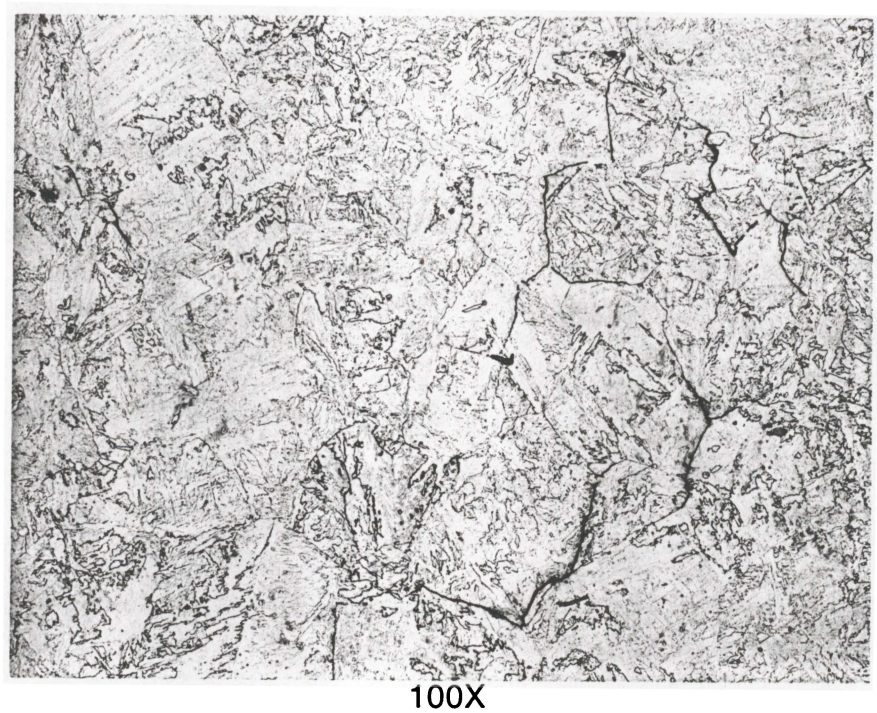


100X



1,000X

Figure 4.109 Hydrogen attack damage in cold rolled material (MPC-3, 20%, 900°F-900 psi H_2-1248 hrs. + 950°F-900 psi H_2-288 hrs.).

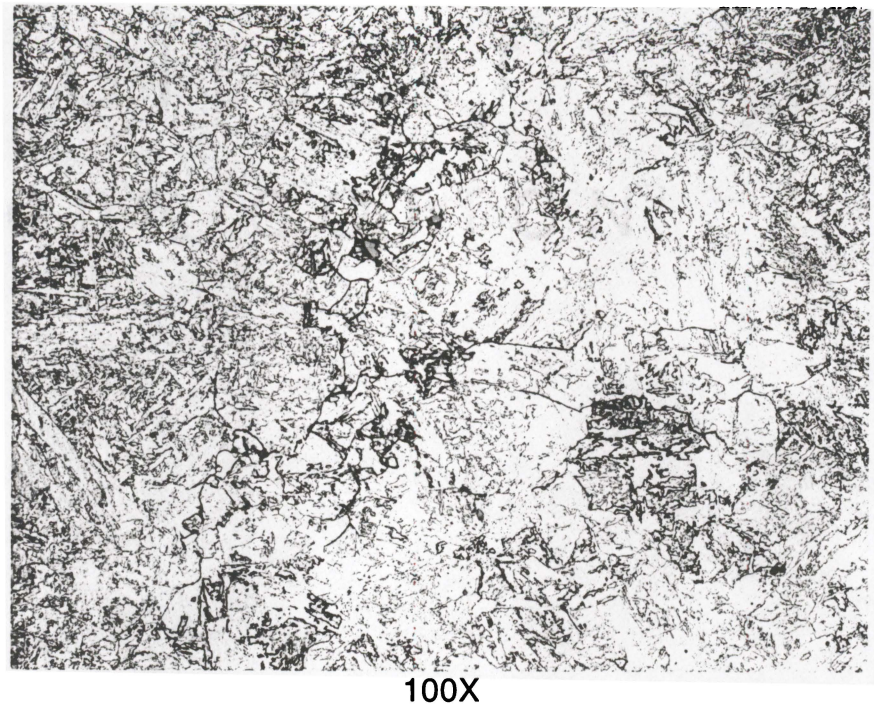


100X



1,000X

Figure 4.110 Hydrogen attack damage in hot rolled material (MPC-3, 5%, 900°F-900 psi H_2-1248 hrs. + 950°F-900 psi H_2-288 hrs.).

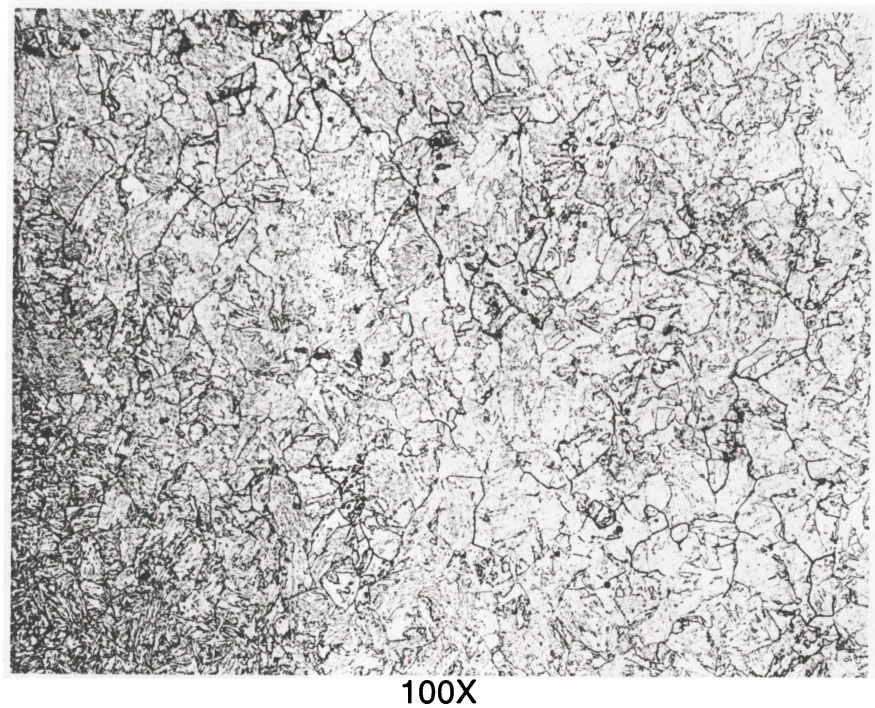


100X



1,000X

Figure 4.111 Hydrogen attack damage in hot rolled material (MPC-3, 10%, 900°F-900 psi H_2-1248 hrs. + 950°F-900 psi H_2-288 hrs.).



100X



1,000X

Figure 4.112 Hydrogen attack damage in hot rolled material (MPC-3, 20%, 900°F-900 psi H_2-1248 hrs. + 950°F-900 psi H_2-288 hrs.).

similar, however, they are improved compared to the cold worked and annealed only materials.

4.2.6. Summary of Autoclave Exposure Results

The one-side hydrogen exposure testing successfully simulated the hydrogen attack behavior in the pressure vessels piping applied in the petroleum industry. Hydrogen attack damage profiles were determined through the wall thickness of the one-side exposed assembly using quantitative image analysis and gas chromatography. The relationship of the hydrogen attack damage, average bubble diameter, and hydrogen measurement are comparable with the evaluation results for the service exposed samples. The fraction of damaged depth is approximately 60% of the wall thickness for the three locations evaluated with different wall thickness (44 mm, 29 mm, and 13 mm). It is found that the fraction of damaged depth is independent of the wall thickness if the exposure conditions are the same. This phenomenon implies that hydrogen attack is controlled by the hydrogen concentration established within the wall of pressure vessels and piping. There is a critical hydrogen content above which hydrogen attack simultaneously occurs within the wall. The maximum depth of hydrogen attack damage is determined by the critical hydrogen concentration.

Hydrogen attack susceptibility is greater for MPC-3 with low Mo/C (2.29) compared to MPC-13 with high Mo/C (3.80). It was demonstrated that the

alloying elements of Mn, V, and Cr in steels significantly improved the hydrogen attack resistance. The examination results show that carbon steel is most susceptible to hydrogen attack compared to other alloyed steels. The susceptibility to hydrogen attack for SA-508, SA533, and 1.25Cr-0.5Mo steels is less than that for C-0.5Mo steel (MPC-3, MPC-13).

The effect of heat treatment in terms of N&T, annealed only, and annealed & tempered on hydrogen attack was investigated. It is concluded that a tempering heat treatment enhanced the hydrogen attack resistance by the formation of stable carbides. The hydrogen attack susceptibility of the N&T material is generally equivalent to the annealed & tempered materials.

In C-0.5Mo welds, hydrogen attack occurs in the CGHAZ in short exposure times (88 hours) at 850°F-500 psi H_2 for which no hydrogen attack damage was found in the base metal (MPC-3), FGHAZ, and weld metal (E7018-A1). Therefore, the CGHAZ is the most susceptible weld zone to hydrogen attack. More severe hydrogen damage was observed in the CGHAZ with low heat input (35 KJ/in) than with high heat input (100 KJ/in). PWHT improves the hydrogen attack resistance in the CGHAZ. Hydrogen attack damage was not found in the low carbon weld metal (0.04%C) and the FGHAZ after exposure to 900°F-900 psi-1248 hours plus 950°F-900 psi-288 hours, for which extensive hydrogen attack damage occurred in the base metal and the CGHAZ (MPC-3 and MPC-15). The greater resistance to hydrogen attack in the low carbon weld

metal and the FGHAZ was also observed in the service-exposed heat exchanger channel welds (MPC-18).

Cold working increases hydrogen attack susceptibility of C-0.5Mo steel. The extent of hydrogen damage was promoted with an increase in cold working deformation. However, the extent of hydrogen attack damage decreases as the hot working deformation increases. It is demonstrated that the cold worked and annealed only materials have the highest susceptibility to hydrogen attack compared to the N&T, annealed & tempered, and hot rolled materials. The annealed & tempered material with higher tempering temperature (1337°F-15 hrs.) shows less susceptibility to hydrogen attack than the annealed and tempered material with lower tempering temperature (1283°F-15 hrs.). The N&T, annealed & tempered, and hot rolled materials have similar susceptibility to hydrogen attack but they are less susceptible than the cold worked and annealed materials.

4.3 Phase Transformations and Carbide Evolution

Hydrogen attack susceptibility is strongly dependent on chemical composition, heat treatments, and carbides as discussed in the early sections. Phase transformation and carbide evolution are important in the understanding of the mechanism of hydrogen attack in C-0.5Mo steel. Therefore, the continuous cooling transformations for MPC-3 and MPC-13, representing high carbon (0.21%C) and low carbon (0.15%C) respectively, were investigated for

heat treatment and welding conditions using Gleeble thermal simulation and high speed dilatometry techniques. In addition, optical light microscopy, scanning electron microscopy, and transmission electron microscopy were applied to evaluate the microstructure and carbide types.

4.3.1 Heat Treatment CCT Diagrams

Figure 4.113 shows the heat treatment CCT diagram for MPC-3 (0.21%C). The Ac_1 and Ac_3 temperatures were determined as 1382°F (750°C) and 1598°F (870°C), respectively, by heating the specimen to the austenitizing temperature 1670°F (910°C) at a heating rate of 448 C°/min. The CCT diagram shows four austenitic transformation products: martensite, bainite, ferrite, and pearlite depending on cooling rate. Martensite transformation starts at 788°F (420°C) and finishes at 482°F (250°C). The critical cooling rate for 100% martensite is 1940 C°/min. The martensite hardness is 463 HV at a cooling rate of 6000 C°/min. The transformation of bainite, ferrite, and pearlite extends over a broad range of cooling rates with hardness from 337 to 153 HV.

In addition to the dilatometric determination of the CCT diagram (MPC-3), metallographic examination was supplemented using OLM and SEM. The metallographic observation results are consistent with the transformation products shown on the CCT diagram. As predicted from the CCT diagram, only martensite was observed in the specimen with a cooling rate of 6000 C°/min as shown in Figure 4.114. In the sequence of decreasing cooling rate to 20 and 10

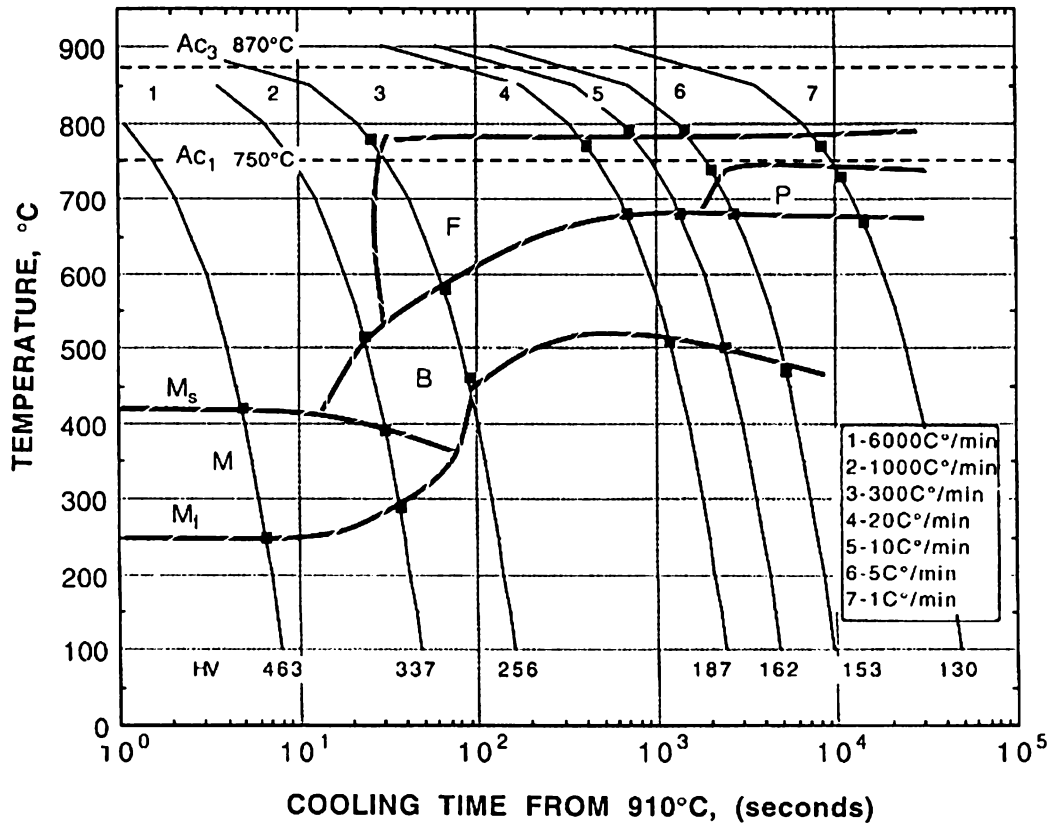


Figure 4.113 CCT diagram for C-0.5Mo steel with high carbon content (MPC-3, 0.21%C).



400X



1,000X

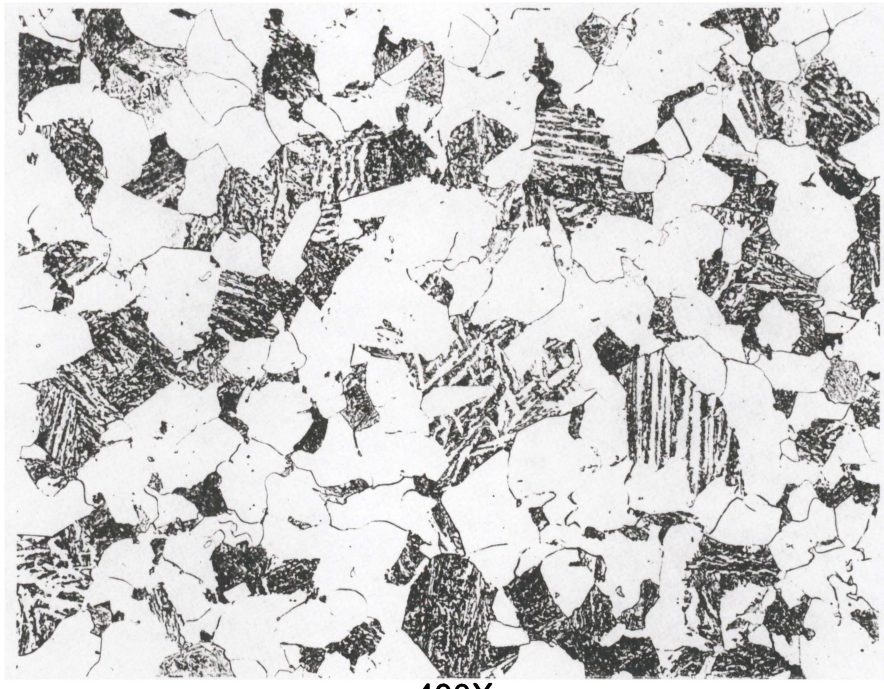
Figure 4.114 Martensite microstructure at cooling rate of 6000 C°/min (MPC-3, 463 HV).

C°/min, the transformation products are ferrite and bainite as shown in Figure 4.115 (20°C/min). The fraction of bainite is approximately 90%, 50%, and 30% corresponding to cooling rates of 300, 20, and 10 C°/min. The microstructures at cooling rates of 20 and 1 C°/min are similar to the normalized microstructure (ferrite & bainite) and annealed microstructure (ferrite & pearlite).

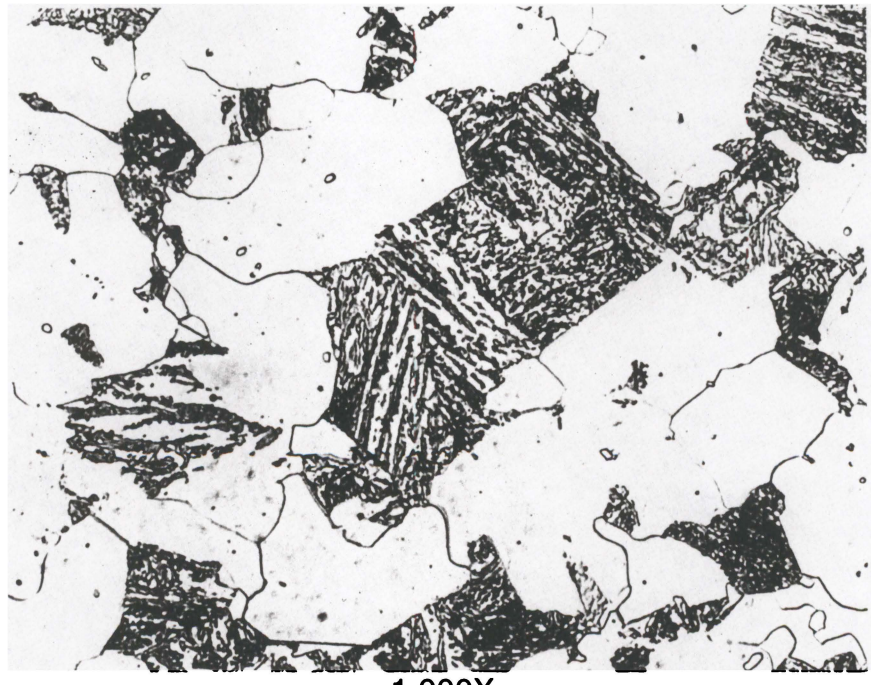
The CCT diagram for the low carbon content heat of MPC-13 (0.15%C) was developed as presented in Figure 4.116. The Ac_1 and Ac_3 temperatures were determined as 1400°F (760°C) and 1670°F (910°C), respectively. Being analogous to the CCT diagram of MPC-3, there are four phase transformation regions, martensite, bainite, ferrite, and pearlite from cooling rates of 1 C°/min to 6000 C°/min. However, it is evident that the CCT diagram of MPC-13 is shifted to the left and the martensite start transformation temperature rises relative to the MPC-3 CCT diagram as shown in Figure 4.113. In this respect, it is concluded that the hardability of MPC-3 is greater than MPC-13. Metallographic examination demonstrated that the microstructure is consistent with the prediction from the CCT diagram for MPC-13.

4.3.2 Welding CCT Diagrams

Conventional CCT diagrams provide useful information for predicting microstructures in steels for heat treatment. However, the conventional CCT diagram can not be directly applied to determine microstructure in the HAZ, especially in the CGHAZ, because of the rapid heating and cooling attendant



400X



1,000X

Figure 4.115 Microstructure of ferrite and bainite at cooling rate of 20 C°/min (MPC-3, 187 HV).

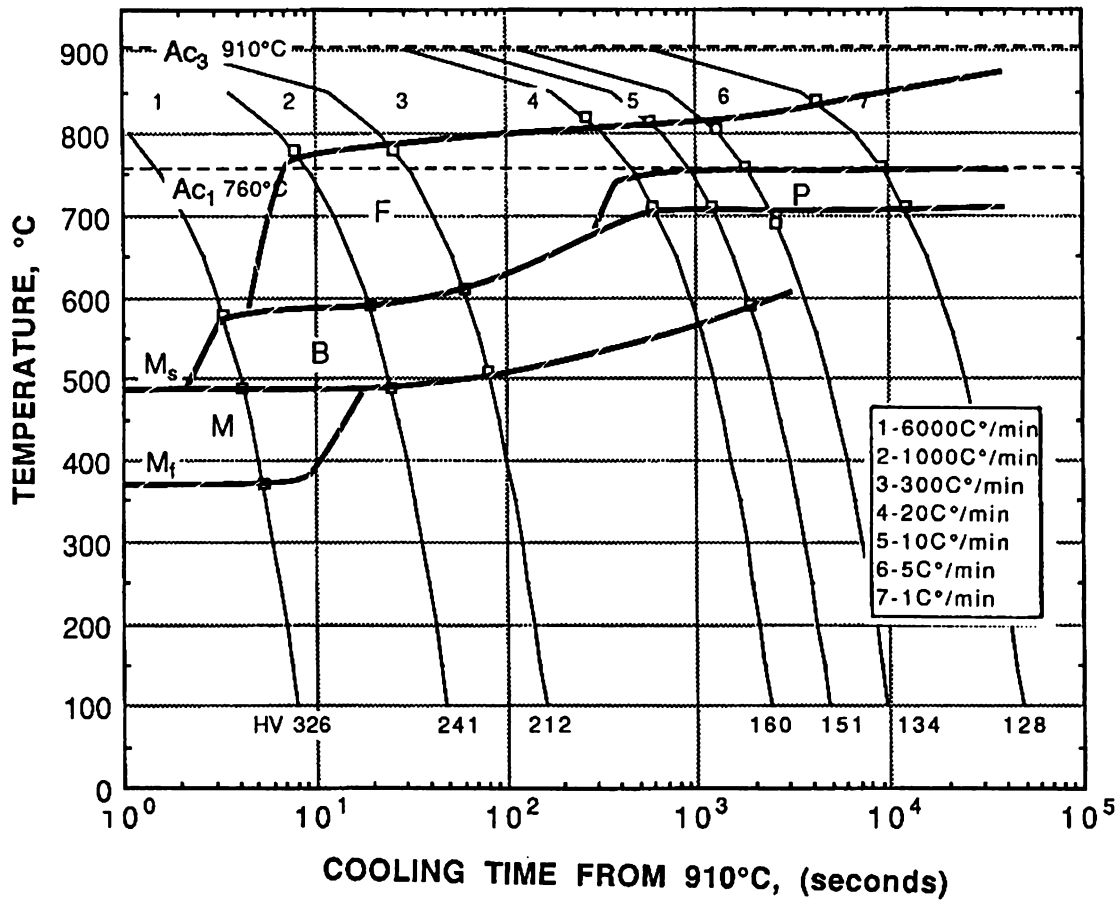


Figure 4.116 CCT diagram for C-0.5Mo steel with low carbon content (MPC-13, 0.15%C).

upon welding. Therefore, a welding CCT diagram should be established for microstructural determination in the HAZ. The Gleeble thermal simulation technique provides a successful method for establishing a welding CCT diagram.

To simulate practical welding conditions, weld thermal cycles for the coarse grained HAZ of 1" thick plate at preheat temperature of 350°F (175°C) and peak temperature of 1316°C (2400°F) were simulated for MPC-3 and MPC-13 at heat inputs of 12, 50, and 120 KJ/in ($t_{8/5}$: 3, 10, 20 seconds).

Figure 4.117 shows the welding CCT diagram for MPC-3 in which only martensite and bainite are formed from 12 to 120 KJ/in. The Ac_1 and Ac_3 temperatures are 1418 °F (770 °C) and 1670 °F (910 °C), respectively, which are higher than the Ac_1 (1382°F/750°C) and Ac_3 (1598°F/870°C) in the heat treatment CCT diagram as shown in Figure 4.113. Martensite transformation occurred at a heat input of 12 KJ/in with a martensite start transformation temperature of 788°F (420°C). Martensite and bainite transformations occurred at a heat input of 50 KJ/in. With increasing heat input from 50 to 120 KJ/in, there is only bainite transformation. The hardness of the CGHAZ at 12, 50, and 120 KJ/in is 474, 424, and 340HV, respectively. Microstructure observed using OLM is consistent with the prediction from the welding CCT diagram.

The welding CCT diagram for MPC-13 (0.15%C) is shown in Figure 4.118 with heat inputs of 12, 50, and 120 KJ/in. The Ac_1 and Ac_3 temperatures were determined as 1400°F (760°C) and 1706°F (930°C), respectively. Similar

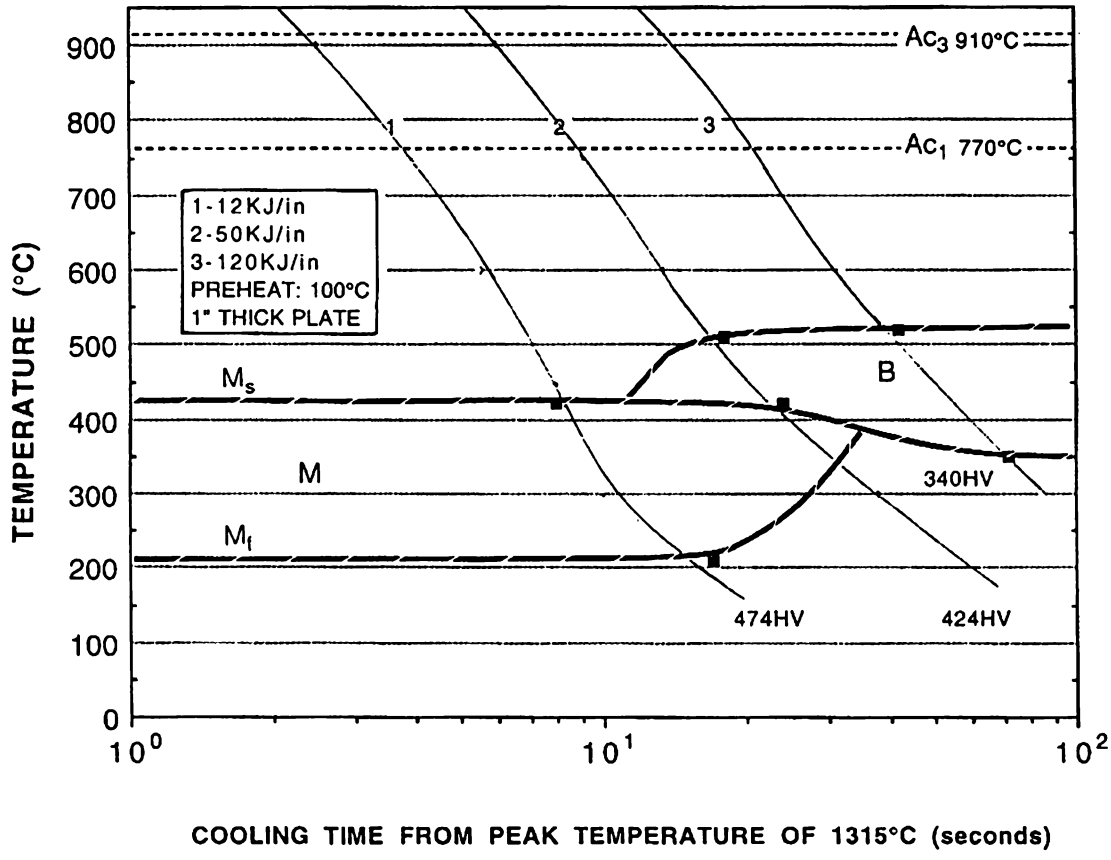


Figure 4.117 Welding CCT diagram for the CGHAZ of C-0.5Mo steel with high carbon content (MPC-3, 0.21%C).

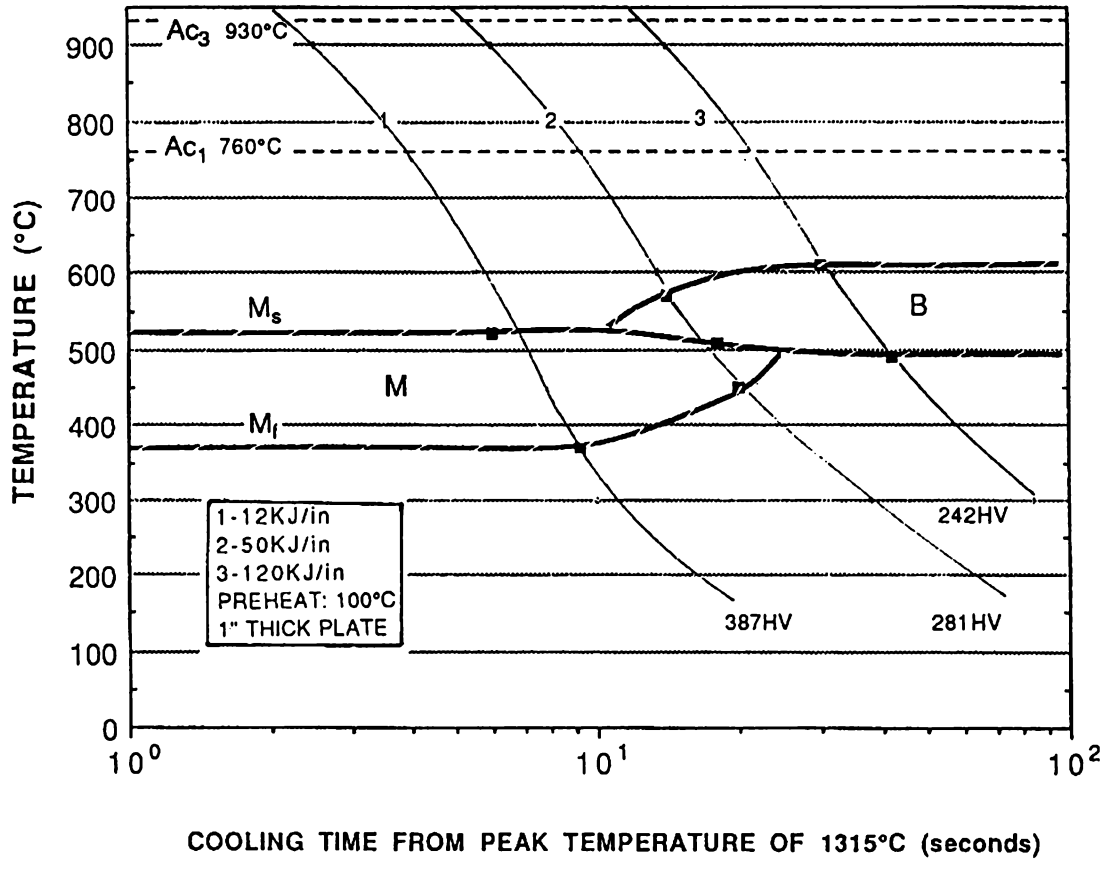
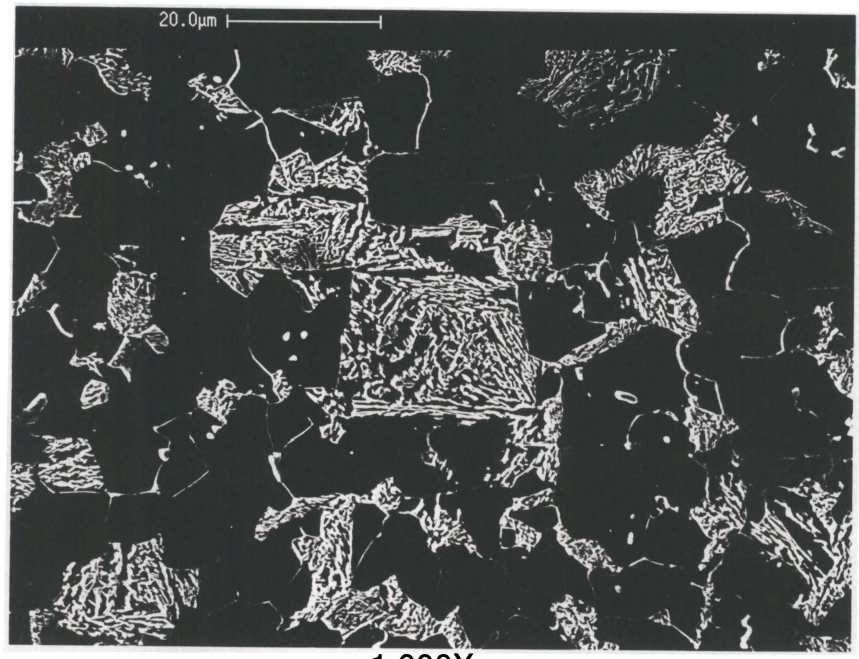


Figure 4.118 Welding CCT diagram for the CGHAZ of C-0.5Mo steel with low carbon content (MPC-13, 0.15%C).

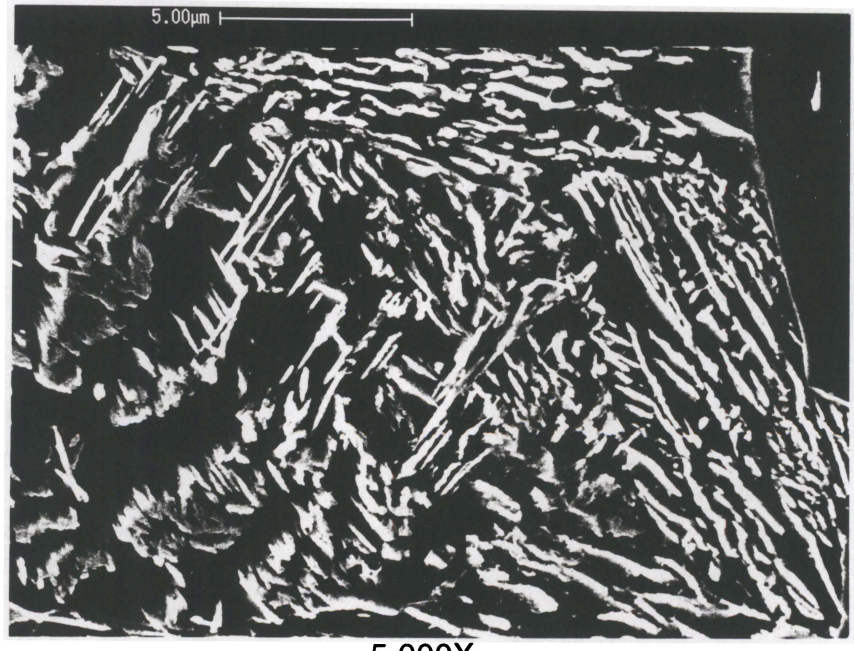
to the welding CCT diagram for MPC-3, only martensitic and bainitic transformation occurred in the CGHAZ with heat inputs from 12 to 120 KJ/in. As heat input increases from 12 to 120 KJ/in, the hardness decreases from 387 to 242HV. The microstructures predicted by using welding CCT diagram compare well with the metallographic examination results.

4.3.3 Carbide Evolution

Carbide morphology, type, and chemistry were examined for MPC-3, MPC-25, and MPC-18 (service exposed, central portion of heat exchanger channel) using SEM, TEM, EDS and X-ray diffraction. Figures 4.119 through 4.122 show a typical carbide morphology in the MPC-3 material with cooling rates of 20 and 1 C°/min, which corresponds to the normalized and annealed conditions, respectively. Rod-like carbides were observed in the bainitic regions with a cooling rate of 20 C°/min. In contrast to the carbides in the bainitic region, the carbides in the pearlitic region with a cooling rate of 1 C°/min are characterized as lamella-like carbides. The type of carbides for both the normalized (20 C°/min) and annealed condition (1 C°/min) was identified as M_3C by using selected area diffraction and EDS. Figures 4.123 and 4.124 show a typical selected area diffraction pattern and EDS spectrum from the M_3C carbide (20 C°/min). A small amount of fine Mo_2C carbides were observed in the ferrite grain matrix at both cooling rates.

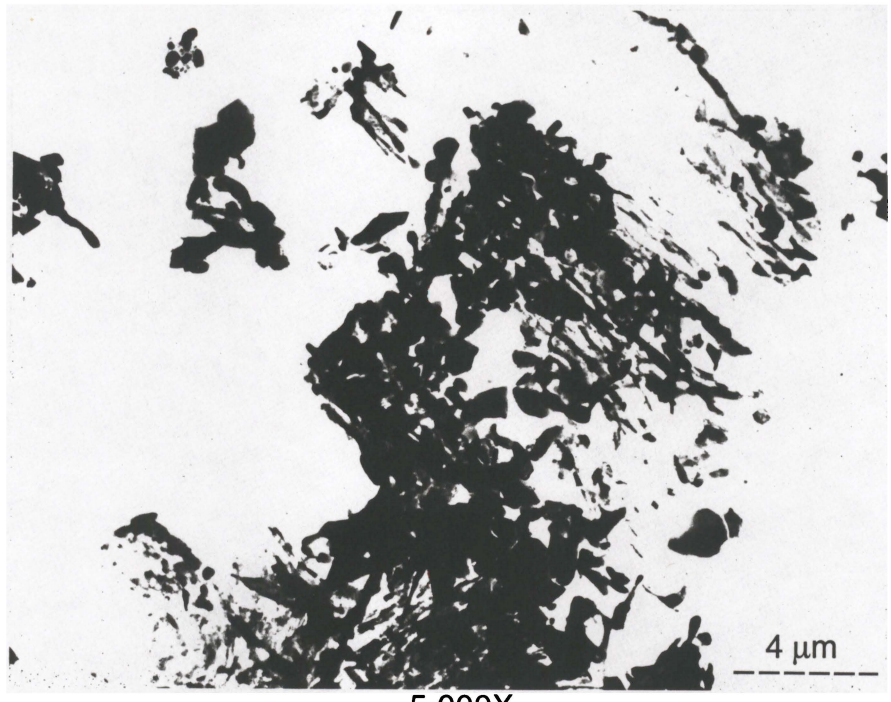


1,000X

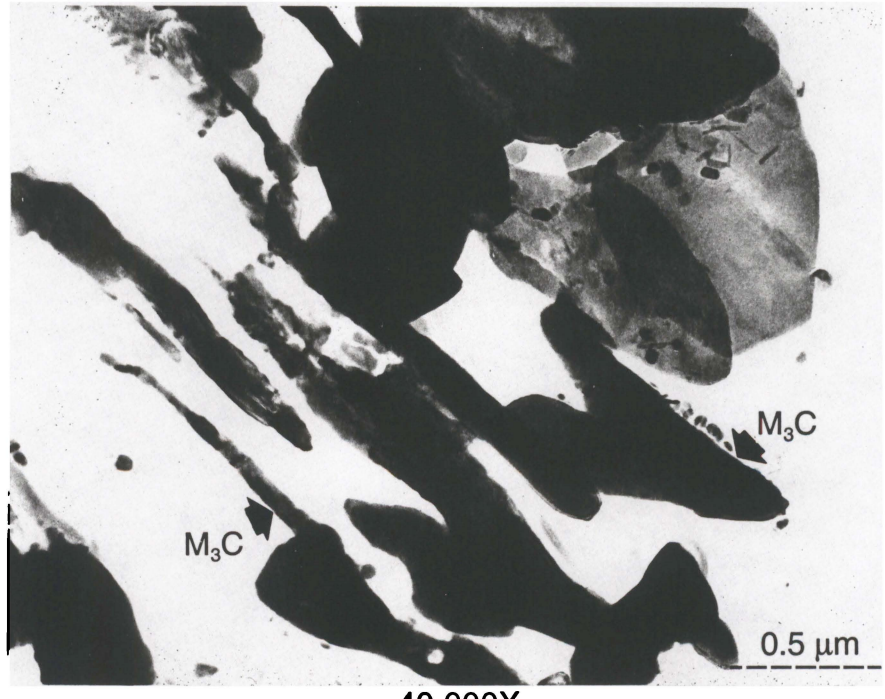


5,000X

Figure 4.119 Carbide morphology in bainitic region (MPC-3, 20 C°/min, SEM).

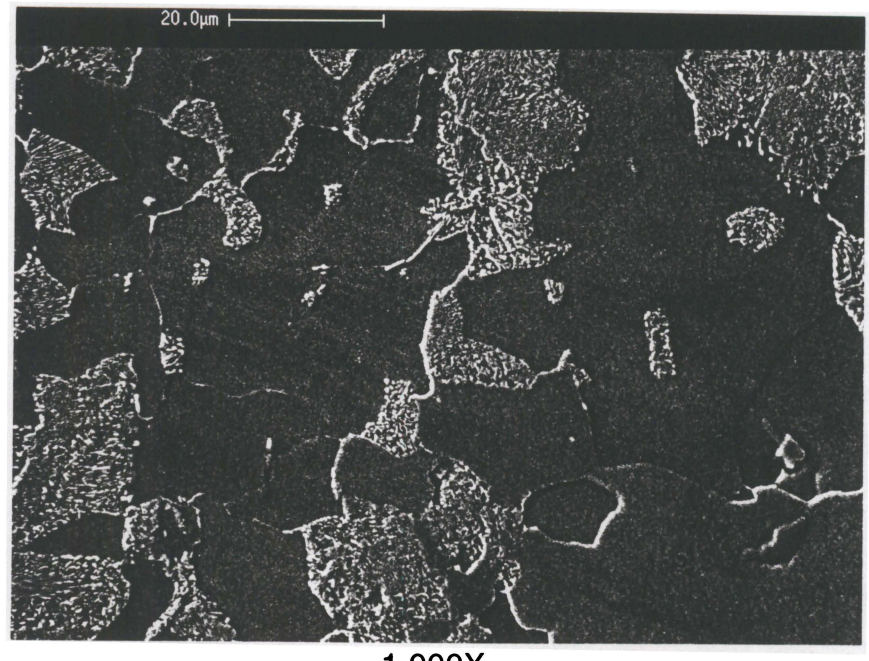


5,000X



40,000X

Figure 4.120 Carbide morphology in bainitic region (MPC-3, 20 C°/min, TEM).

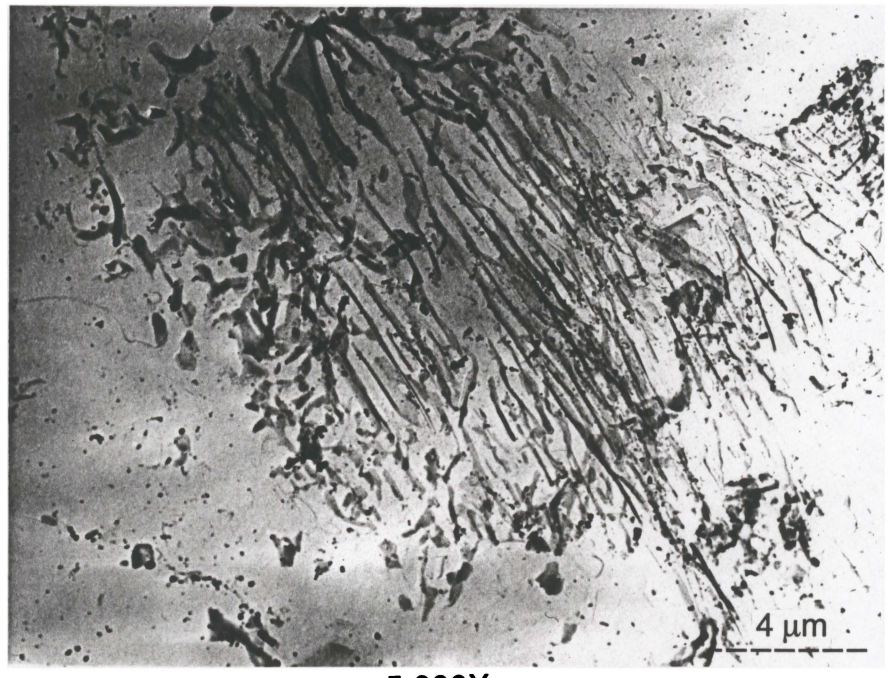


1,000X

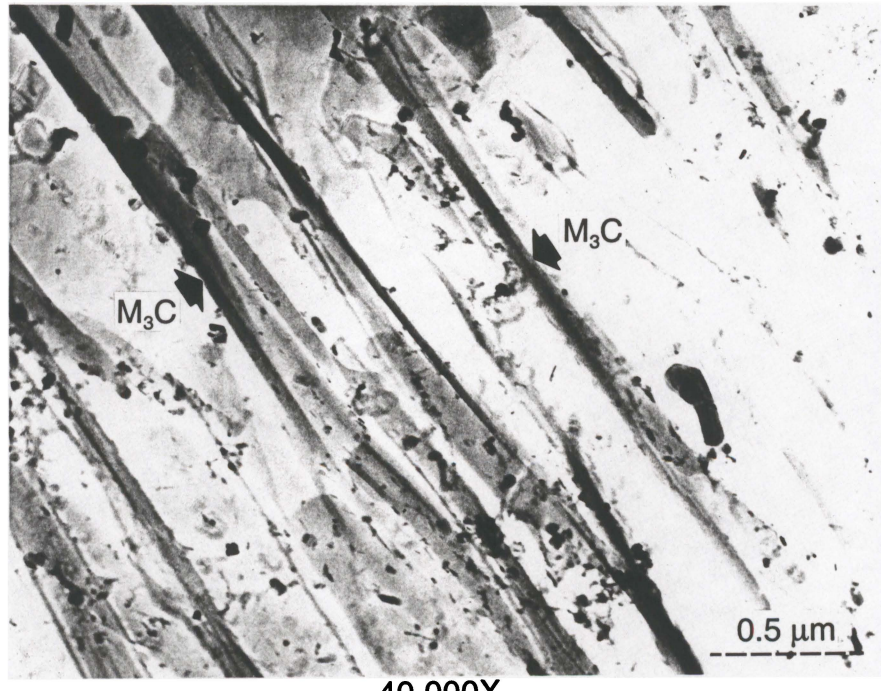


5,000X

Figure 4.121 Carbide morphology in pearlitic region (MPC-3, 1 C°/min, SEM).



5,000X



40,000X

Figure 4.122 Carbide morphology in pearlitic region (MPC-3, 1 C°/min, TEM).

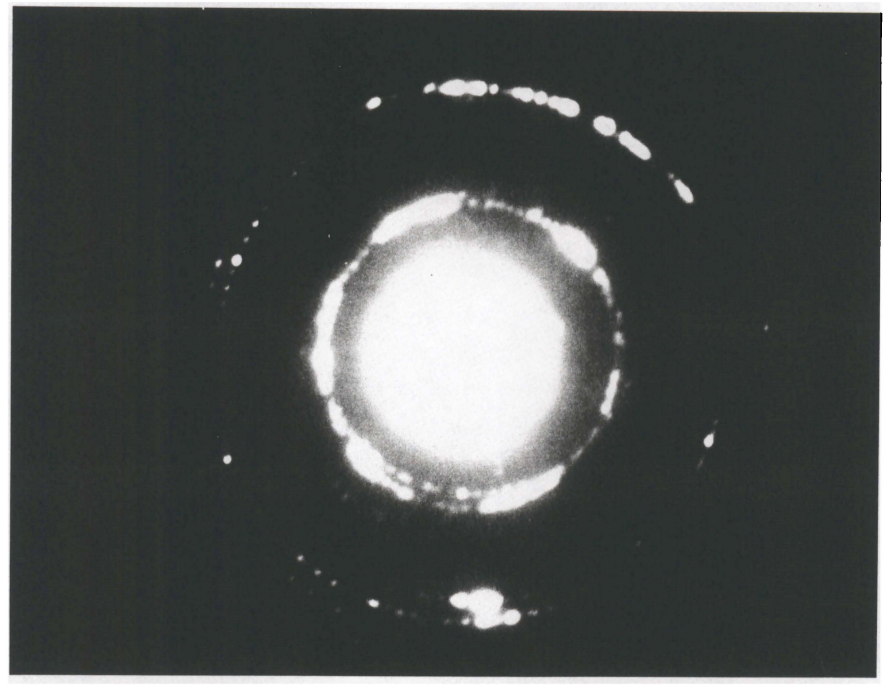


Figure 4.123 Diffraction pattern of M_3C carbide in the bainitic region (MPC-3, 20 C°/min).

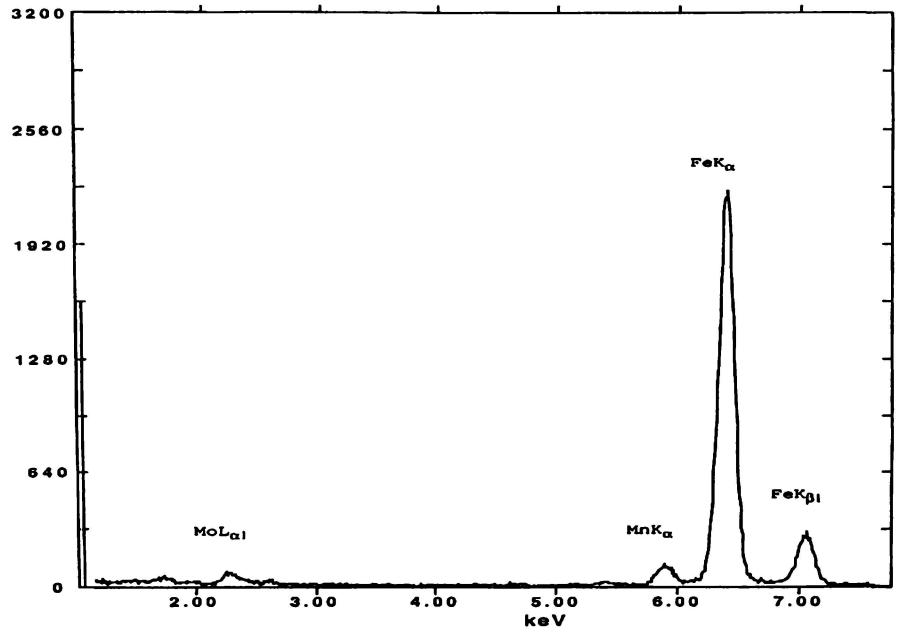
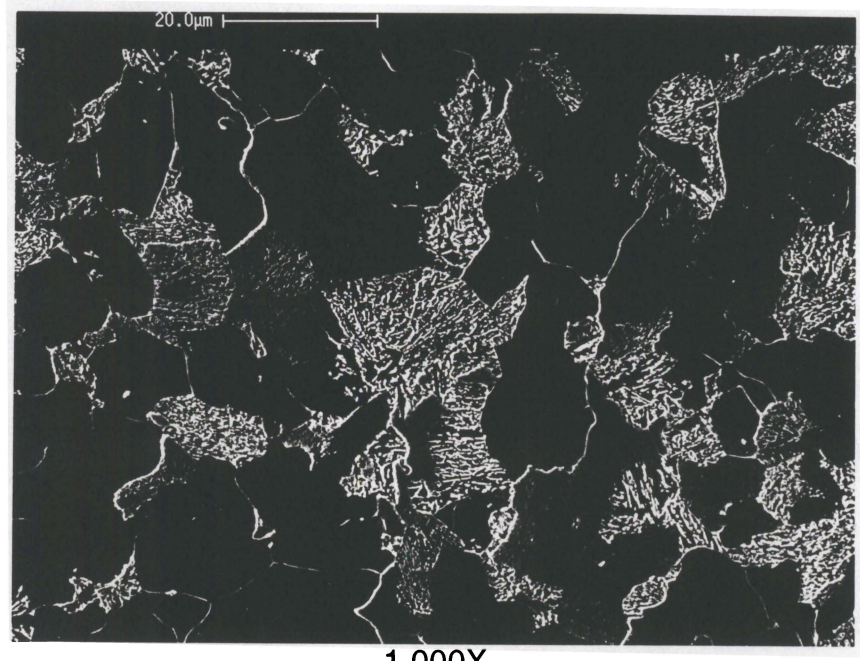


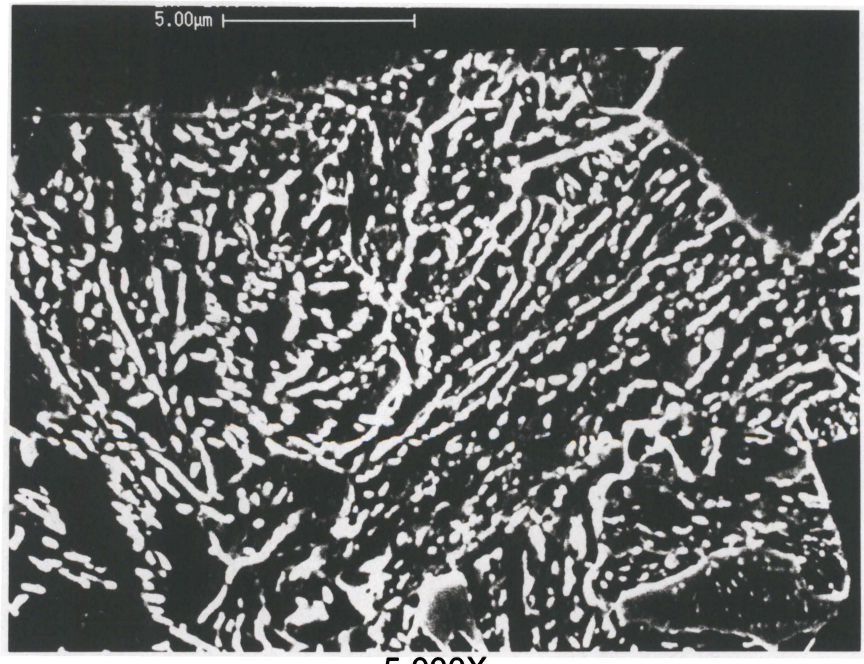
Figure 4.124 EDS spectrum of M_3C carbide (MPC-3, 20 C°/min).

The specimens (MPC-3) with cooling rates of 20 C°/min and 1 C°/min were tempered at 1150°F (621°C) for 15 hours to study the carbide evolution in C-0.5Mo. Carbide spheroidization occurred in the bainitic and pearlitic regions after tempering as shown in Figures 4.125 and 4.126. The majority of the carbides are identified as $M_{23}C_6$ in accord with the electron diffraction patterns and the EDS spectra as shown in Figures 4.127 and 4.128. More Mo_2C type carbides were observed in the ferrite grain matrix after tempering.

Carbides in the annealed only and annealed & tempered materials (MPC-25) were evaluated using TEM and EDS. The annealing heat treatment was conducted at 1652°F (900°C) for 3 hours with furnace cool at a cooling rate of 1 C°/min. After annealing, the material was tempered at 1283°F (695°C)-15 hours and 1337°F (725°C)-15 hours. Figure 4.129 shows the SEM images of the microstructures and carbide morphology of the annealed material. The carbide morphology in the pearlite regions is a mixture of globular and lamellar carbides. Figures 4.130 and 4.131 represent the TEM images of carbides in pearlite region, ferrite matrix, and at F/F grain boundaries. The carbide type in the pearlite regions was identified as M_3C using selected area diffraction of TEM. The M_3C carbides in the pearlite region were verified as Fe-Mo alloy carbides using EDS as presented in Figure 4.132. Some carbides at the F/F grain boundaries and in the ferrite grain matrix were identified as Mo_2C by using EDS. Figure 4.133 is a typical EDS spectrum of Mo_2C carbides [100].

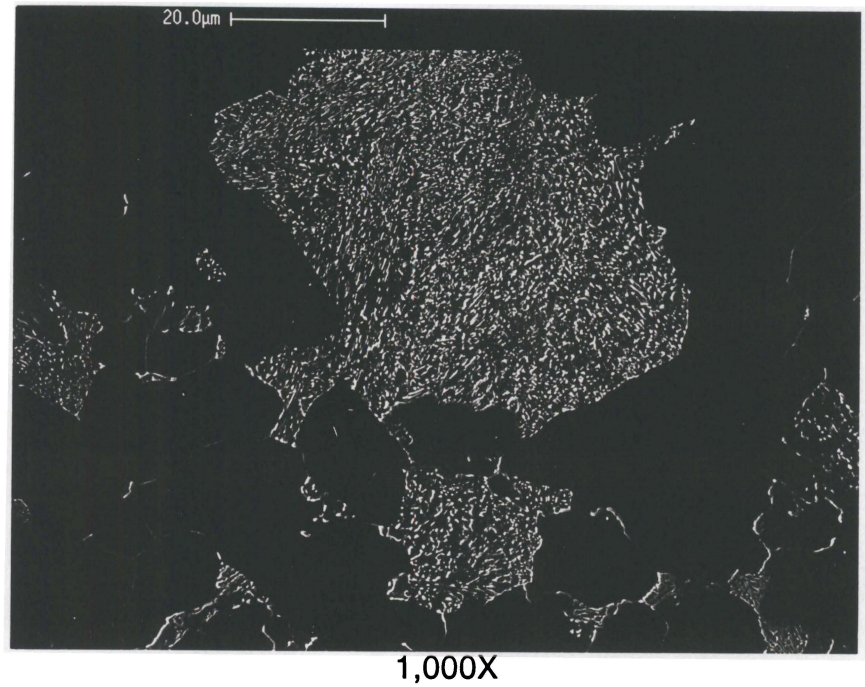


1,000X

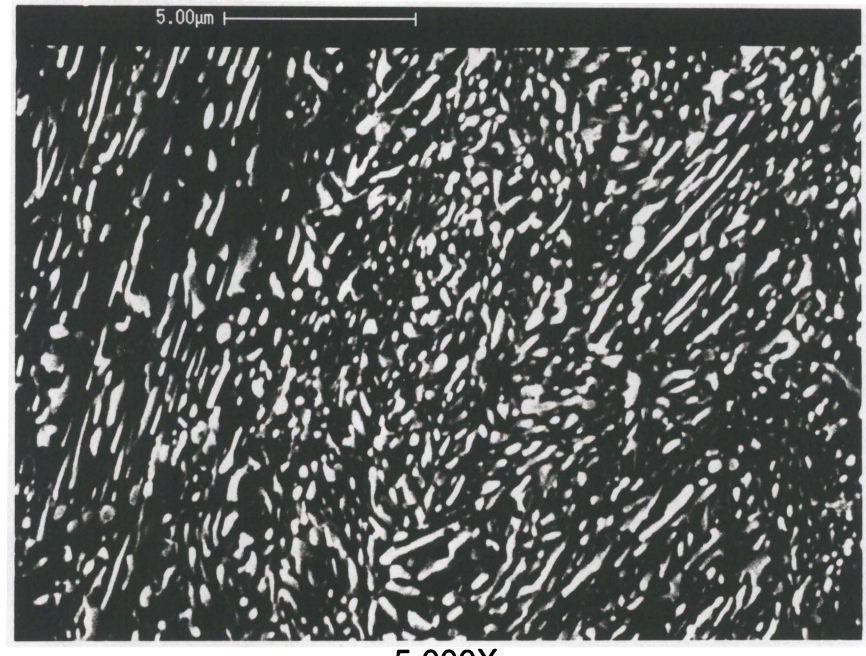


5,000X

Figure 4.125 Spheroidized carbides in tempered bainite region (MPC-3, 20 C°/min, 1150°F for 15 hrs., SEM).



1,000X



5,000X

Figure 4.126 Spheroidized carbides in pearlite region after tempering (MPC-3, 1 C°/min, 1150°F-15 hrs., SEM).

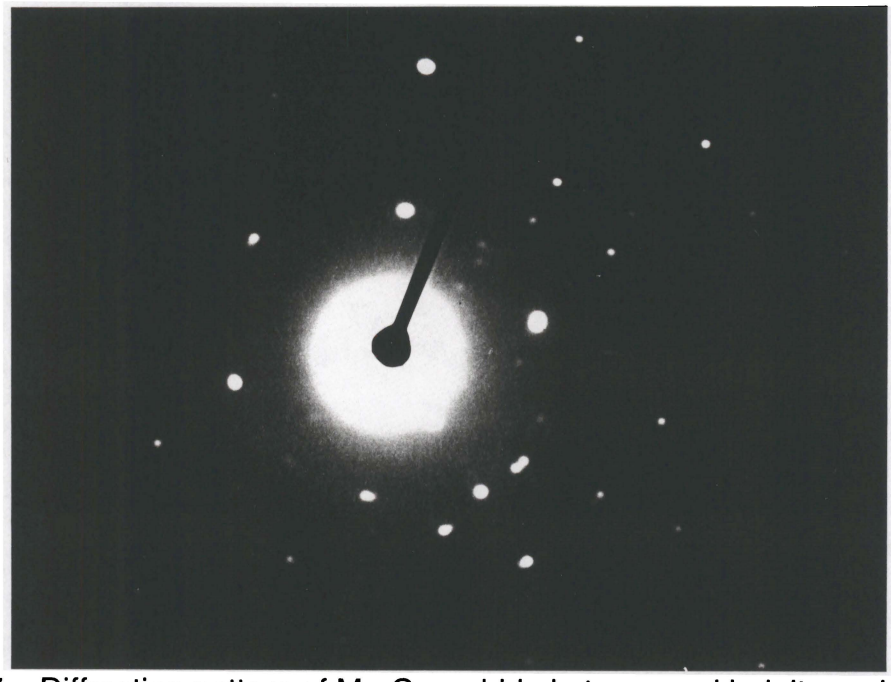


Figure 4.127 Diffraction pattern of $M_{23}C_6$ carbide in tempered bainite region (MPC-3, 20 C°/min, 1150°F-15 hours).

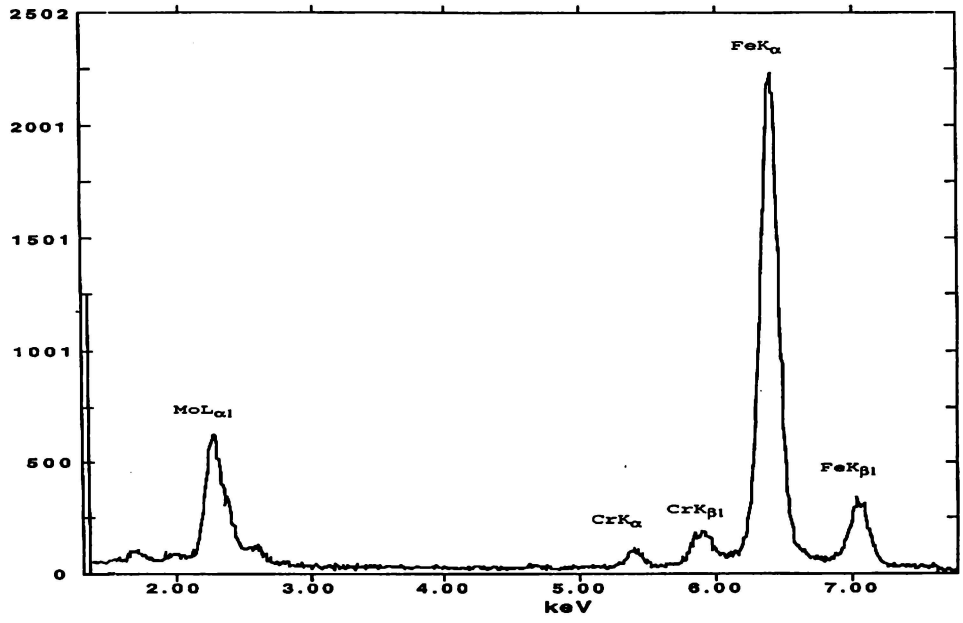
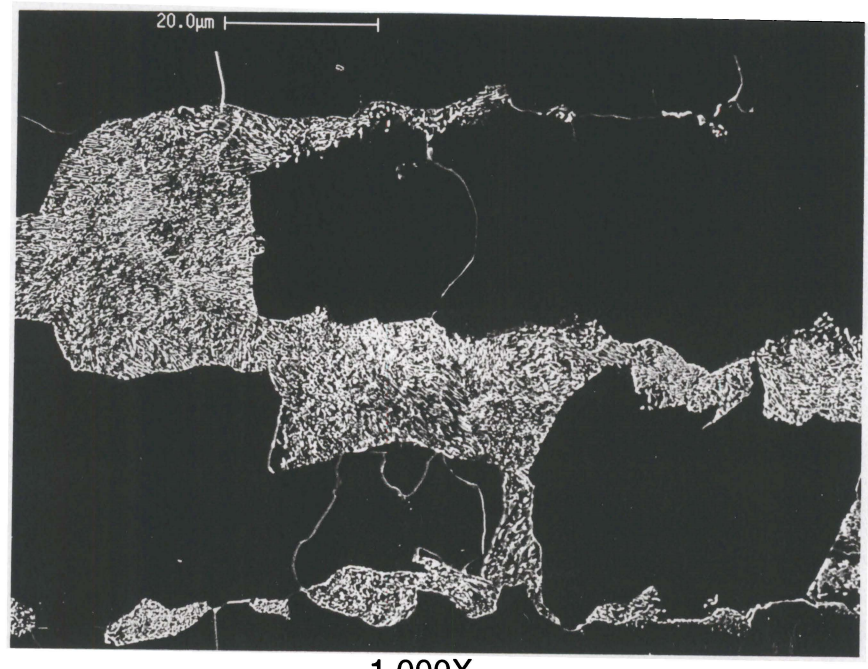
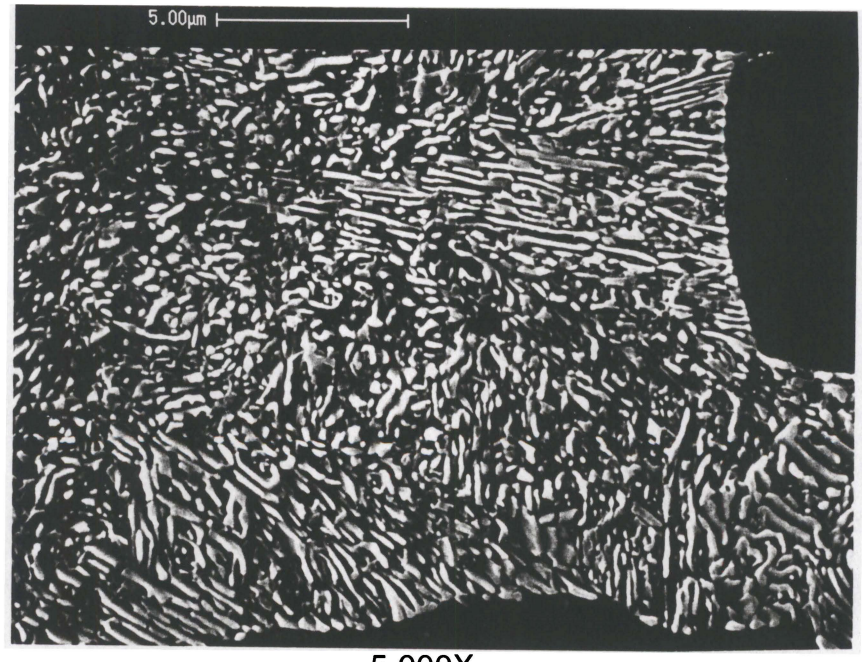


Figure 4.128 EDS spectrum of $M_{23}C_6$ carbide in tempered bainite region (MPC-3, 20 C°/min, 1150°F-15 hours).



1,000X

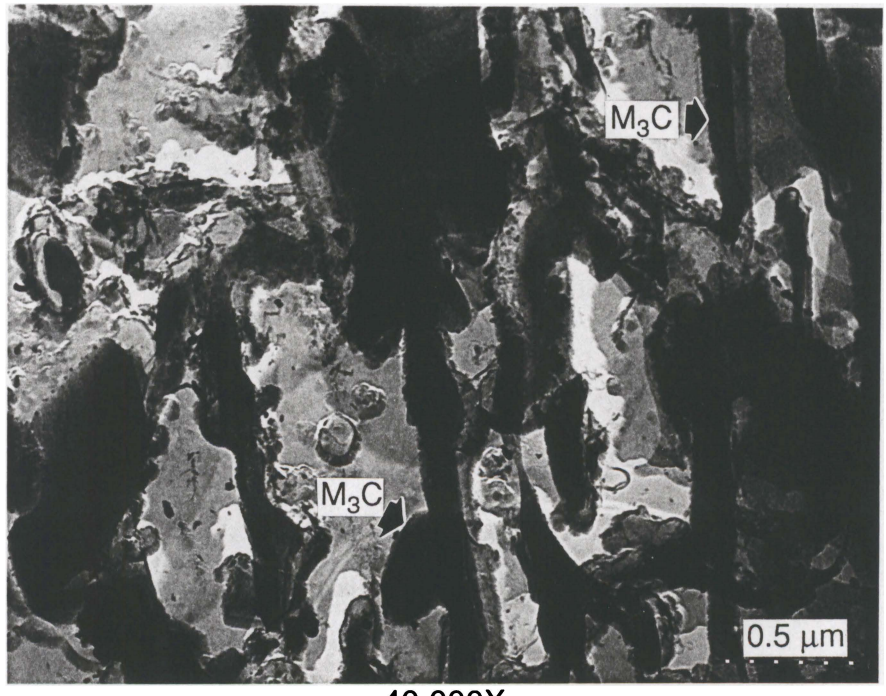


5,000X

Figure 4.129 Pearlite microstructure in annealed material (MPC-25).

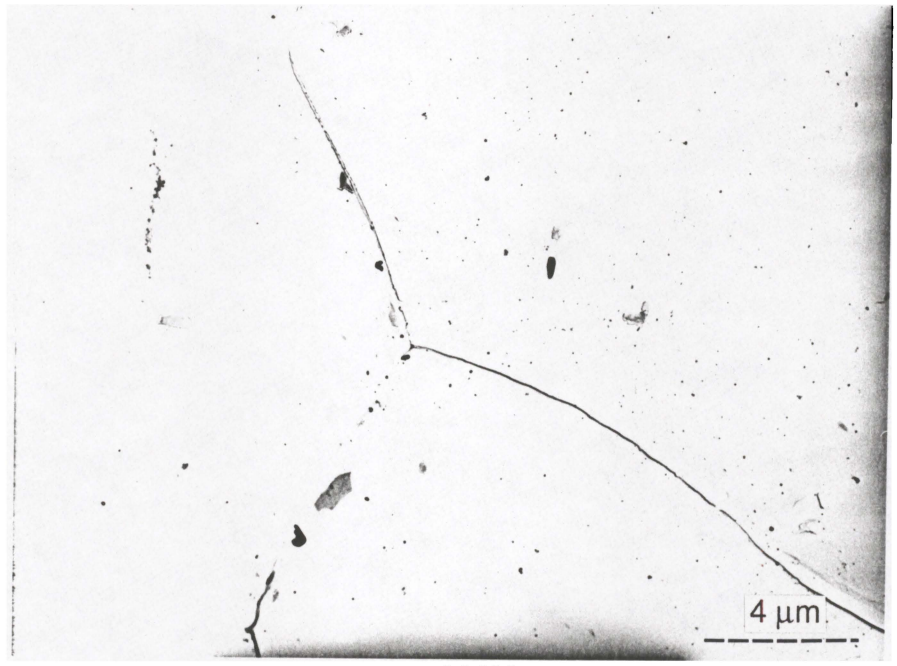


5,000X

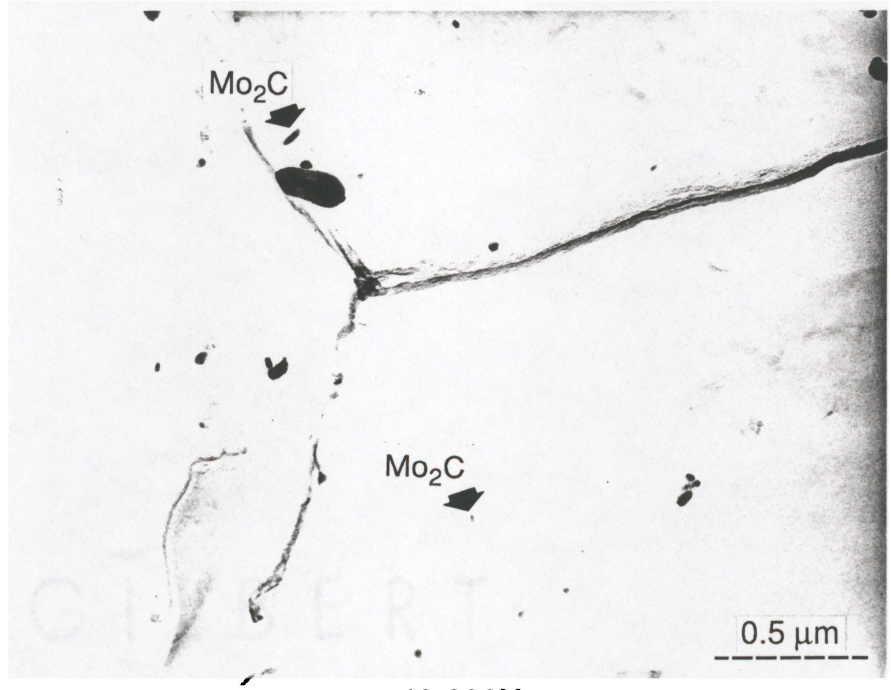


40,000X

Figure 4.130 TEM carbide images in pearlitic region of the annealed material (MPC-25).



5,000X



40,000X

Figure 4.131 TEM carbide images at F/F grain boundaries and in ferrite grain matrix in the annealed material (MPC-25).

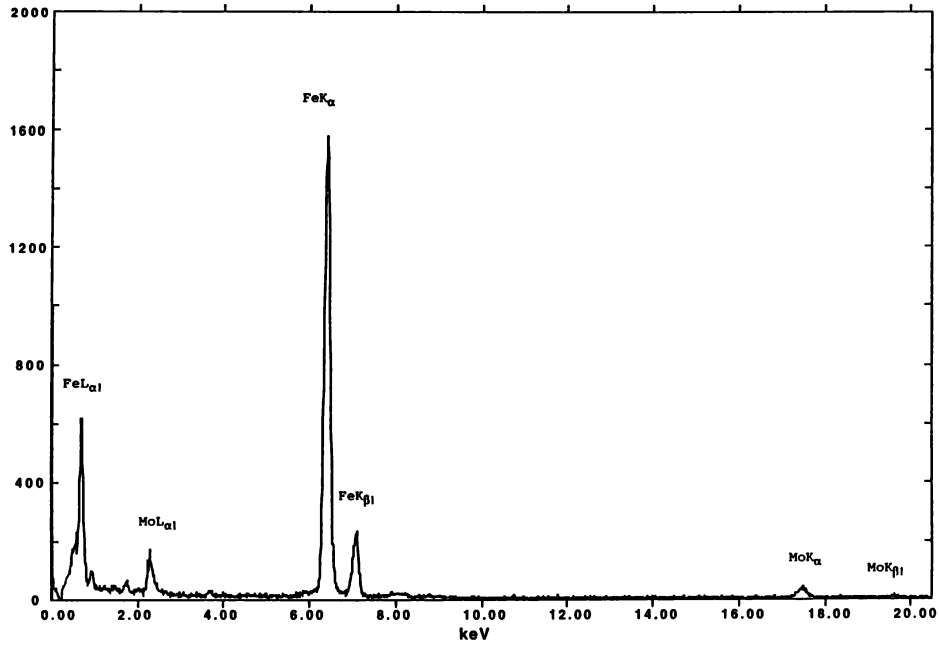


Figure 4.132 A representative EDS spectrum of M_3C carbide in the annealed material (MPC-25).

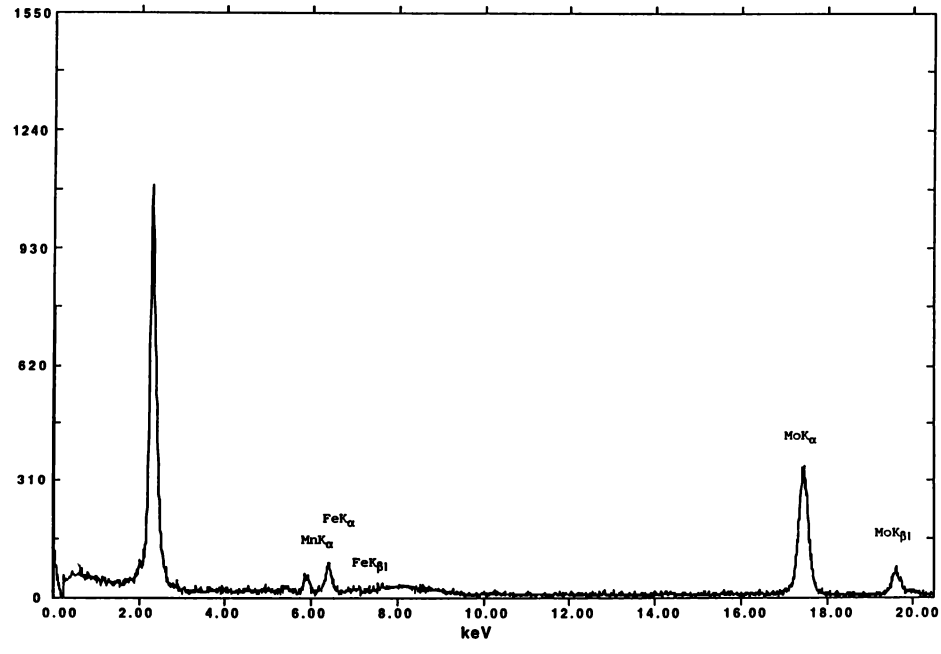
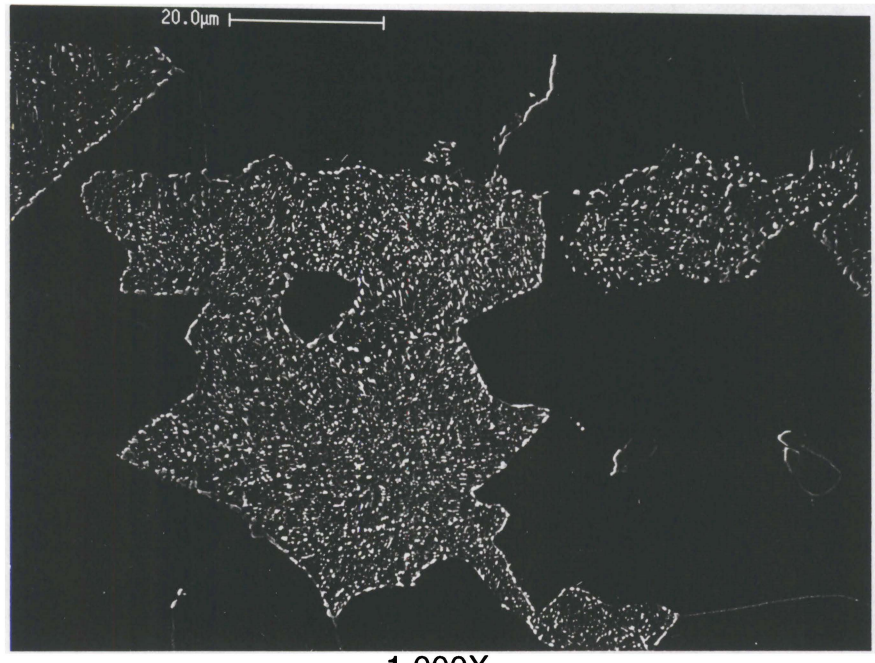


Figure 4.133 A representative EDS spectrum of Mo_2C carbide in the annealed material (MPC-25).

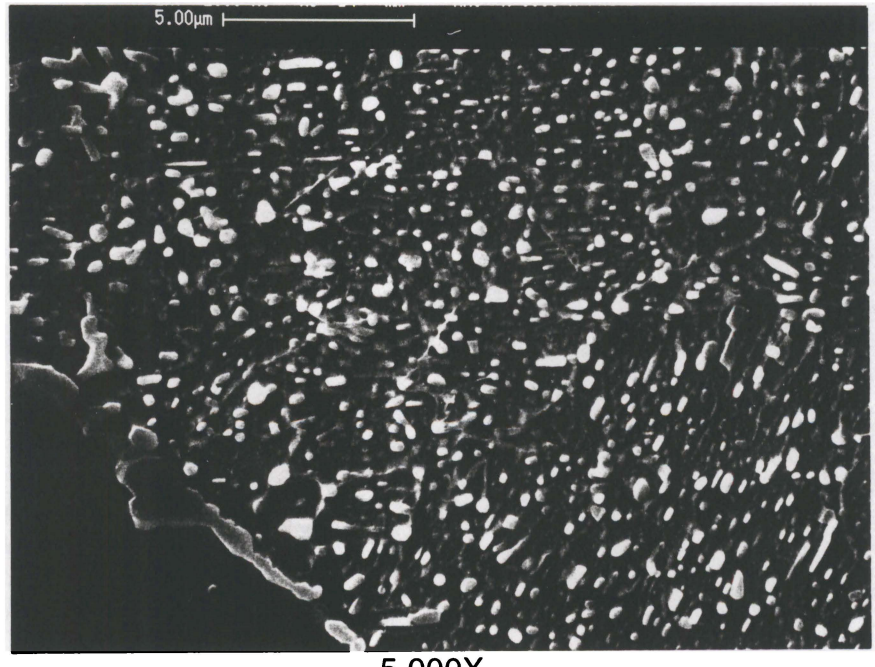
Acquirement of selected area diffraction from the Mo_2C carbides is difficult due to the small size of Mo_2C carbides.

Carbides in the annealed & tempered MPC-25 material (1283°F-15 hrs. and 1337°F-15 hrs.) were coarsened and changed to a globular shape compared to the lamellar carbides in the annealed material. Figures 4.134 through 4.136 show the typical carbide morphology in the annealed & tempered MPC-25 materials (1283°F-15 hrs.). In general, the coarsened carbides in the pearlite regions were identified as $M_{23}C_6$ using selected area diffraction. The chemical elements in the coarsened carbides were analyzed using EDS as shown in Figure 4.137. It should be noted that the carbides consist of Fe, Mo, Mn, and Cr. Some coarsened M_3C carbides were also found in the annealed & tempered material using TEM. Fine carbides are randomly distributed in the ferrite grain matrix as shown in Figure 4. 136. The fine needle-like carbides in the ferrite grains and at the F/F grain boundaries were identified as Mo_2C carbides with Fe, Mn, and Cr.

In addition to the selected area electron diffraction and EDS, X-ray diffraction was applied for carbide identification for the annealed and annealed & tempered MPC-25 materials. Carbides were extracted using electrolytic extraction technique. A sample was place in a methanol solution (10% HCl) with a constant voltage of 10 volts referred to a platinum electrode for 2 hours. The carbides were separated from the solution using a centrifuge device. The

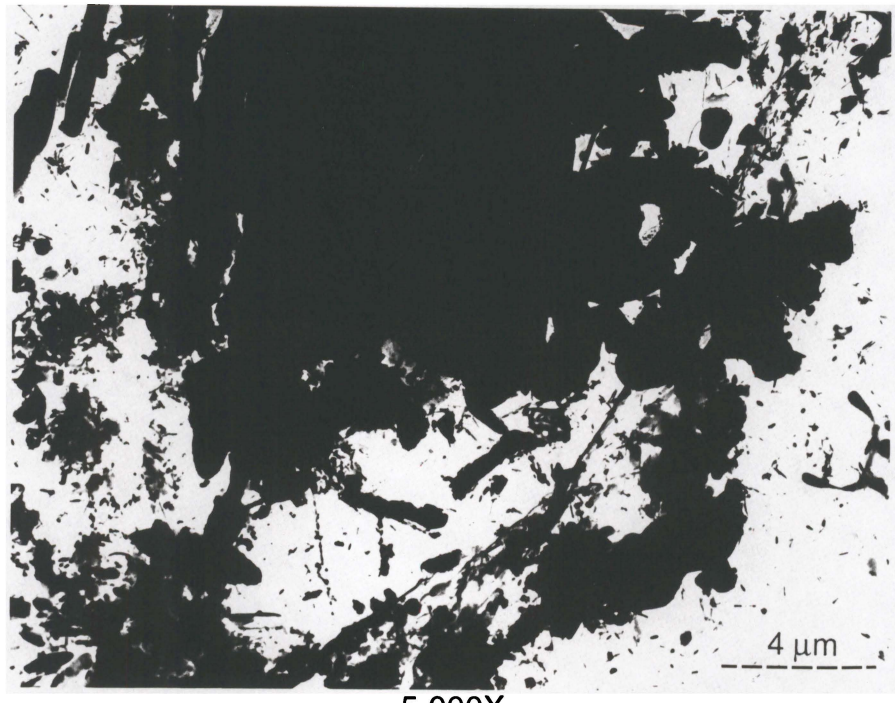


1,000X

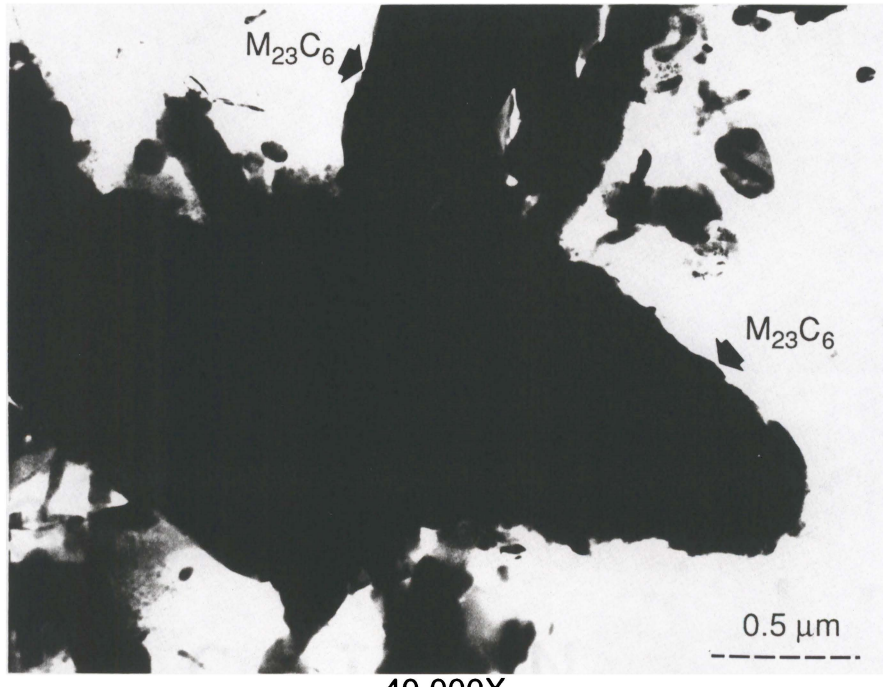


5,000X

Figure 4.134 Spheroidized carbides in pearlite region in the annealed & tempered material (MPC-25, 1283°F-15 hrs., SEM).

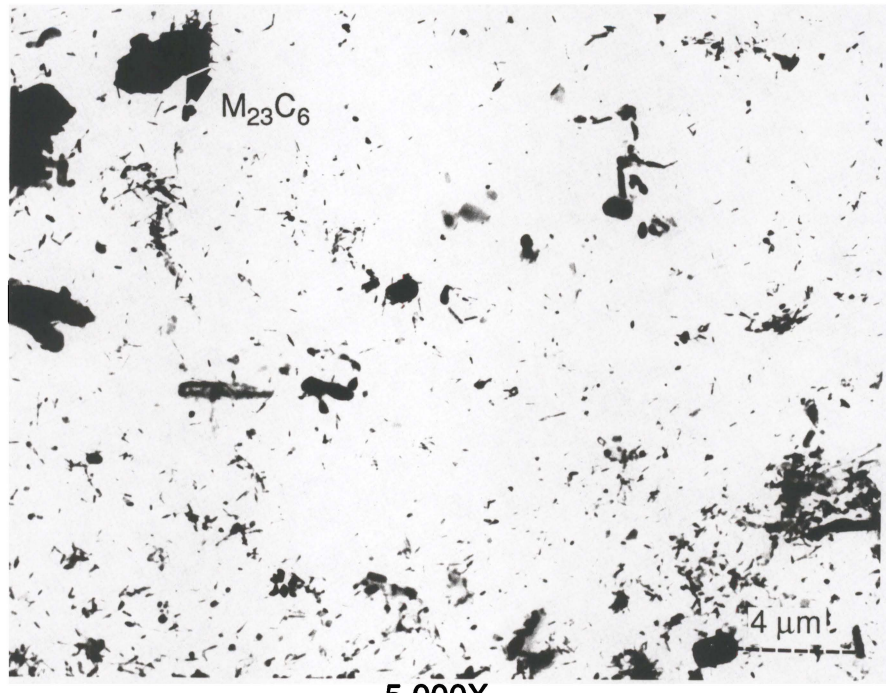


5,000X

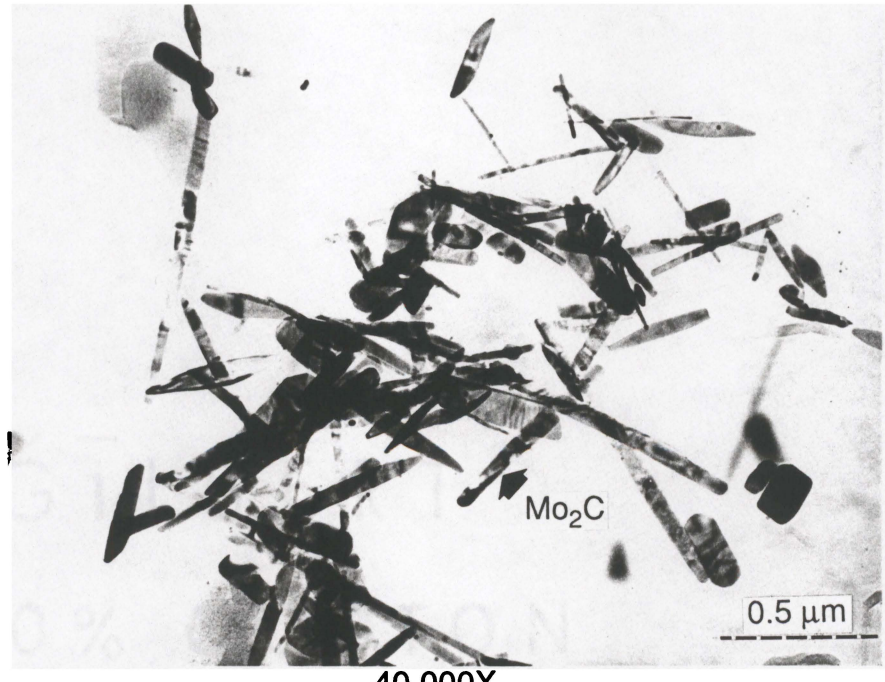


40,000X

Figure 4.135 Carbide morphology in pearlite region of annealed & tempered material (MPC-25, 1283°F-15 hrs., TEM).



5,000X



40,000X

Figure 4.136 Carbide morphology in ferrite grain matrix of annealed & tempered material (MPC-25, 1283°F-15 hrs., TEM).

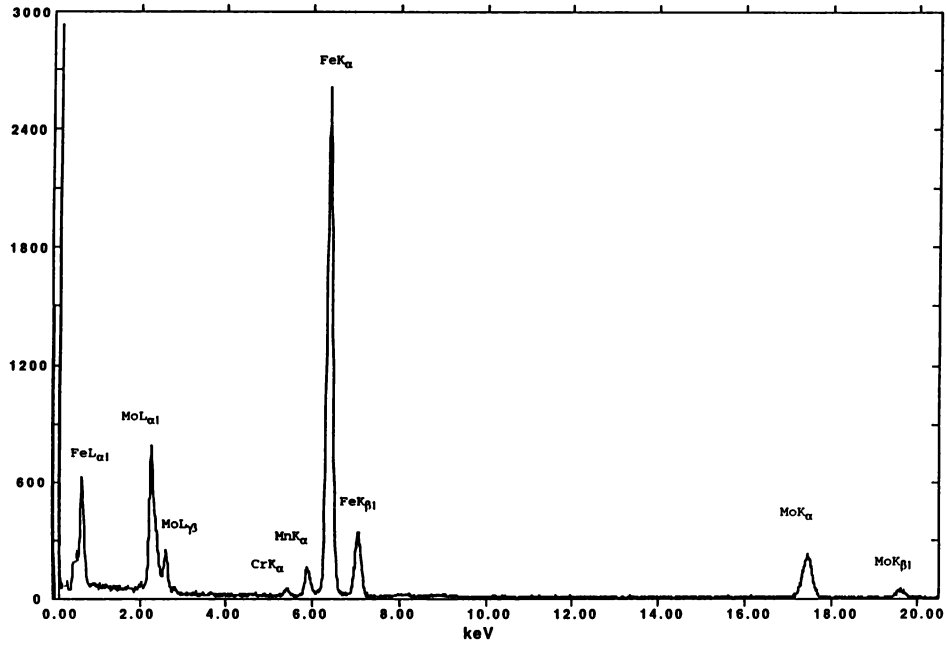


Figure 4.137 A representative EDS spectrum of $M_{23}C_6$ carbide in the annealed & tempered material (MPC-25, 1283°F-15 hrs.).

Table 4.4 Carbide identification results for annealed and annealed & tempered MPC-25 materials using X-ray diffraction technique.

MPC-25	M_3C	$M_{23}C_6$	Mo_2C
Annealed	Strong	None	Weak
Annealed & Tempered (1283°F-15 hrs.)	Weak	Moderate	Strong
Annealed & Tempered (1337°F-15 hrs.)	Weak	Moderate	Strong

carbides collected from the solution were cleaned using high purity methanol. The results are summarized in Table 4.4. It is noticed that the intensity of Mo_2C appears strong for annealed & tempered materials. Figure 4.138 is a typical X-ray diffraction spectrum from the annealed & tempered material (1283°F-15 hrs.).

In the service exposed C-0.5Mo material (MPC-18), majority of the carbides was identified as M_3C as shown Figures 4.139 and 4.140. Fine Mo_2C carbides were observed in the ferrite grain matrix as shown in Figures 4.141 and 4.142. $M_{23}C_6$ carbide was not found in the service exposed C-0.5Mo material.

In summary, most carbides in the normalized or annealed C-0.5Mo materials were identified as M_3C type in bainite or pearlite regions. Some fine Mo_2C carbides were found in ferrite grain matrix and at grain boundaries. After tempering heat treatment (1150°F-15 hours), coarsened carbides were observed and the shape of the carbides changed from rod-like or lamellar carbides into globular carbides. Most globular carbides were identified as

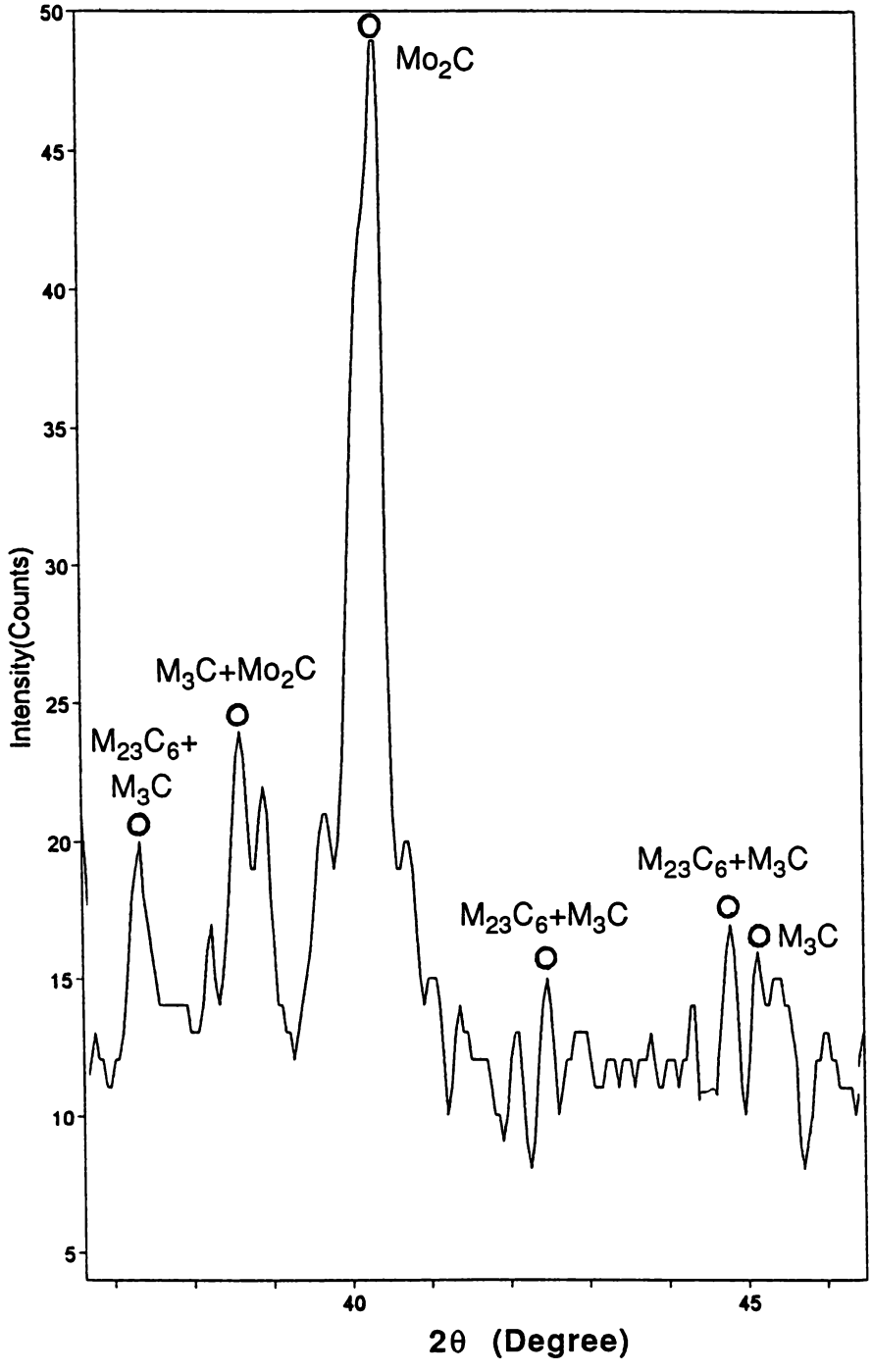
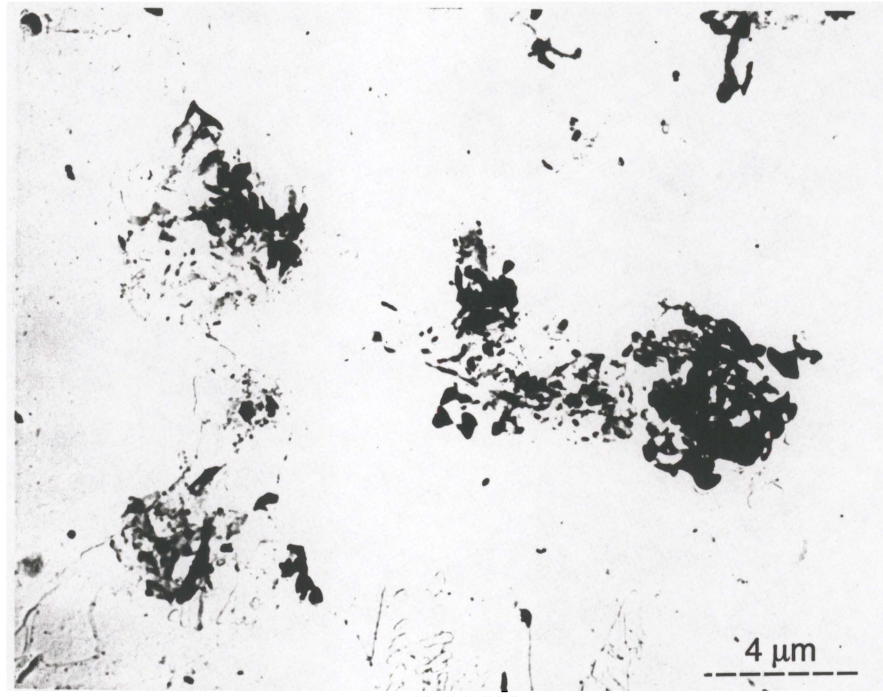
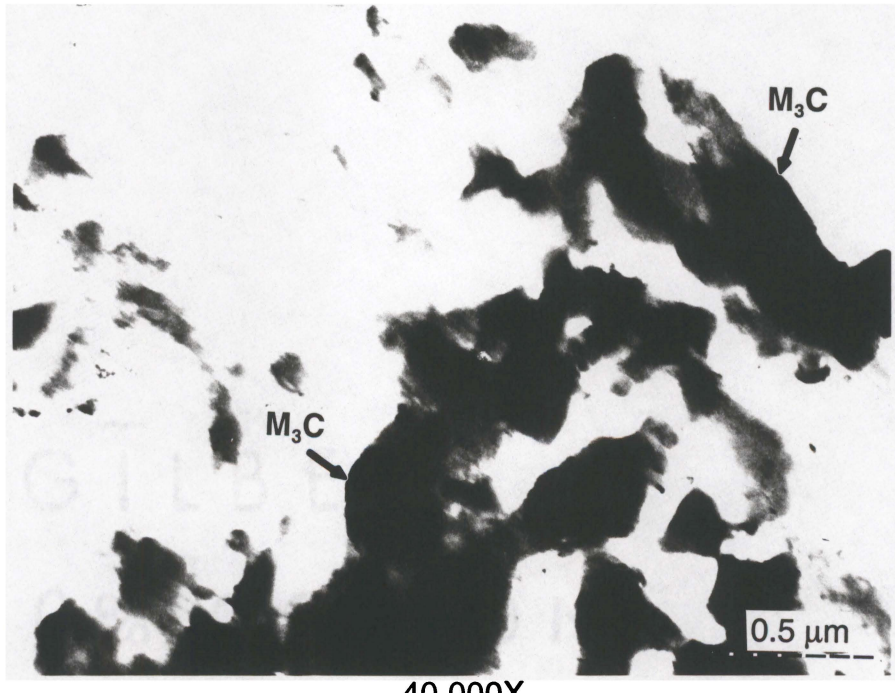


Figure 4.138 Typical X-ray diffraction spectra of the carbides extracted from annealed & tempered material (MPC-25, 1283°F-15 hrs.).



5,000X



40,000X

Figure 4.139 Carbide morphology in bainitic regions of service exposed material (MPC-18).

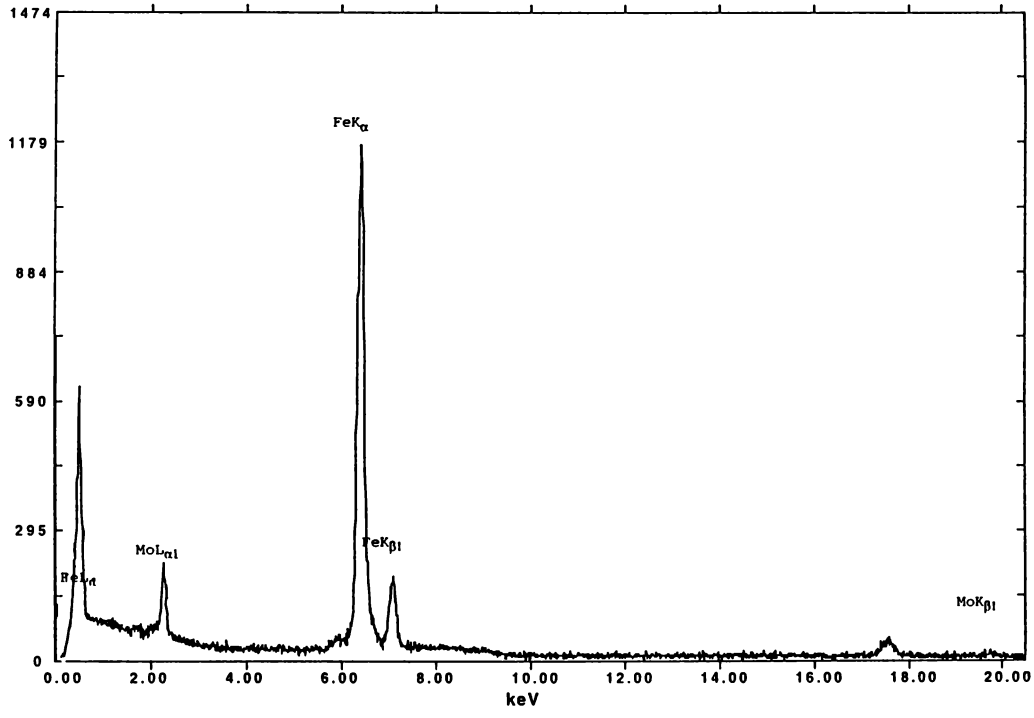
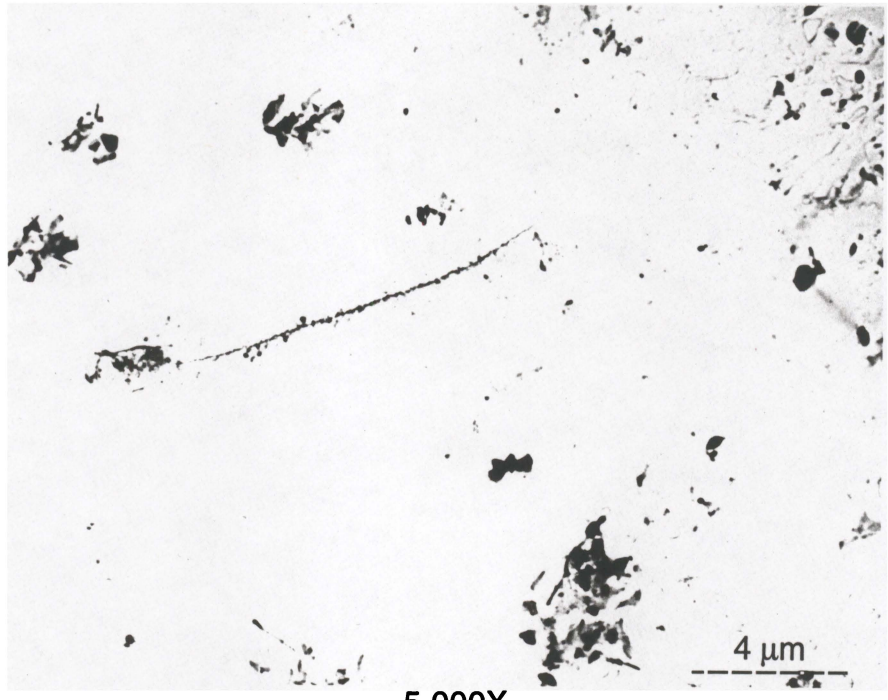
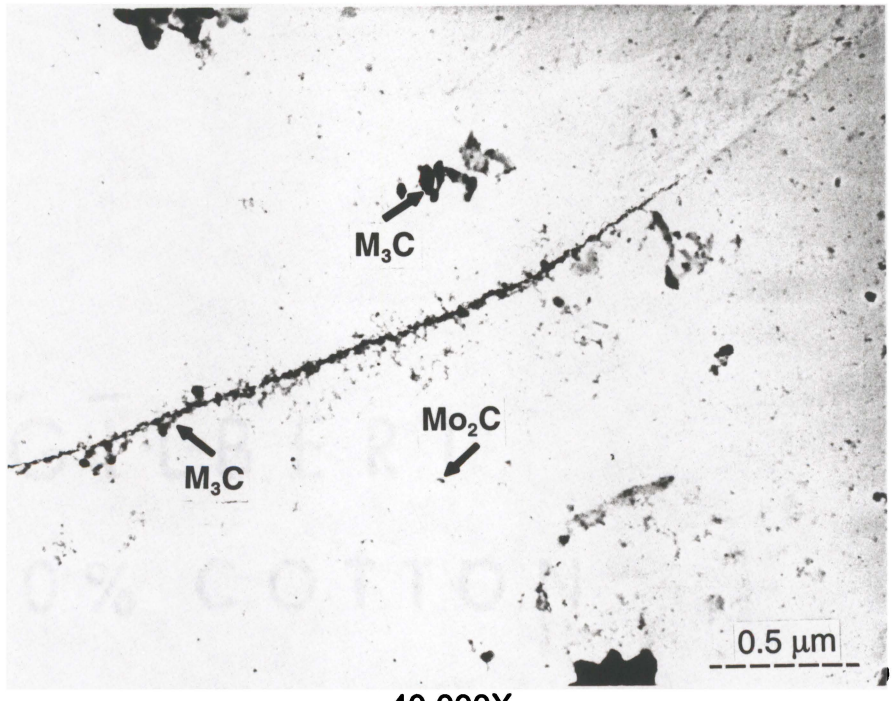


Figure 4.140 A representative EDS spectrum of M_3C carbide in the annealed & tempered material (MPC-25, 1283°F-15 hrs.).



5,000X



40,000X

Figure 4.141 Carbide morphology in ferrite grain matrix and along F/F grain boundary of service exposed material (MPC-18).

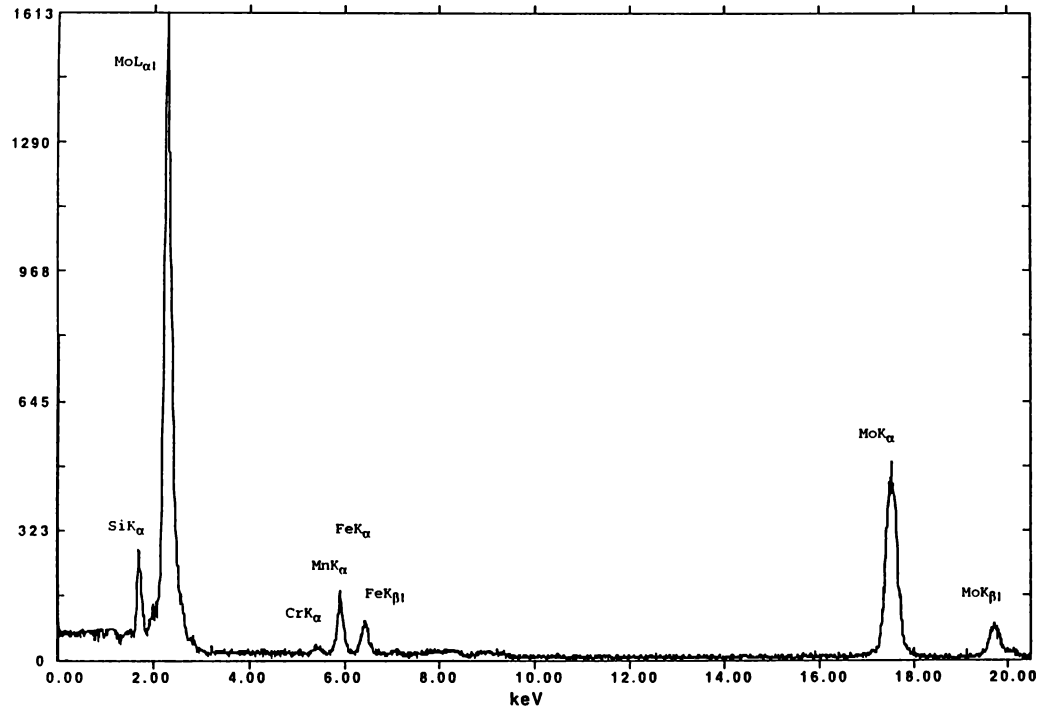


Figure 4.142 A representative EDS spectrum of Mo_2C carbide in service exposed material (MPC-18).

$M_{23}C_6$ in accord with the electron diffraction patterns and the EDS spectrums. More Mo_2C carbides were observed in the ferrite grain matrix after tempering. Therefore, during tempering heat treatment or PWHT, carbide evolution occurs to form $M_{23}C_6$ and Mo_2C type carbides, which are more stable than and can enhance hydrogen attack resistance for C-0.5Mo steel as demonstrated in the hydrogen exposed tests.

CHAPTER 5

MECHANISM OF HYDROGEN ATTACK

The previous sections detailed the characterization of hydrogen attack damage in the service exposed components and autoclave exposed samples using quantitative metallographic analysis and methane determination. In following sections, a hydrogen attack mechanism is approached from the standpoint of hydrogen absorption and diffusion, methane bubble nucleation, methane evolution, and methane bubble growth to form microcracks. A model for hydrogen attack limits (Nelson Curve) was developed for C-0.5Mo steel based on hydrogen attack kinetics and the database established in this research. A methodology for hydrogen attack evaluation is recommended by using methane determination and a correlation between hydrogen damage level and morphology.

It is well known that methane pressure is the driving force for hydrogen attack [101]. Therefore, methane pressure in bubbles within the wall of one-side hydrogen exposure assembly was approached based on hydrogen solubility, free energy of methane formation, and the correlation between methane fugacity and methane pressure. The hydrogen solubility distribution was determined in accord with Sievert's law and Fick's law [102]. The free energy of methane formation by hydrogen and carbide (Fe_3C) reactions is derived based on thermodynamic theory. Applying the hydrogen solubility

distribution to the equations of methane pressure as a function of "hydrogen pressure", the methane pressure distribution was calculated for the one-side exposed assembly. The methane pressure distribution explains the hydrogen attack damage profiles through wall thickness for one-sided hydrogen exposure. In addition, methane pressures were calculated resulting from the reactions of hydrogen and Fe_3C, Mo_2C, and $Cr_{23}C_6$ to demonstrate the effect of carbide types on hydrogen attack susceptibility.

Hydrogen attack limits (Nelson Curve) were modeled for C-0.5Mo in accord with a hydrogen attack parameter (P_w) [103] and the database developed in this research. Hydrogen attack is a time dependent process. From this model, hydrogen attack limits (combination of temperature and hydrogen partial pressure) are expressed as a function of exposure time. A modified Nelson Curve for C-0.5Mo was defined for a long term operation (approximately 28 years).

A methodology is recommended for hydrogen attack damage evaluation using methane determination (gas chromatography or vacuum fusion techniques) combined with two master curves (FA%/FL% vs. methane, FA%/FL% vs. bubble size) developed in this research. The early stages hydrogen attack can be detected by methane determination using a small amount of material.

5.1 Methane Bubble Nucleation and Methane Evolution

Methane evolution was studied by determining the hydrogen concentration dissociated from the methane as a function of exposure time in the static autoclave exposed samples. The MPC-3 material utilized for the methane evolution study was re-normalized (1650°F-2 hrs.) and tempered (1150°F-2 hrs.) to eliminate any in-service effect. The samples were exposed at a temperature 850°F and a hydrogen pressure of 500 psi with time increments of 159, 185, 300, 410, 485, and 498 hours.

Figure 5.1 presents the methane concentration as a function of exposure time at temperature 850°F and hydrogen pressure 500 psi. Methane concentration (C_{CH4}, ppm) increases upon an increase in exposure time in a linear relationship:

$$C_{CH4} = A\,t$$

where "A" is the rate of methane formation depending upon exposure temperature, hydrogen partial pressure, and material; "t" is exposure time (hours). From Figure 5.1, it is noticed that the reaction rate is constant at an exposure temperature of 850°F and hydrogen pressure of 500 psi (early stages of methane formation). For these testing conditions, the methane accumulation rate is determined to be 1.83×10^{-2} ppm/hr for MPC-3.

SEM examination demonstrated that hydrogen attack occurrence was in the form of insolated bubbles at grain boundaries and carbide/ferrite interfaces in the bainitic regions of the sample (MPC-3) exposed at 850°F-500 psi H_2 for

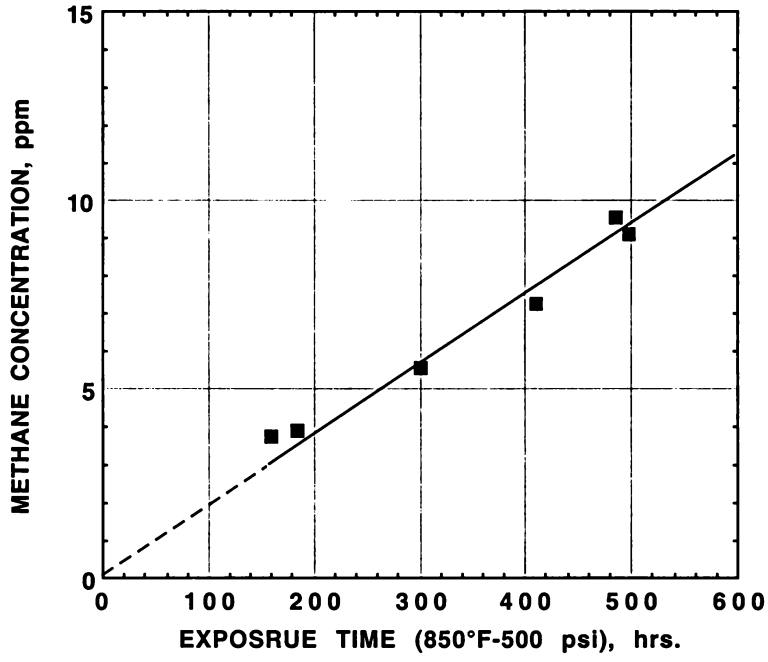
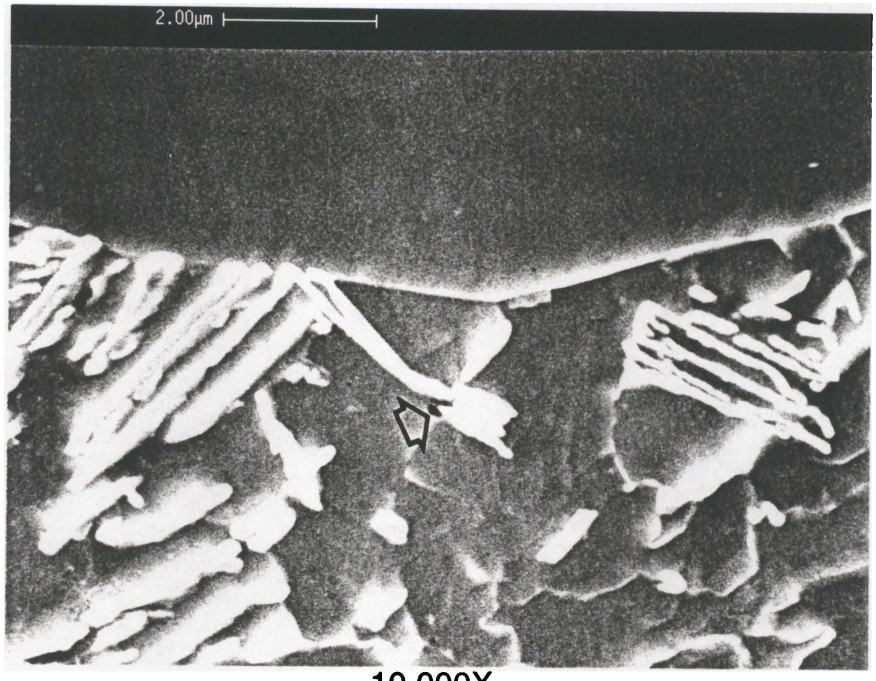


Figure 5.1 Methane concentration as a function of exposure time (MPC-3, N&T, 850°F-500 psi H_2).

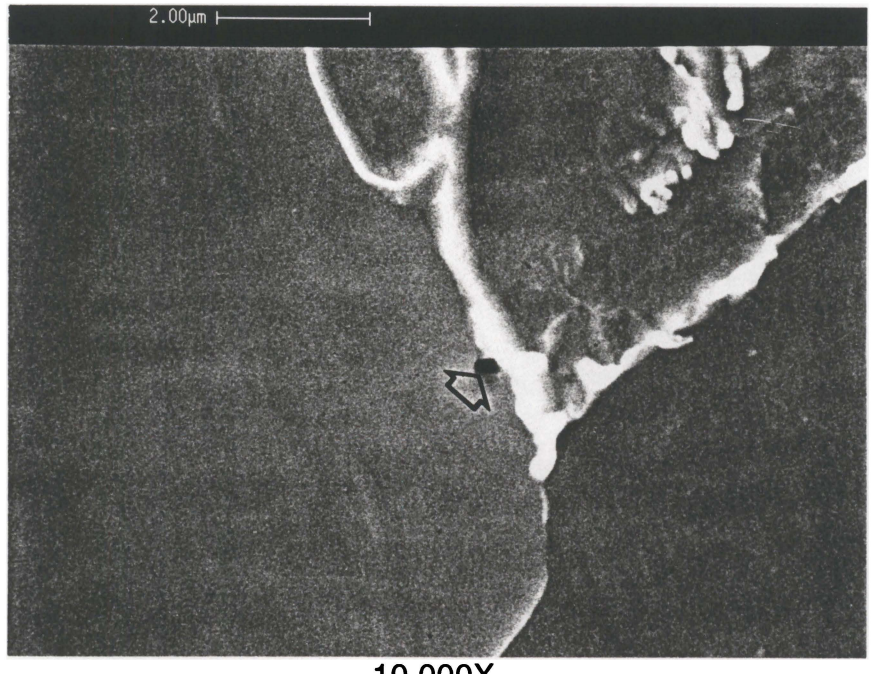
159 hours (3.8 ppm CH_4) as shown in Figure 5.2. The fraction of damaged boundaries (FL%) was determined as approximately 1%. The average bubble diameter is approximately 0.2 microns.

Extrapolating the plot as shown in Figure 5.1, the methane concentration is zero for the condition without hydrogen exposure. This indicates that methane gas evolution begins at the instant of hydrogen exposure in the test condition of 850°F-500 psi H_2. This phenomena was independently observed by Geiger [31] and Sundararajan [103] by measuring hydrogen permeability, methane formation rate and swelling rate as well as metallographic examination. The hydrogen permeation and methane formation were observed at the beginning of hydrogen exposure for C-0.5Mo, 1.25Mn-0.5Mo, 1Cr-0.5Mo, 1.25Cr-0.5Mo-0.5Si, and 2.25Cr-1Mo steels [31]. It was recognized that increased hydrogen permeability was related to the depth of hydrogen attack damage in the wall [31]. Hydrogen attack nucleation was investigated by Sundararajan and Shewmon for high strength low alloy steels using dilatometric swelling tests [103]. They found that the expansion caused by hydrogen attack started immediately once the sample was exposed to high temperature and high hydrogen pressure.

A mechanism for methane bubble nucleation was proposed using a concept of pre-existing voids prior to high temperature hydrogen exposure [54, 104]. The pre-existing voids are present on the interfaces of grain boundary precipitates, carbides/matrix and inclusions/matrix [105]. Numerous pre-



10,000X



10,000X

Figure 5.2 Isolated methane bubbles initiated at carbide/ferrite interfaces and grain boundaries (MPC-3, N&T, 850°F-500 psi H_2-159 hrs.).

existing voids were observed with sizes (diameter) in the range of 0.01~0.22 μm in quenched and tempered Cr-Mo steel using TEM replicas [104]. It was proposed that the pre-existing voids were caused as a result of plastic strain and long range tensile stresses developed by the misfit of carbide growth rates and creep relaxation rates [104].

In addition to the pre-existing void mechanism, an in-situ nucleation of methane bubbles was proposed [106] in accordance with the calculation of the volume change caused by the reaction of hydrogen and carbides (Fe_3C)

$$Fe_3C + 2H_2 = 3Fe + CH_4$$

Based on this reaction and the densities of Fe_3C carbide (7.694 g/cm^3) and iron (7.86 g/cm^3) [107], the void volume formed by 1 mole Fe_3C can be estimated by:

Volume of 1 mole Fe_3C:

$$(3 \times 55.847 + 12.011) / 7.694 = 23.3 \text{ cm}^3$$

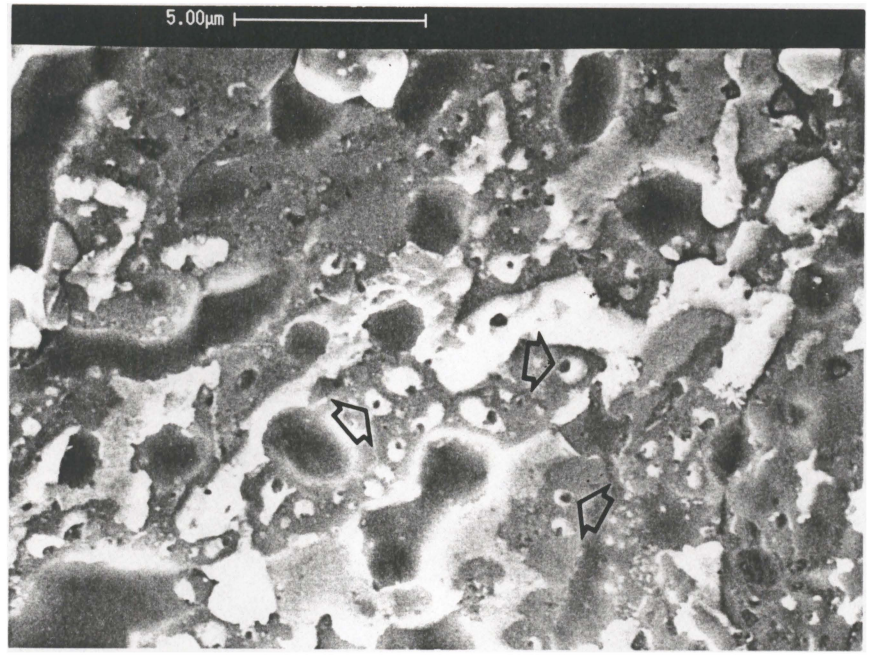
Volume of 3 moles of Fe:

$$3 \times 55.847 / 7.86 = 21.3 \text{ cm}^3$$

Therefore, the volume of voids generated by the reaction of 1 mole Fe_3C is

$$23.3 - 21.3 = 2.0 \text{ cm}^3\text{/ mole } Fe_3C$$

The mechanism of in-situ methane bubble nucleation was demonstrated by "Cryo-cracking" fractographic examination of hydrogen service exposed material (MPC-15, 770°F-550 psi H_2-30 years) using SEM as shown in Figure 5.3. It is evident that methane bubble formation is related to the reaction of



5,000X

Figure 5.3 In-situ methane bubble nucleation by the reaction of carbides and hydrogen in service exposed C-0.5Mo material (MPC-15, 770°F-550 psi H_2-30 years).

hydrogen with carbides. The minimum bubble size was determined as 0.1 micron in this hydrogen exposed C-0.5Mo material (MPC-15).

5.2 Hydrogen Diffusion and Concentration through the Wall of One-Sided Exposure Assembly

Hydrogen solubility ($\underline{H}$) under equilibrium conditions between hydrogen gas and hydrogen dissolved in steel is expressed by Sievert's law [108] at a given temperature:

$$\underline{H} = K P_{H2}^{1/2}$$

in which P_{H2} is hydrogen pressure, and K is an equilibrium constant depending on temperature. The applicability of Sievert's law is valid for gaseous hydrogen pressures up to 14700 psi (101.3 MPa) and 1110°F (872°K) [102]. The correlation between hydrogen solubility in α-Fe, temperature, and hydrogen pressure was established as [109]:

$$\underline{H} = 42.7 P_{H2}^{1/2} \exp\{-27280/RT\}$$

where H is in ppm, P_{H2} in atm, T in °K, and R is ideal gas constant (8.314 J/mole °K).

Hydrogen concentration was calculated for the one-sided hydrogen exposure assembly (MPC-3). Using an exposure temperature of 900°F (755°K) and hydrogen pressure of 900 psi (61.3 atm) the hydrogen solubility adjacent to the hydrogen exposed surface is calculated to be 4.3 ppm.

Hydrogen diffusion occurs through the wall of the one-side exposure Assembly. Therefore, the hydrogen concentration within the wall can be computed in accord with the Fick's law [110]:

$$\partial \underline{H}/\partial t = - D\nabla^2 \underline{H}$$

A steady-state condition is considered for the one-sided exposure assembly (MPC-3) and thus hydrogen concentration is independent of time ($\partial \underline{H}/\partial t = 0$) and only a function of the depth within the wall. Therefore, the Fick's law is simplified as:

$$D\nabla^2 \underline{H} = 0$$

Hydrogen diffusion in the one-side exposure assembly (MPC-3) is considered as a case of diffusion through a plate-walled sample with a wall thickness of L (one dimensional diffusion). It is assumed that the hydrogen pressure on the outside (x=0) surface of the plate-walled sample is maintained at constant (900 psi H_2) and hydrogen pressure is zero on the inside surface. The hydrogen concentrations adjacent to outside and inside surface are $\underline{H}_1$=4.3 ppm and $\underline{H}_0$=0 ppm, respectively. Assuming the diffusion coefficient D is constant for the steady-state condition, the diffusion equation is simplified with a solution as follows:

$$d\underline{H}/dx = \text{constant}$$

$$\underline{H} = \underline{H}_1 (1 - x / L)$$

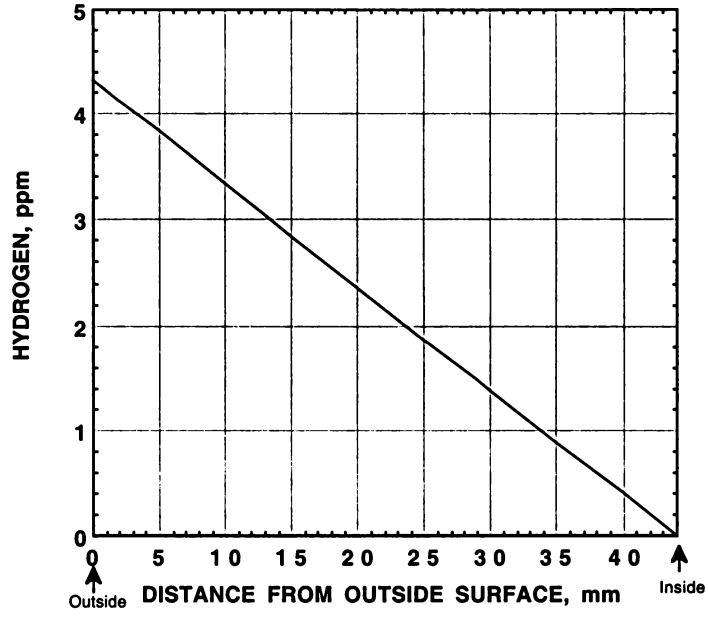
Based on Sievert's law and the hydrogen concentration equation, the hydrogen concentration and the equivalent "hydrogen pressure" through the

wall of the one-side exposure assembly (MPC-3) can be calculated. Figures 5.4 through 5.6 show the calculated hydrogen concentration and equivalent "hydrogen pressure" profiles through the wall (44, 29, 13 mm). From the hydrogen concentration equation, it is to be noticed that the hydrogen concentration only depends on the fraction of wall thickness and the hydrogen concentration (equivalent "hydrogen pressure") adjacent to the exposed surface if the exposure temperature and hydrogen pressure are maintained the same. This explains the measured results of the methane concentration and hydrogen damage profiles as a function of the fraction of wall thickness for different wall thickness (44, 29, and 13 mm) as presented in Figures 4.88 and 4.95.

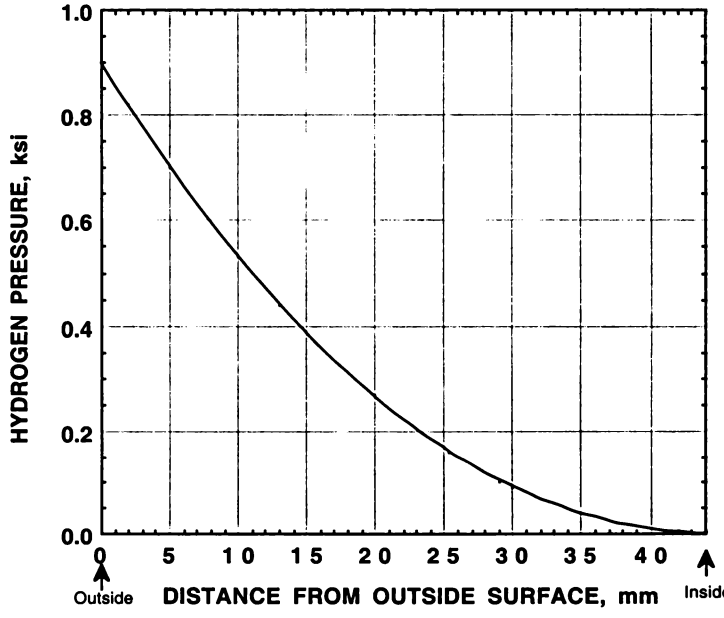
5.3 Methane Pressure

Methane pressure through the wall of one-sided exposure assembly is determined using thermodynamic modeling. During the reaction of hydrogen and carbon to form methane, carbon is removed from solution and a carbon concentration gradient extending from the methane bubble to the surrounding carbide particles is established. This carbon gradient is the driving force promoting the dissolution of the carbides. Based on the carbide study in this research, the predominant carbides were identified primarily as Fe_3C in the N&T MPC-3 material. Therefore, an overall methane reaction can be written as

$$Fe_3C + 2H_2 = 3Fe + CH_4$$

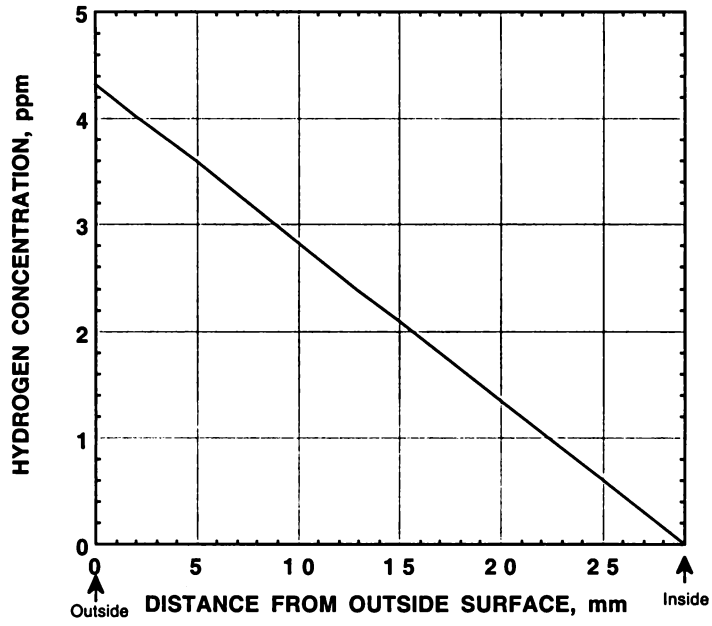


(a) Hydrogen concentration

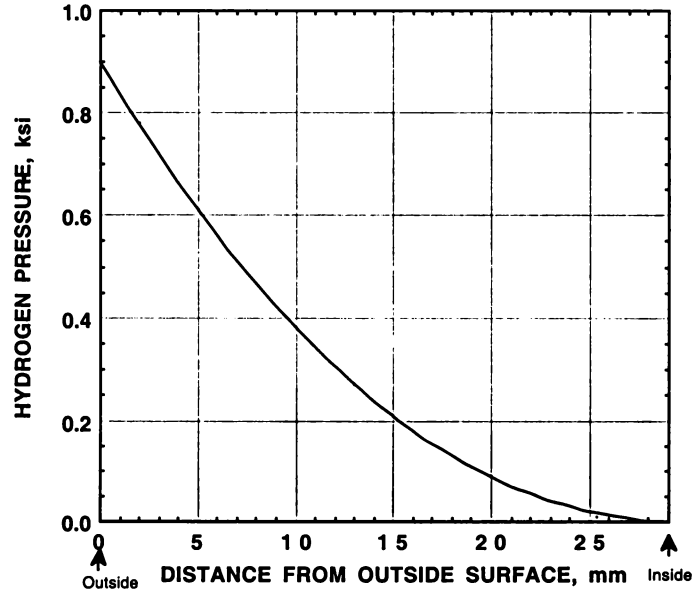


(b) Equivalent "hydrogen pressure"

Figure 5.4 Calculated hydrogen concentration (a) and equivalent "hydrogen pressure" (b) profiles through the wall (44 mm) of one-sided exposure assembly (900°F-900 psi H_2-1248 hrs.+950°F-900 psi H_2-288 hrs.).

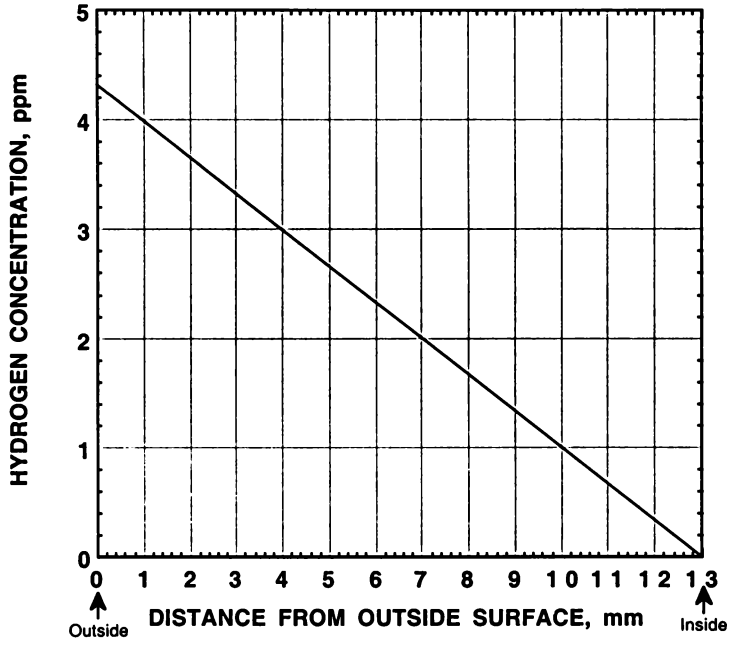


(a) Hydrogen concentration

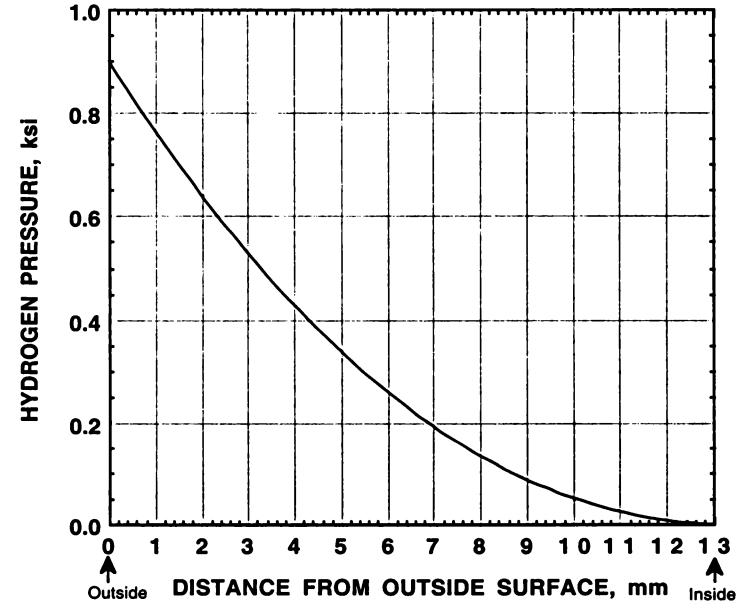


(b) Equivalent "hydrogen pressure"

Figure 5.5 Calculated hydrogen concentration (a) and equivalent "hydrogen pressure" (b) profiles through the wall (29 mm) of one-sided exposure assembly (900°F-900 psi H_2-1248 hrs.+950°F-900 psi H_2-288 hrs.).



(a) Hydrogen concentration



(b) Equivalent "hydrogen pressure"

Figure 5.6 Calculated hydrogen concentration (a) and equivalent "hydrogen pressure" (b) profiles through the wall (13 mm) of one-sided exposure assembly (900°F-900 psi H_2-1248 hrs.+950°F-900 psi H_2-288 hrs.).

The standard state free energy (ΔG^0) and equilibrium constant (k) for the reaction are expressed as

$$\Delta G^0 = -RT \ln k$$

$$k = f_{CH4} \, a_{Fe}^{\,3} / f_{H2}^{\,2} \, a_{Fe3C}$$

where f_{CH4} is methane fugacity, a_{Fe} is iron activity, f_{H2}, is hydrogen fugacity, and a_{Fe3C} is cementite activity.

For overall reaction, the standard state free energy can be calculated based on

$$\Delta G^0 = \Delta G^0_{CH4} + 3\Delta G^0_{Fe} - \Delta G^0_{Fe3C} - 2\Delta G^0_{H2}$$

It is to be noted that the activities of iron and cementite have a value of unity since iron is the matrix material and cementite is assumed in its standard state. In addition, the formation energies of iron and hydrogen is zero in the standard state condition. Therefore, the reaction constant and the overall standard state free energy are simplified as

$$k = f_{CH4} / f_{H2}^{\,2}$$

$$\Delta G^0 = \Delta G^0_{CH4} - \Delta G^0_{Fe3C}$$

The free energies of formation of methane and F_3C in α-Fe were determined to be [111]:

$$\Delta G^0_{CH4} = -69120 + 51.25\ T \log T - 65.35\ T \quad \text{(J/mole, 298~1200°K)}$$

$$G^0_{Fe3C} = 27783 - 26.67\ T \quad \text{(J/mole, ~1000°K)}$$

Therefore, the free energy for overall reaction is

$$\Delta G^0 = -96903 - 38.68\ T + 51.25\ T \log T \qquad \text{(J/mole, 298~1000°K)}$$

Figure 5.7 presents the free energy of methane formation by the reaction of hydrogen and Fe_3C as a function of temperature. The free energy of methane formation increases with increase in temperature. The methane formation free energy is zero at temperature 1100°F, which indicates that methane dissociation would occur and thus hydrogen attack would not take place when temperature is above 1100°F.

Hydrogen fugacity (f_{H2}) was approximated to be as same as hydrogen pressure (P_{H2}) in the range of $P_{H2} < 4.4$ ksi [112]. Methane fugacity is expressed as

$$f_{CH4} = k\ P_{H2}^{\ 2} \qquad k = \exp\{-\Delta G^0 / RT\}$$

The correlation between methane fugacity and equilibrium methane pressure (P_{CH4}) was derived as [113]:

$$f_{CH4} = P_{CH4} \exp\{C(T)\ P_{CH4}\}$$

$$C(T) = 2.375 / T + 1.1776 \times 10^{-3} \qquad f_{CH4} \geq 10^4 \text{ MPa}$$

$$C(T) = 1.1875 / T + 3.0888 \times 10^{-3} \qquad 10^3 < f_{CH4} < 10^4 \text{ MPa}$$

$$C(T) = 0.005 \qquad f_{CH4} < 10^3 \text{ MPa}$$

Combining the above equations, methane pressure as a function of hydrogen pressure is given by:

$$P_{CH4} \exp\{C(T)\ P_{CH4}\} = k\ P_{H2}^{\ 2}$$

Hence, methane pressure through the walls of one-side exposure assembly (MPC-3) can be calculated. Figures 5.8 through 5.10 present the

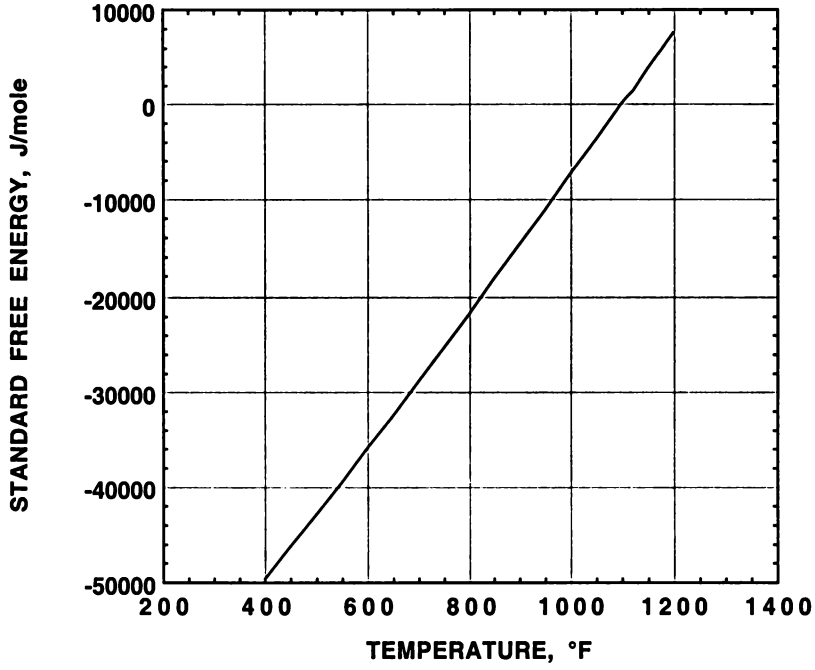


Figure 5.7 Methane formation free energy as a function of temperature for the reaction of hydrogen and Fe_3C carbide.

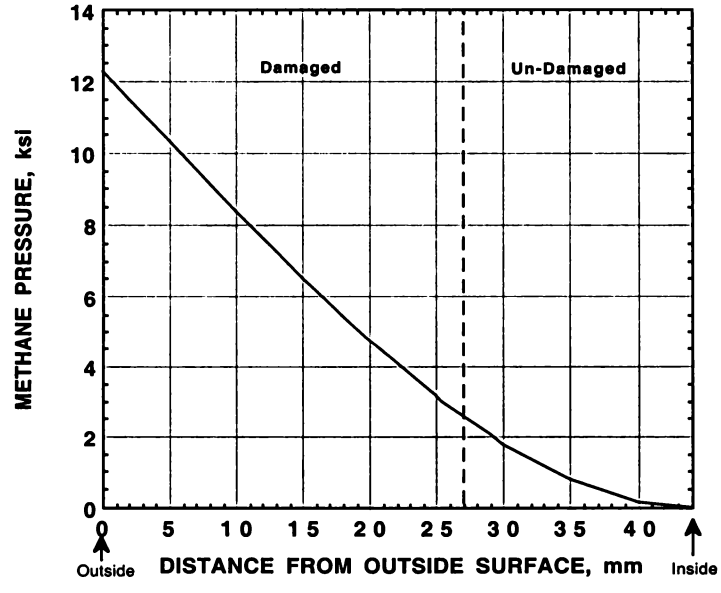


Figure 5.8 Calculated methane pressure profile through the wall (44 mm) of the one-sided exposure assembly (900°F-900 psi H_2-1248 hrs.+950°F-900 psi H_2-288 hrs.).

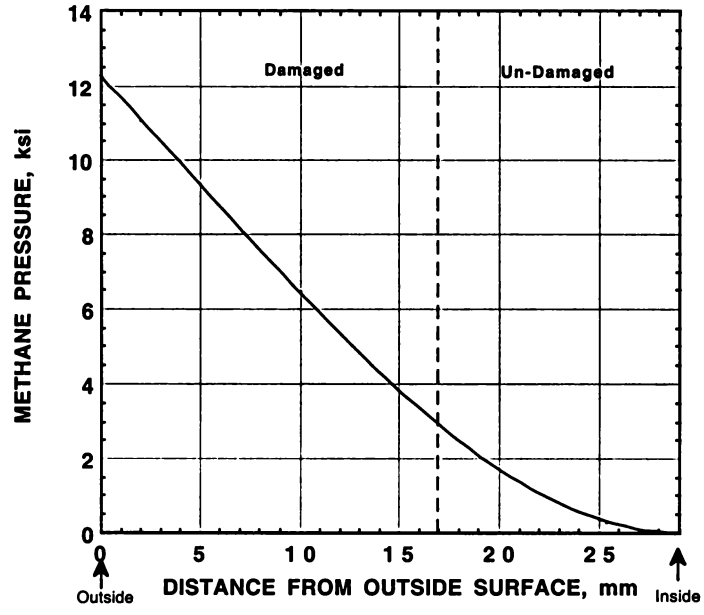


Figure 5.9 Calculated methane pressure profile through the wall (29 mm) of the one-sided exposure assembly (900°F-900 psi H_2-1248 hrs.+950°F-900 psi H_2-288 hrs.).

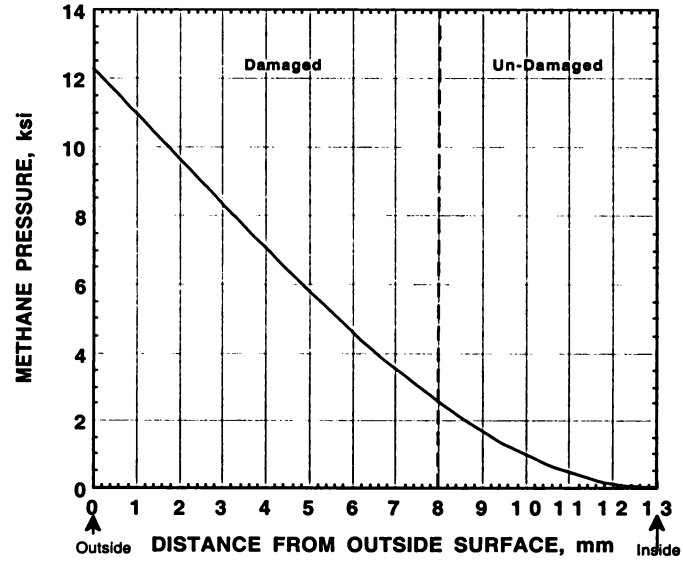


Figure 5.10 Calculated methane pressure profile through the wall (13 mm) of the one-sides exposure assembly (900°F-900 psi H_2-1248 hrs.+950°F-900 psi H_2-288 hrs.).

equilibrium methane pressure profiles within wall thickness of 44, 29, and 13 mm of the one-side exposure assembly (MPC-3). The equilibrium methane pressure is the highest adjacent to the outside surface (exposed to hydrogen) and decreases toward the inside surface. The maximum methane pressure was determined as 12.5 ksi adjacent to the surfaces exposed to hydrogen. Therefore, the methane pressure distributions explained the hydrogen attack damage profiles through the wall thickness for the one-side hydrogen exposure assembly.

In accordance with the fraction of hydrogen attack damaged grain boundaries, methane bubble diameters, and methane contents, methane pressure was estimated through the wall thickness for the one-side exposed assembly. Methane was assumed as an ideal gas. Figure 5.11 shows the methane pressure distribution through the wall thickness derived from the experimental data compared to the calculated results. A fair agreement is noticed for the methane determination using the two methods.

Since the methane bubble growth is caused by the methane pressure overcoming the resistance of sintering force, $2\gamma/r$ (γ - surface tension, r - bubble radium), the methane bubble growth criterion is established to be [67]:

$$P_{CH4} > 2\gamma/r$$

The values of the surface tension are approximately 1 J/m^2 for the Fe/Fe_3C interface [114]. The average methane bubble diameter was determined to be approximately 0.1 μm at the maximum damage depth for the one-side exposure

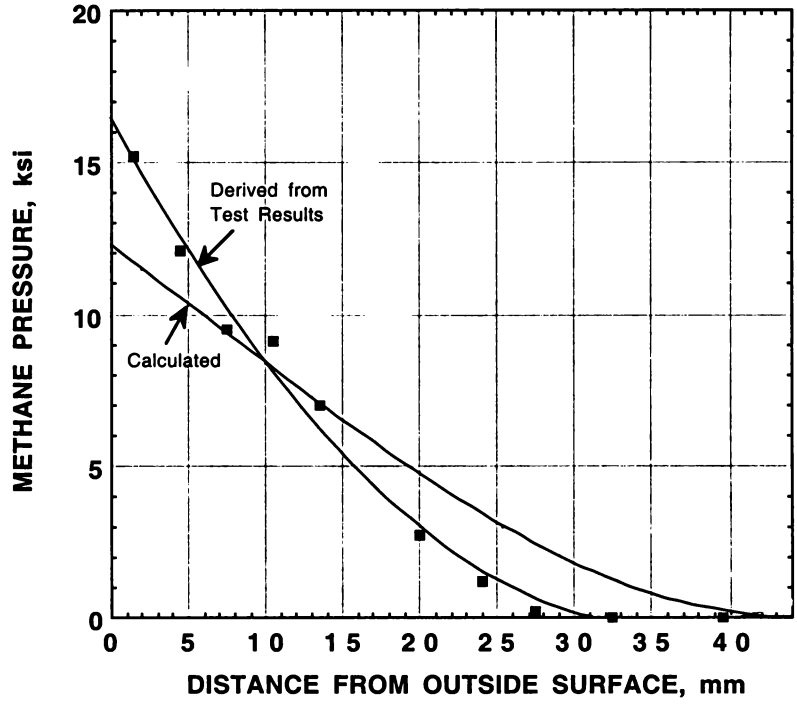


Figure 5.11 Comparison of methane pressure derived from the experimental data and calculated results.

assembly (MPC-3). Therefore, assuming r = 0.1 μm, the equilibrium methane pressure within the bubbles was computed to be 3 ksi, which is consistent with the calculated methane pressure at the maximum damage depths of the one-side exposure assembly as shown in Figures 5.9 through 5.11.

In addition to the one-side exposure assembly, a maximum hydrogen damage depth was back calculated using the equilibrium methane pressure value of 3 ksi for the service exposed heat exchanger channel (MPC-18, central portion, 580°F-950 psi H_2-28 years). Assume r = 0.1 μm for the calculation. A maximum damage depth was predicted as 21 mm from the ID surface, which satisfies the measured result of 20 mm as shown in Figures 4.31 and 4.47 using SEM image analysis and methane determination.

Effect of the carbide types on hydrogen attack susceptibility was evaluated using the thermodynamic modeling discussed above. In addition to Fe_3C type carbides, methane pressures generated by the reaction of hydrogen with M_2C and $M_{23}C_6$ type carbides were calculated as a function of hydrogen pressure. For the reason of using available thermodynamic data and simplifying the calculation, only pure metal carbides (Fe_3C, Mo_2C, and $Cr_{23}C_6$) are considered to demonstrate the influence of different types of carbides on hydrogen attack susceptibility. The methane reactions and free energies for Fe_3C, Mo_2C, and $Cr_{23}C_6$ carbides are presented as follows [28, 111, 115]:

$$Fe_3C + 2H_2 = 3Fe + CH_4$$

$$\Delta G^0 = -96903 - 38.68\ T + 51.25\ T \log T \quad \text{(J/mole, 298~1000°K)}$$

$Mo_2C + 2H_2 = 2Mo + CH_4$

$\Delta G^0 = -41087 - 65.35\ T + 51.25\ T \log T$ (J/mole, 298~1000°K)

$Cr_{23}C_6 + 12H_2 = 23Cr + 6CH_4$

$k = 2.50 \times 10^{-6} \exp(1758 / T)$

Figure 5.12 shows the calculated methane pressure as a function of hydrogen pressure at temperatures of 500°F and 700°F for Fe_3C, Mo_2C, and $Cr_{23}C_6$ carbides. The methane pressure increases with an increase in hydrogen pressure. The increase in temperature will reduce the methane pressure. The methane pressure generated by the reaction of hydrogen with Fe_3C is greater than that for the reaction of hydrogen with Mo_2C and $Cr_{23}C_6$ carbides. It implies that hydrogen attack susceptibility is greater in the steels with Fe_3C carbides than that with Mo_2C and $Cr_{23}C_6$ carbides. From a practical standpoint of view, the addition of carbide forming elements in steels and tempering heat treatment can form stable carbides (Mo_2C, $M_{23}C_6$) to enhance hydrogen attack resistance. It is to be noted that only pure metal carbides were considered for simplifying the calculation. In practice, carbides contain other alloying elements and their combined effect should be considered for the methane pressure calculation.

5.4 Hydrogen Attack Mechanism

A flow chart is presented in Figure 5.13 to show the hydrogen attack progression in steels. In hydrogen attack, a number of reactions are involved in sequence or parallel. The individual reactions involved is illustrated as follows:

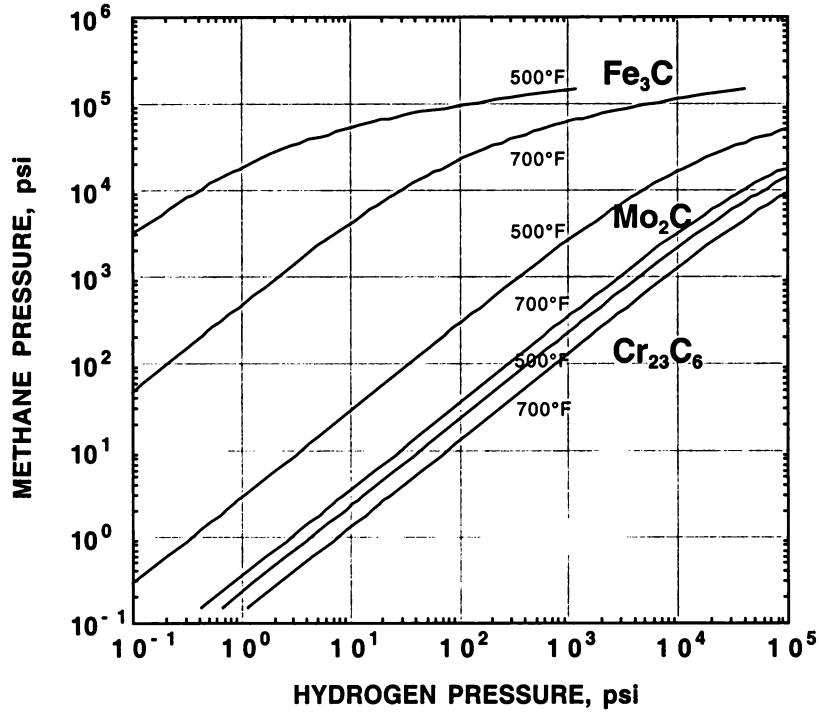


Figure 5.12 Methane pressure as a function of hydrogen pressure at temperatures of 500°F and 700°F for the reactions of hydrogen and Fe_3C, Mo_2C, and $Cr_{23}C_6$.

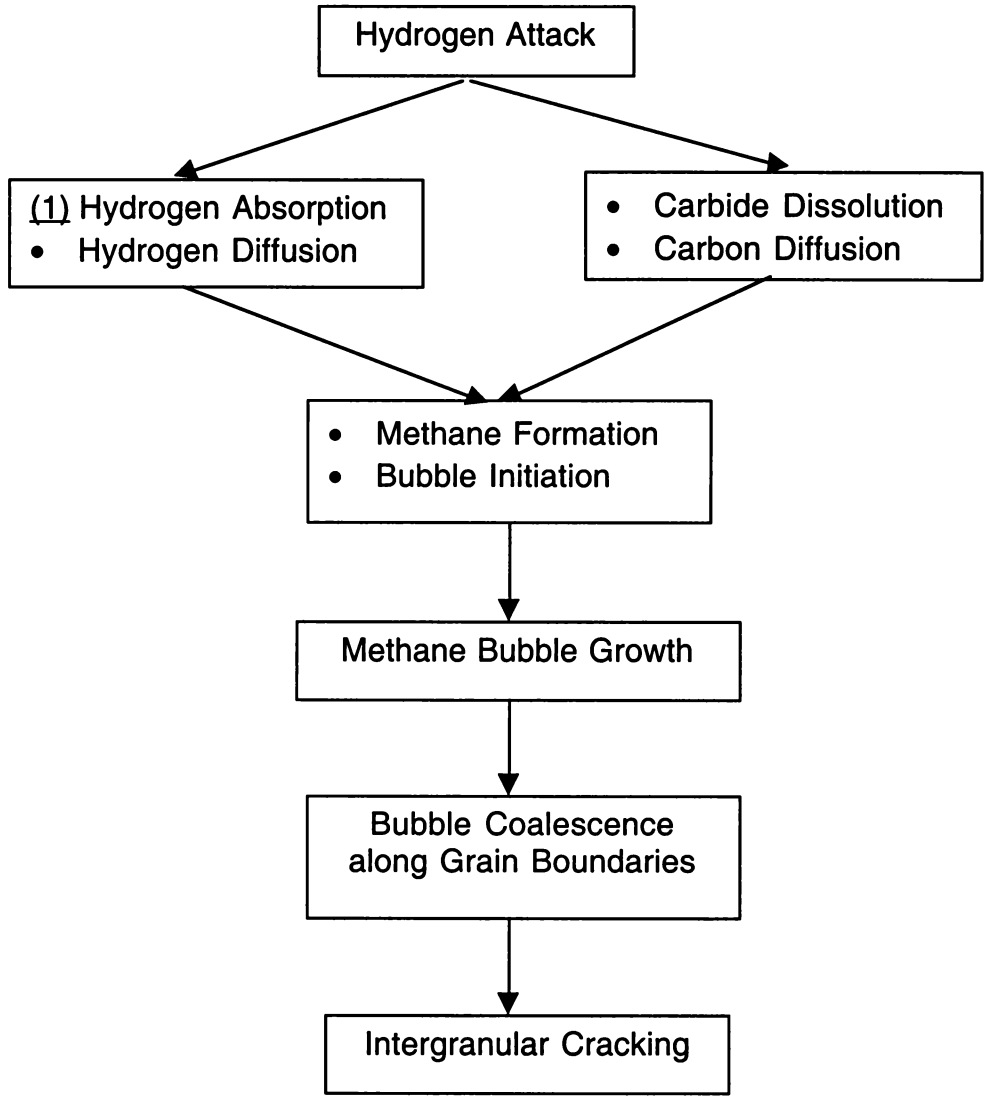


Figure 5.13 A flow chart showing hydrogen attack progression in steels.

(1). Hydrogen gas adsorption and dissociation

$$H_2\ (g) \rightarrow 2H\ (\text{adsorbed and dissociated})$$

(2). Hydrogen absorption

$$2H\ (\text{adsorbed}) \rightarrow 2\underline{H}\ (\text{absorbed})$$

(3). Hydrogen diffusion

$$\underline{H} \rightarrow \text{diffuses to reaction sites}$$

(4). Carbide dissolution

$$M_xC_y \rightarrow xM + yC$$

(5). Carbon diffusion

$$C \rightarrow \text{Diffuses to reaction sites}$$

(6). Methane formation

$$2H_2 + C \rightarrow CH_4$$

Methane may directly form by the reaction of hydrogen and carbon in solution.

In general, hydrogen gas adsorption, dissociation, and absorption are not considered as rate controlling reactions for methane formation. However, it was recognized that the gas composition, surface preparation, and surface coatings influence the time of hydrogen attack [116]. Hydrogen diffusion is rapid at high temperature and thus does not control the hydrogen attack rate. It has been demonstrated that the steady state condition for hydrogen permeation is established long before methane formation or hydrogen attack becomes evident [84]

Carbide dissociation is a major factor controlling hydrogen attack. It was found that strong carbide-forming elements in steels reduced the carbon activity and improved the resistance to hydrogen attack [67, 117]. Carbon diffusion may become a rate controlling factor in the advanced stages of hydrogen attack when diffusion distances to reaction sites become significant.

In accordance with the hydrogen attack evaluation of the service exposed and hydrogen autoclave exposed samples, a physical model of hydrogen attack is proposed for one-sided hydrogen exposure condition as illustrated in Figure 5.14. In petroleum refineries, pressure vessels and piping are insulated on the outside surfaces. Therefore, it is reasonable to assume an isothermal condition through the wall thickness of pressure vessels or piping. During exposing to hydrogen for one-side at high temperature, hydrogen adsorption, dissociation, and absorption occur on the surfaces exposed to hydrogen. The hydrogen concentration gradient is established through the wall thickness by hydrogen diffusion. Hydrogen permeation reaches a steady-state condition a short time long before methane formation or hydrogen attack occurrence. The hydrogen concentration gradient within wall is then established and satisfies Sievert's law and Fick's law as shown in Figure 5.14a.

The reaction of hydrogen and carbon or carbides occurs through the wall thickness simultaneously resulting in the formation of methane and bubbles at grain boundaries or carbide/matrix interfaces. Methane bubbles may nucleate in-situ where the reaction of carbides (Fe_3C) and hydrogen takes place. The

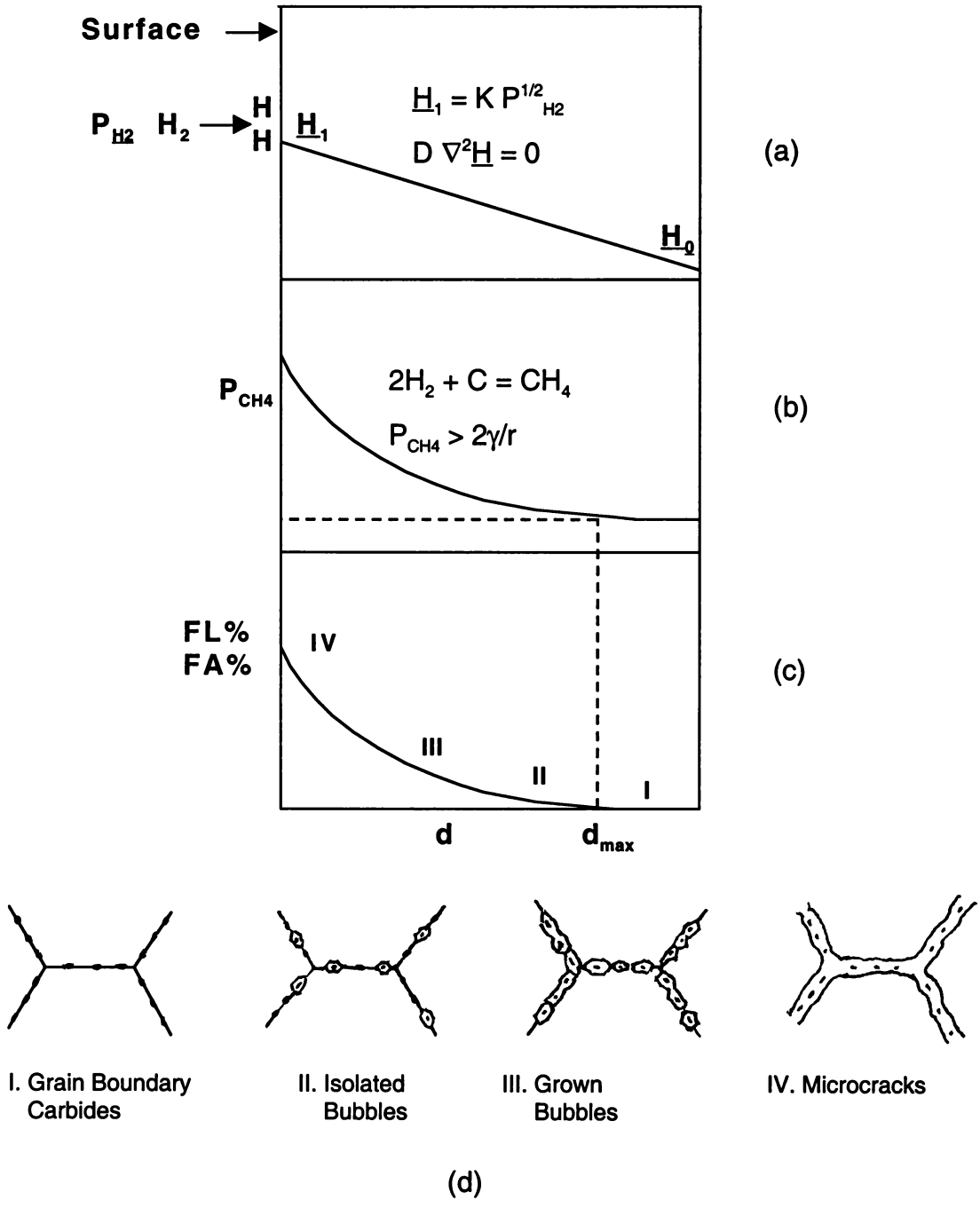


Figure 5.14 Hydrogen attack mechanism within the wall of the one-side exposed assembly.

rates of methane formation, bubble nucleation and growth depend on hydrogen pressure and temperature. Because of the hydrogen concentration gradient within the wall, methane bubble nucleation rate is faster near the hydrogen exposed surface than that in a distance from the surface. With the reaction of hydrogen and carbides or carbon and accumulation of methane, methane pressure builds up in the bubbles. Consequently, a gradient of methane pressure is established within the wall as indicated in Figure 5.14b. The methane bubbles grow when the methane pressure is greater than the sintering force ($2\gamma/r$) [67]. Therefore, a gradient of hydrogen attack damage and a maximum damage depth can be observed through the wall as demonstrated in the service exposed and one-side hydrogen exposure assembly. The progression of hydrogen attack in terms of the methane bubble formation, bubble coalescence, and microcracking can be viewed through the wall thickness as depicted in Figures 5.14c and 5.14d.

5.5 Modeling of Hydrogen Attack Limits (Nelson Curve)

As discussed in Chapter 2, Nelson Curves have been applied to the design and fabrication of pressure vessels and piping for petroleum refinery and petrochemical industries. However, a series hydrogen attack incidents in the C-0.5Mo steel equipment have questioned the confidence of the application of the C-0.5Mo Nelson Curve [6]. It is to be noted that the final version of C-0.5Mo Nelson Curve was defined in the 1977 edition of API Publication 941

[21]. In this edition, total 39 data points were used for the establishment of the C-0.5Mo Nelson Curve. Among these 39 data points, only 8 show hydrogen attack and 31 show no hydrogen attack. 10 out of the 31 un-attacked data points were attained from the C-0.5Mo steel components with stainless steel cladding, which is not directly applicable to the C-0.5Mo Nelson Curve. In the 1977 edition of API Publication 941, it states that all of the 39 data points used for the C-0.5Mo Nelson Curve development were received through private communications to the Subcommittee on Corrosion of API [21]. Operating times and the methodologies applied for hydrogen attack assessment were not documented. It can be concluded that the C-0.5Mo Nelson Curve in the 1977 edition of API Publication 941 was defined based on a limited and questionable database.

In the subsequently revised editions of API Publication 941 (1983, 1990, 1997), a total of 27 incidents of hydrogen attack were experienced in petroleum refinery and petrochemical industries [6]. In these revised editions, the operating conditions in terms of temperature, hydrogen partial pressure, and operating time were well documented. The operating temperature, hydrogen partial pressure, and time for the instances of hydrogen attack are in the ranges of 530 ~ 775°F, 170 ~ 2200 psi, and 17,500 ~ 283,000 hours, respectively. In addition to the published data in the 1997 edition of API Publication 941, 15 instances of hydrogen attack experienced in industry were accumulated from this research and literature [59, 118, 119] as presented in Figure 5.15. In

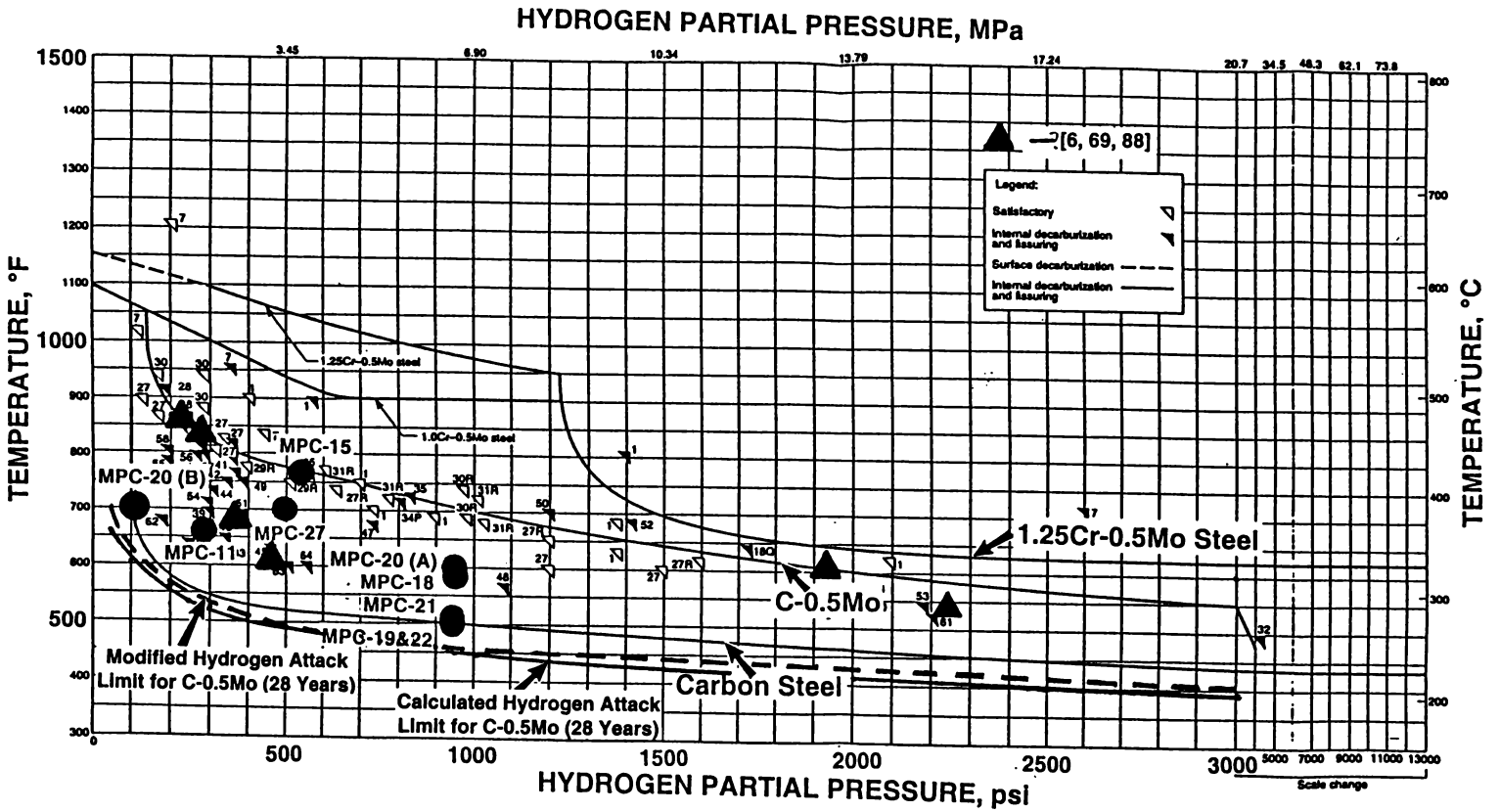


Figure 5.15 Comparison of modified hydrogen attack limit and modeling with the C-0.5Mo Nelson Curve in API Publication 941.

accordance with the database generated in this research, modified hydrogen attack limits are defined for C-0.5Mo steel as shown in Figure 5.15 (dashed line). Below this operating limit, hydrogen attack would not occur for approximate 28 years. In comparison with the Nelson Curves of C-0.5Mo and carbon steels defined in the 1997 edition of API Publication 941, the modified hydrogen attack limits are below the carbon steel Nelson Curve. Because hydrogen attack is a time-dependent process, a safe operational time should be included on the Nelson Diagrams.

Sundararajan and Shewmon [103] studied the hydrogen attack in steels using dilatometric swelling. Sample expansion caused by methane bubble formation and growth was monitored in-situ. It was found that the expansion rate was a function of temperature, hydrogen pressure, and exposure time. A relationship of the expansion ($\Delta l/l$) as function of hydrogen pressure, temperature, and exposure time was established based on the experimental data

$$\Delta l / l = A\, P_{H2}^{n}\, t \exp\{-Q / RT\}$$

where "A" and "n" are constants depending on materials. The activation energy and hydrogen pressure exponent (n) were determined as approximately 190 KJ/mole and 3 for plain carbon, Mn-Mo-Nb, and 2.25Cr-1Mo steels [103].

In accord with the empirical equation developed by Sundararajan and Shewmon [103], the JPVRC Subcommittee on Hydrogen Embrittlement defined a hydrogen attack parameter, P_w, for C-0.5Mo steel [32]:

$$P_w = \log\{(\Delta l / l)/A\}$$

$$= 3 \log P_{H2} + \log t - 9918 / T$$

where "P_{H2}" is hydrogen partial pressure in kgf/cm^2, "t" is exposure time in hours, and "T" is absolute temperature (°K).

The hydrogen attack parameter (P_w) was correlated with hydrogen attack damage in terms of the fraction of damaged grain boundary length and area (FL%, FA%) to assess hydrogen attack susceptibility. According to the database developed in this research, the fraction of damaged grain boundaries (FA%, FL%) was plotted as a function of hydrogen attack parameter (P_w) as presented in Figure 5.16. A critical value of the hydrogen attack parameter ($P_w^{cr.}$) was determined as -9.0, below which hydrogen attack would not occur for approximately 28-year safe operation. The critical value (-9.0) for the hydrogen attack parameter determined in this research is less than that determined by JPVRC (-4.8) [32] as indicated in Figure 5.16. It is to be noted that the operating time used for determination of the critical value -9.0 is in the range of 1,536 ~ 262,800 hours based on service exposed heats and one-side exposure C-0.5Mo material. However, the critical value of -4.8 determined by JPVRC was only based on the hydrogen attack assessment for one heat of C-0.5Mo steel and 1000 hour exposure time, which does not represent prolonged exposure to hydrogen.

A model for the hydrogen attack limits for C-0.5Mo steel was developed by applying the critical value of -9.0 to the hydrogen attack parameter (P_w).

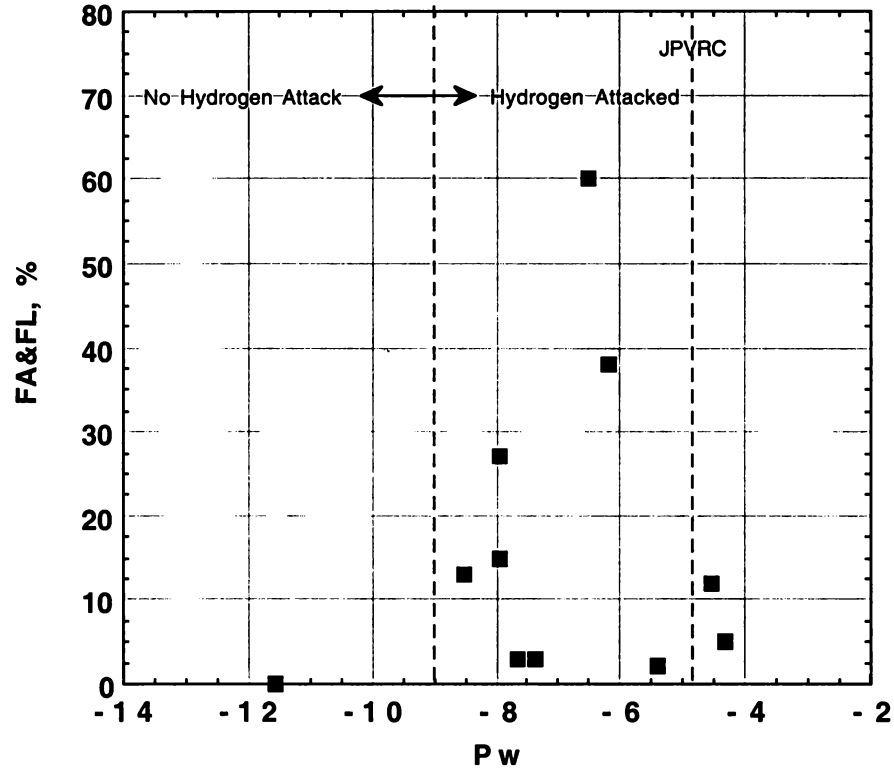


Figure 5.16 Relationship of hydrogen attack damage (FA% & FL%) and the hydrogen attack parameter (P_w).

Applying the critical $P_w^{cr.}$ value of -9.0 and the exposure time of 28 years to the hydrogen attack parameter, a relationship of temperature and hydrogen partial pressure (Nelson Curve) was derived for C-0.5Mo steel:

$$T = 9918 / (3\log P_{H2} + 14.2)$$

This relationship was plotted on Figure 5.15 as shown by the solid line. It is evident that the hydrogen attack limit determined by this modeling shows a good agreement with the modified hydrogen attack limit for a safe operational time of 28 years.

In addition to the operating temperature and hydrogen partial pressure, hydrogen attack limit is related to the exposure time for a safe operation. Therefore, general modeling of hydrogen attack limit can be expressed based on the hydrogen attack parameter [32]:

$$T = 9918 / (3\log P_{H2} + \log t + P_w^{cr.})$$

$P_w^{cr.}$ is a critical hydrogen attack parameter that depends on materials and evaluation methodologies. The critical parameter can be determined by experiment. Hydrogen attack limits as a function of time were calculated for C-0.5Mo in accord with the model. For calculation, the critical values of the hydrogen attack parameter for different times were derived from Figure 2.16 [6]. Figure 5.17 reveals that the hydrogen attack limits decrease with an increase in exposure time. Based on this model, the exposure time for the C-0.5Mo Nelson Curve defined in API Publication 941 was derived to be 10,500 hours (approximately 14 months). It further indicates that the C-0.5Mo Nelson Curve

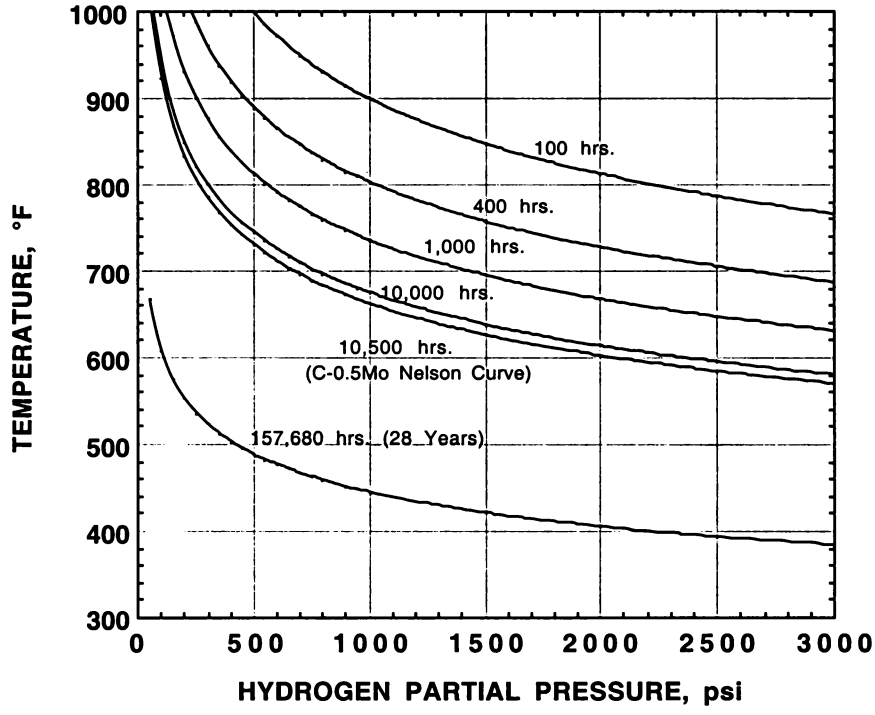


Figure 5.17 Hydrogen attack limits as a function of time defined by modeling.

defined in API Publication 941 is not valid for long term operation. Figure 5.18 shows the comparison of hydrogen attack limits as a function of time calculated from the model and the hydrogen attack limits documented in API Publication 941 [6]. The modeling results are consistent with the hydrogen attack limits in API Publication 941 for operating times of 100, 400, 1000, and 10000 hours.

5.6 Methodology for Hydrogen Attack Evaluation

A methodology for hydrogen attack evaluation by methane determination combined with two master curves was developed in this research. In accord with the evaluation of hydrogen attack damage in the service exposed components and hydrogen autoclave exposed samples for C-0.5Mo, two master curves were developed as shown in Figures 5.19 and 5.20. In these two master curves, the relationship between methane content (or hydrogen content dissociated from methane) and hydrogen damage level (FL%, polished and etched sample; FA%, "Cryo-cracking" samples) as well as the average bubble diameter and hydrogen damage level (FL% and FA%) are established. Hydrogen damage morphology is classified as isolated bubbles, aligned & isolated bubbles, and microcracks & bubbles and this is shown on the master curve (Figure 5.20). In addition, the methods for effective detection of hydrogen attack damage, such as OLM, UT, and SEM, are recommended for different damage levels (Figure 5.20). Hydrogen attack microcracks can be detected by

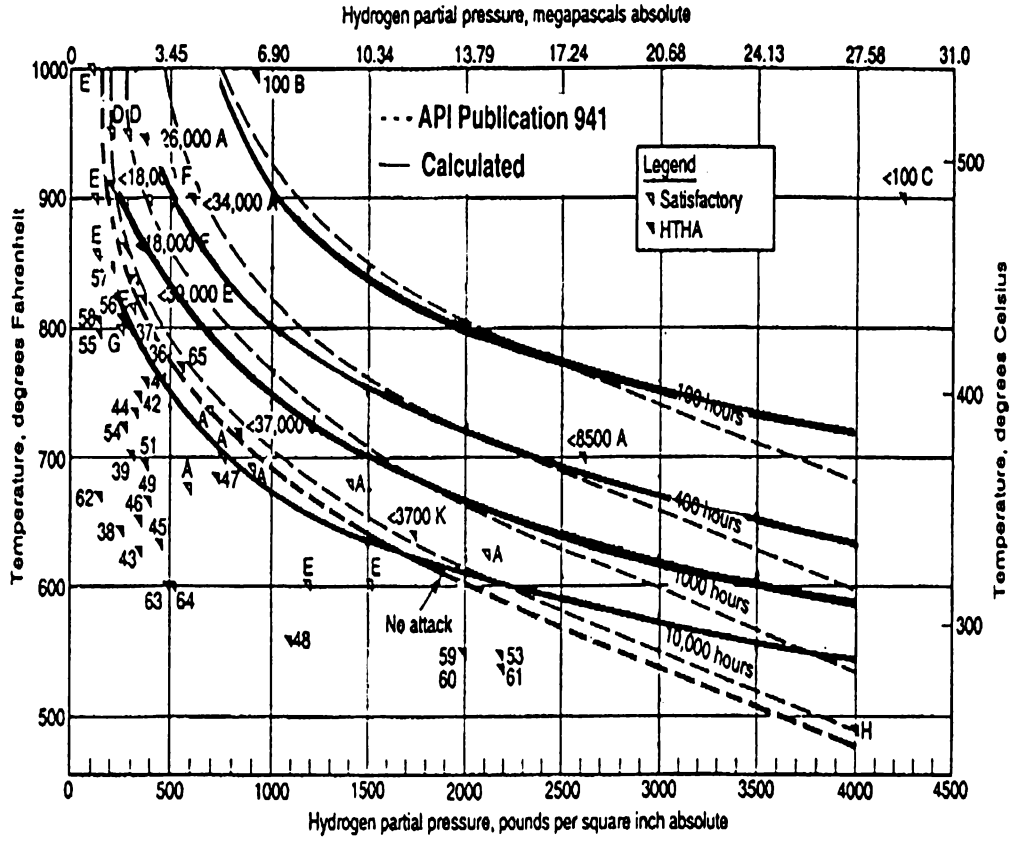


Figure 5.18 Comparison of hydrogen attack limits as a function of time defined by modeling and documented in API Publication 941 for C-0.5Mo.

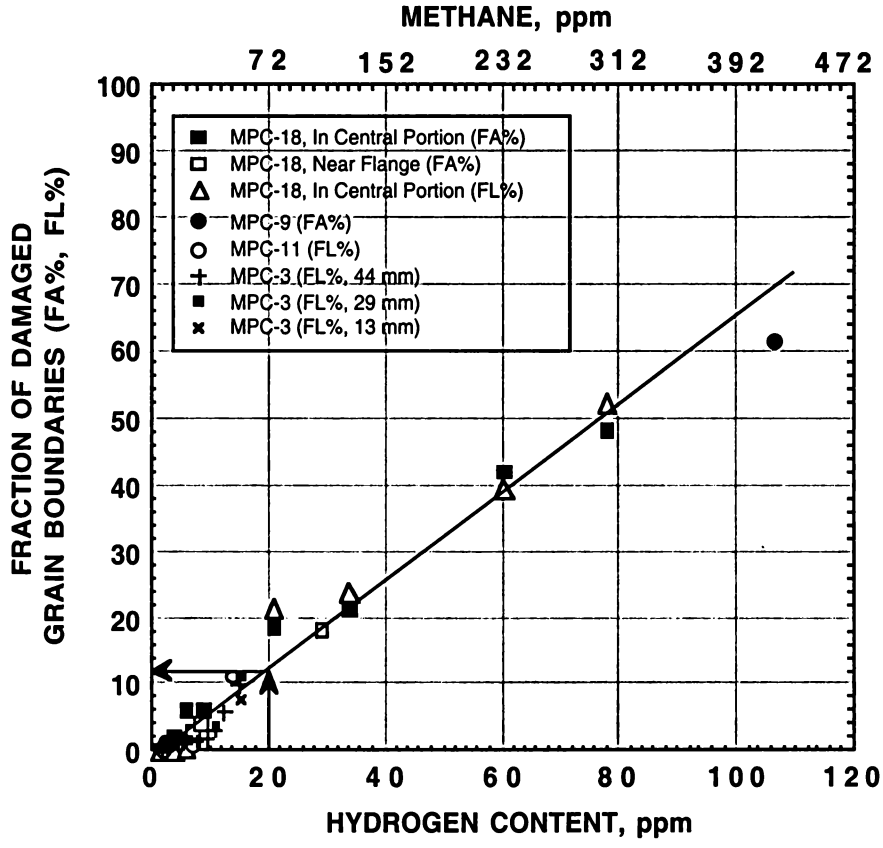


Figure 5.19 Relationship of hydrogen attack damage (FA% and FL%) and hydrogen content dissociated from methane.

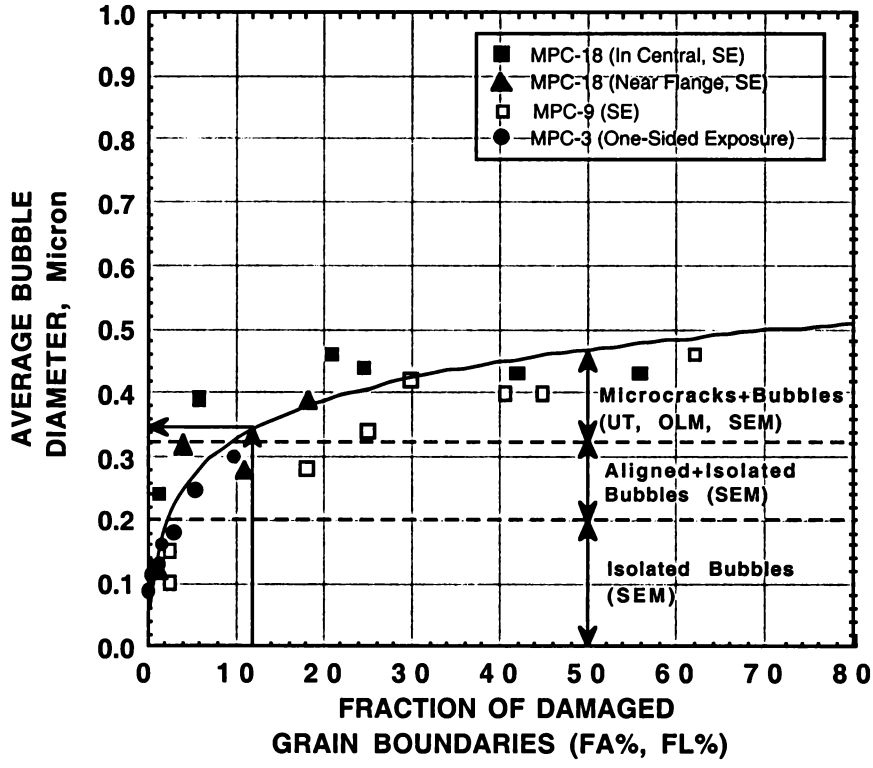


Figure 5.20 Relationship of average bubble diameter and hydrogen attack damage level (FA% and FL%).

OLM and UT. SEM is required for the examination of early stages of hydrogen attack damage (aligned or isolated methane bubbles).

Methane content can be determined by hydrogen measurement using gas chromatography (Oerlikon-Yanaco Hydrogen Analyzer, ≥ 0.1 ppm) or Leco vacuum fusion method (≥ 1 ppm). Using the methane content (hydrogen dissociated from methane) determined and the master curve in Figure 5.19, the fraction of damaged grain boundaries can be derived. The average bubble diameter and hydrogen attack morphology can be determined by using the value of the fraction of damaged grain boundaries and the master curve in Figure 5.20. Effective methods in terms of OLM, UT, and SEM for detecting hydrogen damage are suggested on this master curve.

An example is provided in Figures 5.19 and 5.20 to explain the application of this recommended methodology for hydrogen attack damage assessment. Assume 72 ppm methane content (20 ppm hydrogen) was determined by hydrogen measurement. The fraction of damaged grain boundaries is determined to be 12% using the master curve in Figure 5.19. Using the value of 12% and the master curve in Figure 5.20, the average bubble diameter can be determined to be 0.35 μm. In this case, the morphology of hydrogen attack damage is predicted to be microcracks plus methane bubbles which may be resolved by using UT, OLM, and SEM.

The advantage of using this recommended methodology is that the early stages of hydrogen attack in the forms of aligned or isolated bubbles can be

detected by methane determination, of which the detectability is equivalent to SEM. In addition, only a small amount of bulk material (minimum 6 grams) is required for methane determination. To achieve a definitive assessment of hydrogen attack damage, a sample must be extracted from internal surface of a pressure vessel or piping at location where the exposure conditions are considered most severe, such as location exposed to higher temperatures and higher hydrogen pressures. The material to be extracted must come from a location remote from the weld deposit because weld metal generally has a greater resistance to hydrogen attack than base metal.

CHAPTER 6

CONCLUSIONS

From this fundamental research on hydrogen attack in C-0.5Mo steel and weldments, significant conclusions were drawn regarding: 1) screening tests of hydrogen attack damage in service exposed components; 2) characterization of hydrogen attack damage in high temperature hydrogen service exposed components; 3) development of one-side hydrogen exposure techniques to simulate hydrogen attack in pressure vessel and piping; 4) quantitative hydrogen damage evaluation through the wall using OLM, SEM, quantitative image analysis, and methane determination. Additional conclusions pertinent to the effects of carbon, alloying elements, heat treatment, hot and cold work, welding, and PWHT on hydrogen attack susceptibility are highlighted below. Furthermore, studies on methane evolution, methane pressure calculation, and bubble nucleation led to a fundamental understanding of hydrogen attack mechanism in steels. An effective methodology was recommended for hydrogen attack damage evaluation by methane determination and application of two master curves developed in this research. Modeling of hydrogen attack limit (Nelson Curve) emphasizes that hydrogen attack is a time dependent process and safe operating times should be stated on "Nelson Curves" for design and fabrication.

(1) Hydrogen attack damage was found in the base metal of heat exchangers (MPC-18 and 11) using an advanced ultrasonic testing equipment (PortaScan 007). Maximum depths of the hydrogen damage were defined as 0.5" for MPC-18 (1" thick, in central portion of heat exchanger channel) and 0.33" for MPC-11 (0.625" thick) from the ID surfaces in accord with the UT images. Hydrogen damage was not found in the long seam weld metal (MPC-18) by using ultrasonic testing.

(2) OLM examination substantiated the UT results in terms of maximum depth of hydrogen damage within the walls. Hydrogen attack cracks were observed in the base metal and the CGHAZ of the heat exchanger channel (MPC-18) using OLM. Hydrogen attack cracking in the CGHAZ terminated in the overlapped regions where the initial coarse grains were refined by the following welding thermal cycle.

(3) Hydrogen damage was significantly reduced in the fine grained HAZ region (FGHAZ) with a maximum damage depth of 0.039" from the ID surface in comparison with the base metal (0.5") and the CGHAZ (0.2") in the heat exchanger channel (MPC-18).

(4) It is noteworthy that hydrogen damage was not found in the long seam weld metal with low carbon content (0.053%) even though extensive hydrogen damage occurred in the base metal (FA%~60% near the ID) and the CGHAZ (MPC-18).

(5) The fractions of damaged grain boundary area (FA%) and length (FL%) were denoted to quantify hydrogen damage by using quantitative metallographic analysis. The extent of the hydrogen damage was extensive in proximity to the ID surfaces and decreased within wall. The fraction of the damage grain boundaries at the ID surface is in the range of approximately 1% (MPC-27) to 60% (MPC-18 and 9) for the 9 damaged heats.

(6) The progression of hydrogen attack in terms of bubble nucleation, bubble coalescence, and microcracking was revealed by the examination through the wall thickness using OLM and SEM.

(7) One-sided hydrogen exposure test successfully simulated the hydrogen attack phenomena in pressure vessels and piping.

(8) SEM "Cryo-cracking" technique was demonstrated as a unique method for hydrogen damage evaluation and methane bubble size determination. As anticipated, SEM is required for minor hydrogen damage in the form of isolated and aligned bubbles.

(9) A correlation of the bubble size and the fraction of damaged grain boundaries was established. The average bubble diameter increases with the increase in the fraction of damaged grain boundaries. The bubble size begins to level off when the fraction of damaged grain boundaries (FL%, FA%) is greater than 10%.

(10) Only isolated bubbles were observed when the fraction of damaged grain boundaries (FA%, FL%) was less than approximately 3%. A mixture of isolated and aligned bubbles were observed as the damaged grain boundaries (FA%, FL%) are 3% ~ 10%. Mircocracks were found when the fraction of damaged grain boundaries (FA%, FL%) was greater than 10%.

(11) Methane concentration was determined by hydrogen measurement using gas chromatography and Leco vacuum fusion method. Methane gas in the bubbles and cracks could be completely dissociated into hydrogen and extracted by treating a sample encapsulated in a quartz tube at 1290°F (700°C) for 72 hours for hydrogen measurements.

(12) Methane concentration was the greatest adjacent to the ID surfaces and decreased through the wall thickness of the service exposed samples. The methane concentration profiles are similar to the hydrogen damage profiles (FA% and FL%) through the wall.

(13) A cut-off line of hydrogen damaged / no hydrogen damage was determined as 2 ppm hydrogen, above which hydrogen damage was found within wall. Hydrogen contents in the unexposed materials were measured as approximately 2 ppm, which was considered as the hydrogen background for methane determination

(14) A relationship of hydrogen damage and methane content was established:

$$FA\% \text{ or/and } FL\% = 0.17\ C_{CH4}\ (ppm)$$

This equation can be applied to determine the hydrogen damage by methane determination using a small amount of sample (minimum 6 grams of bulk sample).

(15) Decarburization and reduction in hardness were observed in the hydrogen damaged region. However, the measurements of carbon content and hardness for hydrogen damage evaluation show less sensitive than SEM and methane determination.

(16) Hydrogen attack susceptibility was significantly reduced with the increase in Mo/C ratio (MPC-3: Mo/C 2.29, MPC-13: Mo/C 3.80). The addition of carbide forming alloying elements, such as Mn, V, and Cr (SA-508, SA-533, and 1.25Cr-0.5Mo), decreased the hydrogen attack tendency by carbide stabilization.

(17) Hydrogen attack susceptibility of annealed only material (C-0.5Mo) was ranked as the greatest among the annealed & tempered (1283°F-15 hrs. and 1337°F-15 hours) and normalized & tempered material conditions. A tempering heat treatment enhanced the resistance to hydrogen attack by the formation of stable carbides.

(18) Autoclave hydrogen exposure tests demonstrated that the CGHAZ is the most susceptible location to hydrogen attack in a weld, which is consistent with the results observed in the service exposed weldments.

The CGHAZ with low heat input is more susceptible to hydrogen attack compared to the high heat input.

(19) Postweld heat treatment enhanced the resistance of hydrogen attack in the CGHAZ.

(20) Hydrogen attack was not found in the SAW (service exposed) and SMAW (autoclave exposed) weld metals, which indicated that the weld metals with low carbon are not susceptible to hydrogen attack.

(21) The fine-grained HAZ (FGHAZ) was demonstrated to be less susceptible to hydrogen attack compared to the CGHAZ and base metals in the long seam SAW and SMAW welds.

(22) Cold working increased hydrogen attack susceptibility in comparison with the N&T and hot worked materials. Hydrogen attack damage was promoted with the increase in cold work deformation. The acceleration of hydrogen attack in cold worked materials was explained by the introduction of localized residual stress and microvoids around carbides during cold working.

(23) There is no significant difference in hydrogen attack susceptibility for the hot worked materials with different levels of plastic deformation (5, 10, 20%). Hydrogen attack susceptibility of the hot worked materials is equivalent to the N&T material.

(24) Phase transformation and carbide evolution were investigated using MPC-3 and MPC-13 representing high carbon (0.21%) and low carbon

(0.15%) materials. Heat treatment CCT diagrams were developed for C-0.5Mo steel with high and low carbon contents using Gleeble thermal simulation and high speed dilatometry.

(25) Four possible austenitic transformation products were determined to be martensite, bainite, ferrite, and pearlite at cooling rates from 6000 to 1 C°/min.

(26) Welding CCT diagrams were developed for the CGHAZ of C-0.5Mo steel (MPC-3, MPC-13). Martensite and bainite were formed in the CGHAZ for heat inputs of 12, 50, and 120 KJ/in.

(27) The CCT diagram for MPC-13 with low carbon content (0.15%) was shifted to the left and the martensite starting transformation temperature is higher relative to the CCT diagram for MPC-3 with high carbon content (0.21%). This indicates that MPC-3 material with high carbon content is more hardable than MPC-13 material with low carbon content.

(28) Metallographic examinations using OLM and SEM demonstrated one-to-one agreement with the microstructure prediction by the CCT diagrams.

(29) Carbides in the bainitic and pearlitic regions were identified as M_3C type for material cooled at 20 and 1 C°/min, which is generally corresponding to normalizing and annealing heat treatments. A small amount of Mo_2C carbides were observed in the ferrite grain matrix for both cooling rates.

(30) After tempering at 1150°F (621°C) for 15 hours, the predominant carbides were identified as $M_{23}C_6$ for both the rates of 20 and 1 C°/min.

In addition, more Mo_2C carbides were found in the ferrite grain matrix and grain boundaries after tempering.

(31) More stable carbides formed in C-0.5Mo steel after tempering heat treatment or PWHT enhance hydrogen attack resistance.

(32) Methane evolution was investigated for the early stage of hydrogen attack (500 hrs.) by determining the methane concentration as a function of exposure time. Methane concentration (C_{CH4}, ppm) increases with the increase in exposure time (t, hour) in a linear relationship as expressed as:

$$C_{CH4} = A\,t$$

where "A" is methane formation rate depending upon temperature, hydrogen partial pressure, and materials. Methane evolution study demonstrated that the methane formation started at the beginning of hydrogen exposure in the experimental conditions of 850°F-500 psi H_2.

(33) An in-situ methane bubble nucleation mechanism was proposed in accord with the reaction of cementite (Fe_3C) and hydrogen. The in-situ nucleation mechanism was verified by "Cryo-cracking" fractographic examination using SEM.

(34) The methane pressure through the wall of the one-side exposure assembly was calculated based on hydrogen diffusion, hydrogen concentration distribution, and methane formation free energy.

(35) The hydrogen attack mechanism through the wall thickness of the one-side hydrogen exposure was proposed to illustrate the progression of hydrogen attack in terms of hydrogen gas adsorption, dissociation, absorption, and diffusion; carbide dissolution and diffusion; methane formation; methane bubble initiation, growth, coalescence to form microcracks.

(36) In accordance with the examination of the database for the C-0.5Mo Nelson Curve development, it was found that the C-0.5Mo Nelson Curve in API Publication 941 was defined only based on an insufficient and unreliable database.

(37) A model of hydrogen attack limit (Nelson Curve) for C-0.5Mo steel was developed by using a critical value (-9.0) determined in this research to hydrogen attack parameter (P_w) as expressed as follows:

$$T = 9918 / (3 \log P_{H2} + \log t + 9.0)$$

Assuming operating time is approximately 28 years, a relationship of temperature and hydrogen partial pressure (hydrogen attack limit or Nelson Curve) for C-0.5Mo can be stated as:

$$T = 9918 / (3 \log P_{H2} + 14.2)$$

This temperature and hydrogen partial pressure relationship satisfies the hydrogen attack limit defined in this research for safe operation for approximately 28 years.

(38) Hydrogen attack is characterized as a time dependent process by the demonstration of the modeling of hydrogen attack limits for different exposure times. The hydrogen attack limit decreases with the increase in exposure time. In accord with the modeling, the exposure time for the C-0.5Mo steel defined in API publication 941 was derived as 10,500 hours (approximately 14 months), which is, on its face, not valid for long term operation.

(39) Because of the time-dependence of hydrogen attack, it is suggested that the time for safe operation should be recommended on Nelson Curves. In according to the updated database in this research, a hydrogen attack limit was defined for C-0.5Mo for a safe operation for approximately 28 years, which is below the carbon steel Nelson Curve.

(40) A general model of hydrogen attack limit is expressed as follows:

$$T = 9918 / (3 \log P_{H2} + \log t + P_w^{cr.})$$

where $P_w^{cr.}$ is a critical hydrogen attack parameter that depends on materials, exposure time, and evaluation methodologies.

(41) A methodology for hydrogen damage evaluation is recommended by methane determination incorporated with two master curves (fraction of damaged grain boundaries vs. methane content and bubble size vs. fraction of damaged grain boundaries) which were developed in this research. Using this methodology, the fraction of damaged grain

boundaries and methane bubble size can be quantitatively derived from methane determination.

(42) Hydrogen attack morphology in terms of isolated bubbles, aligned bubbles, and microcracks corresponding to the fraction of damaged grain boundaries can be predicted by using the methodology recommended. Microcracks can be resolved by OLM and advanced ultrasonic testing technique (such as PortaScan007). SEM is required for the examination of isolated and aligned methane bubbles.

CHAPTER 7

FUTURE WORK

(1) Effect of hydrogen attack damage on mechanical properties through the wall thickness of the one-sided hydrogen exposure assembly should be conducted to establish an additional criterion for fitness-for-service evaluation.

(2) Further studies of the influence of microstructure, carbon content, and Mo/C on hydrogen attack susceptibility should be extended for different heat treatment conditions in terms of sub-critical heat treatment, normalizing, annealing, and tempering using one-side hydrogen exposure techniques.

(3) The effect of external stress on the characteristics of methane bubble initiation and growth should be studied by exposing samples with in situ loading to develop a model for inclusion of the effect of external stress.

(4) The calculation of equilibrium methane pressure should be refined and extended to the reaction of hydrogen with alloying carbides by using more accurate thermodynamic models.

(5) Refine a screening methodology for hydrogen attack evaluation for in-service petroleum refinery and petrochemical equipment.

REFERENCES

REFERENCES

[1] C. Bosen, "Attack of Steel under Conditions of Ammonia Synthesis," *Die Chem. Fabrik*, pp. 127, 1933.

[2] N. P. Inglis and W. Andrews, "The Effect on Various Steels of Hydrogen at High Pressures and Temperatures," *The Journal of the Iron and Steel Institute*, vol. 128, pp. 383-408, 1933.

[3] T. C. Evans, "Hydrogen Attack on Carbon Steels," *Mechanical Engineering*, vol. 70, pp. 414-416, 1948.

[4] G. A. Nelson, "Metals for High Pressure Hydrogenation Plants," *Transactions of the American Society of Mechanical Engineers*, vol. 73, pp. 205-213, 1951.

[5] P. F. Timmins, "Solutions to Hydrogen Attack in Steels,". Materials Park, OH: ASM International, 1997, pp. 135-168.

[6] API, "Steels for Hydrogen Service at Elevated Temperatures and Pressures in petroleum Refineries and Petrochemical Plants," *API Publication 941, 5th Edition*, 1997.

[7] D. E. Moore and M. Prager, "An Overview of Carbon-0.5Moly Research Activities and Problems," presented at Serviceability of Petroleum, Process, and Power Equipment, Pressure Vessels and Piping Conference, New Orleans, USA, 1992.

[8] G. R. Prescott, P. Blommaert, and L. Grisolia, "Failure of High Pressure Synthesis Pipe," *AIChE Technical Manual*, vol. 26, 1986.

[9] C. D. Lundin and P. Liu, "Evaluation of Hydrogen Attack Damage in C-1/2Mo Weldment (MPC-18)," *MPC Technical Report, MolyHy-13*, 1998.

[10] T. Ishiguro, K. Kimura, T. Hatakeyama, T. Tahara, and K. Kawano, "Effect of Metallurgical Factors on Hydrogen Attack resistance in C-0.5Mo Steel," presented at Second International Conference on Interaction of Steels with Hydrogen in Petroleum Industry Pressure Vessel and Pipeline Service, Vienna, Austria, 1994.

[11] T. Ishiguro, "Communication Letter,"., 1997.

[12] M. W. D. van der Burg and E. van der Giessen, "Non-Uniform Hydrogen Attack Cavitation and the Role of Interaction with Creep," *Materials Science and Engineering*, vol. A220, pp. 200-214, 1996.

[13] M. W. D. van der Burg, E. van der Giessen, and R. C. Brouwer, "Investigation of Hydrogen Attack in 2.25Cr-1Mo Steels with a High-Triaxiality Void Growth Model," *Acta Materials*, vol. 44, pp. 505-518, 1996.

[14] M. W. D. van der Burg, E. van der Giessen, and V. Tvergaard, "A Continuum Damage Analysis of Hydrogen attack in a 2.25Cr-1Mo Pressure Vessel," *Materials Science and Engineering*, in print.

[15] S. M. Schlogl, van der Burg, M.W.D., van der Giessen, E., and Koers, R., "Theoretical Hydrogen Attack Modeling in Europe," presented at API/MPC Workshop and Working Group, Dallas, Texas, 1997.

[16] T. A. Parthasarathy, H. F. Lopez, and P. G. Shewmon, "Hydrogen Attack Kinetics of 2.25Cr-1Mo Steel Weld Metals," *Metallurgical Transactions A*, vol. 16A, pp. 1143-1149, 1985.

[17] G. A. Nelson, "Hydrogenation Plant Steels," presented at API Proceedings, 1949.

[18] G. A. Nelson and R. T. Effinger, "Blistering and Embrittlement of Pressure Vessel Steels by Hydrogen," *Welding Journal*, vol. 34, pp. 12s-21s, 1955.

[19] G. A. Nelson, "Section II - Action of Hydrogen on Steel at High Temperature and High Pressures," *WRC Bulletin 246*, pp. 33-42, 1969.

[20] API, "Steels for Hydrogen Service at Elevated Temperatures and Pressures in Petroleum Refineries and Petrochemical Plants," *API Publication 941, First Edition*, 1970.

[21] API, "Steels for Hydrogen Service at Elevated Temperatures and Pressures in Petroleum Refineries and Petrochemical Plants," *API Publication 941, Second Edition*, 1977.

[22] API, "Steels for Hydrogen Service at Elevated Temperatures and Pressures in Petroleum Refineries and Petrochemical Plants," *API Publication 941, Third Edition*, 1983.

[23] API, "Steels for Hydrogen Service at Elevated Temperatures and Pressures in petroleum Refineries and Petrochemical Plants," *API Publication 941, Fourth Edition*, 1990.

[24] D. Eliezer and H. G. Nelson, "Hydrogen Attack of 1020 Steel: Influence of Hydrogen Sulfide," *Corrosion*, vol. 35, pp. 17-21, 1979.

[25] N. Bailey, *Welding Institute Research Bulletin*, pp. 2-33, 1977.

[26] D. Stone, Z. J. Su, S. Rouff, J. Wanagel, and C. Y. Li, "Hydrogen Attack in Cr-Mo Steels at Elevated Temperatures," Cornell University Final Technical Report (CU/MSE-07963-01), August 1983.

[27] D. Stone, S. Rouff, J. Wanagel, and C. Y. Li, "Hydrogen Attack in Cr-Mo Steels at Elevated Temperatures," Cornell University Final Technical Report (ORNL/Sub/80-7963/01), August 1985.

[28] R. J. Stueber, "A Study of Hydrogen Attack of Steel under Dynamic Exposure Conditions," in *Ph.D. Dissertation*: The University of Wisconsin, 1966.

[29] R. R. Arnold, "A Study of Hydrogen Attack in Low Alloy Steels by the Dynamic Exposure Technique,".: The University of Wisconsin, 1968.

[30] R. E. Bisaro and G. H. Geiger, "Effects of Columbium in Steel on Elevated Temperature Hydrogen Attack," *Corrosion*, vol. 23, pp. 289-296, 1967.

[31] G. H. Geiger, "A Study of the Effects of High-Temperature, High-Pressure Hydrogen on Low-Alloy Steels," *API Publication 945*, June 1975.

[32] JPVRC, "Hydrogen Attack Limit of C-1/2Mo Steel," *JPVRC Document*, May 1987.

[33] W. E. Erwin and J. G. Kerr, "The Use of Quenched and Tempered 2 1/4Cr-1Mo Steel for Thick Wall Reactor Vessels in Petroleum Refinery Processes: An Interpretive Review of 25 Years of Research and Application," *WRC Bulletin 275*, pp. 1-63, February 1982.

[34] M. Prager, "Hydrogen Attack Susceptibility of Chrome-Moly Steels and Weldments," presented at Proceedings on Serviceability of Petroleum Process, and Power Equipment, ASME 1992, The 1992 Pressure Vessels and Piping Conference, New Orleans, USA, 1992.

[35] C. D. Lundin, K. Khan, P. Liu, and M. Prager, "Study of Hydrogen Attack Susceptibility of 2 1/4Cr-1Mo Steel," presented at Second International Conference on Interaction of Steels with Hydrogen in Petroleum Industry Pressure Vessel and Pipeline Service, Vienna, Austria, October 19-21, 1994.

[36] J. Wanagel, T. Hakkarainen, and C. Y. Li, "Hydrogen Attack in Thick-Section 2 1/4Cr-1Mo Steels at Elevated Temperatures," *A Symposium on Application of 2 1/4Cr-1Mo Steel for Thick-Wall Pressure Vessels, ASTM STP 755*, pp. 93-109, May19-20, 1980.

[37] J. D. Landes, "Understanding Toughness Testing for Hydrogen Embrittlement," presented at MPC/API Task Group on Materials for

Pressure vessel Service with Hydrogen at High Temperatures and Pressures, 1987.

[38] P. G. Shewmon and Y. H. Xue, "Effect of High -Pressure Hydrogen on Crack Growth in Carbon Steel," *Metallurgical Transactions A*, vol. 22A, pp. 2703-2707, 1991.

[39] L. C. Chen, P. G. Shewmon, and M. Prager, "Stress Assisted Hydrogen Attack Cracking in 2.25Cr-1Mo Steels at Elevated Temperatures," presented at Second International Conference on Interaction of Steels with Hydrogen in Petroleum Industry Pressure Vessel and Pipeline Service, Vienna, Austria, 1994.

[40] L. C. Chen and P. G. Shewmon, "Stress-Assisted Hydrogen Attack Cracking in 2.25Cr-1Mo Steels at Elevated Temperatures," *Metallurgical Transactions A*, vol. 26A, pp. 2317-2327, 1995.

[41] T. Watanabe, T. Ishiguro, T. Iwadate, and K. Ohnishi, "Hydrogen Embrittlement of 2.25-1Mo and 3Cr-1Mo-0.25V-Ti-B Pressure Vessel Steels," presented at API/MPC Meeting, Atlanta, USA, May 14-15, 1987.

[42] M. Mckimpson and P. G. Shewmon, "Initial Hydrogen Attack Kinetics in a Carbon Steel," *Metallurgical Transactions A*, vol. 12A, pp. 825-834., 1981.

[43] K. Kawano, F. Sakota, K. Hattori, H. Okada, H. Yamamoto, T. Tahara, H. Tanaka, and T. Ishiguro, "UT and Metallurgical Evaluations on Hydrogen Attacked C-1/2Mo Steel Pressure Vessels," presented at The

Proceedings on Serviceability of Petroleum, Process, and Power Equipment, The 1992 Pressure Vessels and Piping Conference, New Orleans, Louisiana, June 21-25 1992.

[44] A. S. Birring, J. Elliott, and C. P. Hsiao, "Detection of Hydrogen Attack in Base Metal and Weld HAZ," presented at The Proceedings on International Pressure Vessels and Piping Codes and Standards, The 1995 Pressure Vessels and Piping Conference, Honolulu, Hawaii, July 23-27, 1995.

[45] T. Nomura and T. Imanaka, "Ultrasonic Detection of Hydrogen Attack in Low Alloy Steel," presented at The Proceedings on Determining Material Characterization: Residual Stress and Integrity with NDE, The 1994 Pressure Vessels and Piping Conference, Minneapolis, Minnesota, June 19-23, 1994.

[46] M. Nakashiro, Y. Skai, T. Yoshida, S. Shibata, and H. Yoneyama, "Failure Analysis of Carbon Steel Elbow Damaged in Long-Term Service at Petrochemical Plant and Verification of Ultrasonic Noise Analysis Method of Creep Damage Assessment," presented at The Proceedings on Determining Material Characterization: Residual Stress and Integrity with NDE, The 1994 Pressure Vessels and Piping Conference, Minneapolis, Minnesota, June 19-23, 1994.

[47] T. P. Groeneveld, "The Effect of Austenitic Stainless Steel Weld Overlay or Cladding on the Hydrogen Content and Hydrogen Attack of the

Underlying Steel in Petrochemical Reactor Vessels," presented at Proceedings of the International Conference on Interaction of Steels with Hydrogen in Petroleum Industry Pressure Vessel Service, Paris, France, Mach 28-30, 1989.

[48] Y. Tomita and H. Yamamoto, "Properties Evaluation of 0.5Mo Steel Damaged by Hydrogen Attack," *Technical Report*, 1998.

[49] T. Imanaka and J. Suetsugu, "Detection of Hydrogen Attack Sound Wave Velocity and Acoustic Emission Measurements," presented at The Proceedings on Fitness-for -Service and Decisions for Petroleum and Chemical equipment, The 1995 Pressure Vessels and Piping Conference, Honolulu, Hawaii, July 23-27, 1995.

[50] S. F. Clugston, J. R. Weertman, and P. G. Shewmon, "The Enhancement of Hydrogen Attack in Steel by Prior Deformation," *Metallurgical Transactions A*, vol. 14A, pp. 695-699, 1983.

[51] B. J. Cocke, C. D. Buscemi, and D. E. Moore, "Hydrogen Attack of Cr-Mo Reactor Steels," *Proceedings of the International Conference on Interaction of Steels with Hydrogen in Petroleum Industry Pressure Vessel Service, Paris*, pp. 149-165, March 28-30, 1989.

[52] J. E. Cantwell, "High Temperature Hydrogen Attack: A 50 Year Overview,," *Corrosion 93 The NACE Annual Conference and Corrsion Show*, pp. 583/2-583/9, 1993.

[53] F. H. Vitovec, "The Growth Rate of Fissures during Hydrogen Attack of Steels," presented at Proceedings of American Petroleum Institute, New York, 1964.

[54] P. G. Shewmon, "Hydrogen Attack of Pressure-Vessel Steels," *Materials Science and Technology*, vol. 1, pp. 2-11, 1985.

[55] G. R. Prescott, "Hydrogen Attack of C-1/2Mo Steel," *MOLYHY-6, MPC Document*, pp. 111-145, October 30-31, 1995.

[56] A. Berzolla, A. Bertoni, T. Bocquet, and G. Hauck, "The New 2 1/4Cr and 3Cr1Mo1/4V Steels for Pressure Vessels Operating in Hydrogen Environment," presented at Second International Conference on Interaction of Steels with Hydrogen in Petroleum Industry Pressure Vessel and Pipeline Service, Vienna, Austria, October 19-21, 1994.

[57] B. Panda, "Kinetics of Hydrogen Attack in a 1020 Steel,".: The Ohio State University, 1982.

[58] C. D. Lundin, P. Liu, and G. Zhou, "Metallographic Evaluation of the Service Exposed C-1/2Mo Steel Welds," Technical Report, The University of Tennessee December 1995.

[59] R. Chiba, K. Ohnishi, K. Ishii, and K. Maeda, "Effect of Heat Teatment on Hydrogen Attack REsistance of C-0.5Mo Steels for Pressure Vessels, Heat Exchanges, and Piping," *Corrosion*, vol. 41, pp. 415-426, 1985.

[60] R. Chiba, K. Ohnishi, K. Ishii, and K. Maeda, "Effect of Heat Treatment on the Resistance of C-0.5Mo Steels Base metal and Its Welds to Hydrogen Attack," *Corrosion and Materials Engineering*, pp. 57-74, 1985.

[61] K. Kimura, T. Ishiguro, K. Kawano, K. Hattori, H. Yamanoto, H. Okada, and K. Skamoto, "Metallurgical Effect on Hydrogen Attack Damage in C-1/2Mo Steels," presented at Proceedings on Structural Integrity, NDE, Risk and Material Performance for Petroleum, Process, and Power, Vol. 336, 1996.

[62] T. G. Su, X. H. Luo, F. C.G., Y. Y. Li, X. Chen, and A. M. Guo, "Tempering Precipitates of Steel 1.25Cr-0.5Mo and Their Effects on Its Hydrogen Attack Resistance," *Acta Metallurgica Sinica*, vol. 34, pp. 393-399 (in Chinese), 1998.

[63] T. Sakai, Asami, K., Kondo, N., and Hayashi, T., "Effects of Carbide Forming Elements on Hydrogen Attack and Embrittlement in 2.25Cr-1Mo Steel," *Journal of the Iron and Steel Institute of Japan*, vol. 73, pp. 372-379, 1987.

[64] H. L. Schick, *Thermodynamics of Certain Refractory compounds*: Academic Press, 1966.

[65] R. G. Baker and J. Nutting, "The Tempering of 2 1/4%Cr-1%Mo Steel after Quenching and Normalizing," *Journal of the Iron and Steel Institute of Japan*, pp. 257-267, 1959.

[66] K. Natesan, O. K. Chopra, and T. F. Kassner, "Compatibility of Fe-1/4 wt% Cr-1 wt% Mo Steel in a Sodium Environment," *Nuclear Technology*, vol. 28, pp. 441-451, 1976.

[67] T. A. Parthasarathy and P. G. Shewmon, "Effects of Tempering on the Carbon Activity and Hydrogen Attack Kinetics of 2.25Cr-1Mo Steel," *Metallurgical Transactions A*, vol. 15A, pp. 2021-2027, 1984.

[68] K. Natesan and T. Kassner, "Monitoring and Measurement of Carbon Activity in Sodium Systems," *Nuclear Technology*, vol. 19, pp. 46-57, 1973.

[69] K. Natesan and T. F. Kassner, "Thermodynamics of Carbon in Nickel, Iron-Nickel and Iron-Chromium-Nickel Alloys," *Metallurgical Transactions A*, vol. 4, pp. 2557-2566, 1973.

[70] J. H. Woodhead and A. G. Quarrell, "The Role of Carbides in Low-Alloy Creep-Resisting Steels," The University of Sheffield.

[71] A. Vyrostkova, A. Kroupa, J. Janovec, and M. Svoboda, "Carbide Reactions and Phase Equilibria in Low Alloy Cr-Mo-V Steels Tempered at 773-993 K, Part I: Experimental Measurements," *Acta Materials*, vol. 46, pp. 31-38, 1998.

[72] A. Kroupa, A. Vyrostkova, M. Svoboda, and J. Janovec, "Carbide Reactions and Phase Equilibria in Low Alloy Cr-Mo-V Steels Tempered at 773-993 K, Part II: Theoretical Calculations," *Acta Materials*, vol. 46, pp. 39-49, 1998.

[73] J. H. Holloman and L. D. Jaffe, "Time-Temperature Relations in Tempering Steel," *Transactions of AIME*, vol. 162, pp. 223-249, 1945.

[74] B. J. Shaw, "A Study of Carbides Formed in Low Alloy Cr-Mo steels," presented at The 1984 PVP Conference and Exhibition, San Antonio, Texas, June 17-21, 1984.

[75] K. J. Irvine and F. B. Pickering, "The tempering Characteristics of Low-Carbon Low-Alloy Steels," *Journal of the Iron and Steel Institute of Japan*, vol. 194, pp. 137-153, 1960.

[76] D. Raynor, J. A. Whiteman, and R. W. K. Honeycomb, "In-Situ Transformation of Fe_3C to Mo_2C in Iron Molybdenum-Carbon Alloys," *Journal of the Iron and Steel Institute of Japan*, vol. 204, pp. 1114-1116, 1966.

[77] C. H. M. Jenkins and E. A. Jenkinson, "Investigation of the Behaviour of Metals under Deformation at High Temperatures," *Journal of The Iron and Steel Instititute*, vol. 185, pp. 23-46, 1957.

[78] D. J. Dyson and K. W. Andrews, "The Structure and Mtallurgical Significance of The Iron-Molybdenum Carbide Fe2MoC," *Journal of the Iron and Steel Institute of Japan*, vol. 202, pp. 325-329, 1964.

[79] B. Panda and P. G. Shewmon, "Kinetics of Methane Bubble Growth in a 1020 Steel," *Metallurgical Transactions A*, vol. 15A, pp. 487-494, 1984.

[80] T. A. Parthasarathy, "Mechanisms of Hydrogen Attack of Carbon and 2 1/4Cr-1Mo Steels," *Acta Metallurgica*, vol. 33, pp. 1673-1680, 1985.

[81] T. Nomura and T. Sakai, "Theoretical and Parametric Methods for Evaluating Hydrogen Attack Limit," presented at Proceedings of PVP Conference on Fitness for Adverse Environments in Petroleum and Power Equipment, Orlando, Florida, July 27-31, 1997.

[82] P. G. Shewmon and P. Anderson, "Void Nucleation and Cracking at Grain Boundaries," *Acta Materials*, vol. 46, pp. 4861-4872, 1998.

[83] O. T. Saugerud, D. E. Moore, and G. R. Odette, "A Model-Based Approach to Evaluating the Probability and Criticality of Hot Hydrogen Attack in C-1/2Mo Equipment," presented at The Proceedings on Serviceability of Petroleum, Process, and Power Equipment, The 1992 Pressure Vessels and Piping Conference, New Orleans, Louisiana, June 21-25, 1992.

[84] R. J. Steuber and G. H. Geiger, "Hydrogen Attack of Steel under Dynamic Exposure Conditions," *Corrosion*, vol. 22, pp. 309-319, 1966.

[85] S. S. Vagarali and G. R. Odette, "A Model for the Growth of Hydrogen Attack Cavities in Carbon Steels," *Metallurgical Transactions A*, vol. 12A, pp. 2071-2082, 1981.

[86] API, "The Effect of Outgassing Cycles on the Hydrogen Content in Petrochemical-Reactor-Vessel Steels," *API Publication 946*, July 1981.

[87] M. Yamashita, A. Sumihiro, T. Watanabe, and N. Kato, "Detection of carbides in CrMoV Steel by Electrochemical Method," presented at The Proceedings on Determining Material Characterization: Residual Stress

and Integrity with NDE, The 1994 Pressure Vessels and Piping Conference, Minneapolis, Minnesota, June 19-23, 1994.

[88] T. Lyman, *Metals Handbook*, vol. 8, 8th ed. Ohio: American Society for Metals, 1973.

[89] ASTM, *Standard Test Method for Determing Volume Fraction by Sysmetic Manual Point Count*, vol. 03.03: ASTM, 1999.

[90] NIH, *NIH Image Manual*, 1998.

[91] H. E. McGannon, *The Making, Shaping, and Treating of Steel*, 9th ed. Pittsburgh, Pennsylvania,: Herbick & Held.

[92] Y. Houbaert and J. Dilewijns, "Study of the Toughness of Hydrogen Attacked Steel," presented at Proceedings of the International Conference on Interaction of Steels with Hydrogen in Petroleum Industry Pressure Vessel Service, Paris, France, Mach 28-30, 1989.

[93] M. Prager, "Proposed Test Plan and ATACKPRO.WKZ Spreadsheets," *MPC Technical Report*, January 1997.

[94] T. G. V. JPVRC, "Assessment of Hydrogen Attack in 0.5Mo Steels,", 1997 (in Japanese).

[95] M. L. Hill and E. W. Johnson, "The Solubility of Hydrogen in Alpha Iron," *Transactions of the Metallurgical Society of AIME*, vol. 221, pp. 622-628, 1961.

[96] ASME, *Rules for Construction of Pressure Vessels*, vol. Section VIII, Division 1. New York: ASME, 1995.

[97] ASME, *ASME Boiler and Pressure Vessel Code, Materials, Part D-Properties*, vol. Section II. New York: ASME, 1995.

[98] M. Ransick and P. G. Shewmon, "Effect of Cold Work on Hydrogen Attack," *Metallurgical Transaction A*, vol. 12A, pp. 17-22, 1981.

[99] H. H. Podgurski, "Trapping of Hydrogen in Cold-Worked Steel," *Transactions of The Metallurgical Society of AIME*, vol. 221, pp. 389-394, 1961.

[100] J. A. Todd, "The Early Stages of Tempering in a 3Cr-1.5Mo Steel," *Metallugica Scripta*, vol. 20, pp. 269-274, 1986.

[101] M. Prager, "Report to API on the Technical Basis for API 941," The Materials Properties Council, Inc., New York, NY, 2001.

[102] J. D. Fast, *Gases in Metals*. London: The Macmillan Press LTD, 1976.

[103] G. Sundararajan and P. G. Shewmon, "The Hydrogen Attack of HSLA Steel," *Metallurgical Transaction A*, vol. 11A, pp. 509-516, 1980.

[104] H. Lopez and P. G. Shewmon, "Precipitation induced Voids in Quenched and Tempered Steel," *Acta Metallurgica*, vol. 31, pp. 1945-1950, 1983.

[105] T. J. Hakkarainen, J. Wanagel, and C. Y. Li, "Direct Obervation of Methane Bubbles in a 2-1/4Cr-1Mo Steel after Hydrogen Exposure," *Metallurgical Transaction A*, vol. 11A, pp. 2035-2036, 1980.

[106] F. R. Hutchings and P. M. Unterweiser, *Failure Analysis*. Metals Park, OH: American Society for Metals, 1981.

[107] R. C. Weast, *CRC Handbook of Chemistry and Physics*, 58 ed. Cleveland, OH: CRC Press, Inc., 1978.

[108] M. H. Armbruster, "The Solubility of Hydrogen at Low Pressure in Iron, Nickel and Certain Steels, at 400 to 600°C," *Journal of American Chemistry Society*, vol. 65, pp. 1043-1054, 1943.

[109] W. Geller, and Sun, T.H., "Influence of Alloy Addition upon the diffusion of Hydrogen in Iron and Contibution to the Fe-H System," *Arch. Eisenhuttenwesen*, vol. 21, pp. 423-430, 1950.

[110] P. G. Shewmon, *Diffusion in Solids*. New York: McGraw-Hill Book Company, Inc., 1963.

[111] J. Chipman, "Thermodynamics and Phase Diagram of the Fe-C System," *Metallurgical Transactions*, vol. 3, pp. 55-64, 1972.

[112] R. Baboian, *Corrosion Tests and Strandards: Application and Interpretation*. Philadelphia: ASTM Publisher, 1990.

[113] G. R. Odette and S. S. Vagarali, "An Equaiton of State for Methane for Modeling Hydrogen Attack in Ferritic Steels," *Metallurgical Transactions A*, vol. 13A, pp. 299-303, 1982.

[114] W. Jackson, *Grain Boundaries in Metals*. London: Oxford University Press, 1957.

[115] F. D. Richardson, "The Thermodynamics of Metallurgical Carbides and Carbon in Iorn," *Journal of The Iron and Steel Instititute*, vol. 175, pp. 33-51, 1953.

[116] F. H. Vitovec, "Modeling of Hydrogen Attack of Steel in Relation to Material and Environmental Variables," presented at Proceedings of the First International Conference on Current Solutions to Hydrogen Problems in Steels, Washington DC, November 1-5, 1982.

[117] G. Sundararajan and P. G. Shewmon, "The Kinetics of Hydrogen Attack of Steels," *Metallurgical Transaction A*, vol. 12A, pp. 1761-1775., 1981.

[118] K. Hattori and S. Aikawa, "Scheduling and Planning Inspection of C-1/2Mo Equipment Using the New Hydrogen Attack Tendency Chart," presented at The Proceedings on Serviceability of Petroleum, Process, and Power Equipment, The 1992 Pressure Vessels and Piping Conference, New Orleans, Louisiana, June 21-25, 1992.

[119] K. Hattori, "An Advanced Hydrogen Attack Tendency Chart as a Life Assessment Strategy for C-1/2Mo Equipment," presented at Proceedings on Fitness for Adverse Environments in Petroleum and Power Equipment, The 1997 ASME Pressure Vessels and Piping Conference, Orlando, Florida, July 27-31, 1997.

VITA

Peng Liu was born in Shannxi, P.R. China. He graduated from a public high school in 1973. He received the degree of Bachelor of Science from the Xi'an Jiaotong University of China in 1981 and the degree of Master of Science from the Institute of Metal Research, The Chinese Academy of Science, in 1983. After graduation, he was a scientist in the Institute of Metal research, The Chinese Academy of Science. He joined the Ph.D. program in the Department of Materials Science and Engineering at The University of Tennessee, Knoxville. He was awarded the degree of Doctor of Philosophy with a major in Metallurgical Engineering in 2001.

During his graduate student study at The University of Tennessee, Knoxville, Peng Liu received the 1999 Henry Granjon Prize from the International Institute of Welding to recognize his fundamental research on advanced high temperature materials. He is a member of American Welding Society, American Society of Materials International, and American Minerals, Metals and Materials Society.